T-4432

GEOLOGY OF THE EAGLE CRAGS VOLCANIC FIELD, NORTHERN MOJAVE DESERT, CHINA LAKE NAVAL AIR WEAPONS STATION, CALIFORNIA

by
Andrew E. Sabin

T-4432

A thesis submitted to the Faculty and the Board of Trustees of the Colorado School of Mines in partial fulfillment of the requirements for the degree of Doctor of Philosophy in Geology.

Golden, Colorado
Date 3-1-94

Signed: _____
Andrew E. Sabin

Approved: _____
Richard W. Hutchinson
Thesis Advisor

Golden, Colorado
Date 3/3/94

_____
Roger M. Slatt, Head
Department of Geology and
Geological Engineering

ABSTRACT

A series of intermediate to silicic tuffs, tabular flows, flow breccias, dikes, plugs and hypabyssal rocks ranging from tholeiitic basalt to high-silica rhyolite comprise a volcanic field, herein referred to as the Eagle Crags Volcanic Field (ECVF). The ECVF formed during the Late to Middle Miocene and is dominated by the eroded and tectonized remains of a stratovolcano. Andesitic and dacitic tuffs and flows constitute the greatest volume of volcanic rocks in the region.

The compositionally diverse, interfingering flows, tuffs and vent facies rocks indicate a stratovolcano source. Gently southwest-dipping sheet-like flows, tuffs and lahars in the southern part of the field are distal products from the volcano's central vent. An arcuate-shaped, high-angle normal fault forms the southern, structural rim of a caldera formed after one of the last central vent eruptions. This vent was obliterated by this collapse feature. The thicknesses and components of all units exposed in the fault scarp indicate that these exposures are vent-proximal.

Multiple sites and styles of vents and feeder dikes have been identified. They include: 1) fissure vents; 2) high-silica, rhyolitic feeder dikes; 3) a pyroclastic eruptive center, and 4) volcanic necks or hypabyssal plugs composed of rhyolite and dacite. Most of these features appear to parallel local and regionally extensive NW- and NE-trending faults. These faults probably controlled the location of volcanic vents and late syn- or post-volcanic hydrothermal fluids.

Apparent low temperature alteration is silicic, propylitic and argillic. Anomalously high concentrations of Hg, Sb, As, Ba and W ±Au ±Ag ±Cs were found in these altered rocks. The combination of ephemeral hot-springs and high concentrations of trace elements characteristic of epithermal, precious metal deposits makes this region prospective for geothermal resources and possibly precious metals.

$^{40}Ar/^{39}Ar$ geochronology constrains the duration of volcanism in this field from at least 18.7 Ma to 12.4 Ma. Intermediate composition volcanism constitutes the basal portions of the volcanic field. Approximately 18.5 Ma rhyolitic dikes cut some of these units. A limited number of age determinations constrain the duration of rhyolitic volcanism to 200,000-300,000 years.

The Late Miocene formation of rhyodacitic domes was the last volcanic avtivity in the volcanic field. It is unclear whether rhyodacitic activity was the last volcanism in a long-lived volcanic field or if it represents the onset of volcanism after a repose period.

Rhyodacitic volcanism occurred in an extensional environment. Local tilting of small "intracaldera" blocks indicates that the formation of half-grabens may have been synchronous with viscous rhyodacitic doming and northeast-directed extension. A northeast-trending lineament that transects the volcanic field is subparallel to the Garlock fault. An alluvial valley southeast of this lineament may be a transtensional basin formed during right-slip along this linear feature. The structural rim of the caldera is on the southwestern margin of this basin and may be a "breakaway fault", a high-angle normal listric fault that marks the southern limit of localized, northeast-directed extension. Dip measurements of up to 75°SW on young rhyodacitic flows that occupy the former central vent region of this stratovolcano and the configuration of alluvium valleys separating the structural rim from these steeply-dipping beds suggests northeast-directed extension along

a sole fault. This sole fault is the low angle extension of a listric fault that originates at the structural rim.

Field and petrographic characteristics suggest that flows and tuffs of the ECVF were generated from a heterogeneous magma chamber. Most andesitic flows are hybrids. Field relations and petrography suggest they may be the product of mixing of a tholeiitic basaltic melt with a granitic melt. Petrographic and geochemical evidence also point toward fractional crystallization and crustal assimilationas processes that contributed to the evolution of magmas in the ECVF.

TABLE OF CONTENTS

LIST OF FIGURES

LIST OF TABLES

LIST OF PLATES (IN POCKET)

ACKNOWLEDGEMENTS

Many people provided assistance, equipment, financial and moral support during my time here at the Colorado School of Mines. Without their help, I would not have been able to complete this thesis.

I would like to thank my committee members, Professors Dick Hutchinson, Sam Romberger, Craig Simmons and Ric Wendlandt. Their lectures, field trips and informal discussions offered me invaluable insights and perspectives into the field of geology.

I am indebted to Larry Snee, Steve Harlan, and Russ Yeoman of the U.S. Geological Survey, Branch of Isotope Geology, Denver. They taught me the practical aspects of argon geochrnology and allowed me the use of their facilities.

I spent many hours of discussion with Craig Ford, George Langstaff, Jeff Miller and many other former students at CSM. During the rare moments, these conversations sometimes turned to geology. I do and will always appreciate their help, suggestions and friendship.

Dick Hutchinson has not only been a lecturer/tour guide/friend/performer, but he has been an inspiration. His knowledge, enthusiasm, and passion for the field of geology, and his perspective on, as Dan Jenkins would say, "life its ownself," made the travails of graduate school extremely rewarding.

Dr. Frank Monastero of the Geothermal Program Office provided me with the greatest opportunity to excell as a geologist and a graduate student. Frank provided me the opportunity to consider several research ideas, he allowed me the chance to make mistakes,

and he was always available to assist with field work and to discuss all aspects of my research. Solely through Frank's efforts, the field portions of this research and much of the analytical work was funded by the Department of Navy's Geothermal Program Office. I have benefited tremendously from Frank's encouragement, friendship and his tireless advocacy of my work.

Finally, I must thank my parents and family for their support and encouragement. Margaret, Meghan, Katie and Madeleine provided me with the desire to do this.

"...Bend to the persuasion which is flowing to you from every object in nature, to be its tongue to the heart of man, and to show the besotted world how passing fair is wisdom. Forewarned that the vice of the times and the country is an excessive pretension, let us seek the shade, and find wisdom in neglect. Be content with a little light, so it be your own. Explore, and explore. Be neither chided nor flattered out of your position of perpetual inquiry. Neither dogmatize nor accept another's dogmatism. Why should you renounce your right to traverse the star-lit deserts of truth, for the premature comforts of an acre, house, and barn? Truth also has its roof, and bed, and board. Make yourself necessary to the world, and mankind will give you bread, and if not store of it, yet such as shall not take away your property in all men's possessions, in all men's affections, in art, in nature, and in hope."

Ralph Waldo Emerson, address to the Literary Societies,
Dartmouth College, July 24, 1838

"...We are not adequately using the knowledge that we have or...we are not sufficiently producing the knowledge that we actually need."

George E. Brown, Chairman of the House Committee on Science,
Space and Technology
1992

CHAPTER 1
INTRODUCTION

The study area, hereafter referred to as the Eagle Crags Volcanic Field (ECVF), is in the South Ranges of the Naval Air Weapons Station (NAWS), China Lake, CA (Fig. 1). Since the NAWS was created in 1943, all ranges were restricted from public use. The only available geologic map covering the South Ranges is the Trona Sheet (Jenning et al., 1962; 1:100,000 scale). The ECVF is underlain by Mesozoic granites, Tertiary age volcanic rocks, pyroclastic flows and Quaternary alluvium.

Reconnaissance resource evaluations of the region indicate the presence of ephemeral springs with reservoir temperatures of up to 165°C (Austin et al., 1983). Anomalously high soil concentrations of mercury (>6 ppm Hg) near the Myrick Spring area, elevated mercury values in rock analyses in a hydrothermally altered flow ("myrickite") and elevated concentrations of Au and Ag from prospects in the northern portion of the ECVF have also been identified (Austin et al., 1983). A combination of these features in a Tertiary volcanic field suggests a genetic link among hot water, epithermal metal concentrations and volcanism.

Field work was initiated in order to gain a better understanding of alteration and its relationship, if any, to warm water springs in the area. In order to understand local alteration and hot springs, however, the geologic setting needed to be understood. Since virtually nothing was known about the stratigraphy, age or structural setting of the volcanic field, this research evolved into a broad investigation of the geology of the ECVF.

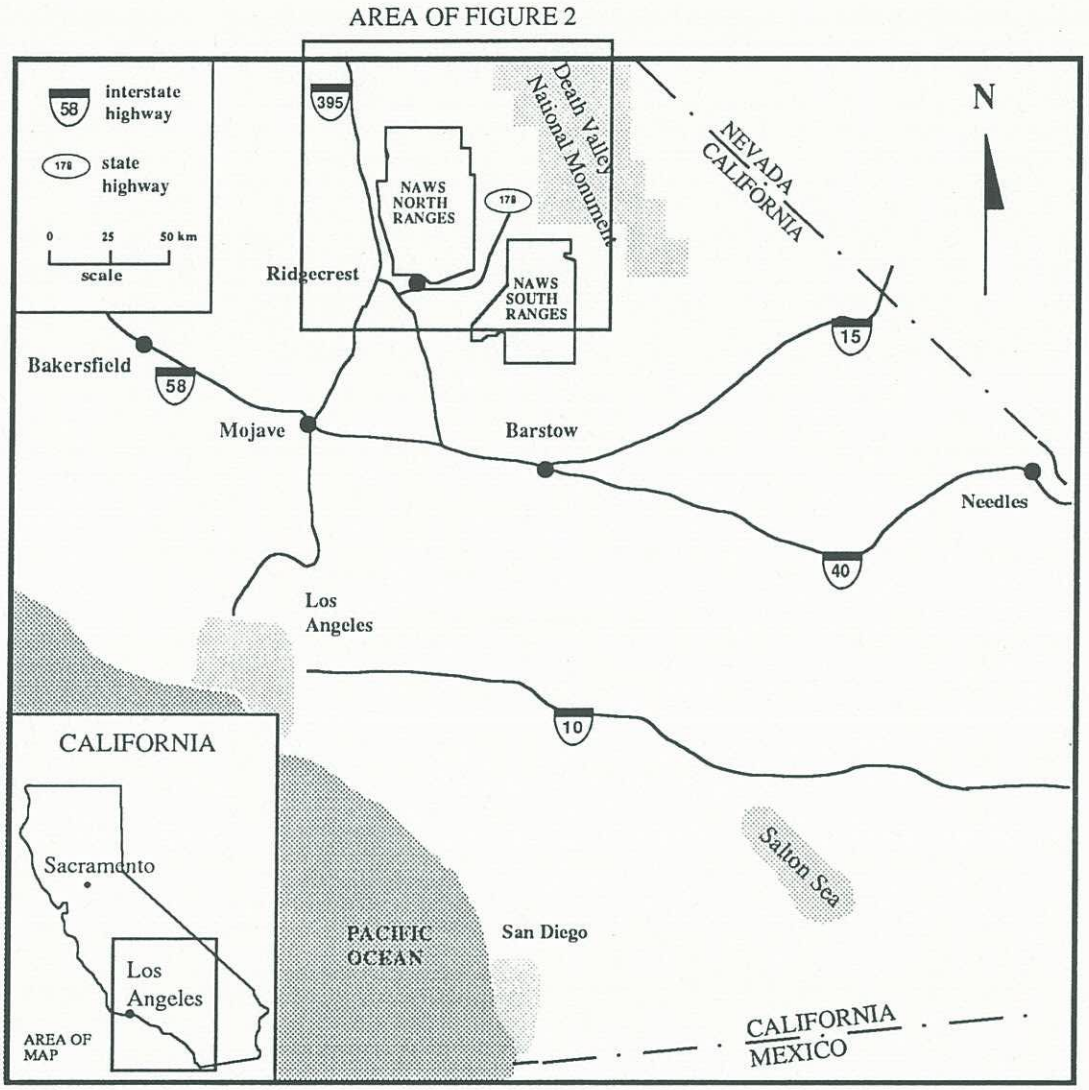

Figure 1. Index map of China Lake Naval Air Weapons Station (NAWS), North and South Ranges.

Through detailed mapping, geochemistry, petrography, geochronology, gravity data interpretation and petrogenetic modeling, this thesis describes dominant units of the ECVF and interprets how the ECVF formed. This research also establishes a foundation upon which detailed geothermal exploration can proceed and regional metal occurrence models can be based. Results of the study also contributes to the understanding of the volcanic and tectonic history of the northern Mojave Desert.

1.1 Purpose

The purposes of this study were to: 1) determine the mineralogy and stratigraphy of the dominant units of the ECVF; 2) reconstruct the timing of volcanism and the relative timing of alteration; 3) identify structures and determine the controls that they may have had on the location of volcanism, alteration and hot springs; and 4) understand the geochemical relationships among the volcanic rocks and hypothesize and evaluate petrogenetic models in an attempt to explain the origin of some of the widespread flows.

Mapping and petrography were performed to determine the types and extent of eruptive products. Age determinations were performed to bracket the age and duration of volcanism and to aid in the correlation among flows in the region. Age determinations also helped in understanding the relative ages of some of the structures in the region. Because alteration appears to be structurally-controlled, knowledge of the relative timing of alteration would assist in geothermal and precious metal exploration.

An evaluation of petrogenetic models was performed in order to reconcile some enigmatic field and petrographic characteristics observed in many of the flows. Additionally, if the type and timing of ECVF volcanism were controlled by the tectonic regime, then an understanding of the origin and evolution of eruptive products may

enhance the understanding of Middle and Late Tertiary tectonics in the Mojave Desert.

1.2 Location and Access

The NAWS occupies over 4,400 km^2 in the northern Mojave Desert and southern Basin and Range provinces. It is directly east of the Sierra Nevada and includes portions of the Coso, Argus, Slate and Granite Mountain ranges, intervening alluvial valleys and many unnamed ranges and valleys (Fig. 2). The southern boundary of the NAWS is 40 km north of Barstow. Its main base near Ridgecrest, California, is about 270 km north of Los Angeles.

State Route 178 divides the NAWS into the North and South Ranges. The volcanic field is bordered to the north by the Randsburg Wash Valley, an east-northeast-trending valley that parallels the southern side of the Garlock fault (Fig. 2). The eastern border of the investigated portion of the ECVF is the common boundary between the NAWS and Fort Irwin (Fig. 3). The southern and western borders of the ECVF are the southern and western limits of flows and tuffs.

This ECVF includes well over 600 km^2 of undifferentiated Tertiary volcanic rocks, alluvium, granitoids and minor Paleozoic metamorphic rocks. It is accessible from the west via the Randsburg Wash Road off of State Route 178, or from the east through gates along a common border between the NAWS and the adjacent Fort Irwin Military Reservation (Figs. 1, 3). All of the ECVF can be reached on foot from other directions although such practice is illegal and dangerous considering the climate and the nature of the tests being performed at the NAWS.

This arid high desert region is characterized by flat, barren alluvial valleys (> 500 m elevation) and abrupt, sparsely vegetated ranges. Annual precipitation averages less than

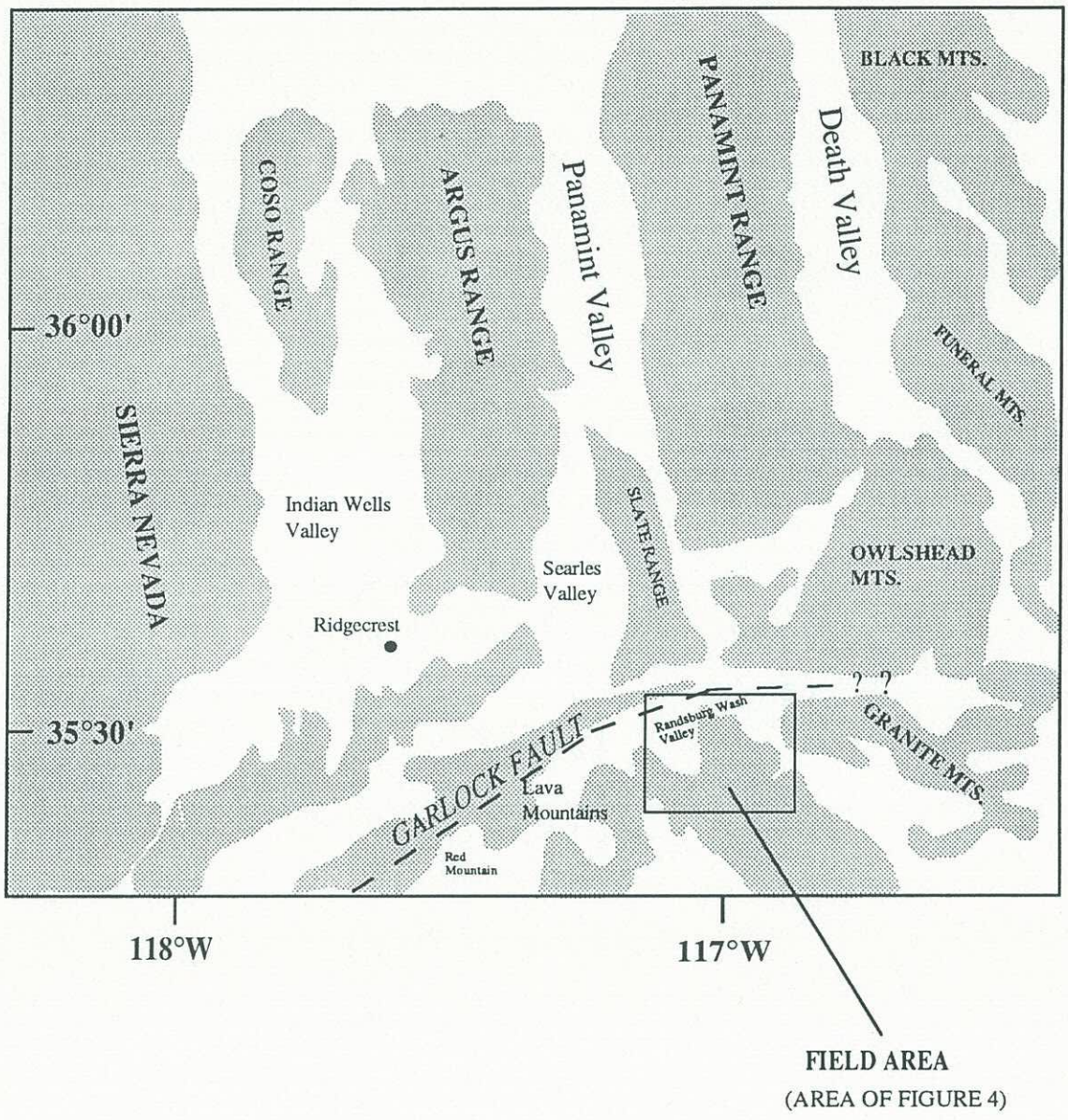

Figure 2. Location of the Eagle Crags Volcanic Field and prominent physiographic features.

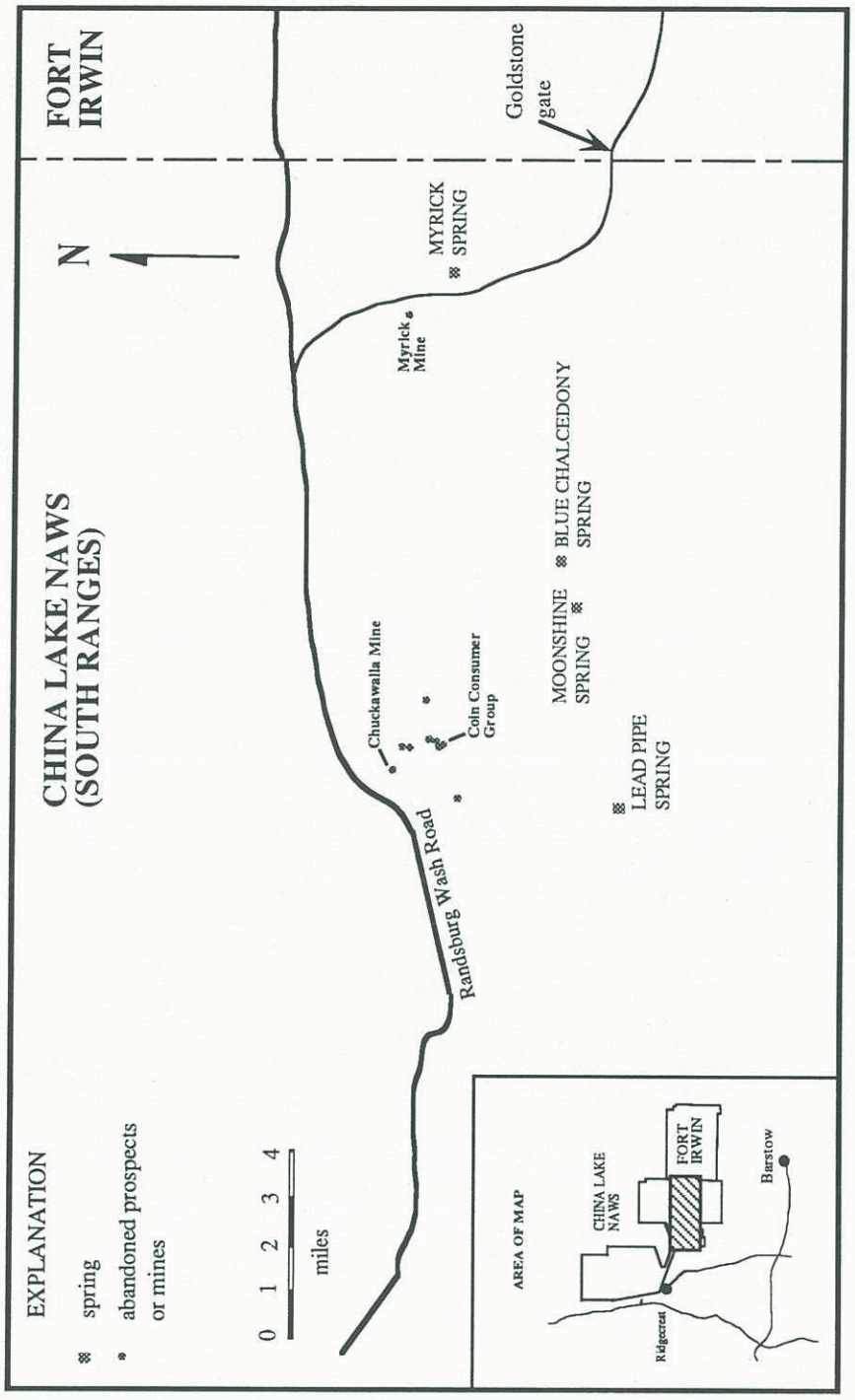

Figure 3. Prospects, mines and springs in the Eagle Crags Volcanic Field.

10 cm (Norris and Webb, 1990). The valleys step down in elevation eastward toward Death Valley, one of the lowest and hottest places on the earth's surface. A unique geographic aspect of this region and a testament to the tectonic evolution of the southwestern U.S. is the proximity of the continental U.S.'s lowest (Death Valley; minus 282 ft) and highest points (Mt. Whitney; 14,495 ft), less than 130 km apart.

1.3 Methodology

Small- and large-scale mapping was conducted over a period of two years. A regional geologic map was prepared at a 1:62,500 scale (Plate 1). Three areas within this region, Myrick Spring, Goldstone and Blue Chalcedony, were mapped at a scale of 1:15,000.(Fig. 4; Plates 2, 3 and 4). These areas were selected because they contain distinct volcanic landforms, interpretations of which are necessary to understand the geologic setting of the ECVF. The stratigraphy, morphology and mineralogy of the rocks that underlie these areas provide a basis for understanding the sequence of events, petrology and tectonic history of the region.

Qualitative facies analyses were employed to identify the products of volcanic eruptions and to determine if they traveled far from their source (vent-distal facies), were deposited near their source (vent-proximal facies), or comprised remnants of the source (vent facies).

Mapping facilitated the identification of small-scale volcanic landforms, important stratigraphic relationships and alteration. All mapping was augmented by the use of color infrared, high altitude aerial photographs (NHAP). NHAP coverage was at a scale of 1:15,000.

Field work emphasized the identification of: 1) rock types; 2) contacts; 3) flow

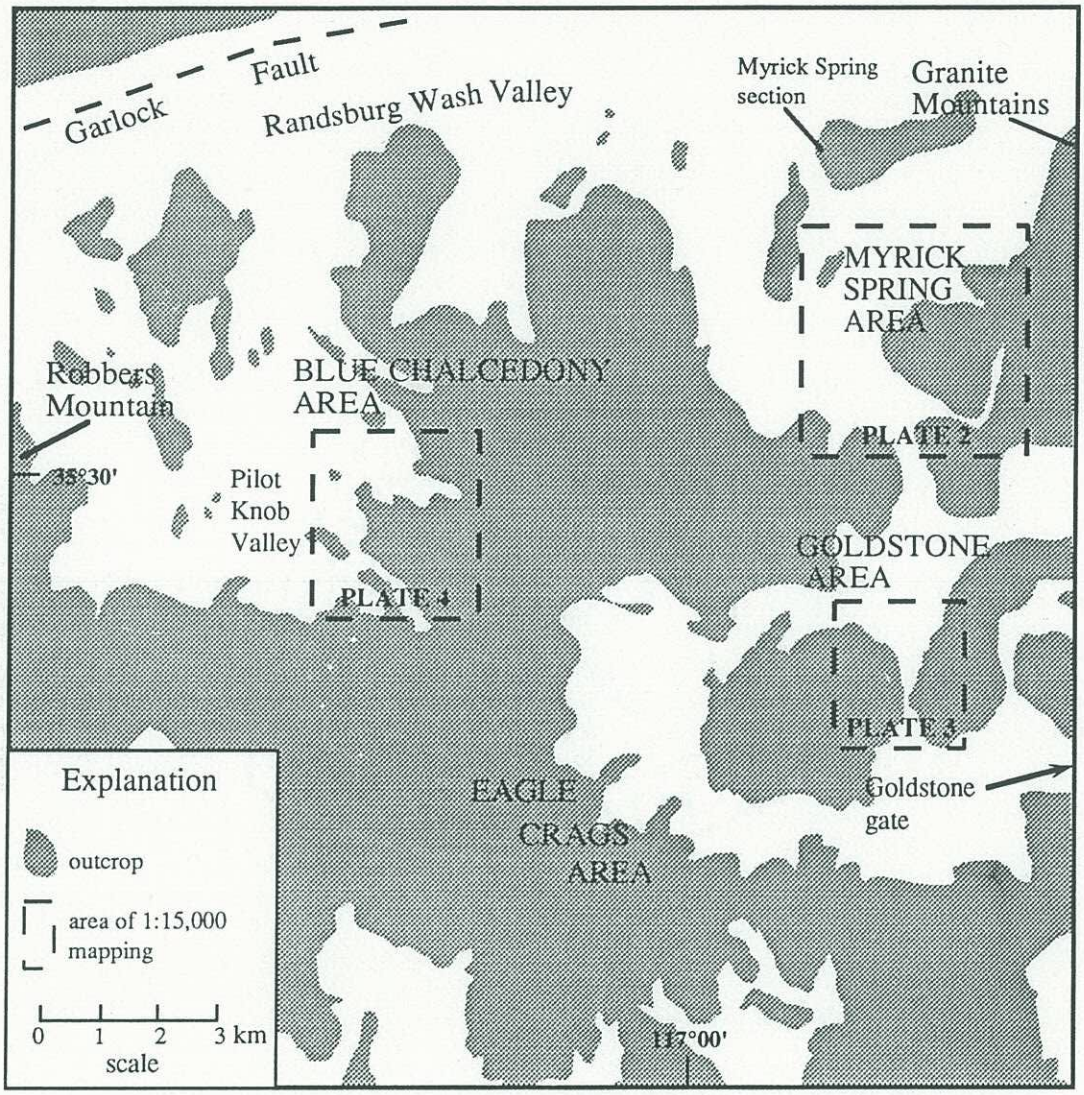

Figure 4. Index map of the Eagle Crags Volcanic Field.

facies (top, bottom, vent proximity); 4) tuff facies (welded, unwelded; air-fall, ash-flow, surge; vent proximity); 5) dikes, sills, plugs and vents; 6) stratigraphic relationships; 7) structures and 8) alteration. Structural features were described and measured in the field, where applicable. These data were plotted on stereonets. Lineaments identified on aerial photographs were field checked and included on maps where relevant.

Almost 1,000 gravity-magnetometer stations were established in order to define the shape of a large regional Bouguer gravity low centered in the southeastern portion of the volcanic field (Nilsen and Chapman, 1971). Interpretations of these data enhanced the understanding of previously unknown structural features in the field. Data acquisition, terrain corrections and data reduction were conducted by personnel from the Geothermal Program Office.

Over 300 samples ranging from 2 kg aggregates to individual hand samples were collected in the region during a 2 year period. Although facies differences, such as variable phenocryst concentrations or glassy versus devitrified portions of a unit, and hydrothermal alteration often hampered mapping, an effort was made to sample only unaltered rocks that best represented a particular flow or tuff. When necessary, multiple samples of the same unit were selected to aid in understanding the volcanic stratigraphy. Thin section slabs were oriented to yield a representative cross-section of each sample. Almost 200 thin sections and polished thin sections were prepared and examined. Over 70 of these sections were "quick plates" (~100 micron thick thin sections) prepared for cursory fluid inclusion investigations and petrography. No fluid inclusions suitable for geothermometry or geochemical analyses were found. Twelve polished thin sections were also prepared in order to investigate the opaque mineral assemblages and textures.

Seventy-two samples were sent to the X-Ray Assay Laboratories (XRAL) in Don

Mills, Ontario, for whole rock x-ray fluorescence, neutron activation and atomic absorption analyses. Analytical procedures used at XRAL are described in Bloom (1993). Additional information regarding sample preparation and precision statistics are included in Appendix A.

Samples were primarily selected for analyses in an attempt to determine the geochemical composition of dominant flows and tuffs from the ECVF. Whole rock XRF analyses were performed for chemical discrimination of rocks, to quantify the styles and extent of alteration and to provide major and trace element data for generalized petrogenetic modeling. Variation diagrams and CIPW norms were calculated from water-free normalized XRF analyses (Tables A.1 and A.2). CIPW weight percent norms were calculated with the computer programs CIPW and MOLES (Musselman, 1987). MOLES contains an iron weighting factor that calculates $Fe^{2+}/(Fe^{2+} + Fe^{3+})$ for each Fe-bearing mineral in the norm. A ratio of 0.9 was used because the calculated norms derived with this weighting factor best approximated modal mineralogy.

Twelve samples were prepared, irradiated and analyzed for $^{40}Ar/^{39}Ar$ age determinations at the U.S. Geological Survey's Branch of Isotope Geochemistry, Denver, Colorado. Sample preparation and analytical techniques are described in Appendix B.

The interpretation and presentation of much of the data in this research were facilitated by various computer programs. Where relevant, these programs are acknowledged and described in the body of this report or in the appendices.

1.4 Previous and Ongoing Investigations

The Naval Ordnance Test Station (NOTS; now NAWS) was established in 1943. All NAWS property was removed from public use and excluded from most local and

regional geologic investigations, with the exception of Department of Navy-sponsored cursory geothermal investigations and mineral resource inventories (Austin et al., 1979; Austin et al., 1983).

Geologic investigations performed prior to establishment of the Naval base or in regions outside of the NAWS include those by Hess (1910), Hulin (1925), Thompson (1929), Jenkins (1938), Bowen (1954), Hewett (1954), Jennings et al. (1962), Bassett and Kupfer (1964), Smith (1964), Dibblee (1967; 1968), and Burke et al. (1982). The most recent publicly available studies are a U.S. Bureau of Mines mineral investigation of the Golden Valley Wilderness Study Area, west of the western border of the South Ranges (Gaps, 1985), and a U.S.G.S. study of the Paleozoic rocks in the Pilot Knob Valley (Carr et al., 1993).

Mining in and around the region began as early as the late-1800's. Hulin (1925) reported that over 10M oz. of combined silver and gold were produced from the Randsburg/Atolia mining regions, adjacent to Red Mountain (Fig. 2). An investigation of public records and claim markers discovered during this investigation suggests that the region extending east from Red Mountain through the central portion of the ECVF was actively prospected through the beginning of World War II. According to Gaps (1985), portions of the Lava and Almond Mountains, adjacent to the western border of the South Ranges, were staked and prospected for precious metals through the 1980's.

There have been numerous regional-scale structural and tectonic investigations of eastern California. An overview of the salient points in these investigations relevant to this study area is included in this dissertation.

1.4.1 Randsburg Wash Test Range

Austin et al. (1983) identified gold-bearing rocks from 11 shafts, pits and prospects, and mercury from one prospect directly on or adjacent to the region within the borders of the South Ranges (Fig. 3). A description of the Chuckawalla mine indicates that workings rest on a block of pre-Cretaceous metasedimentary rock that overlays a rhyolitic tuff. Samples from the nearby Coin Consumer Group prospect contained 0.281 oz./ton gold and 0.180 oz./ton silver (Austin et al., 1983; p. 36). Mineralization at the Coin Consumer Group mine is hosted by shear zones within rhyolite and near the rhyolite/metasedimentary rock contact. The description in Austin et al. implies that metamorphic rocks were thrusted over younger volcanic rocks, with precious metal mineralization possibly localized along the fault plane.

An unnamed prospect north of Lead Pipe Spring was developed in a porphyritic rhyolite with veins containing rhodochrosite, rhodonite and cerrusite. According to Austin et al. (1983), geodes from rhyolitic tuff in the Blue Chalcedony area contain white quartz pseudomorphs of barite. Other unnamed prospects apparently were also developed within shear zones in the porphyritic rhyolite. Based on small-scale mine maps, linear shear zones trend northeast and northwest.

Mineralization at the Myrick mine (Fig. 3) includes traces of cinnabar with realgar in bodies of milky white quartz. Mercury (6.93 ppm), traces of arsenic and minor traces of native sulfur were also found in samples from the Myrick mine which was described as a fossil hot spring occurrence (Austin et al., 1983; p. 61).

1.4.2 Red Mountain/Almond Mountain Geothermal System

Andesitic flows, domes and intrusions in the Red Mountain area, west of the ECVF

(Fig. 2), are cut by a series of northwest-trending faults called the Brown's Ranch fault zone (Smith, 1964). To the north of this fault zone is the northwest-trending Dome Mountain anticline.

Hematitic alteration, opal and steam wells with boiling at depths of 415 ft. have all been documented at Red Mountain (Austin et al., 1983). These hot spring features have been mapped and drilled by geothermal explorationists in the past (Austin et al., 1983). Austin et al. (1983) suggested that geothermal fluids in the Red Mountain region may be controlled by the northwest-trending features of the Brown's Ranch fault zone.

1.4.3 Ongoing Regional Investigations

There are several university-affiliated groups currently investigating areas adjacent to the study area. To the north, the Slate Range is being investigated by Walker from the University of Kansas (F.C. Monastero, personal communication, 1992). Walker has suggested that the Slate Range is a metamorphic core complex associated with Late Tertiary extension in the southwestern portion of the northern Basin and Range. Walker, his students and other collaborators are generally interested in the development of core complexes, related structural features and associated Tertiary magmatism in the Mojave Desert (Wernicke et al., 1986; Walker et al., 1990). His collaborators include Bartley, University of Utah, and Glazner, University of North Carolina (Bartley et al., 1989; Glazner and Bartley, 1991). Glazner's research includes crustal dynamics and Cenozoic tectonics in the Mojave Desert (Glazner and Ussler, 1989; Glazner et al., 1990; Glazner et al., 1991; Glazner and O'Neil, 1991).

Another group led by Dokka, Louisiana State University, is interested in the tectonic development of the southern Cordillera, also with an emphasis on the Mojave

Desert. Dokka and his students are actively mapping and conducting remote sensing studies of the Goldstone Lake area, east of the western margin of Fort Irwin (Dokka, 1986; Dokka, 1990; Dokka and Travis, 1990).

CHAPTER 2

GEOLOGY AND GEOCHEMISTRY

2.1 Introduction

The ECVF encompasses over 600 km^2 of unexplored terrain in the northern Mojave Desert. This chapter briefly describes the geology of the Mojave Desert and then describes in detail the geology of four areas within the ECVF. Each of these areas contains unique volcanic features and structural elements. An understanding of the geology of each area provides the foundation for an overall understanding of the geologic setting of the ECVF.

Although a few of the flows and at least one tuff were identified in multiple areas throughout the ECVF, the complex interfingering and limited exposures of volcanic units makes it difficult to correlate most flows or pyroclastic rocks from area to area.[1] Consequently, each area is presented as a unique succession of volcanic rocks.

With the exception of a prominent arcuate scarp, most of the structures observed appear to postdate volcanism. A description of all major structures is presented separately in a later chapter. The conclusion to this chapter compares and contrasts geologic and geochemical features in these areas. Interpretations of these features are made in the context of the entire volcanic field.

2.1 Mojave Desert Geology

The western Mojave Desert is a distinct physiographic province bounded by the San

[1] Sample numbers presented in the text are consistent with sample numbers presented in tables, figures and plates.

Andreas fault to the southwest and the Garlock fault to the northwest (Hewett, 1954). The northwest-trending San Andreas and the eastnortheast-trending Garlock fault intersect in western California, at the southeast corner of the Tehachapi Mountains. The San Andreas fault is a transform fault with up to 80 km right-lateral movement in the western Mojave Desert and cumulative displacement of up to 560 km (Hill and Dibblee, 1953; Dibblee, 1967). Recent reconstructions suggest that as much as 1360 km of right lateral motion has occurred along this Pacific-North American plate boundary since the inception of the San Andreas fault at about 35 Ma (Stock and Molnar, 1988).

The Mojave Desert consists of 65,000 km^2 of broad alluvial, arid basins and adjacent ranges in eastern California (Norris and Webb, 1990). It is composed of Precambrian metamorphic and igneous rocks ranging in age from 1.87 to 1.2 Ga, Precambrian-Paleozoic miogeoclinal and platformal rocks, Mesozoic back-arc and intra-arc marine and continental sequences, Mesozoic batholithic rocks and Cenozoic volcanic cover rocks and Quaternary alkalic volcanic and sedimentary rocks (Dibblee, 1967; Burchfiel and Davis, 1980). Tertiary rocks of the Mojave Desert include nonmarine sedimentary, pyroclastic and volcanic rocks and minor amounts of marine sedimentary rocks near the San Andreas fault. These rocks rest unconformably on highly eroded pre-Tertiary crystalline rocks (Dibblee, 1967).

The Mojave Desert formed as early as Oligocene time (Norris and Webb, 1990). The left-lateral Garlock fault forms the boundary between the Basin and Range physiographic province to the north and the Mojave Desert. Two major differences between the two provinces are in the basement rocks and structures. Cenozoic faults in the Basin and Range have large vertical displacements and control the topography whereas the amount of vertical displacement and topographic control exerted by faults in the Mojave

Desert are not as great (Smith, 1964). Mesozoic plutonic rocks constitute the basement of the Mojave Desert whereas pre-Mesozoic sedimentary, metasedimentary and metaigneous rocks form the basement of the southwestern Basin and Range (Smith, 1964). Prior to the development of the Garlock fault at about 10 Ma (Davis and Burchfiel, 1973; Burbank and Whistler, 1987), the western Mojave Desert was part of the Basin and Range physiographic province (Norris and Webb, 1990).

2.2 Descriptive Geology of the ECVF

The Eagle Crags Volcanic Field is so termed because it forms an extensive series of spatially and temporally related volcanic rocks and vents on the northwestern edge of the Mojave Desert (Fig. 2). The ECVF is composed of a complex series of interfingered flows, volcaniclastic breccias, dikes, tuffs and hypabyssal rocks forming mesas and ridges separated by Quaternary alluvial valleys (Plate 1). These rocks compositionally include basalt, basaltic andesite, andesite, dacite, rhyodacite and rhyolite.

The most abundant rocks of the ECVF include tuffs and flows of andesitic and dacitic composition. Mesozoic granitoids and small outcrops of Paleozoic metamorphic rocks are partially exposed throughout the volcanic field. The following sections describe the generalized stratigraphy, morphology and mineralogy of rocks from four areas within the ECVF.

2.2.1 Myrick Spring Area

The Myrick Spring is located on the northern margin of the ECVF and is bordered to the north by the Randsburg Wash Valley and the Garlock fault and to the east by the Granite Mountains (Fig. 4; Plate 2). A generalized stratigraphic section for the Myrick

Spring area, described below, is representative of the overall stratigraphy in the northeastern ECVF.

The rocks described in this area include granite, hypabyssal basalt, flows of basaltic andesite, andesite and dacite, and pyroclastic units. Three features in the Myrick Spring area relevant to the genesis of the ECVF include a thick, vertically-oriented dacitic flow, a greater than 100 m thick succession of rhyolitic tuff and the contact between basal granitic rocks and overlying volcanic rocks.

2.2.1.1 Stratigraphy

The Myrick Spring area is dominated by intermediate and silicic tuffs that are in fault contact with a large stock of Cretaceous granite (Kg; Plates 1 and 2). Capping sheet-like flows from the northeastern ECVF dip gently northwest while similar rocks 15 km to the south at Eagle Crags dip gently to the southwest.

A generalized stratigraphic column presented in Figure 5 was based on a section about 7 km north-northwest of Myrick Spring. This section is described because its basal tuff was observed in the northern and southern portions of the ECVF and serves as one of the few marker horizons for stratigraphic correlations. This section also represents the most complete and accessible stratigraphic section of pyroclastic rocks and volcanic flows in the northern ECVF.

Regional investigations and other exposures in the ECVF suggest that volcanic rocks disconformably rest on Mesozoic granitoids (Jennings et al., 1962; Smith, 1964; Norris and Webb, 1990). Directly overlying these granitoids is a vesicular brown, porphyritic andesite (Ma^1). This andesite constitutes the exposed base of volcanic successions in the Myrick Spring area (Fig. 6a, b, c). It strikes northwest, has a steep to

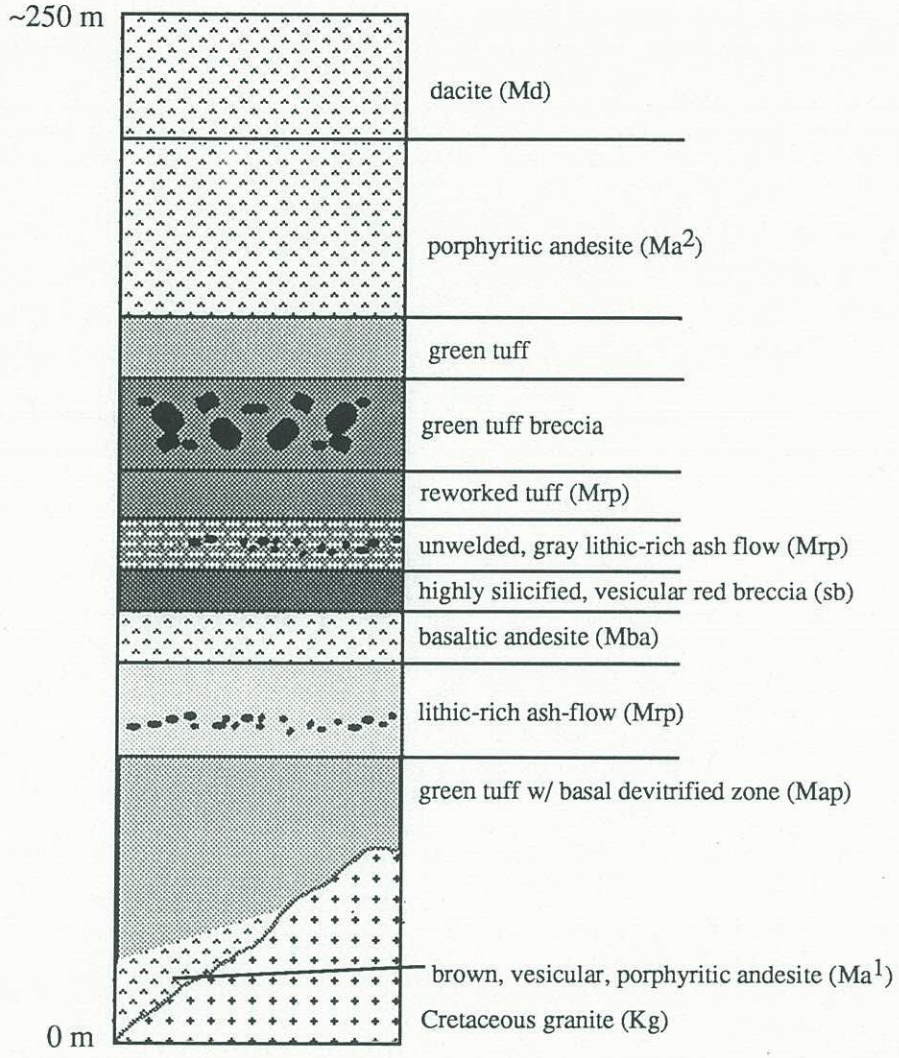

Figure 5. Generalized stratigraphic column for the Myrick Spring area.

Figure 6 Captions

Figure 6a. Contact between the brown vesicular andesite and unconformably overlying, olive green tuff (Map).

Figure 6b. Northwest-dipping strata of examined section with steeply-dipping, vesicular andesite (Ma^1) in foreground. Section is ~100 m thick.

Figure 6c. Photomicrograph of vesicular andesite (Ma^1, sample 1276) with greater than 60% resorbed plagioclase phenocrysts and microphenocrysts in a glassy, vesicular matrix with less than 5% opaque minerals plus altered, fine-grained mafic minerals. Field-of-view (FOV) ~ 3 mm across. Cross-polarized light (XP).

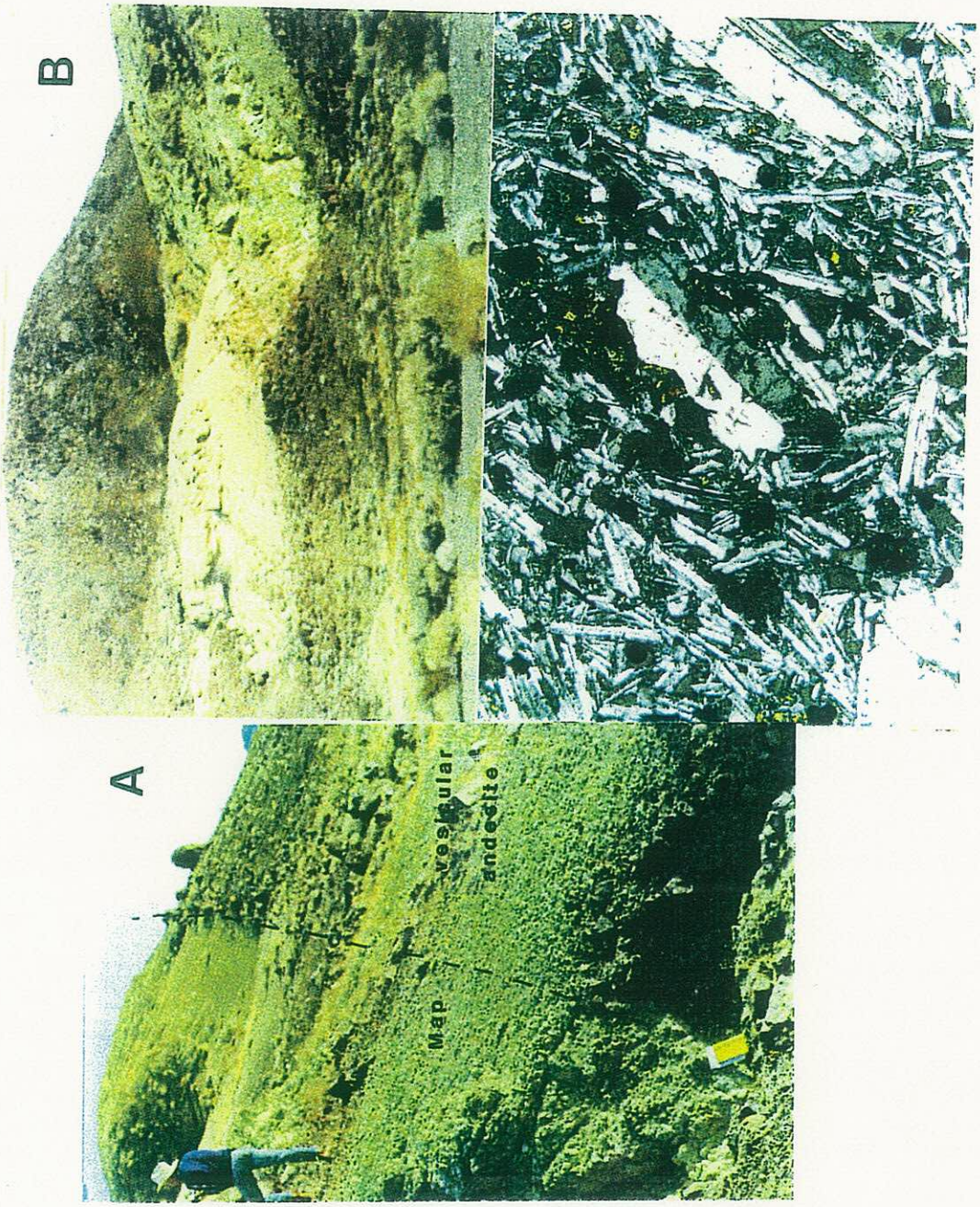
B
A
vesicular
andesite

vertical dip and is no more than 1-3 m thick. A similar andesite forms a northwest-trending, dike-like outcrop 11 km to the west-southwest in the Blue Chalcedony area where it is overlain by a rhyolitic tuff and flow. A limited number of outcrops makes this andesite difficult to stratigraphically place in the geologic setting. Its vesicular nature and extreme dip indicate that it is probably a flow top that formed part of a steep-sided paleovalley in which subsequent volcanic eruptive products were focused.

This vesicular andesite is unconformably overlain by an unwelded andesitic tuff (Map; Plates 2, 4), the base of which is composed of 15 m of an olive green, devitrified, lithic-rich zone (Fig. 7a). The latter forms more resistant slopes than the upper, crystalline portions of this tuff. The same tuff, although much thicker, is located in the Eagle Crags area 15 km to the southwest (Fig. 7b). Besides its distinctive olive green color, the basal portion of this tuff has a matted texture indicative of it having undergone devitrification. A relatively sharp break distinguishes the top of this devitrified zone from a 10-15 m thick, pastel-colored to white glassy zone (Mrp).

The pastel-colored tuff is overlain by a 1.5 m thick, green-brown, highly vesicular and altered flow of basaltic andesite (Mba; Plate 2). This flow is conformably overlain by 2-5 m of a red, highly silicified, vesicular breccia (sb). Individual clasts of this rock are laminated and bear a resemblance to an aphyric rhyolite identified at the Goldstone area. Unlike the aphyric rhyolite, this red unit is extremely hard and locally brecciated. This relatively thin rock is not well-exposed although float blocks are quite common. Nonbrecciated float blocks of this rock could be described as red chert. This breccia is overlain by approximately 5 m of a gray lithic-rich tuff which in turn is overlain by a less than 1 m thick reworked tuff conglomerate. Reworked tuff is conformably overlain by 5-10 m of another green-colored tuff which is capped by greater than 50 m of red,

Figure 7 Captions

Figure 7a. Basal olive-green, devitrified tuff (Map) from measured section 7 km north-northwest of Myrick Spring.

Figure 7b. View of Eagle Crags scarp with basal olive-green tuff (Map) overlain by 30 m of a mafic flow in the foreground of photo.


A

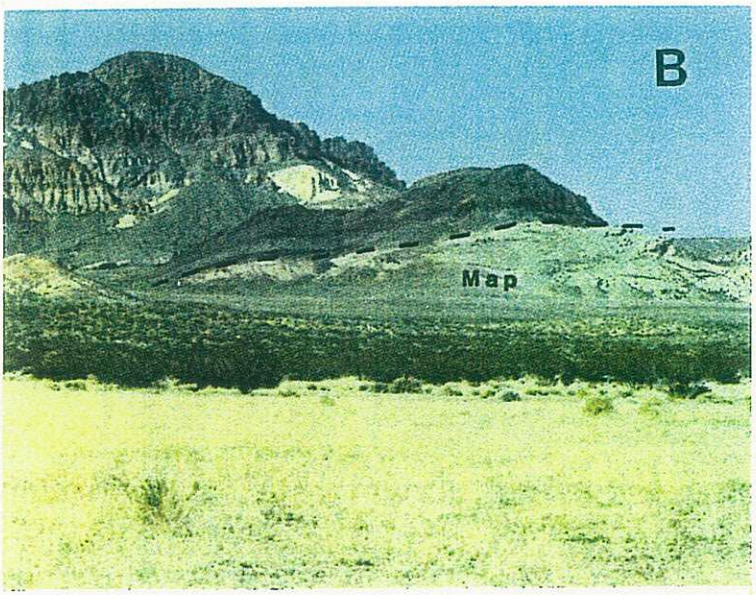
B
Map

andesitic and dacitic flows.

2.2.1.2 Cretaceous Granite

The northeast corner of the ECVF is buttressed by a coarse-grained, biotite granite (Kg; Plates 1 and 2; Fig. 8a). It is composed of quartz, orthoclase, plagioclase and biotite with accessory opaque minerals, minor accessory pyroxene±garnet and minor deuteric alteration products including chlorite after biotite and sericite after feldspar (Fig. 8b and c).

The western margin of this pluton has a distinct gneissic texture whereas the interior portions tend to be porphyritic with coarse, euhedral feldspar megacrysts. Simple pegmatite dikes transect the granite locally. Left-lateral offset of these dikes coincides with left-lateral offset of the western terminus of the pluton as identified at outcrop scale and on aerial photographs (Fig. 8a).

The contact between the western margin of the granite and younger flows and tuffs of intermediate to silicic composition is an apparent fault zone marked by intense silicification and localized brecciation (Fig. 9a, b). This north-northeast-trending fault zone occupies a 50-100 m wide strip of alluvium with small, discrete outcrops (~5 x 10 m) of silicified breccia (Fig. 9c). Fault zone rocks are mylonitized and largely composed of granite (Fig. 9a, b).

The fault zone may be a strike-slip, detachment or thrust fault. Although north-directed compressional features have been identified in mid-Miocene rocks to the south (Bartley et al., 1991), limited exposures and lack of kinematic indicators preclude any interpretations.

Figure 8 Captions

Figure 8a. Color infrared aerial photograph of Myrick Spring area. (Up to the north. FOV~6 km across.) Granite Mountains occupy eastern 1/3 of photograph. Bright white color at base of photo is Myrick tuff (Mrp). Dark colors are flows.

Figure 8b. Biotite-granite (Kg, sample 1081) from Granite Mountains with consertal texture of plagioclase feldspar, quartz and biotite. FOV~1.5 mm across. XP.

Figure 8c. Chlorite after biotite in typical Granite Mountain granite (sample 1081). FOV~0.75 mm across. Plane polarized light (PP).

Figure 8d. Simple pegmatite from the western margin of the Granite Mountains truncated by an east-west trending, left-lateral fault.

Figure 9 Captions

Figure 9a, b. Photomicrograph of brecciated zone between granite and disconformably overlying Tertiary volcanic rocks (sample 1129). Contact is silicified and has zones of elongate, recrystallized - mylonitized - granite. a) PP, FOV~1.5 mm, b) elongate quartz and plagioclase crystals juxtaposed against breccia. XP, FOV~1.5 mm.

Figure 9c. West-trending valley on south side of pyroclastic succession (Mrp) composed of poorly welded tuff (valley is south of white tuff in figure 8a) Outcrop in foreground is fault contact between granite and Tertiary volcanic rocks.

Figure 9d. Looking northwest at pyroclastic succession with thin lens of basaltic andesite (Mba, sample 1127) toward base and small outcrop of a brown, basaltic plug (sample 1133) in foreground.

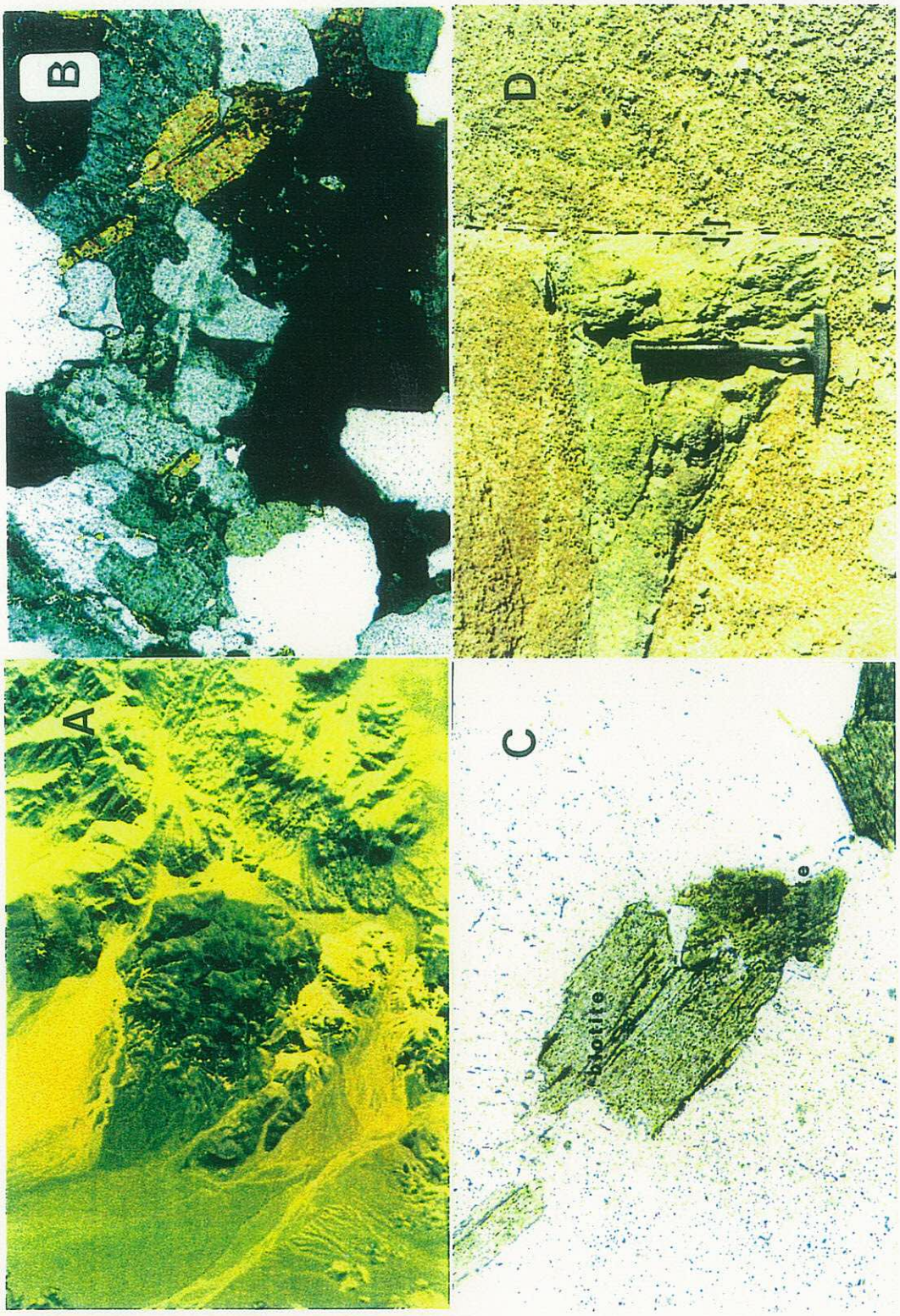
B
D
A
C
Perlite

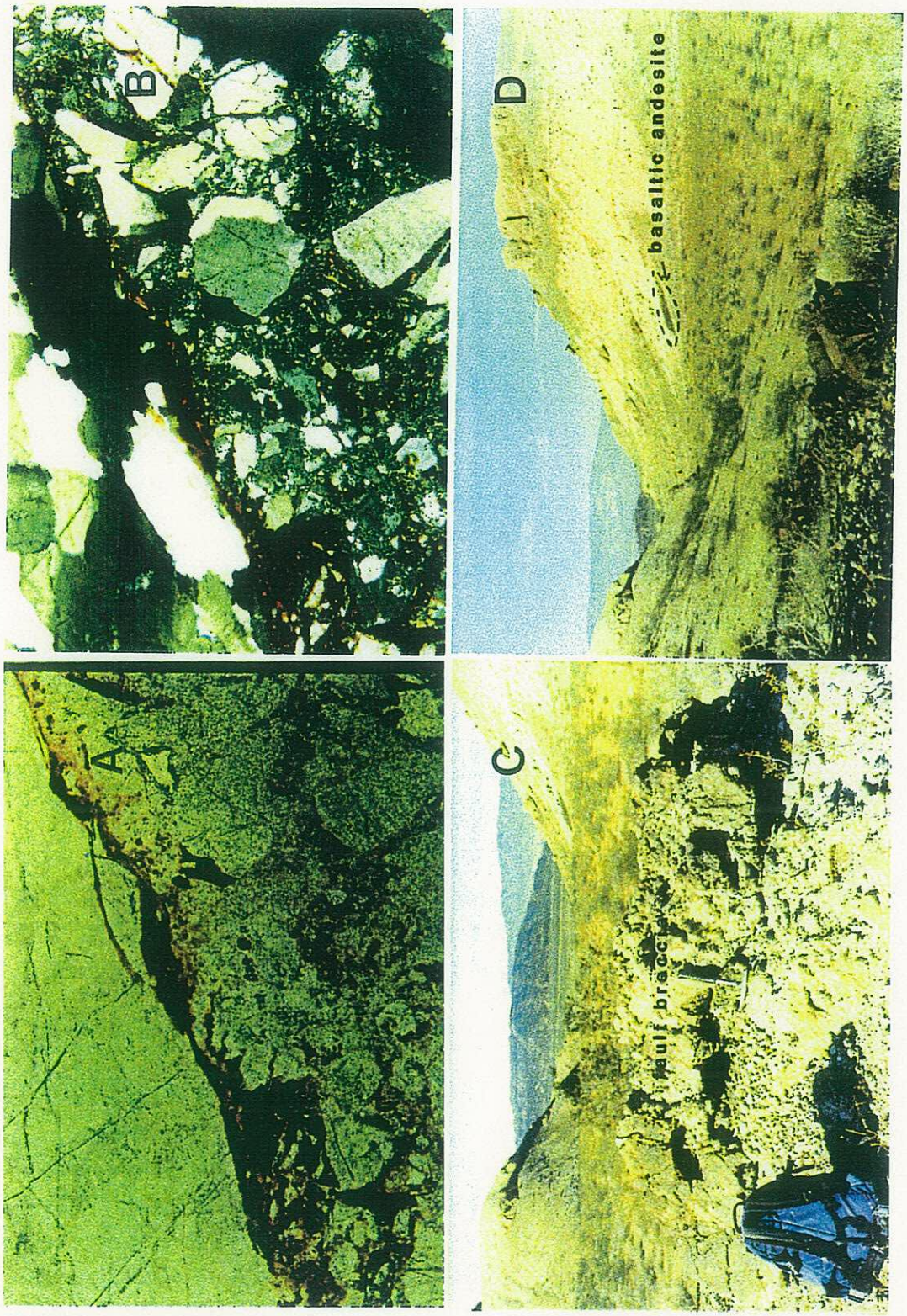
A
B
C
D
basaltic andesite

2.2.1.3 Myrick Basalt

Although basalts have been mapped and described regionally (Jennings et al., 1962; Dibblee, 1967), the only basalt examined in the ECVF is near the granite-Tertiary volcanic rock contact (Plate 2). The Myrick basalt (Mb; Plate 2) is dark green to brown, fine- to medium-grained and holocrystalline. It crops out in the west-trending alluvial valley that borders the thick pyroclastic succession (Fig.9d). The basalt is not in contact with any of the nearby volcanic rocks.

The Myrick basalt is composed of greater than 70% plagioclase, 5-10% pyroxene, 1-3% olivine, accessory zircon±apatite and minor Fe-Ti oxides (magnetite ±titanomagnetite). Pyroxenes are anhedral augite crystals, up to 5 mm in length, subophitically textured with lath-like plagioclase (Fig. 10a and b). Plagioclase ($\sim An_{50}$) crystals are subhedral and up to 4 mm long. Olivine is typically equant with translucent red to opaque alteration rims and conchoidal, altered fractures (Fig. 10c, d).

The basalt mineralogy is similar to that of an altered basaltic andesite flow described below. Unlike the unaltered, holocrystalline basalt, basaltic andesite is clearly interlayered within the thick succession of pyroclastic rocks (Fig.9d). The basalt is not in contact with any other rocks in the region which makes it is unclear if the basalt is a late, valley-filling flow with a mineralogical assemblage similar to nearby mafic flows or if it is a basaltic plug or hypabyssal intrusion that is contemporaneous with the pyroclastic successions and its interlayered mafic flows.

2.2.1.4 Myrick Basaltic Andesite

The Myrick basaltic andesite (Mba; Plate 2) is a relatively flat lying and locally altered dark green to brown flow. It occurs as a thin (less than 10 m thick) lens or

Figure 10 Captions

Figure 10a, b Photomicrograph of basalt (Mb) with subophitically-textured augite, plagioclase (~An_{50}) and minor, altered olivine on right side of photo (sample 1133). FOV~3 mm across. a) PP. b) XP.

Figure 10c, d Photomicrograph of basalt (Mb, sample 1066). Equant, opaque rimmed minerals are olivine with iddingsite+FeOx alteration along fractures and crystal faces. c) PP. d) XP.

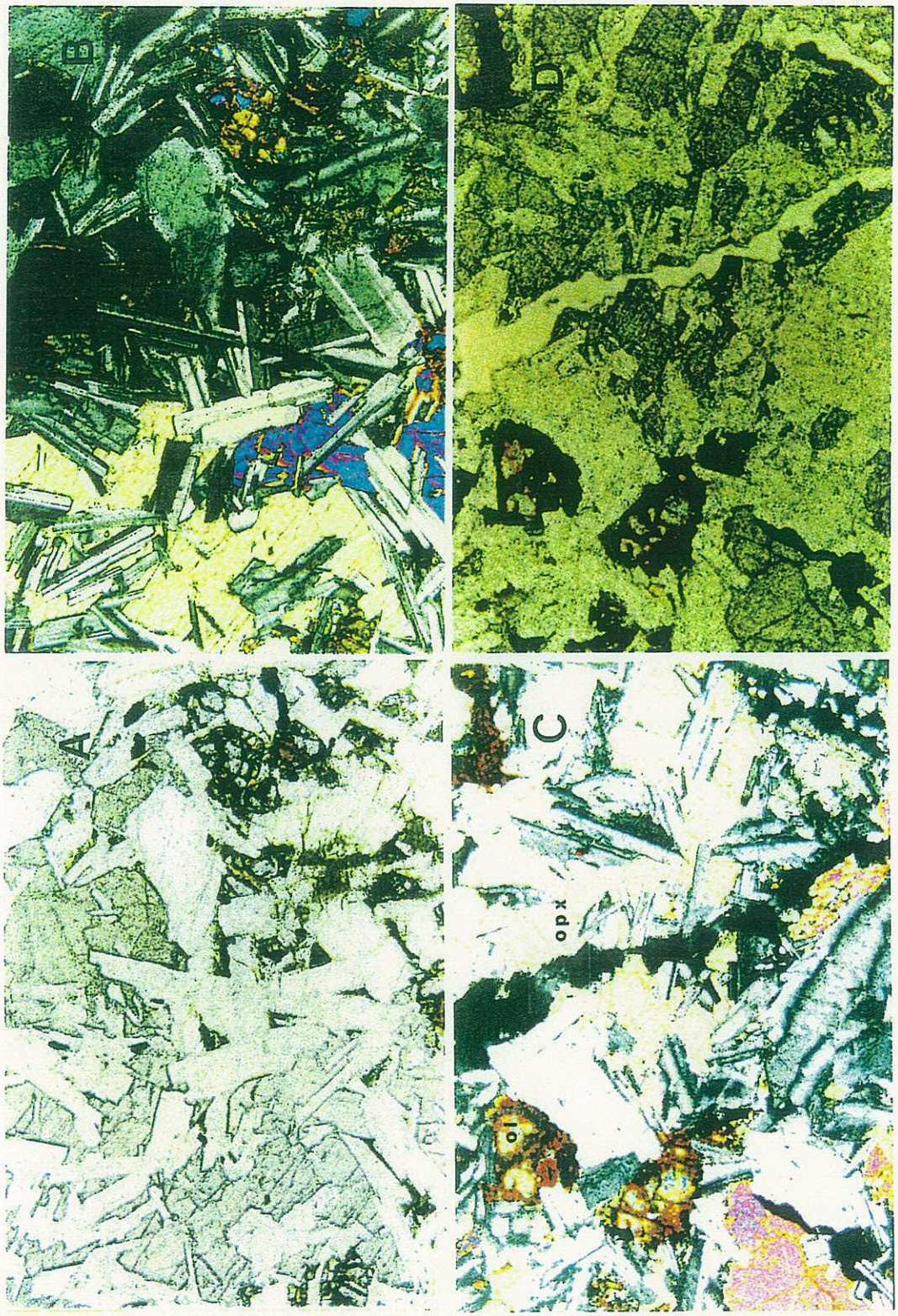
B
D
A
C
opx
ol

discontinuous flow interlayered within unwelded tuff or as angular, xenolithic inclusions within pyroclastic flows (Fig. 11a, b, c, d; Plate 2).

Basaltic andesite tends to be porphyritic and glassy. It is composed of greater than 30% plagioclase phenocrysts and 1% altered euhedral phenocrysts (presumably altered olivine) in a microlitic and glassy matrix composed of plagioclase, minor pyroxene and opaque minerals (Fig. 12a, b, c). Glomerophyric clots of plagioclase are commonly found in many of these rocks (Fig. 12d). The morphology and apparent cleavage in some of the opaque minerals indicates that they may be pseudomorphic after clinopyroxene. Unlike the basalt, olivine in the basaltic andesite is fine-grained (<0.1 mm) and intensely altered with black to dark red and/or green rims and cores of Fe- and Mg-bearing minerals, iddingsite and bowlingite.

Highly altered basaltic andesite contains sub- to anhedral, fine-grained mafic minerals that have been replaced by epidote±carbonate±opaque minerals (e.g. sample 1126; Fig. 12b, c). The major distinctions between basaltic andesite and andesite, described below, are the amount of altered Fe-Mg silicates and the intense alteration distinctive in most basaltic andesites.

2.2.1.5 Myrick Andesite

Five varieties of andesite (Ma^{1-5}) were identified in the Myrick Spring area (Figs. 13a, b, c, d; Plate 2). They include a steeply-dipping, brown vesicular flow (Ma^1; sample 1276), a green to brown, orthopyroxene-rich porphyritic flow (Ma^2, Fig. 13c; sample 1015), a dark brown to gray, two-pyroxene andesitic flow (Ma^3; sample 1034), and a dark green, biotite±Fe-Mg silicate andesite flow (Ma^4; sample 1255). A trachytic andesitic flow (Ma^5; Fig. 13b; sample 1099), identified throughout the ECVF, may be the quenched flow

Figure 11 Captions

Figure 11a. Angular fragment of basaltic andesite (Mba) entrained in a white, transitional tuff-dacitic flow that was most likely plucked from a basal flow during a pyroclastic eruption.

Figure 11b. Fragment of basaltic andesite (Mba) in volcanic flow. Unlike figure 11a, the fragment appears uniformly laminated (red and dark green). Both the fragment and the host dacitic flow are silicified.

Figure 11c. White tuff (Mrp) apparently draped over a basal basaltic andesite.

Figure 11d. Lens of altered green basaltic andesite (Mba) within a thick succession of unwelded tuff from the Myrick Spring area.

Figure 12 Captions

Figure 12a. Photomicrograph of relatively unaltered andesite (Ma^2, sample 1080) containing a rounded, oscillatory zoned plagioclase mantled by clear plagioclase overgrowth in lower center. PP. FOV~3 mm.

Figure 12b. Photomicrograph of an altered, vesicular basaltic andesite (Mba, sample 1126). An apparent Fe-Mg silicate has been replaced by epidote plus a carbonate mineral. XP. FOV~3 mm.

Figure 12c. Photomicrograph of carbonate alteration from in a basaltic andesite. This basaltic andesite is adjacent to a northeast-trending, highly silicified vein. XP. FOV~3 mm.

Figure 12d. Photomicrograph of a glomerophyric clot typically found in basaltic andesites. The clot of plagioclase±quartz±altered biotite appears to be a fragment from the granitic basement. PP. FOV~ 3mm.

Figure 13 Captions

Figure 13a. Photomicrograph of coarse-grained, anhedral augite intergrown with plagioclase and opaque minerals in a two pyroxene andesite (Ma^3, sample 1034). XP. FOV~3 mm.

Figure 13b. Photomicrograph of trachytic andesite (Ma^5, sample 1099) composed of greater than 80% oriented laths of simple-twinned plagioclase, 5% opaque minerals, less than 2-3% altered mafic silicates (pyroxene) in a glassy matrix. XP. FOV~3 mm.

Figure 13c. Photomicrograph of orthopyroxene-bearing andesite (Ma^2, sample 1015) with 15-35% plagioclase phenocrysts and ~5% clinopyroxene phenocrysts in a microlitic to glassy ground mass with fretted or sieve textured plagioclases with a corona of clear plagioclase. FOV~ 3mm. PP.

Figure 13d. Photomicrograph of a mafic inclusion within a dacitic flow (sample 1078). This plagioclase-rich, vesicular inclusion is similar to the steeply-dipping vesicular andesite described earlier with the exception that plagioclase phenocrysts in sample 1078 are highly resorbed and overgrown. PP. FOV~0.75 mm.


B
D
basaltic andesite
A
C

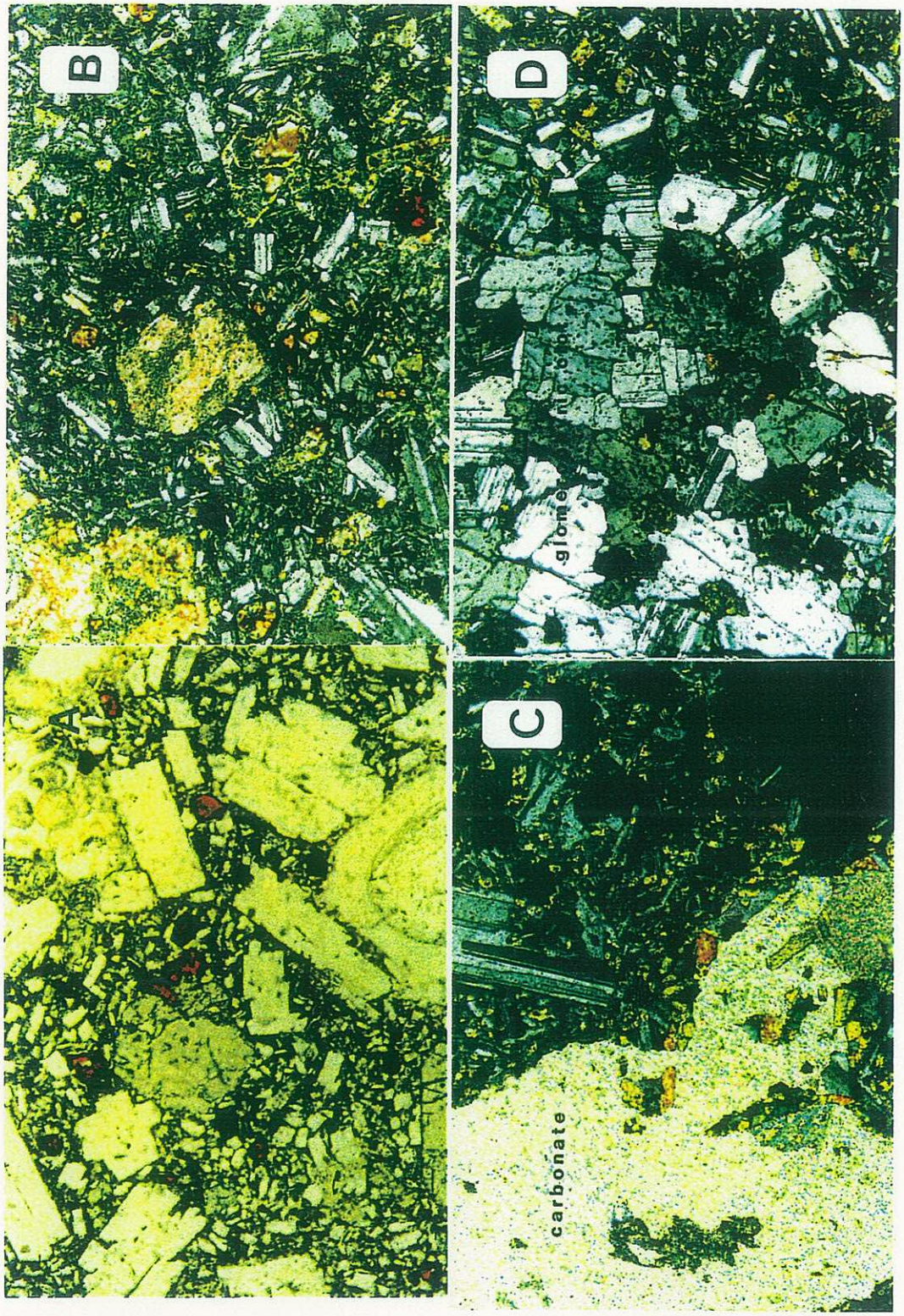
B
D
glome
A
C
carbonate

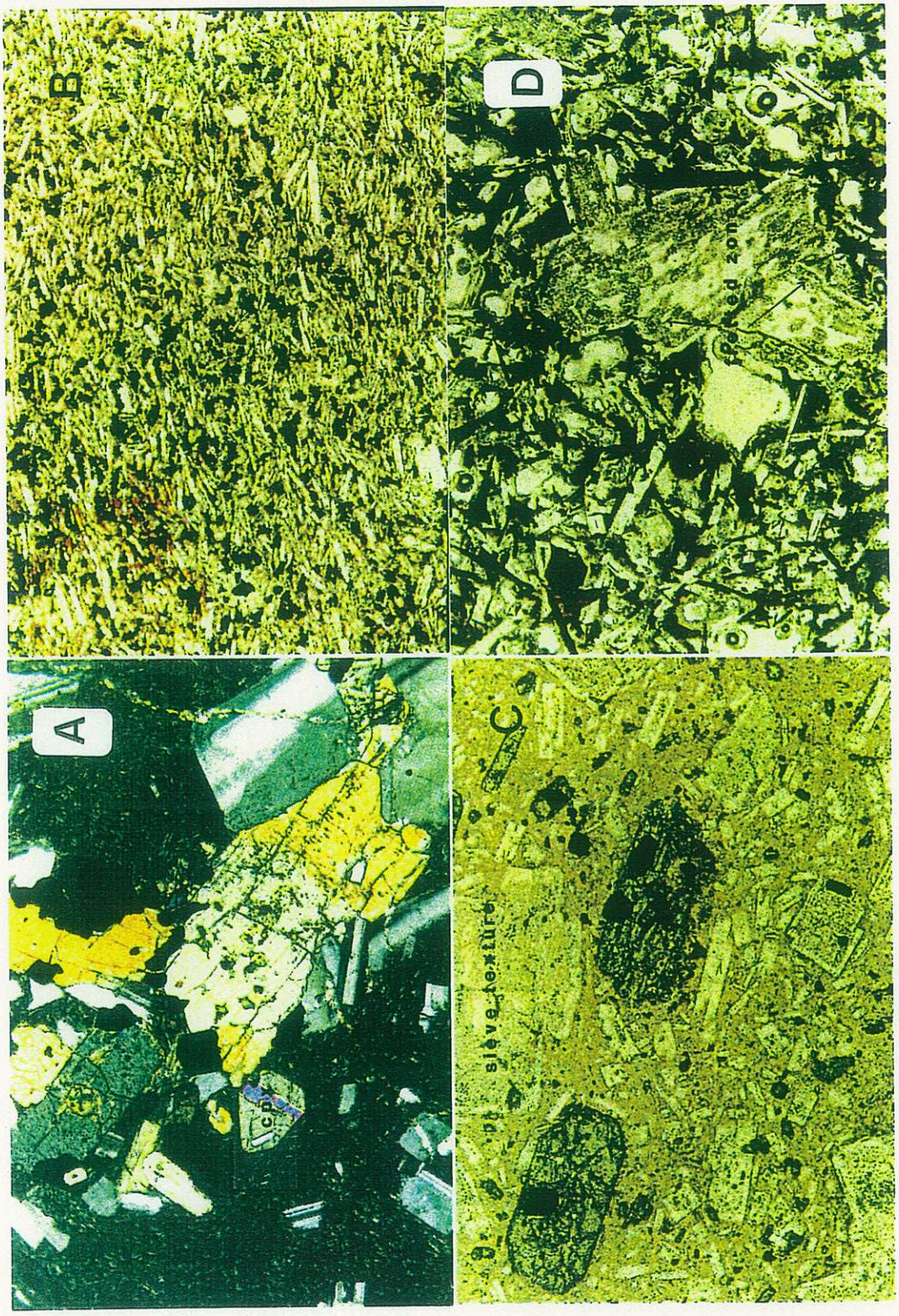
A
B
C
D
pl. sieve texture

top to one of the other varieties. Trachytic andesite is composed almost entirely of plagioclase laths and 5-10%, fine-grained equant and anhedral opaque grains.

The most common andesite within the central Myrick Spring area is the dark green to brown, orthopyroxene-rich flow (Ma^2). It typically contains 15-35% euhedral to subhedral plagioclase phenocrysts, 5-7% hypersthene phenocrysts and 1-3% opaque minerals in a fine-grained (microlitic) to glassy groundmass. Accessory Fe-Ti oxides, apatite and rutile comprise less than 1% of this rock. Apatite crystals have been identified only as inclusions in plagioclase and pyroxene phenocrysts. A highly resorbed quartz xenocryst (<1%) with a fine-grained overgrowth of an unknown mineral(s) was identified in one thin section.

Plagioclase phenocrysts are euhedral to subhedral, fine to medium-grained (up to 4 mm), with inclusions of apatite, glass, minor Fe-Ti spinels and hypersthene. Many plagioclase phenocrysts are distinctive from those found in dacitic flows in that they exhibit disequilibrium textures such as embayed and resorbed phenocrysts, with fretted, spongy or sieve textures (Fig. 13c, d). A thin mantle of clear plagioclase usually rims most of these phenocrysts (Fig. 13d, 14a). Oscillatory zoning, common in many larger phenocrysts, is not observed in the smaller, lath-like phenocrysts. Examination of extinction angles is often difficult because of the highly resorbed and zoned nature of many plagioclase phenocrysts; however, where measured the An contents range from An_{20} to An_{38}.

Pyroxenes range up to 1.5 mm in maximum dimension, and are euhedral to anhedral. They locally comprise up to 5% of the rock and are dominantly hypersthene. Large orthopyroxene phenocrysts contain inclusions of glass and oxides. In two-pyroxene andesites, augite usually forms twinned, anhedral crystals.

In some flows, mafic phenocrysts are entirely altered, leaving an opaque-rimmed

Figure 14 Captions

Figure 14a. Coarse plagioclase phenocrysts and glomeroporphyroclasts in an andesite (Ma^3, sample 1255), . Fretted texture of mantled plagioclase phenocrysts with unaltered core apparent below the penny.

Figure 14b. Photomicrograph of dacitic host for mafic inclusion in figure 14a. Opaque-rimmed, altered phenocrysts and opaque phenocrysts are pseudomorphic after pyroxene. PP. FOV~3 mm.

Figure 14c. Vent-proximal, lithic-rich zone of unwelded, rhyolitic tuff (Mrp) with block-sized clasts of dark red aphyric rhyolite, dark gray andesite and unflattened, white pumice.

Figure 14d. Vent-proximal, rhyolitic tuff (Mrp) with coarse lithic clasts and black, cognate clasts.


A
C
D
cognate clast

pseudomorph surrounding a core of chlorite±epidote±sericite in a microlitic groundmass (Fig. 14b). Stubby anhedral to hexagonal-shaped, almost entirely opaque minerals are pseudomorphs of Fe-Ti oxide after orthopyroxene.

Some altered andesitic flows are amygdaloidal with lythophysae composed of minor epidote±chlorite and zeolite. Vesiculation and zeolitic lythophysae suggest that these flows may have been volatile-rich and underwent deuteric alteration.

2.2.1.6 Myrick Tuff

The Myrick tuff (Map, Mrp) is a white to pastel-colored, non-welded, andesitic to rhyolitic ash-flow deposit (Fig. 6b, 8a, 9d; Plates 1, 2, 3 and 4). With the exception of an interbedded basaltic andesite flow (Fig. 11d; Plate 2), multiple layers of alternating normally graded, lithic-rich and lithic-poor beds combine to form a greater than 100 m thick section of pyroclastic material. Lithic-rich zones within the tuff are comprised of up to 35% accessory clasts. Some lithic clasts are subangular and greater than 1 m across. Lithic-rich zones are probably lag breccias which denote the base of an individual eruption (Fisher and Schmincke, 1984). Juvenile clasts include pumice lapilli, ash and cognate clasts; cognate clasts are found only in vent or vent-proximal facies described below. The remaining components include broken phenocrysts, apparently from crystal-rich zones, and glass. The size of lithic clasts within the thick succession of pyroclastic units in the southeastern corner of the Myrick Spring area suggests that this was a pyroclastic center.

The two dominant types of lithic clasts in the Myrick tuff are a subrounded, light to dark green andesite and a dark gray or red, laminated, aphyric rhyolite (Fig. 14c). Cognate clasts are friable, generally dark gray to black, globules of glass resembling obsidian (Fig. 14d). These cognate clasts are glassy, rapidly quenched blebs of siliceous material (Wright

et al., 1980). Similar clasts are found within a fissure vent from the Blue Chalcedony area, described below. Granitic clasts identified in basal sections of the tuff are not volumetrically significant but their appearance indicates that regional Mesozoic granites basement rocks were entrained in the eruptive material.

The most abundant phenocysts include broken plagioclase, quartz, minor sanidine and biotite (<1%). Typically glass, bubble walls and pumice are unwelded and only locally compacted. The unwelded nature of these tuffs is apparent in the field by their friable nature and unflattened pumice clasts (Figs. 15a).

A 2-3.0 m-thick, fine-grained, well-sorted, white ash unit about 1/3 of the way up from the alluvium valley (Fig. 9d), lies conformably within the Myrick tuff (Fig. 15b). It is comprised of fine-grained, angular crystals of quartz, plagioclase and opaque minerals in a glassy matrix (Fig. 15c). Apparent ripple marks were identified on the tops of green layers (Fig. 15d). Although these marks may be due to a shallow lake, depositional environment for air-fall tuff, similar types of wave-form bedding are also found in pyroclastic surge deposits (Wohletz and Sheridan, 1979). This ash deposit is overlain by greater than 70 m of tuff at the vent-proximal facies (Fig. 9d), but less than 30 m of tuff one km to the northwest.

Tuffs and overlying flows at Myrick Spring dip gently to the northwest . Tuff is thinner and lithic clasts are smaller to the northwest indicating that these exposures are probably a vent-medial tuff facies (Fig. 16a). Block-sized (>64 mm) lithic clasts, an apparent pyroclastic surge deposit, and the cumulative thickness of pyroclastic successions at the southeast corner of the Myrick Spring area (Plate 2) indicate that this was probably an eruptive center.

Figure 15 Captions

Figure 15a. Photomicrograph of pumice, angular clasts of ash and plagioclase crystals in a glassy tuff (Mrp) matrix with slightly compacted but unwelded bubble walls. Former gas-filled bubbles have spotted, opaque interiors. PP. FOV~3 mm.

Figure 15b. Fine-grained tuff within unwelded tuff at eruptive center.

Figure 15c. Photomicrograph of crystal-rich, glassy tuff shown in figure 11d. Crystals are angular and fairly uniform in size. XP. FOV~3 mm.

Figure 15d. Dark green zone of ripple marks at top of a surge deposit within Mrp eruptive center.

Figure 16 Captions

Figure 16a. Distal facies of surge deposit overlain by unwelded ash-flow tuff which is capped by a dacitic flow.

Figure 16b. Columnar jointing in dacitic flow from Myrick Spring area.

Figure 16c. Columnar jointing in dacitic flow at Goldstone area.

Figure 16d. Sheeting joints below columnar joints in flow (see figure 8a) adjacent to Myrick Spring.

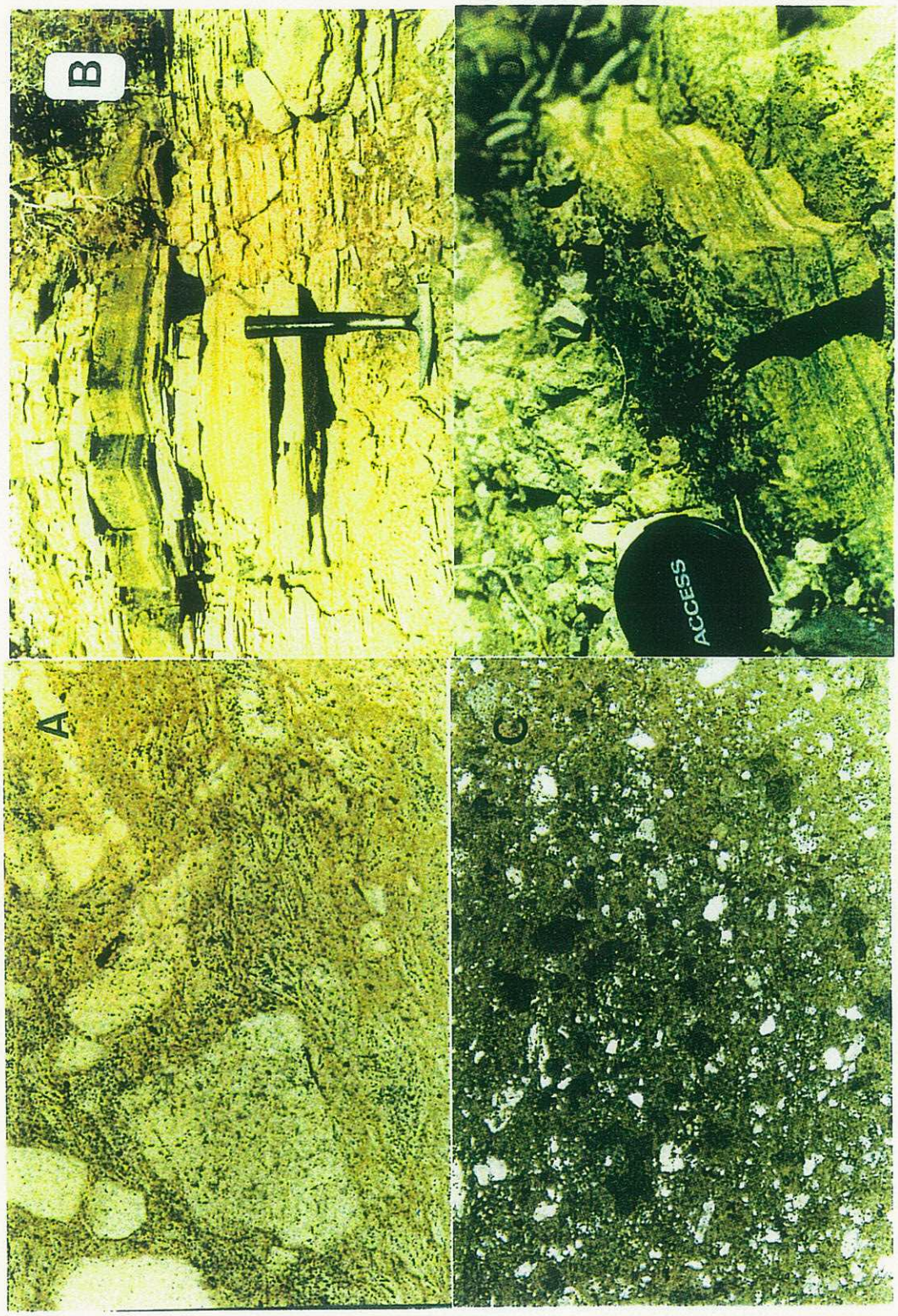
B
ACCESS
A
C

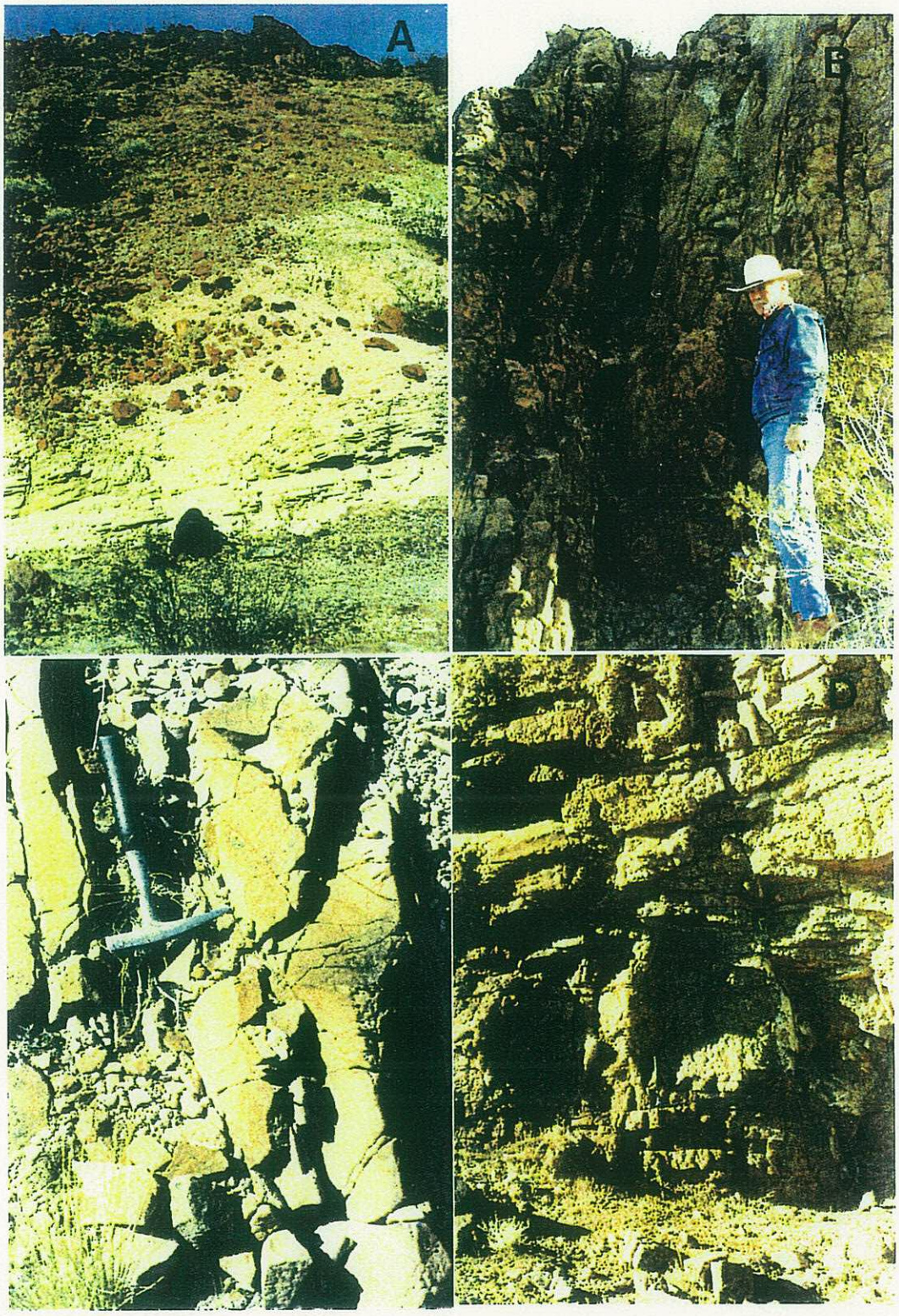
A
B
C
D

2.2.1.7 Myrick Dacite

The Myrick dacitic flows (Md; Plate 2) are tabular, porphyritic and red to gray. Megascopic features distinguishing dacitic flows from underlying tuffs include distinctive jointing, flow structures, flow lobes and pervasive red, iron oxidation (Figs. 16b, c, d; 17a).

Dacite is typically composed of 10-30% plagioclase phenocrysts, 1-3% opaque phenocrysts, groundmass microlites of plagioclase, glass, accessory opaque minerals, apatite and zircon. Most idiomorphic opaque phenocrysts appear to be pseudomorphs after pyroxene±biotite±hornblende. The opaque minerals are titanomagnetite, magnetite and ilmenite.

Plagioclase phenocrysts are sub- to anhedral, subrounded to subangular, broken or fragmented locally and often occur in glomerophyric clots. Unlike basaltic-andesite-andesitic flows in the area, plagioclase phenocrysts in Myrick dacites rarely exhibit sieve textures or oscillatory zoning. Plagioclase phenocrysts are medium- to fine-grained (up to 5 mm), fractured, embayed and seldom resorbed (Fig. 17b, c). Feldspars are primarily andesine (~An_{30-50}). Common inclusions are glass, opaque minerals and apatite.

Most dacitic flows contain elongate opaque mineral grains that appear to be pseudomorphs of an Fe-Mg silicate. The finer grained, hexagonal, equant opaque, presumably Fe-Ti oxide minerals, may be pseudomorphic after olivine. Other opaque pseudomorphs are lath-like or pseudohexagonal, subhedral and range in size from less than 0.1 mm up to 1.5 mm in maximum dimension (Fig. 17d, 18a). The cores of the original mafic minerals have been altered to chlorite±epidote. Accessory Fe-Ti oxides are fine-grained, euhedral to anhedral and comprise up to 3% of the rock locally (Fig. 18b, c).

Locally some dacitic flows have a ropy, bleached appearance (Fig. 18d). Many of

Figure 17 Captions

Figure 17a. View to northwest of Myrick Spring area with dacitic flow lobe overlaying unwelded white tuff (Mrp) in foreground and center of photograph. Garlock fault truncates the southern edge of the gray colored Slate Range in background.

Figure 17b, c. Photomicrograph of coarse broken plagioclase phenocrysts in a glassy to microlitic matrix in a dacite (Md). Unlike phenocrysts in most andesites, dacitic plagioclase may be slightly resorbed but with no fretted textures.

Figure 17d. Photomicrograph of altered, fine-grained pseudomorph presumably after orthopyroxene. These pseudomorphs are typical of dacitic flows. FOV~3 mm. XP.

Figure 18 Captions

Figure 18a. Photomicrograph of largely opaque, fine-grained pseudomorph after orthopyroxene. These opaque pseudomorphs are typical of dacitic flows (Md). FOV~3 mm. PP.

Figure 18b,c. Photomicrograph of opaque accessory minerals in a coarse, embayed plagioclase phenocryst from the Myrick dacite. b) Reflected light, FOV~.75 mm. c) Exsolved/intergrown ilmenite in magnetite. Reflected light and plane polarized light, FOV~350 mm.

Figure 18d. Ropey flow-folded transitional dacitic flow with entrained angular clasts of andesite.

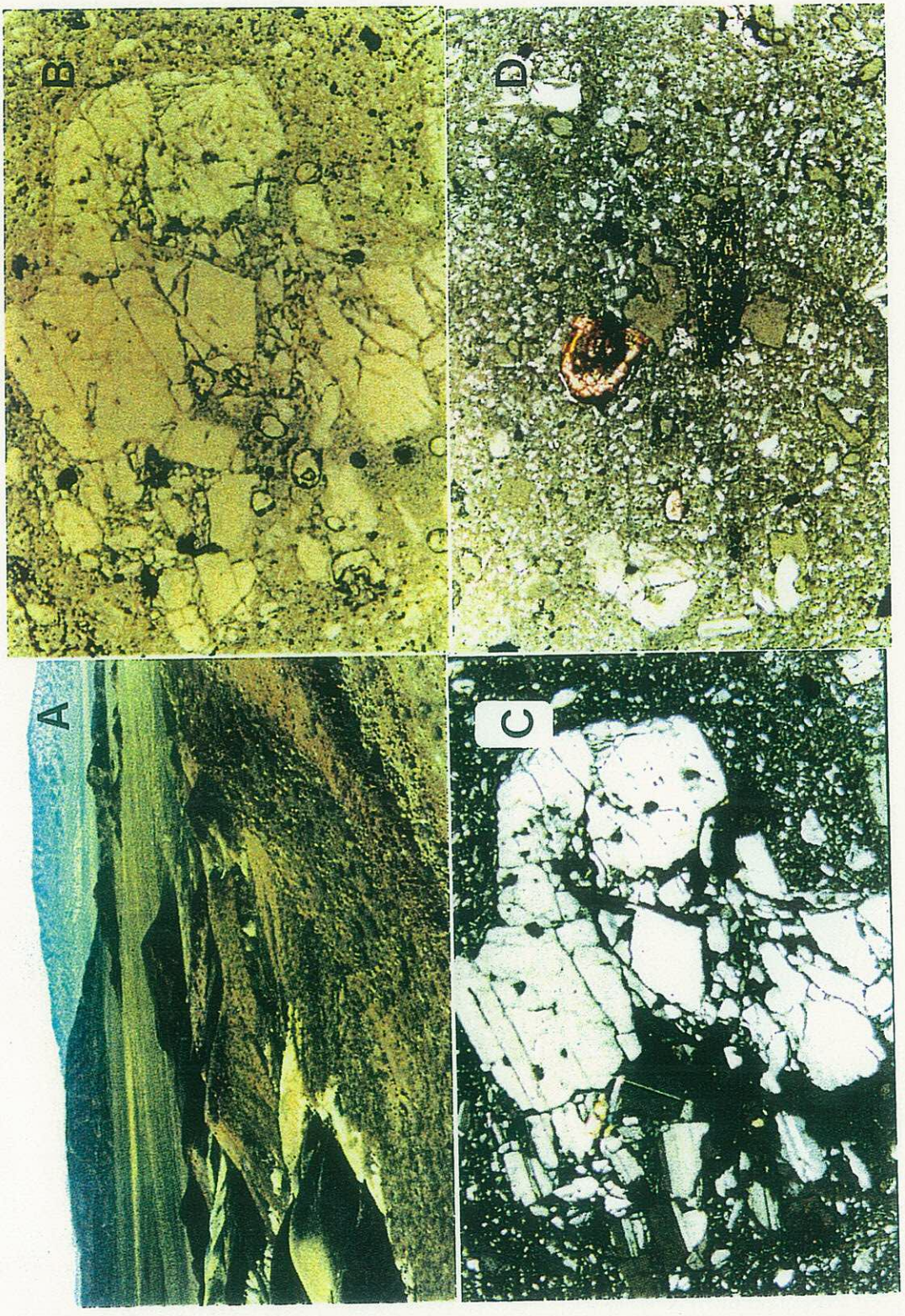
B
D
A
C

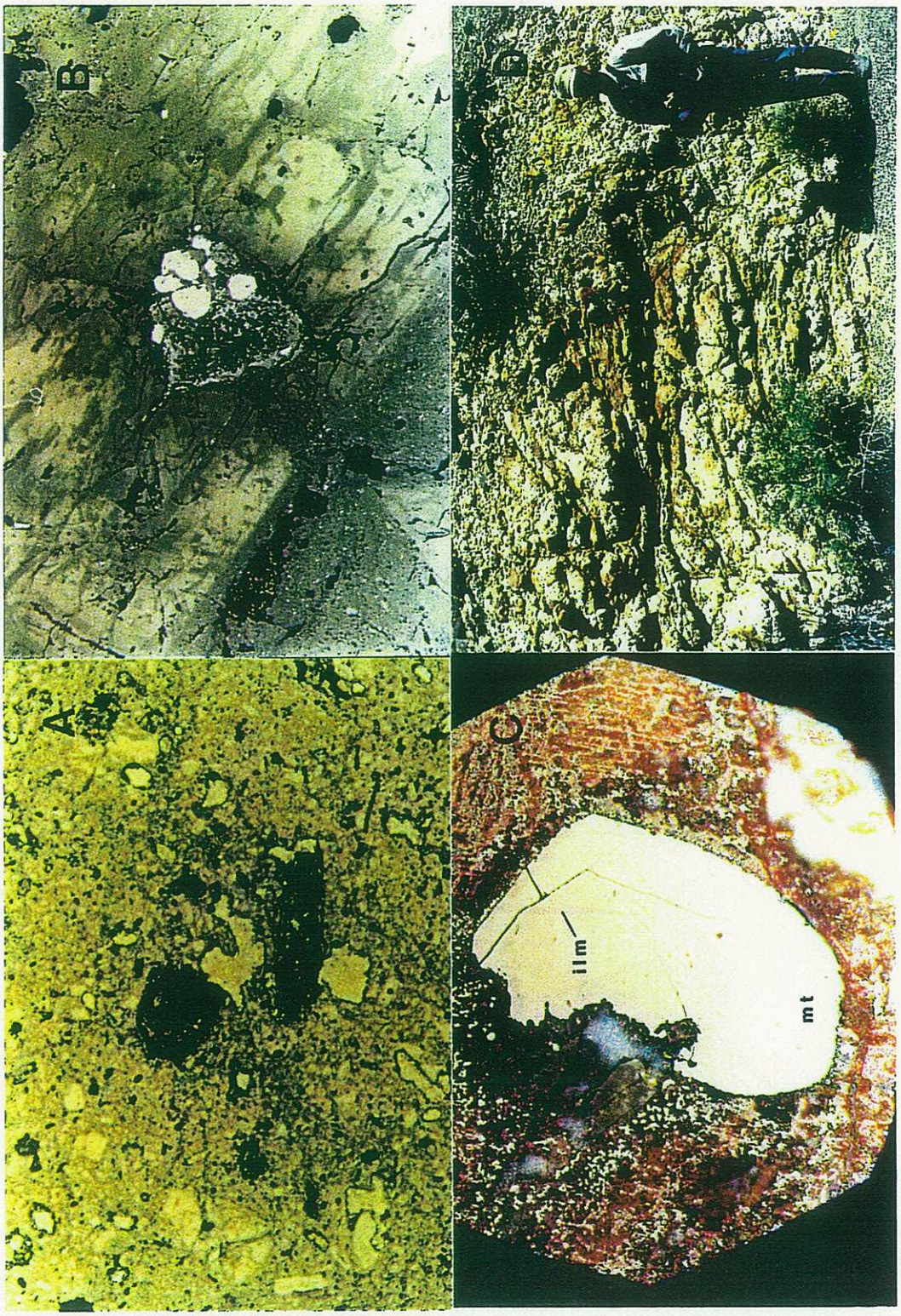
B
C
A
D
ilm
mt

these ropy zones contain angular clasts of dark gray andesite/dacite in a silicified, glassy matrix (Fig. 19a). Thin sections of some of these rocks contain clasts of what appears to be devitrified tuff. These regions are mapped as dacite but may be transitional facies between pumice-flow and dacitic lava flow (Fig. 19b).

An outcrop of dacite on the northeastern margin of the Myrick Spring area is vertically-oriented (Plate 2). With the exception of a crosscutting, northeast-trending, high-angle fault, this outcrop has experienced no major structural offset. Its vertical orientation indicates that it was probably a vent for dacitic flows.

Many of the dacitic flows in the Myrick Spring have been brecciated. Some breccias are the result of flow breccia/autobrecciation, where along the distal edges of flows lava apparently advanced over blocks that had crumbled from the flow front. Other breccias appear to be fault-related and fumarolic or hot-spring breccias. The latter group was probably a post-lithification phenomenon and related to a hydrothermal event (Fig. 19c).

2.2.1.8 Silica Dike

A northeast-trending fracture intersects Myrick Spring (proper) and appears to have controlled the flow of late silica- and carbonate-bearing fluids forming a highly siliceous, brecciated vein (Fig. 14c). This "silica dike" abuts an altered basaltic andesite flow in the northeast portion of the Myrick Spring area (Plate 2; Fig. 20a).

This dike is composed entirely of elongate laths of a simple twinned feldspar, 1-3% euhedral to subhedral phenocrysts of plagioclase, glass, and less than 1% opaque minerals including altered mafic minerals (Figs. 14c, 20b). Gray, quartz-armored clasts of dacite are entrained in silicified zones in this linear feature (Fig. 20c). The 35-45NE strike of this

Figure 19 Captions

Figure 19a. Silicified lithic-rich tuff. Silicification is usually observed in vent-proximal facies of breccia.

Figure 19b. Contact between overlying, oxidized dacite and underlying bleached dacite.

Figure 19c. Matrix-supported, silicified breccia zone which parallels local northwest-trending features such as fissure vent in Blue Chalcedony area.

Figure 19d. Northeast-trending, sheared and brecciated fault zone which parallels an altered fracture zone in the Myrick Spring area.

Figure 20 Captions

Figure 20a. Silicified, brecciated vein ("silica dike") in right foreground and highly altered basaltic andesite adjacent to vein cropping out in left-center foreground of photograph.

Figure 20b. Photomicrograph of slightly resorbed, lath-like plagiolcase phenocrysts with a distinct trachytoidal texture in a groundmass of microlitic plagioclase and glass. From "silica dike" (sample 1057). XP. FOV ~ 3.0 mm.

Figure 20c. Gray and white opaline coating on a fragment of dacite entrained in the silica-dike. The silica dike is best exposed just south of the volcanic conduit in the northern Myrick Spring area (see figure 12a).

Figure 20d. Vertically-oriented dacitic flow from the volcanic neck/conduit in Myrick Spring area. Outcrop is transected by a northeast-trending, high angle normal fault.

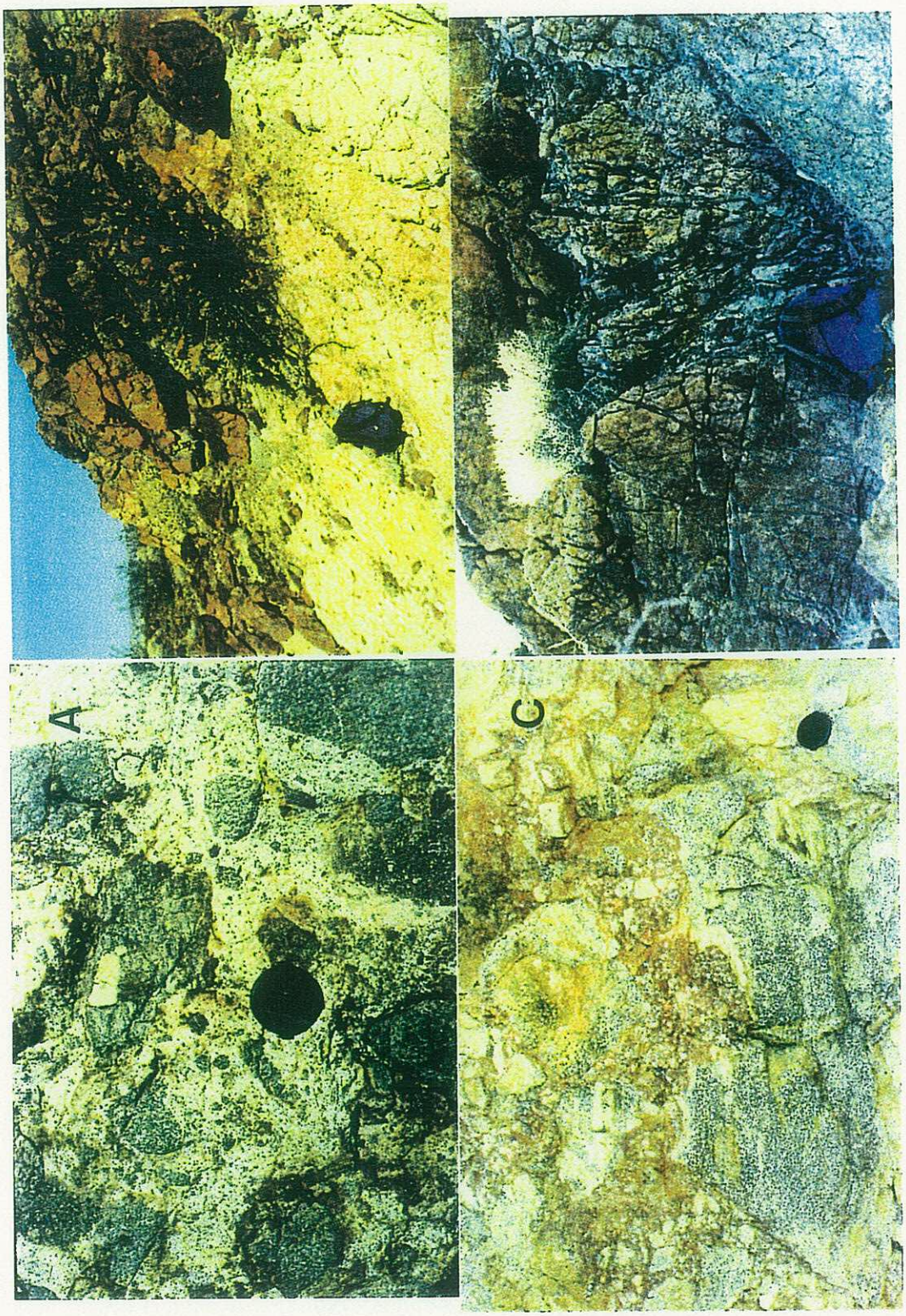
A
C

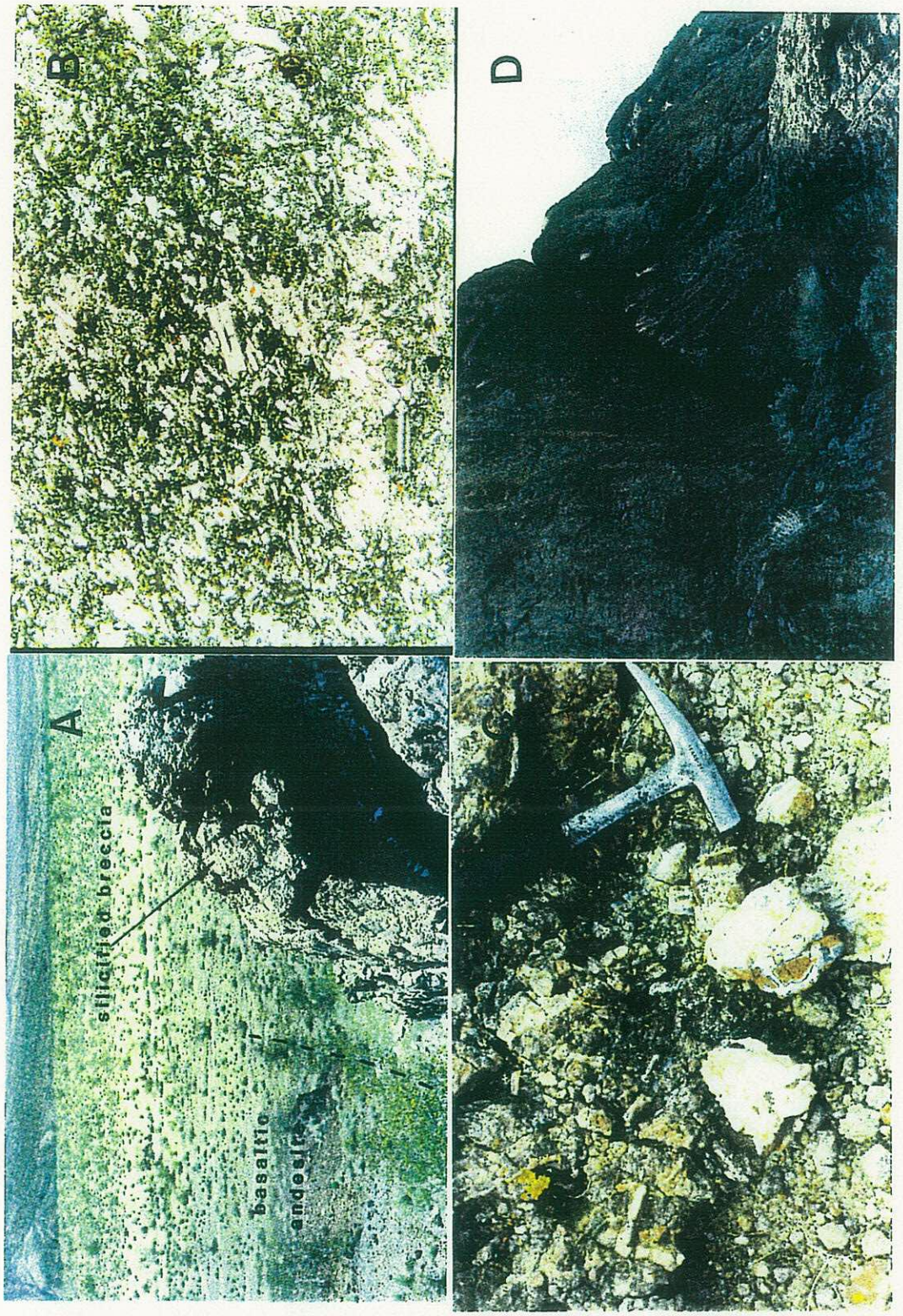
A
silicified breccia
basaltic
andesite
B
C
D

vein, its vertical orientation, and its highly silicified nature are features similar to those of a northwest-trending fissure vent in the Blue Chalcedony area, described below. This feature terminates at the previously described vertically-oriented plug of dacitic flow (Figs. 20d). Silicification of this and other features in the area (e.g. silicified breccia; Plate 2) and its termination under an apparent flow conduit suggests that this dike may be the now silicified portion of a feeder dike associated with the dacitic vent.

2.2.2 Goldstone Area

The Goldstone area is in the east central portion of the ECVF, about 2-3 km west of the Goldstone gate into Fort Irwin (Plates 1 and 3; Fig. 4). The area is dominated by porphyritic biotite±hornblende rhyodacites. The area forms a topographic high and is isolated from the rest of the field by a horseshoe-shaped, alluvial valley. Unlike most of the ECVF, the Goldstone area has undergone block-tilting with a series of steep, west-southwest-dipping homoclines comprising the bulk of the area.

2.2.2.1 Stratigraphy

The major rock types in the Goldstone area are flows of andesite (Ma^3), aphyric rhyolite (Mar), dacite (Md) and rhyodacite (Mrd). Although a tuff is present, it is not well-exposed. The area is dominated by a coalescing dome or flow-dome complex composed of multiple rhyodacitic flows. At least one, greater than 100 m thick, endogenous dome obscures a portion of the scarp, south of the horseshoe-shaped valley (Plate 1). Although no continuous stratigraphic sequence of the Goldstone area rocks has been identified, a general understanding of the stratigraphy can be determined from field relationships (Fig. 21).

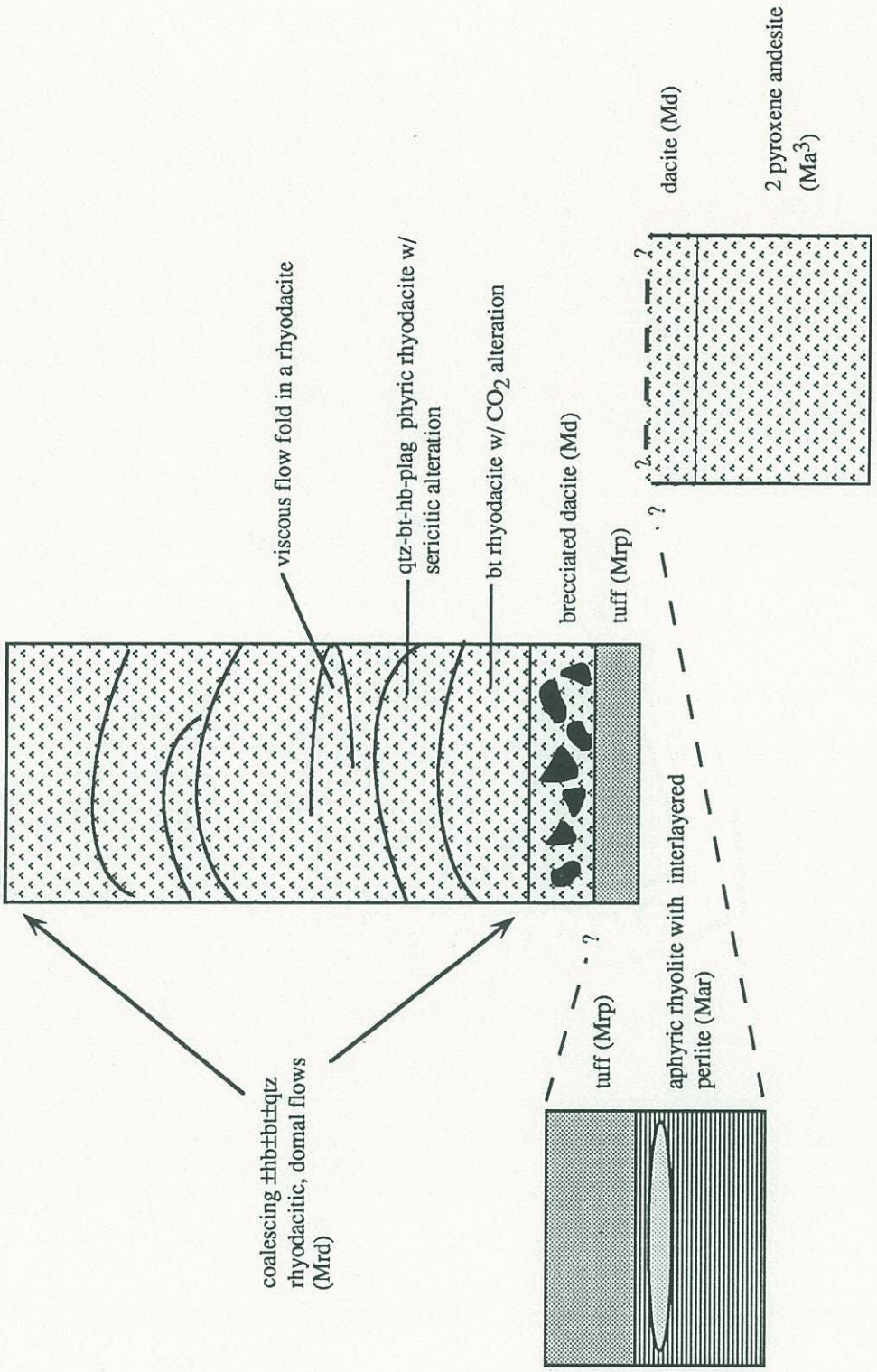

Figure 21. Generalized stratigraphic column for the Goldstone area.

A two-pyroxene andesite (Ma^3), similar to one identified at the Myrick Spring area, lies along the northern edge of the Goldstone area (Plate 3) and is in contact with an overlying rhyodacite. To the east a similar rhyodacitic flow is underlain by an unwelded tuff.

A laminated, aphyric rhyolite is on the southeastern and northwestern edges of the Goldstone area (Plates 1 and 3). The only rock found in contact with this rhyolite is a lens of gray perlite resting conformably on top of the southeast-dipping rhyolite.

The bulk of the Goldstone area is underlain by at least five rhyodacite flows ranging from a vesicular hornblende-biotite rhyodacite to a dark red, biotite rhyodacite. The youngest rhyodacite in the area forms an endogenous dome(s) adjacent to the Eagle Crags scarp (Plate 1).

2.2.2.2 Goldstone Andesite

The andesite at Goldstone (Ma^3, sample 1215; Plate 3) is a dark green to black, porphyritic flow on the north side of the area . The attitude of this rock and its relationship to the structurally higher rhyodacites that form most of the Goldstone area are uncertain.

This two-pyroxene andesite (Ma^3) is composed of about 40% plagioclase, 2-3% orthopyroxene, 1-2% clinopyroxene, 2-3% opaque minerals, minor chloritic alteration after pyroxene, less than 1% quartz xenocrysts and a microcrystalline matrix. Plagioclase phenocrysts range from greater than 2 mm to fine-grained. Coarser-grained phenocrysts typically display sieve-textured cores overgrown by a clear plagioclase (Fig. 22a). Oscillatory-zoned phenocrysts with normal and reverse zones of plagioclase growth are also present. Some plagioclase phenocrysts have overgrowths of a fine-grained pyroxene. The few coarse-grained augite crystals have overgrowths of orthopyroxene (Fig. 22b).

Figure 22 Captions

Figure 22a. Photomicrograph of two-pyroxene andesite with coarse fretted plagioclase overgrown by clear plagioclase and with orthopyroxene replacing twinned augite at the bottom of the photomicrograph. XP. FOV~1.5 mm.

Figure 22b. Photomicrograph of clinopyroxene intergrown with plagioclase with a fine-grained mantle of high birefringent unidentified mineral(s) overgrown on the clinopyroxene. XP. FOV~3.0 mm

Figure 22c. Photomicrograph of opaque lath-like and pseudomorphic phenocrysts after hornblende±biotite in a very fine-grained, plagioclase-rich and glass matrix. Phenocrysts from this aphyric rhyolite constitutes than 1% of the rock (sample 1208, Plate 1). PP. FOV~3 mm.

Figure 22d. Flat-lying aphyric rhyolite with flow lines that wrap around an inclusion of fine-grained rhyolite caught up in the flow.

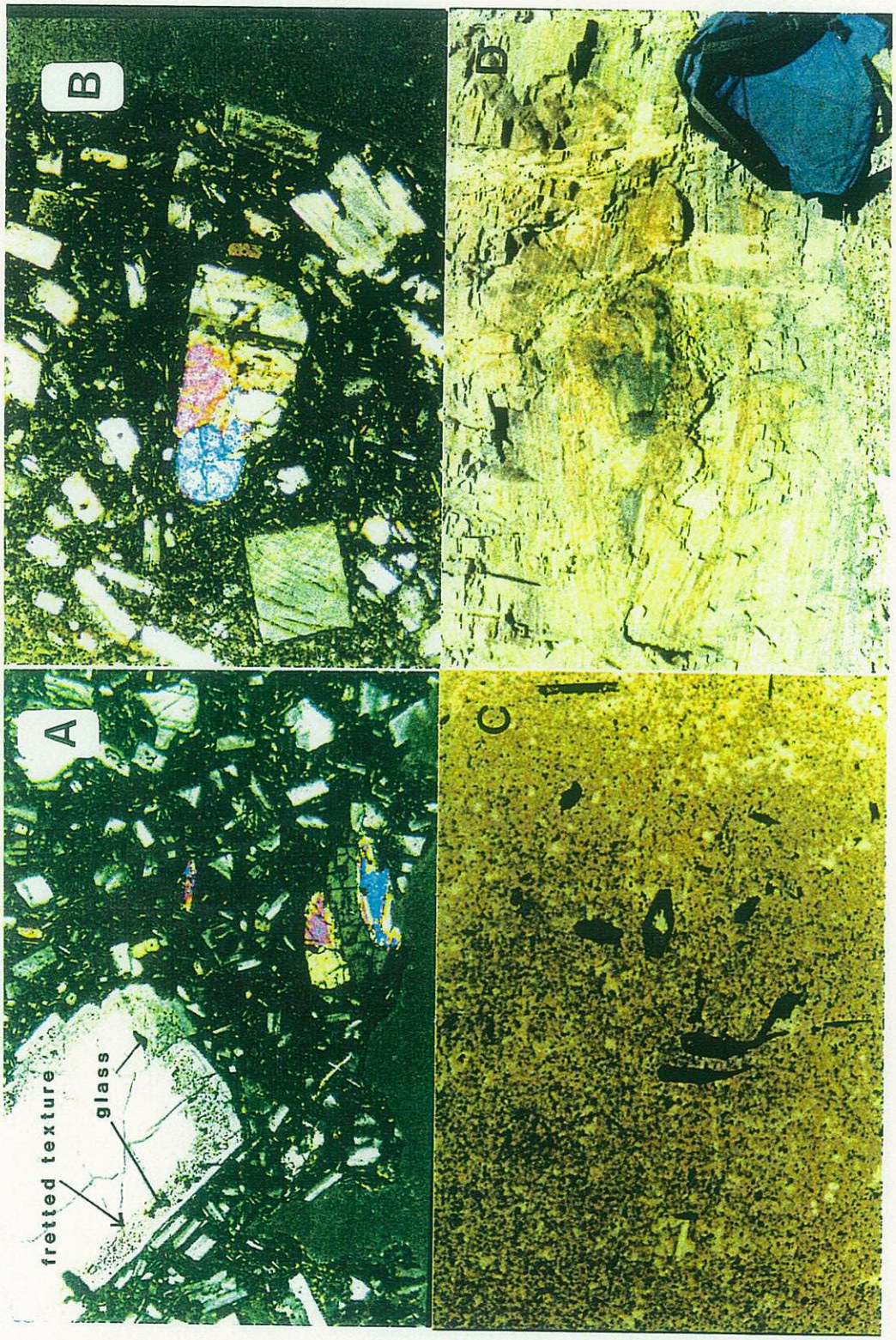
A
fretted texture
glass
B
C
D

Large (3.5 mm) resorbed quartz xenocrysts are also present and have apparently been overgrown by a pyroxene.

2.2.2.3 Goldstone Aphyric Rhyolite

A fine-grained, gray aphyric rhyolite (Mar) forms one of the basal volcanic flows in the Goldstone area (Plate 3). It is composed of greater than 98% euhedral to subhedral, microphenocrysts and microlites of plagioclase and glass. Slightly resorbed plagioclase phenocrysts comprise less than 1% of this rock. Fe-Ti oxide pseudomorphs after hornblende and biotite (<1%) are found only in some sections (Fig. 22c).

Macroscopic features include ramp structures, entrained blocks of fine-grained rhyolite and folded flow laminations (Fig. 22d; 23a). Ramp structures and flow foliations are common in viscous, siliceous flows (Bonnichsen and Kauffmann, 1987). There were no microscopic or megascopic features associated with the aphyric rhyolite to indicate that it may be a rheomorphic tuff.

2.2.2.4 Flow Dome Complex

At least five, west-southwest-dipping, porphyritic flows of rhyodacite comprise a greater than 200 m-thick coalescing, flow-dome complex with individual flows ranging from 3-5 m to greater than 50 m thick. Individual flows can be distinguished in the field by flow lines, jointing, color and phenocryst assemblage (Fig. 23b, c).

The stratigraphically lowest flow in this complex is a bleached, yellow to red, propylitized dacitic breccia that appears to overlie a poorly exposed tuff. Clasts are composed of 15-20%, fine-grained plagioclase phenocrysts in a microcrystalline to glassy matrix. Clasts are variably sized and highly angular. Fine-grained chlorite and silica are

Figure 23 Captions

Figure 23a. Flow folded and argillically altered aphyric rhyolitic flow northwest of the Goldstone rhyodacitic domes.

Figure 23b. Primary flow folds in rhyodacitic flows from the coalesced flow dome complex.

Figure 23c. Propylitically altered porphyritic rhyodacite composed of coarse plagioclase phenocrysts, glomerophyric plagioclase and minor biotite in a glassy matrix (sample 1276).

Figure 23d. Altered dacitic breccia (sample 1223, Plate 1) with stockwork carbonate-rich veining.

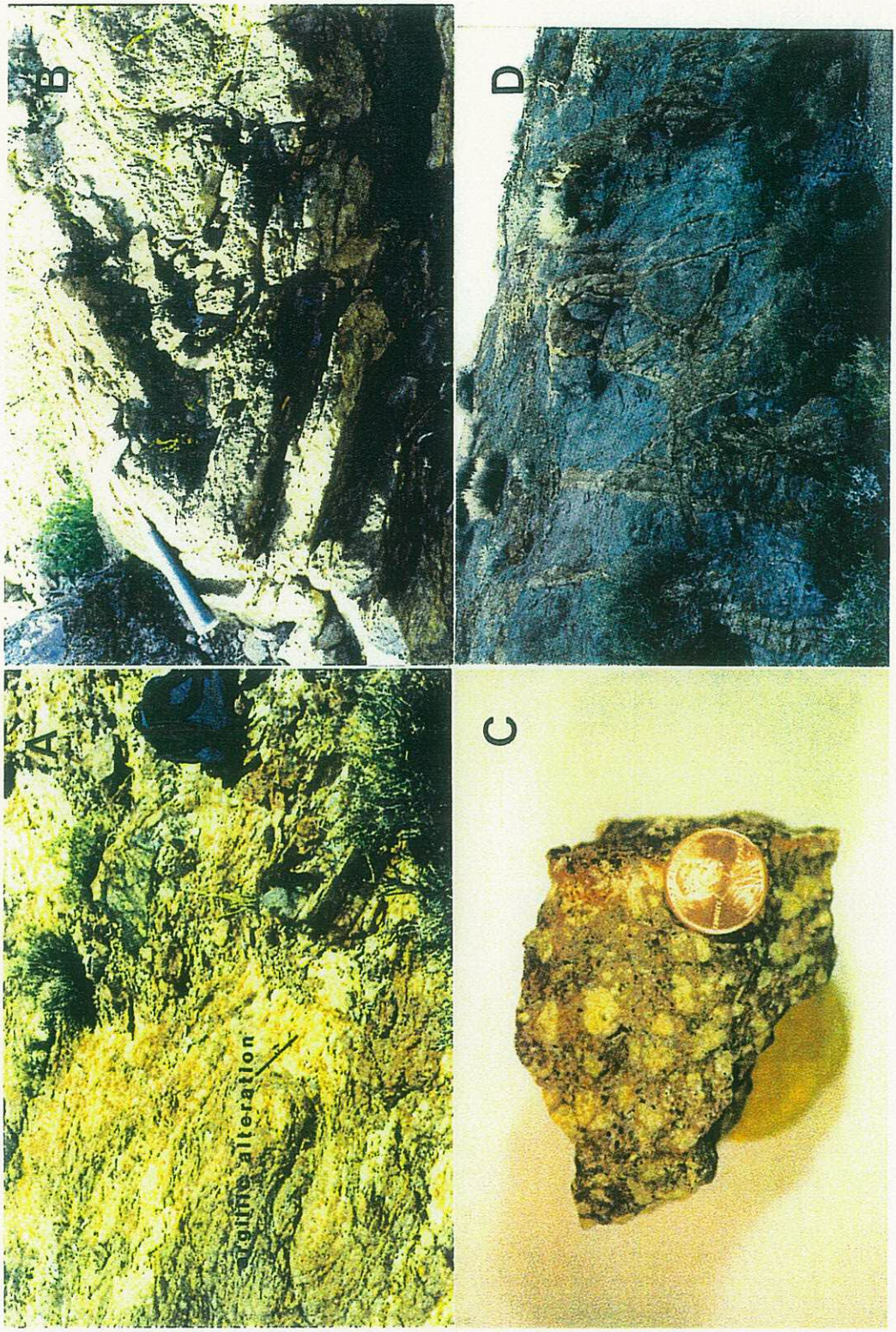
B
D
A
argillic alteration
C

the primary matrix minerals in the breccia's matrix. Concentrations of up to 5% carbonate alteration mineral(s) have been identified. The largest zone of carbonate alteration forms a stockwork vein system in a dacitic breccia northwest of the Goldstone area (Fig. 23d).

The dacitic breccia is overlain by two distinct flows (sample 1205, sample 1206; Plate 3). The lower of these two units is a biotite-plagioclase dacite-rhyodacite, similar to the Myrick dacitic flows. This rock contains about 1% quartz, less than 1% Fe-Ti oxides and a fine-grained, carbonate alteration mineral. Plagioclase phenocrysts have sieve-like textures and are overgrown by a clear plagioclase. Opaque hexagonal crystal outlines now filled with a carbonate mineral make up less than 1% of this flow. The upper flow is a glassy, propylitized plagioclase-biotite-hornblende rhyodacite. Resorbed quartz phenocrysts make up 1-2% of this upper flow and are up to 0.5 mm in maximum dimension. Euhedral phenocrysts of hornblende and biotite, typically with altered opaque rims, make up 2-4% of this rock. Sericitic alteration is pervasive in the upper flow. The matrix of this and similar rhyodacitic flows consists of lathlike plagioclase microlites, glass, fine-grained Fe-Ti oxides and fine-grained chlorite (Fig. 24a).

These two flows are apparently overlain by a red, porphyritic rhyodacite (sample 1216, Fig. 24b; Plate 3). The contact between this rhyodacite and the previously described glassy rhyodacite (sample 1206) is in a saddle zone with no exposures. A northwest-trending lineament identified on aerial photographs crosses through this saddle. Most of the flows east of this lineament are flat-lying or dip gently to the west; to the west, all of the flows are steeply west-dipping. A high-angle, up-to-the-west normal fault through this saddle could explain the observed relationships. A very glassy, vesicular rhyodacite (sample 1217; Plate 3) conformably overlies this red rhyodacite (Fig. 24c). This flow also contains altered mafic phenocrysts and very minor concentrations of fluorite.

Figure 24 Captions

Figure 24a. Photomicrograph of a glassy, propylitized plagioclase-biotite-hornblende rhyodacite with resorbed, embayed quartz. XP. FOV~ 3 mm.

Figure 24b. Photomicrograph of trachytoidal textured plagioclases in a glassy dacite (sample 1216). PP. FOV~ 3 mm.

Figure 24c. Photomicrograph of glassy, vesicular flow top to one of the flow-dome complex rhyodacitic flows (sample 1217) with highly altered pseudomorphic minerals apparently replacing pyroxene. XP. FOV~3 mm.

Figure 24d. Photomicrograph of rhyodacitic flow (sample 1249, Plate 1) with embayed plagioclase phenocrysts, a plagioclase glomerophyric clast, oxyhornblende and oxidized biotite. XP. FOV~1.5 mm.

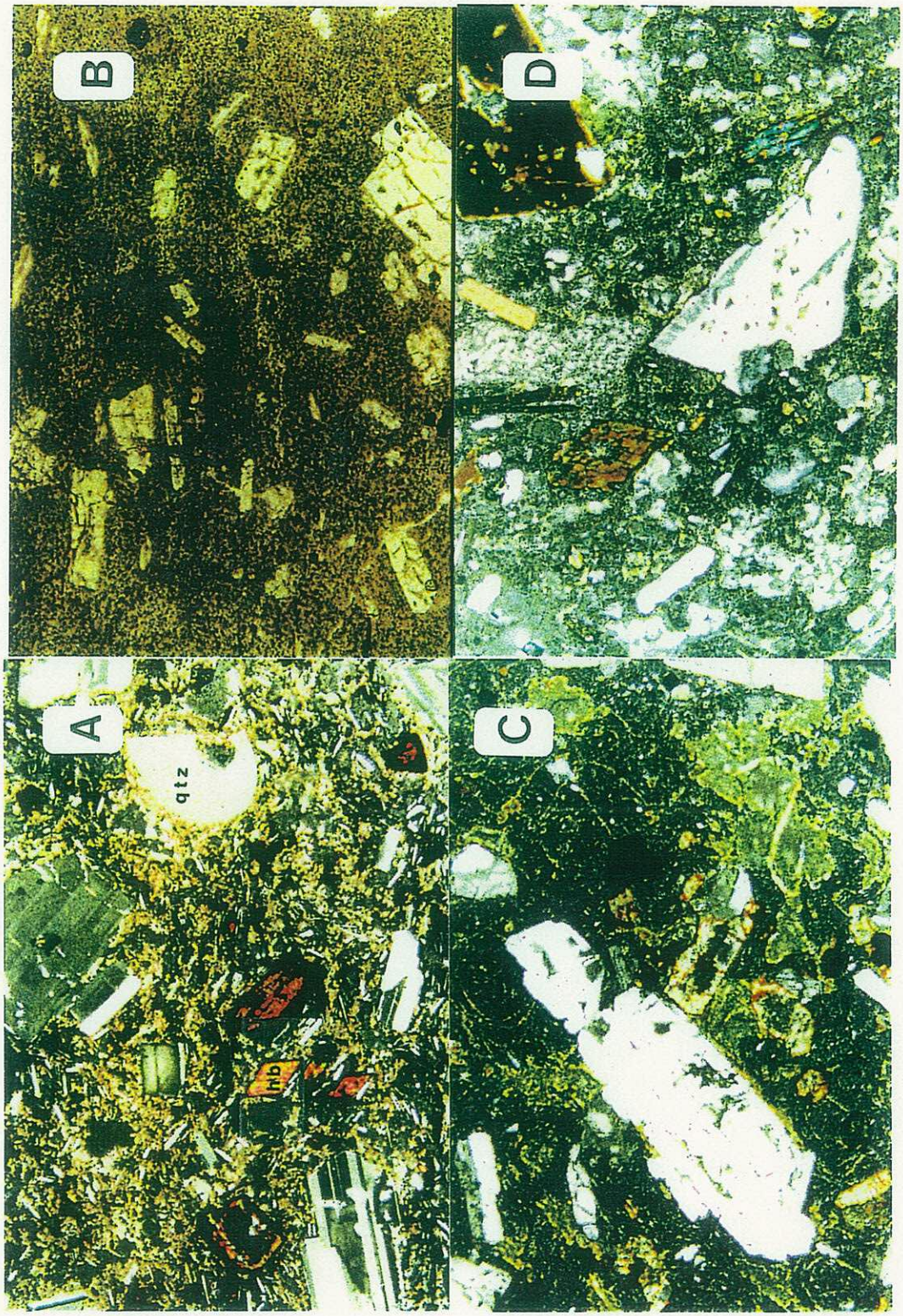
B
D
A
qtz
grt
C

At least two additional rhyodacitic flows form the upper portion of this flow dome complex. The lowermost of these flows is an altered, gray biotite-hornblende rhyodacite containing greater than 15% plagioclase phenocrysts and 3% biotite and hornblende in a fine-grained, glassy matrix. Microfracture-controlled alteration includes the addition of carbonate and silica to this rock. This flow is overlain bt a glassy, plagioclase-biotite-hornblende rhyodacite (sample 1214) containing up to 20% plagioclase phenocrysts. Biotite and hornblende form coarse (>2 mm) unaltered phenocrysts constituting 5-10% of the rock.

2.2.2.5 Goldstone Rhyodacite

Endogenous dome-forming rhyodacites (Mrd^1) are typically beige, vesicular, hornblende±biotite porphyries. Flows are composed of 15-20% plagioclase, 3-5% biotite+hornblende, 1-2% Fe-Ti oxides, and 1-4% resorbed quartz phenocrysts in a matrix of plagioclase microlites and glass.

Phenocrysts are usually not euhedral. Many have been resorbed and embayed or have experienced alteration ranging from oxidation to chloritic alteration. Plagioclase phenocrysts range from untwinned, oscillatory-zoned, resorbed and recrystallized euhedra up to 1.5 cm in length to lath-like subhedral crystals with albite twinning (Fig. 24d). Quartz crystals are generally embayed and resorbed.

2.2.2.6 Mudflow

A thin orange unit composed of nonwelded, tuffaceous material drapes the southeast flank of one of the eroded peaks at Goldstone. Unsorted angular clasts of a rhyodacitic flow, ranging from sand to boulder size constitute less than 20% of this

Figure 25 Captions

Figure 25a. Photomicrograph of clast from mudflow on the southeast side of Goldstone. Dehydrated biotite has been almost entirely replaced by an Fe-Ti oxide. PP. FOV~3 mm.

Figure 25b. Photomicrograph of mudflow matrix composed of plagioclase crystals, fine-grained mafic minerals and glass.

Figure 25c. Panoramic view looking northwest at southwest-dipping tuffs, flows and volcaniclastic breccias at Eagle Crags. Two apparently distinct tuffs near the stratigraphic top of the sequence (left) are actually one rock separated by a ~N30W, high-angle normal fault.

A
altered biotite?
B
C
Map
fault plane
Mrp
Mrp

breccia. The remainder of the unit is a brown to orange clay and ash. Unlike most of the domal rocks, clasts in this unit have been highly altered and are now composed of largely opaque, shredded pseudomorphs after biotite+unidentifiable minerals in a vesicular, glassy matrix (Fig. 25a). Volcanic clast compositions in a friable, clayey matrix, and the limited areal extent of this apparent viscous flowing unit indicates that it was an epiclastic, water-saturated mudflow associated with the flow dome complex.

The mudflow is composed of 10-20% resorbed, oscillatory-zoned plagioclase phenocrysts, 1-2% ±biotite±hornblende phenocrysts and less than 1% opaque minerals in a tuffaceous matrix (Fig. 25b). The stratigraphic position of this mudflow indicates that it was one of the last volcanic product associated with rhyodacitic volcanism in the area.

2.2.3 Eagle Crags Area

Eagle Crags is in the southern portion of the ECVF and is notable for its well-exposed, arcuate-shaped scarp (Figs. 25c; Plate 1). The scarp forms a near vertical wall easily identified on maps by tight topographic contours with over 700 m relief which define its arcuate shape (Plate 1). The difference between rocks on either side of this scarp and the attitudes of gently southwest-dipping, sheet-like strata southwest of the scarp and more steeply southwest- and west-dipping strata in the Goldstone area suggests that this feature is a high-angle normal fault.

2.2.3.1 Stratigraphy

The Eagle Crags area contains excellent exposures of vent-proximal and -distal facies of tuffs, flows and volcaniclastic flow breccias. Many of the well exposed flows, tuffs and breccias identified in the fault scarp at Eagle Crags occur in the Myrick Spring

area.

The Eagle Crags scarp is composed of a series of well exposed, thick, southwest-dipping tuffs, flows and volcaniclastic breccias. The lowermost strata are similar to those at Myrick Spring with a greater than 100m thick tuff succession marked by a basal green, devitrified zone and interlayered with a basaltic andesite. Unlike the section at Myrick Spring, the upper sections of the Eagle Crags area are composed of multiple, thick volcaniclastic breccias and interlayered silicic flows (Fig. 25c).

The entire section at Eagle Crags represents over 700 m of a continuous sequence of volcanic rocks (Fig. 26). A decrease in clast sizes and thinning of all units to the southwest suggests their source was to the northeast, or on the other side of the fault scarp.

2.2.3.2 Rhyolitic Tuff

At least three distinct tuffs are exposed in the scarp at Eagle Crags (Fig. 25c). The lowermost tuff (Map) is similar to that exposed at Myrick Spring and was not examined in detail. Although the upper two successions represent two distinct periods of multiple pyroclastic eruptions, they have similar lithic components and are simply termed rhyolitic tuff (Mrp).

The Eagle Crags rhyolitic tuff is a white, glassy, unwelded tuff comprised locally of less than 10% agglutinate or cognate clasts, 10% pumice, and minor amounts of lithic clasts (sample 1263; Plate 1). Cognate clasts are lapillus-sized, black glassy fragments. The tuff is coarsely graded with alternating basal lag breccias overlain by finer-grained, lithic-poor accumulations of ash. Each of these units represents the product of a single, pyroclastic eruption (Sheridan, 1979). Several of these units within one thick section of tuff reflect multiple pyroclastic eruptions.

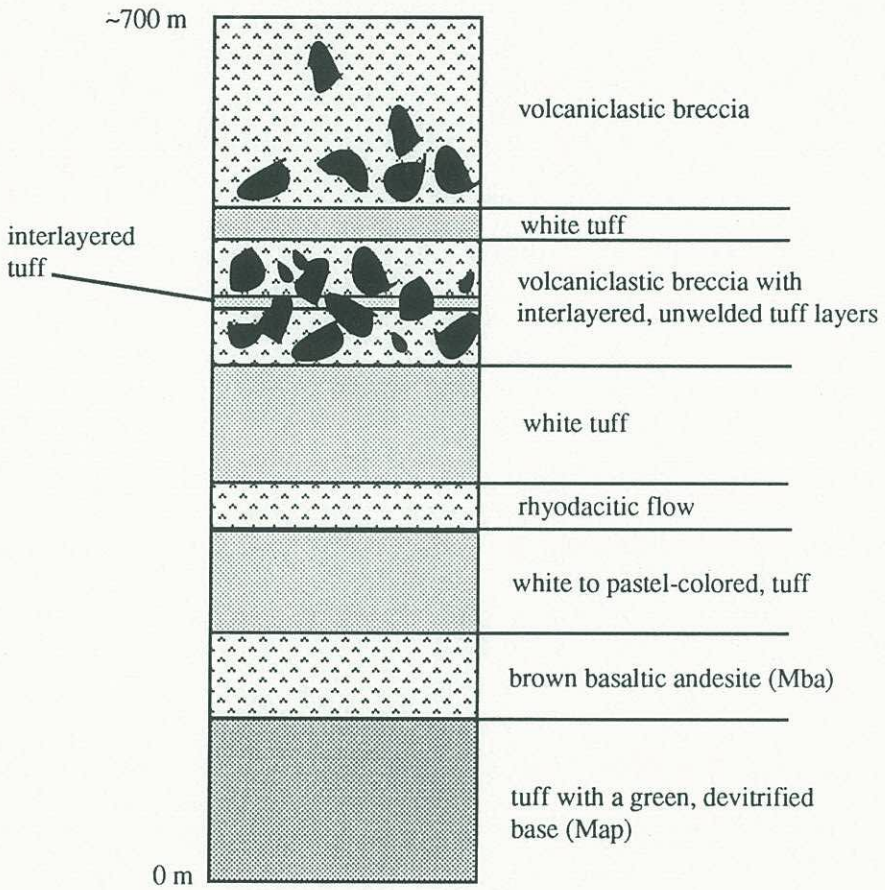

Figure 26. Generalized stratigraphic column for the Eagle Crags area.

2.2.3.3 Volcaniclastic Flow Breccia

Several flows of a blocky, volcaniclastic breccia cover most of the southernmost portion of the area and appear to terminate at the scarp at Eagle Crags (Fig. 25c). These breccias range from clast-supported to matrix-supported and contain up to boulder-sized, angular clasts of dacite and rhyodacite and finely comminuted rock and pumice (Fig. 27a). The pumice is lapillus-sized, rounded, glassy and unwelded.

A rhyodacitic clast from the volcaniclastic breccia is porphyritic with up to 20% phenocrysts of plagioclase and subordinate, altered biotite and amphibole (sample 1232, Fig. 27b). Most of its mafic minerals have been oxidized to Fe-Ti oxides. Where not totally opaque, their crystal morphology and cleavage indicate that they are altered hornblende±biotite. The matrix is composed of microcrystalline laths of plagioclase that have a subtle trachytoidal texture. Mineralogically and texturally this clast is very similar to rhyodacites from the late, endogenous domes at Goldstone.

The southwest-dipping slope of this volcaniclastic breccia, the dacitic and rhyodacitic composition of its large angular clasts, the tuffaceous matrix with noncompacted and unwelded pumice and interlayered ash-flows suggest that this is probably a lahar associated with a pyroclastic eruption. Over 5 kilometers to the south at the Indian Wells spring, an ash-flow overlain by a lahar with the same clast composition as one from the Eagle Crags scarp is less than 5 m thick, an order of magnitude thinner than lahars at the Eagle Crags scarp (Fig. 27c). This thinning to the south of sheet-like units exposed in the scarp indicates a northern paleosource for the tuffs, flows and lahars.

2.2.3.4 Rhyodacite

A red, columnar-jointed rhyodacitic flow rests conformably above a greater than

Figure 27 Captions

Figure 27a. Angular clasts of rhyodacite in a poorly sorted volcaniclastic breccia.

Figure 27b. Photomicrograph of rhyodacitic clast, sample 1232, from volcaniclastic breccia at Eagle Crags with opaque pseudomorphs after wedge-shaped hornblendes and with plagioclase phenocryst with fretted textures. PP. FOV~3 mm.

Figure 27c. Contact of relatively thin (<5 m) pumiceous ash-flow and overlying lahar from a section 5 km south of Eagle Crags fault scarp at Indian Wells spring.

Figure 27d. South side of Eagle Crags fault scarp with gently south- dipping volcaniclastic breccias on left and buff-colored, rounded rhyodacite dome in right foreground.

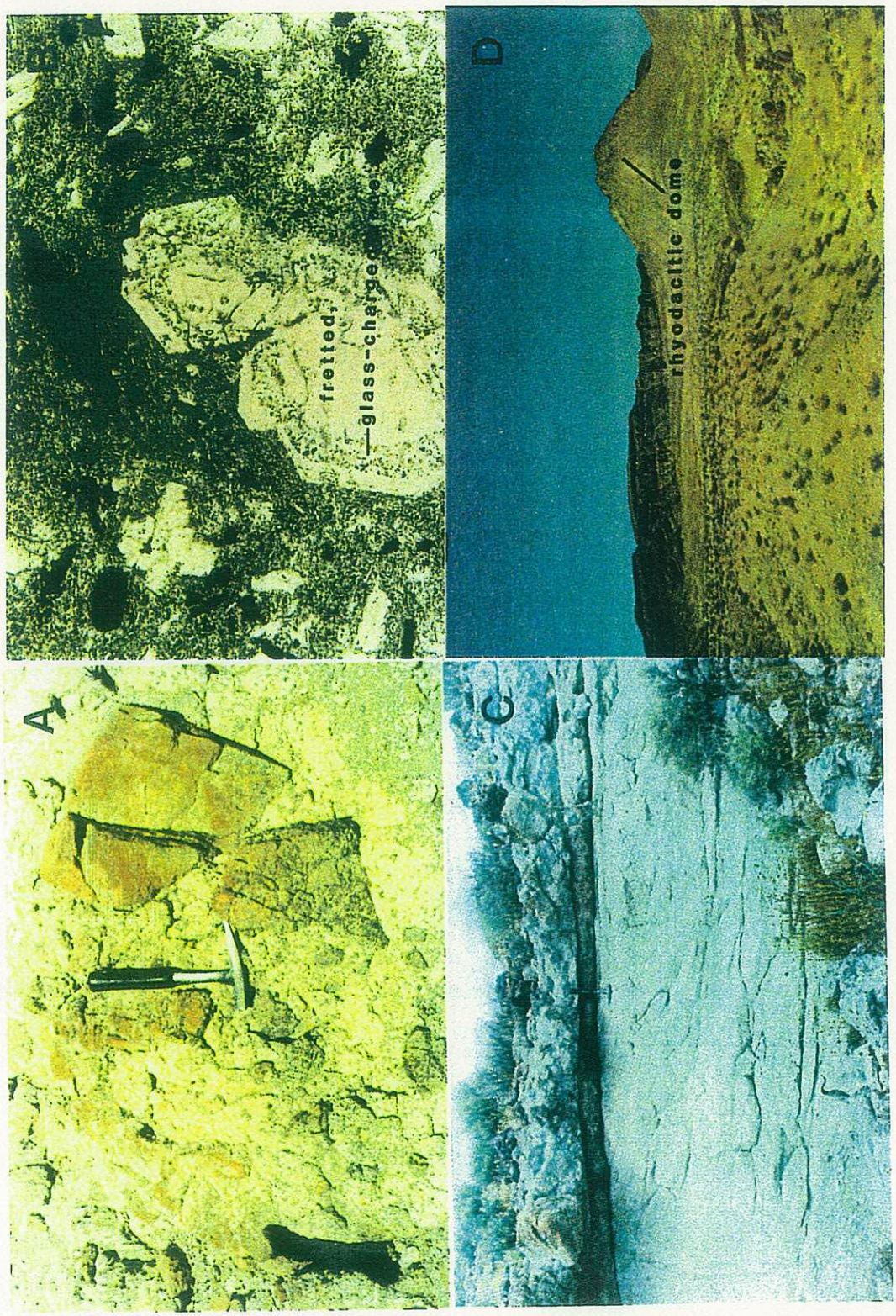
B
fretted, glass-charged
D
rhyodacitic dome
A
C

100 m thick, volcaniclastic breccia. Unlike dacites from the Myrick Spring region, this unit clearly contains opaque pseudomorphs after hornblende±biotite. Mineralogically it is similar to many of the rhyodacites that dominate the Goldstone area; however, most of the rhyodacitic flows at Goldstone are steeply-dipping and interlayered among a series of flows that form a coalesced flow dome complex. This flow, located south of the fault scarp at Eagle Crags, dips gently to the southwest. Sheet-like flows such as this were the source of many of the large, angular clasts found in volcaniclastic breccias in the area.

2.2.3.5 Andesite

A dark gray to brown, mafic flow (sample 1264), less than 3 m thick, is interlayered within a very thick rhyolitic tuff (sample 1263) west of the scarp at Eagle Crags. The mineralogy of this mafic flow is similar to that of a basaltic andesite from Myrick Spring which is also interbedded within an unwelded rhyolite tuff. Both andesites contain up to 35% resorbed plagioclase, 1-3% orthopyroxene, and less than 1% opaque minerals in a glassy and vesicular matrix.

2.2.3.6 Endogenous Domes

The youngest volcanic flows in the ECVF are dome-forming, quartz-hornblende-biotite-rhyodacitic flows. These domes are up to 200 m high and occur in the Eagle Crags area (Fig. 27d; Plate 1). Unlike the steeply-dipping, possibly faulted rhyodacitic flows that coalesced to form a flow dome complex in the Goldstone area, these domes are homogeneous and are not underlain by tuff. Mineralogically, these dome-forming rhyodacites are identical to the vesicular, hornblende±biotite±quartz rhyodacites described in the flow dome complex at the Goldstone area (Figs. 28a, b). Most of the domes are

Figure 28 Captions

Figure 28a. Photomicrograph of biotite intergrown with and replacing hornblende from a glassy, homogeneous dome-forming rhyodacite (sample 1249, Plate 1) at Eagle Crags. XP. FOV~3.0 mm.

Figure 28b. Photomicrograph of rhyodacite with hornblende and biotite phenocrysts in a highly vesicular, glassy matrix with resorbed and pitted plagioclase phenocrysts. XP. FOV~3.0 mm.

Figure 28c. Aerial view looking northeast at a northwest-trending fissure vent in the Blue Chalcedony area. Butte in foreground is composed of flat-lying rhyolitic tuffs.

Figure 28d. Photomicrograph of trachytoidal texture of plagioclase (sample 1244, Plate 4) in the basal andesite from the Blue Chalcedony area. XP. FOV~3.0 mm.

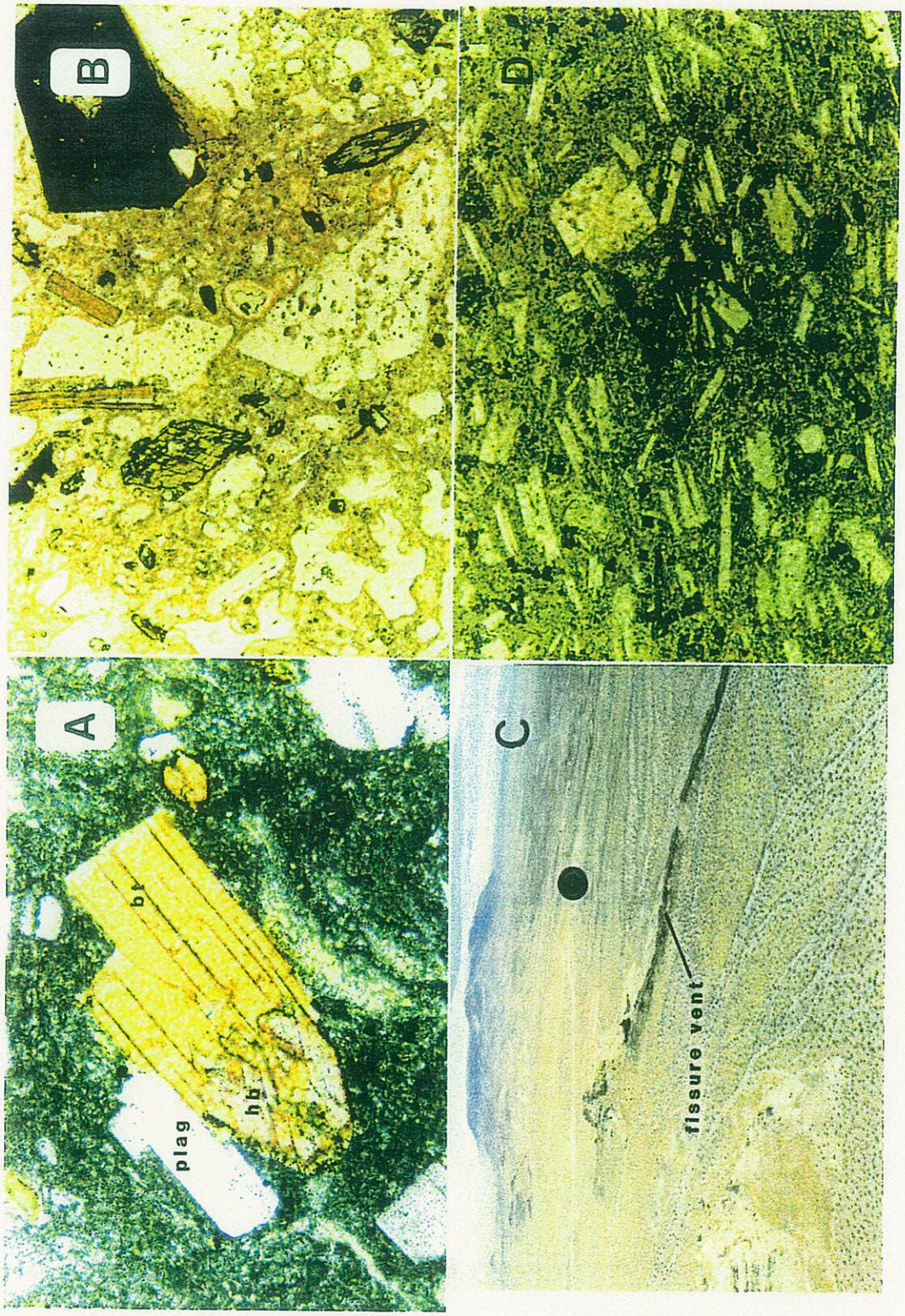
A
plag
bf
hb
B
C
fissure vent
D

steep sided with levees and debris aprons along their flanks suggesting that are endogenous domes.

2.2.4 Blue Chalcedony Area

The Blue Chalcedony area is 11 km southwest of Myrick Spring and was so-named by mineral collectors who found museum-quality blue chalcedony in geodes and in voids within rhyolitic flows (Fig. 4; Plate 4). A unique aspect of the Blue Chalcedony area are the rhyolitic flows which are not found anywhere else in the ECVF. The area is also notable for the Blue Chalcedony spring, an ephemeral spring similar to Myrick Spring. Na-K-Ca geothermometry calculations indicate a reservoir temperatures for this spring as high as 172°C (Austin et al., 1979).

2.2.4.1 Stratigraphy

The Blue Chalcedony area is bordered to the west and north by alluvium of the Pilot Knob Valley. The valley contains discrete outcrops of Paleozoic metamorphic rocks and buttes composed of rhyolitic tuff (Plate 3, Fig. 4). To the east the area is bounded by a complex series of dacitic to rhyolitic tuffs and flows. The southern and southwestern margins of the area are marked by a west-trending scarp very similar to the Eagle Crags scarp. The scarp is bounded to the north by an alluvial valley. It is obscured on its western limit by an elongate, west-trending granite which is cut by westerly trending dikes.

A trachytic andesitic flow unformably overlying altered crystalline basement rocks is the basal basal volcanic unit in the Blue Chalcedony area (Fig. 29). Stocks of Cretaceous granite intruded the Paleozoic rocks throughout area (Carr et al., 1993).

Unwelded rhyolitic tuff at least 20 m thick lay conformably on andesite and is overlain by rhyolitic flows. These tuffs form buttes throughout the Pilot Knob valley. The

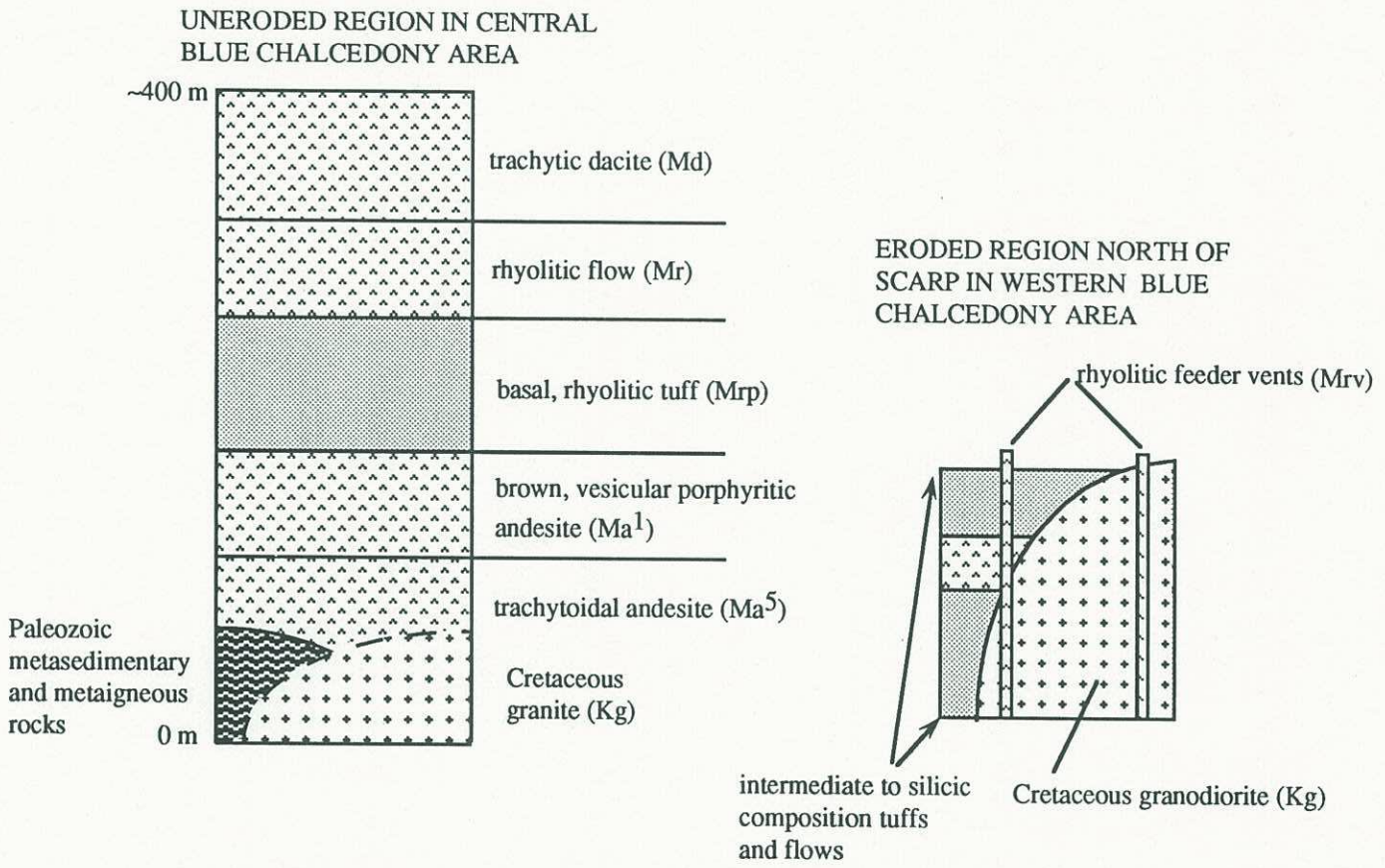

Figure 29. Generalized stratigraphic column for the Blue Chalcedony area.

most distinctive feature in the valley is a butte that is bordered on its western margin by a northwest-trending, fissure vent (Fig. 28c).

A flat-lying, rhyolitic porphyry flow conformably rests on the rhyolitic tuff. Many of these flows can be traced back to plug-like vents and feeder vents on the southern margin of the area. These vertically-oriented plugs are hypabyssal rhyolites. Similar rhyolites form a west-northwest-trending dike swarm that marks the southern boundary of the area.

The caprock of most of the hills in the area is a greater than 50 m-thick flow of trachytic dacite. Like most dacitic flows in the area, these form competent, steep-sided slopes and locally exhibit well defined columnar jointing.

2.2.4.2 Andesite

The two distinct andesite flows found in the were also identified in the Myrick Spring area. They are the steeply-dipping vesicular andesite porphyry (Ma^1) and a flat-lying, fine grained trachytic andesite (Ma^5). Similar to the outcrop at Myrick Spring, the very poor exposure of vesicular andesite makes it difficult to clearly determine its stratigraphic relationship to other volcanic units in the area or within the entire ECVF. The vesicular andesite porphyry (Ma^1) strikes northwest and is in direct contact with overlying rhyolitic tuffs and flows. The entire exposure of this unit is an outcrop approximately 7m x 1 m.

A red to brown, non-porphyritic andesite (Ma^5) contains greater than 70% plagioclase, 2-3% fine-grained mafic minerals, 5-7% opaque pseudomorphs after mafic minerals and accessory Fe-Ti oxides. The red unit contains up to 25% vesicles and greater than 30% subhedral laths of plagioclase, 5-7% subhedral oxidized pseudomorphs,

probably after a mafic mineral, and anhedral Fe-Ti oxides in a very fine-grained, red matrix (sample 1244; Fig. 28d).

2.2.4.3 Tuff

Tuff at Blue Chalcedony (Mrp) is a white, unwelded rhyolite that directly underlies rhyolitic flows. Lithic-poor facies of this tuff are compacted and contain broken phenocrysts, devitrified pumice and clasts of tuff in a glassy, slightly compacted matrix (Fig. 30a). At least 10-20% of the tuff is comprised of variably broken euhedral phenocrysts of quartz, sanidine, plagioclase, biotite and Fe-Ti oxide minerals (Fig. 30b). Lithic-rich zones have up to 20% lithic clasts, including 5-10% of black, glassy cognate clasts and discrete rounded clasts of the fine-grained, red andesite previously described.

2.2.4.4 Fissure Vent

An excellent exposure of a 5-7 m wide, N45W-trending fissure vent is in the north of the Blue Chalcedony area (Figs. 28c, 30c; Plate 4). The vent is almost 1 km long and appears to have been relatively undisturbed since its last eruptive period. Although similar features have been identified from aerial reconnaissance, none have been field checked.

Four lateral zones are apparent in this fissure vent from its center outward (Fig. 30c). These zones have obvious textural and geochemical differences. The core of the vent is 4-5 m wide and is composed of gray, highly friable perlite (sample 1336). Around the core is a red, highly silicified "inner shell" less than 1 m wide; it forms the only competent rock in this outcrop (sample 1335). Surrounding the inner shell is a zone of welded rock composed almost entirely of flattened black, glassy blebs that were mapped as "cognate clasts" in tuffs from the area (sample 1334; Figs. 30d, 31a). These obsidian-like

Figure 30 Captions

Figure 30a. Photomicrograph of slightly compacted and welded bubble walls from the rhyolitic tuff (Mrp, Plate 4). PP. FOV~3.0 mm.

Figure 30b. Photomicrograph of crystal-rich facies of rhyolitic tuff with Carlsbad twinned sanidine, oxidized biotite with bent cleavage traces and a clast of a very fine-grained, trachytic flow in a glassy matrix. XP. FOV~3.0 mm.

Figure 30c. Aerial view looking southeast down the axis of the laterally-zoned fissure vent. Its most prominent features are the highly silicified, "inner shell" walls.

Figure 30d. Welded and compacted fiame forming eutaxitic texture of the welded zone from the fissure vent.

Figure 31 Captions

Figure 31a. Highly silicified, "inner shell" of fissure vent. Camera case is on welded, fiame-rich zone.

Figure 31b. Photomicrograph of rhyolitic flow (sample 1031) with euhedral, twinned sanidine adjacent to a euhedral quartz phenocryst in a fine-grained and glassy matrix. XP. FOV~3.0 mm.

Figure 31c. Photomicrograph of embayed quartz phenocryst from a very glassy, rhyolitic flow top (sample 1106) at Blue Chalcedony. Opaque minerals are after biotite. XP. FOV~ 1.5 mm

Figure 31d. Aerial view of west-trending, 1-2 m thick rhyolitic feeder dike crosscutting a thick tuff from southern side of the Blue Chalcedony area.

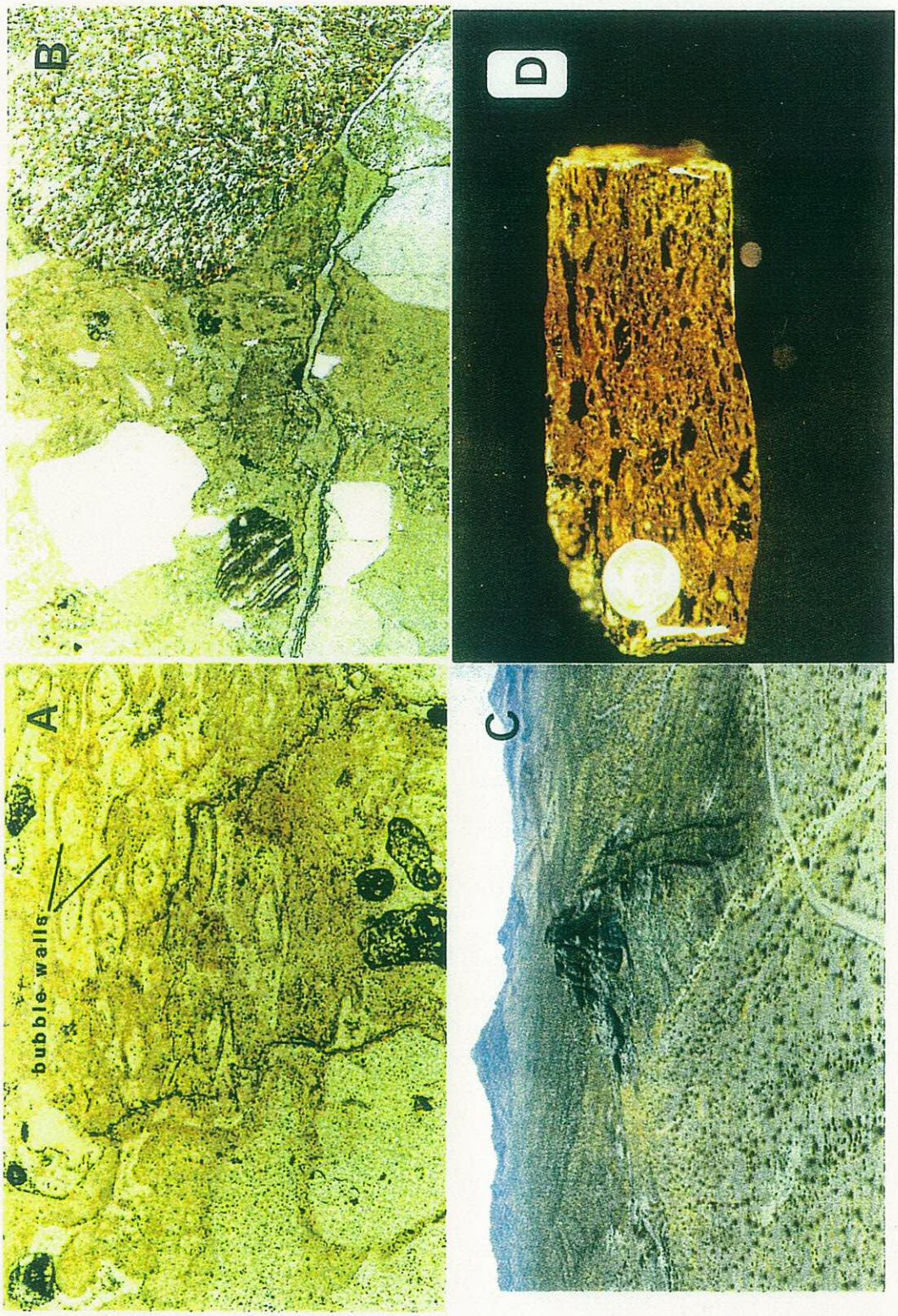
B
D
A
bubble walls
C

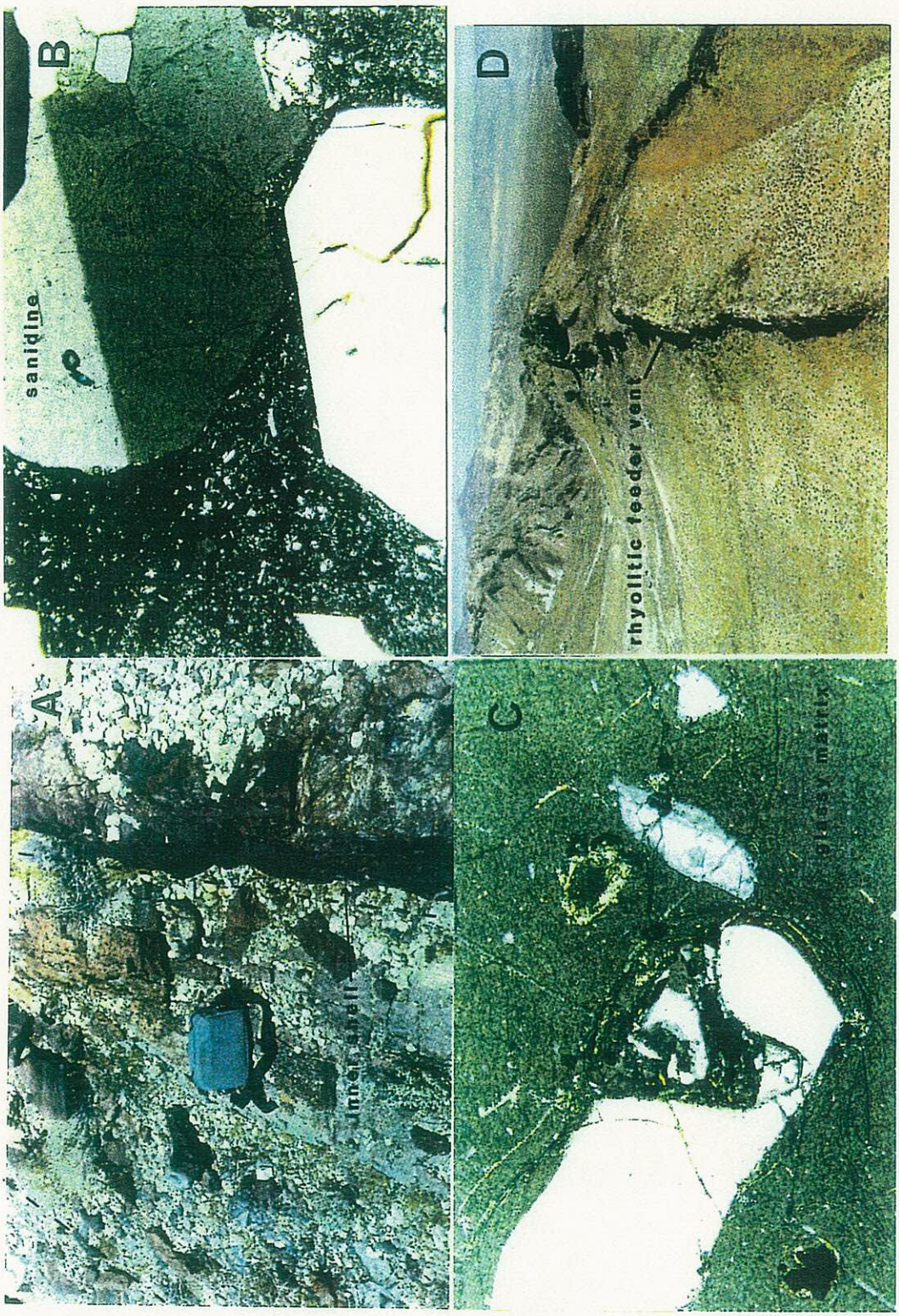
A
B
sanidine
C
glassy matrix
D
rhyolitic feeder vent

clasts are elongate parallel to the strike of the fissure and, as hot viscous blebs of material that didn't discharge from the vent, they probably experienced compression perpendicular to the strike of the fissure vent immediately after eruption. This fiame-rich zone is bordered by a black, glassy, selvage of obsidian (sample 1233).

All four of these zones are vertically oriented and strike northwest. The surrounding butte-forming tuff is flat-lying and contains abundant cognate clasts near the fissure vent. The concentration of cognate clasts decreases away from the vent suggesting that this vent was the source of rhyolitic tuff in Pilot Knob valley (Plates 1 and 4). Unlike tuff in the vent, however, tuff throughout the valley is unwelded and relatively uncompacted.

2.2.4.5 Blue Chalcedony Rhyolitic Flow

The most prominent ridge-former near Blue Chalcedony spring is the red, porphyritic Blue Chalcedony rhyolite (Mr) that conformably rests on unwelded tuff to form a locally extensive coulee. It ranges from 10-50 m thick and thickens toward its vents to the south (Plates 1 and 4). It is composed of up to 30% phenocrysts of quartz, sanidine and plagioclase with biotite, Fe-Ti oxides and pseudomorphs after biotite (Fig. 31b). Quartz phenocrysts range from coarse-grained euhedral phenocrysts to highly resorbed and embayed phenocrysts (Fig. 31c). Sanidine phenocrysts form twinned and untwinned euhedra with inclusions of plagioclase and glass. Sanidine and plagioclase form anhedral glomerophyric clasts locally. Fe-Ti oxides and biotite comprise less than 2% of the matrix minerals.

2.2.4.6 Rhyolitic Feeder Dike

Two distinct styles of rhyolitic vents occur in the area. Vertically-oriented plugs or necks of rhyolite and west-trending rhyolitic feeder dikes to the south of the area (Plate 1) have been identified (Figs. 31d, 32a). The feeder dikes range from 1-5 m thick, are vertical and in the best exposures have black, glassy selvages (Fig. 32b). Rhyolites from this dike swarm have the same mineralogy as the coulee-forming rhyolitic flows.

2.2.4.7 Dacite

A fine-grained, flat-lying, plagioclase-phyric flow caps the rhyolitic flows. This dacite (Md) is similar to trachytic dacites in the Myrick Spring area. Plagioclase phenocrysts are lath-like euhedra aligned to form a trachytoidal texture (sample 1030). Larger euhedral to subhedral plagioclase phenocrysts (~1 mm) comprise less than 1% of this rock.

2.3 Major and Trace Element Geochemistry

Whole rock and trace element geochemical analyses were performed on sixty-one samples from the ECVF primarily to support field and petrographic observations. Results from these analyses are listed in Table 1. Samples were classified into rock types based on a combination of mineralogy, anhydrous, chemical compositions normalized to 100% and CIPW mineralogies (Tables A.1, A.2; Appendix A). Where petrographic characteristics were insufficient to classify samples, chemical compositions became the primary criterion used for classification. Although interpretations of these data and related calculations such as A/CNK ratios, D.I.'s, norms and Mg numbers are limited by statistical and mechanical errors in the data and by assumptions in the Fe-weighting factors, these data offer a

Figure 32 Captions

Figure 32a. Aerial photograph of west-northwest-trending rhyolitic feeder dikes from the southern portion of the Blue Chalcedony area. FOV across is approximately 5 km. North parallels the long axis of photo.

Figure 32b. Rhyolite from feeder dike in the Blue Chalcedony area.

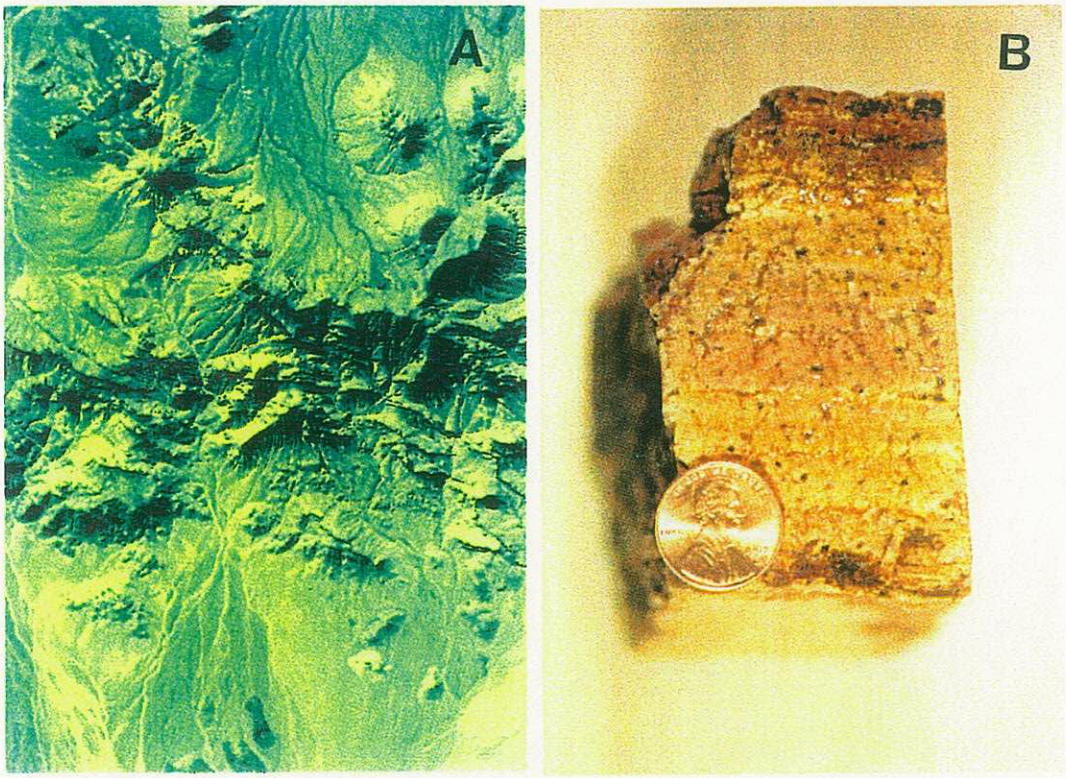
A
B

Table 1. Results of geochemical analyses of selected samples from the Eagle Crags Volcanic Field.

Rock type[1]	basalt	bas and	bas and	bas and	bas and	and	and	and	and	and	and	and	and	and
Map ID	Mb	Mba	Mba	Mba	Mba	Ma^2	Ma^2	Ma^3	Ma^5	Ma^5	Ma^5	Ma^5	Ma^3	Ma^2
Field ID	1133	1039	1040	1126	1315	1015	1018	1034	1244	1245	1246	1099	1215	1264
wt %														
SiO_2	49.8	40.1	50.4	54.5	57.0	62.0	58.1	61.1	60.2	61.2	61.5	57.6	60.9	58.0
Al_2O_3	16.3	13.8	16.6	16.3	17.5	16.5	15.6	16.5	15.9	16.5	15.7	16.0	16.2	17.3
CaO	9.82	16.8	9.56	8.13	6.05	4.35	6.38	4.82	4.3.0	3.43	3.46	4.87	4.72	5.77
MgO	6.52	4.32	3.21	1.81	2.69	1.40	3.32	2.08	1.01	0.41	0.31	1.03	1.97	1.07
Na_2O	3.09	2.28	2.98	3.47	4.03	3.94	3.58	4.10	4.27	4.28	3.46	4.21	3.77	3.52
K_2O	0.62	0.29	0.57	1.84	2.06	2.52	1.34	2.37	2.86	3.31	3.38	2.32	2.76	1.81
Fe_2O_3	9.18	10.0	11.8	7.52	7.13	3.75	7.02	5.02	8.63	8.01	8.32	9.85	5.53	6.60
MnO	0.15	0.35	0.14	0.12	0.10	0.06	0.14	0.09	0.17	0.03	0.04	0.11	0.10	0.06
TiO_2	1.39	1.16	1.52	1.45	1.33	0.68	1.20	0.87	0.77	0.81	0.90	1.20	0.95	1.56
P_2O_5	0.16	0.12	0.21	0.23	0.26	0.16	0.21	0.21	0.34	0.34	0.38	0.55	0.24	0.27
LOI	0.93	9.39	2.54	3.39	1.35	3.00	1.93	1.16	1.30	1.90	2.25	2.35	2.90	3.75
SUM[2]	100.0	98.7	99.6	98.9	99.7	98.6	99.0	98.5	100.0	100.5	100.2	100.3	100.3	99.9
ppm														
Cr	137	121	81	125	137	<10	34	<10	<10	191	14	<10	25	91
Rb	19	<10	15	106	38	122	83	94	113	105	109	70	97	71
Sr	297	284	336	492	523	582	449	564	394	301	279	388	585	431
Y	34	24	28	17	31	10	23	13	42	19	18	35	26	64
Zr	113	74	114	165	188	209	176	197	436	458	320	318	226	247
Nb	<10	37	34	17	20	17	21	37	40	102	43	23	17	44
Ba	192	95	228	414	554	933	568	859	1270	1200	951	808	961	665

[1] Abbreviations: and = andesites; bas and = basaltic andesite; aph rhy = aphyric rhyolite; rhydac = rhyodacite; rhy fd = feeder dike (rhyolitic).
[2] Data may not equal Sum due to rounding of Sum to two significant figures.

Table 1. Results of geochemical analyses of selected samples from the Eagle Crags Volcanic Field.

Rock type	and	and	and	and.	tuff	tuff	dacite	dacite	dacite	dacite	dacite	rhydac	rhydac	rhydac
Map ID	Ma^2	Ma^2	Ma^2	Ma^4	Map	pumice	Md	Md	Md	Md	Md	Mrd	Mrd	Mrd
Field ID	1327	1313	1079	1255	1340	1224	1012	1024A	1030	1010	1130	1205	1272	1260
wt %														
SiO_2	62.9	60.2	63.6	61.8	58.6	60.7	62.8	67.0	64.0	65.8	65.4	64.2	67.9	66.2
Al_2O_3	15.9	17.3	16.3	16.6	16.1	15.8	15.6	14.9	16.8	14.5	15.9	15.8	15.1	16.4
CaO	3.92	5.16	3.94	4.11	5.10	3.52	4.27	3.19	3.64	3.08	3.86	5.38	2.67	3.91
MgO	1.78	0.64	1.07	1.56	1.85	1.33	0.66	0.44	0.38	0.51	0.72	1.29	0.51	0.69
Na_2O	3.90	3.91	4.15	3.91	3.32	3.52	4.19	3.88	4.61	3.99	3.69	4.21	3.16	4.28
K_2O	2.63	1.89	3.21	3.01	2.12	2.63	2.85	2.79	2.87	2.61	3.10	2.56	4.21	2.61
Fe_2O_3	4.52	5.94	4.95	4.89	5.11	4.99	5.83	4.07	4.54	5.12	4.11	3.94	2.28	3.39
MnO	0.09	0.09	0.08	0.06	0.08	0.08	0.06	0.05	0.05	0.03	0.05	0.07	0.04	0.06
TiO_2	0.72	1.24	0.77	0.84	0.97	0.71	0.88	0.69	0.72	0.77	0.65	0.54	0.46	0.53
P_2O_5	0.17	0.18	0.20	0.18	0.25	0.18	0.22	0.20	0.27	0.19	0.17	0.20	0.16	0.14
LOI	2.90	2.65	1.60	2.80	5.60	6.55	2.23	1.70	1.47	2.47	2.10	1.45	3.20	1.45
SUM	99.6	99.4	100.1	100.0	99.2	100.4	99.8	99.1	99.5	99.3	99.9	99.9	100.0	99.9
ppm														
Cr	137	137	45	24	137	137	<10	<10	<10	13	23	68	16	53
Rb	123	33	107	81	71	123	72	85	104	77	86	70	101	79
Sr	458	531	391	441	511	461	405	417	420	406	423	1050	554	782
Y	41	25	32	<10	<10	21	26	34	33	37	<10	11	<10	23
Zr	211	145	237	221	203	265	222	227	220	253	231	140	132	147
Nb	<10	14	32	14	14	23	25	<10	<10	13	23	29	17	36
Ba	712	641	830	885	501	833	918	881	920	964	823	1100	1960	1190

Table 1. Results of geochemical analyses of selected samples from the Eagle Crags Volcanic Field.

Rock type	rhydac	rhydac	rhydac	rhydac	rhydac	rhydac	rhydac	rhydac	rhydac	rhydac	rhydac	aph rhy	aph rhy	aph rhy
Map ID	Mrd	Mrd	Mrd	Mrd	Mrd	Mrd	Mrd	Mrd	Mrb	Mrd	Mrd	Mar	Mar	Mar
Field ID	1269	1213	1249	1232	1276	1212	1248	1206	1214	1209	1251	1057	1060	1323
wt %														
SiO_2	64.5	67.1	66.1	67.6	67.4	67.1	66.1	67.7	64.6	65.7	65.2	72.9	74.0	69.9
Al_2O_3	16.2	15.6	15.7	15.8	15.7	16.0	16.3	16.0	16.1	15.7	16.4	12.4	12.9	13.9
CaO	3.93	2.88	3.62	4.02	2.53	2.64	3.43	3.39	3.30	3.69	3.27	1.05	0.82	1.00
MgO	0.88	0.93	1.50	0.62	0.60	0.28	0.92	0.80	1.17	1.48	1.17	0.20	0.13	0.40
Na_2O	3.64	3.50	3.65	4.13	3.32	4.60	4.11	3.84	3.72	4.00	3.85	4.06	3.99	3.11
K_2O	3.04	2.77	3.16	2.52	4.16	3.50	2.64	2.97	2.78	2.60	3.01	3.48	4.67	4.50
Fe_2O_3	3.79	3.54	3.04	3.11	2.62	3.19	2.77	1.84	3.16	2.82	3.19	2.51	1.35	2.16
MnO	0.06	0.06	0.05	0.04	0.04	0.04	0.06	0.03	0.03	0.06	0.05	0.04	0.03	0.03
TiO_2	0.64	0.37	0.48	0.53	0.51	0.63	0.42	0.53	0.58	0.39	0.57	0.20	0.07	0.16
P_2O_5	0.26	0.11	0.16	0.16	0.13	0.20	0.14	0.17	0.17	0.15	0.17	0.12	0.03	0.04
LOI	3.00	2.15	2.20	1.15	3.10	1.50	3.00	2.50	4.10	3.60	3.05	1.39	0.54	3.25
SUM	100.2	99.3	100.0	100.0	100.3	99.9	100.3	100.1	100.0	100.5	100.2	98.6	98.3	98.7
ppm														
Cr	60	137	22	42	24	19	68	14	12	68	68	<10	<10	137
Rb	81	80	73	83	131	254	55	72	90	62	79	107	152	131
Sr	851	833	965	1040	331	357	1370	730	917	1090	900	165	27	109
Y	14	<10	15	12	18	<10	25	<10	<10	<10	18	38	48	42
Zr	151	119	157	130	198	278	136	170	153	120	143	255	194	234
Nb	38	12	24	23	23	30	32	15	13	<10	17	18	36	16
Ba	1200	1310	1270	1120	899	1330	1730	1520	1090	1400	1260	1180	314	1120

Table 1. Results of geochemical analyses of selected samples from the Eagle Crags Volcanic Field.

Rock type	aph rhy	aph rhy	rhyolite	rhyolite	rhy fd	tuff	tuff	tuff	tuff	tuff	tuff	tuff	tuff
Map ID	Mar	Mar	Mr	Mr	Mrf	Mr	Mrp	Mrp	Mrp	Mrp	Mrp	Mrp	Mrp
Field ID	1208	1093	1118	1031	1332	1333	1029	1339	1016	1123	1263	1314	1065
wt %													
SiO_2	72.6	76.3	76.0	70.9	74.9	70.9	60.0	68.9	74.7	68.6	72.6	71.0	71.7
Al_2O_3	13.2	12.0	11.8	11.6	11.7	15.7	10.7	11.1	10.6	12.6	12.4	11.2	12.8
CaO	0.91	0.69	0.72	3.07	0.44	0.29	1.27	1.64	0.31	1.56	0.82	1.27	1.84
MgO	0.39	0.10	0.15	0.26	0.53	0.35	1.88	2.10	0.46	0.56	0.23	0.52	0.33
Na_2O	1.74	4.26	3.82	3.46	1.15	0.89	7.65	1.05	3.20	2.32	2.90	1.92	2.94
K_2O	4.57	3.77	4.48	4.45	5.14	6.21	1.57	1.16	4.11	3.96	4.58	3.54	4.80
Fe_2O_3	1.94	1.45	1.23	1.06	1.35	1.26	1.68	1.43	1.15	0.80	1.76	1.78	0.86
MnO	0.03	0.06	0.03	0.04	0.02	0.02	0.03	0.07	0.02	0.03	0.03	0.02	0.06
TiO_2	0.18	0.11	0.14	0.12	0.19	0.16	0.13	0.11	0.11	0.08	0.17	0.14	0.06
P_2O_5	0.05	0.04	0.08	0.06	0.05	0.07	0.03	0.03	0.03	0.03	0.05	0.02	0.03
LOI	3.40	0.70	0.93	3.23	2.85	2.95	10.0	12.3	3.93	8.47	4.80	6.80	3.93
SUM	99.3	99.7	99.5	98.3	98.4	98.9	95.1	100.0	98.8	99.2	100.5	98.4	99.5
ppm													
Cr	<10	<10	<10	<10	137	137	<10	137	<10	<10	17	137	<10
Rb	151	130	126	140	152	154	83	71	127	220	192	116	236
Sr	153	83	78	26	52	5149	213	265	178	368	86	151	107
Y	22	63	51	55	<10	12	70	77	174	19	70	66	55
Zr	250	238	168	169	139	159	395	472	453	86	346	389	88
Nb	37	11	13	28	13	16	35	27	45	34	40	57	51
Ba	2290	1220	700	403	594	691	275	124	744	550	256	288	444

Table 1. Results of geochemical analyses of selected samples from the Eagle Crags Volcanic Field.

Rock type	tuff	vent	vent	vent	vent	vent
Map ID	Mrp	Brp	Brp	Brp	Brp	Brp
Field ID	1319	1233	1234	1235	1236	1237
wt %						
SiO_2	79.0	73.1	71.1	74.2	74.3	76.5
Al_2O_3	10.5	12.0	12.8	12.6	10.2	9.62
CaO	0.63	0.63	1.16	0.82	0.82	0.78
MgO	0.42	0.23	0.46	0.23	0.34	0.33
Na_2O	0.02	2.82	3.35	4.32	2.13	1.60
K_2O	4.68	4.92	4.24	4.04	3.87	3.87
Fe_2O_3	0.83	1.69	2.27	2.46	1.49	1.42
MnO	0.02	0.03	0.03	0.02	0.03	0.03
TiO_2	0.19	0.15	0.20	0.21	0.12	0.11
P_2O_5	0.08	0.03	0.03	0.05	0.03	0.04
LOI	3.40	4.00	4.25	1.15	6.45	5.55
SUM	99.9	99.7	100.0	100.5	99.9	100.8
ppm						
Cr	137	110	17	53	26	17
Rb	103	163	131	143	184	150
Sr	106	24	61	84	25	20
Y	<10	69	55	45	57	65
Zr	83	448	405	410	341	372
Nb	29	79	54	54	37	28
Ba	469	230	485	519	448	200

method for classifying tuffs or flows which are largely composed of glass and finely crystalline matrix minerals. Water-free, normalized data were plotted on a total alkali versus silica (TAS) diagram to illustrate compositional similarities among other Mojave Desert and Cordilleran volcanic rocks (Fig. 33). In general, ECVF samples cluster into the andesitic-dacitic and rhyolitic fields. They mimic the trend of calc-alkaline volcanic rocks from the Cascades although, similar to other Mojave Desert volcanic rocks illustrated (Smith, 1964; Glazner, 1986a, b, c), they are more alkaline than those from the Cascades. Also a distinct compositional gap of 3-3.5 wt % SiO_2 separating rhyolites from the other rocks is similar to a compositional gap described for rocks from the Turkey Creek caldera (DuBray and Pallister, 1991).

The only basalt analyzed in the ECVF is from the west-trending alluvial valley on the southeastern corner of the Myrick Spring area (Mb; sample 1133; Plate 2). As previously described, this basalt is not easily correlated with other volcanic units in the area because it is not in contact with any of them and it is poorly exposed. Its holocrystalline texture indicates that it may be hypabyssal. The modal and normative mineralogy and alkali content of this basalt indicates that it is an olivine tholeiite with a high alumina content. In addition to its silica content, this basalt can be chemically distinguished from other rocks by its elevated CaO, MgO, TiO_2 contents, low Rb and Ba contents and modal clinopyroxene+olivine. Normative nepheline plus P_2O_5 values greater than 0.55 ppm are typical of late alkali basalts (~2-4 Ma) in the Mojave Desert (Glazner, 1990). Neither of these are characteristics of basalt from the Myrick Spring area suggesting that the Myrick basalt is not a late, alkaline flow but is contemporaneous with the other volcanic units in the ECVF. The combination of geochemical characteristics and coarse crystallinity suggests that this basalt is not typical of the late, alkaline basalts in the region.

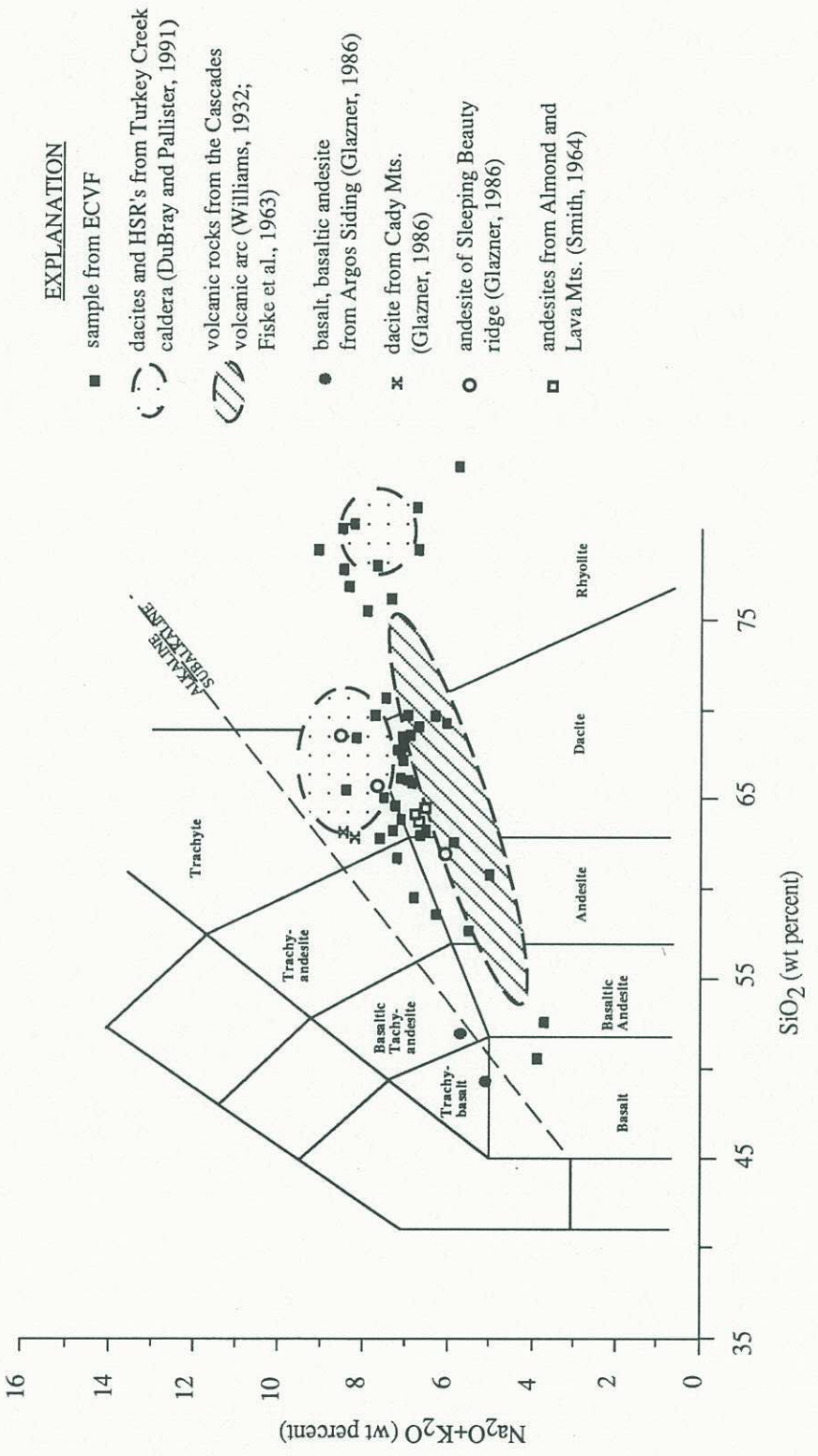

Figure 33. Total alkali vs. silica diagram for the Eagle Crags, Lava Mts. and Sleeping Beauty area volcanic fields of the Mojave Desert and other volcanic fields of the western United States (diagram after Le Bas et al., 1992; Irvine and Baragar, 1971).

Basaltic andesite from the Myrick Spring area appears mineralogically to be a fine-grained, glassy variety of the Myrick basalt. With the exception of the highly altered flow (samples 1039, 1040; Plate 2), basaltic andesites generally contains much less MgO and FeO^T, and greater concentrations of Sr, Zr and Ba than basalt. These chemical variabilities are a reflection of decreased olivine and increased plagioclase contents in the less mafic flows.

Mineralogical differences between andesitic and dacitic flows throughout the ECVF are so subtle that chemical analyses are often the sole descriminant between the two types. Lacking any obvious macroscopic or mineralogical characteristics, hypersthene normative volcanic rocks with an anhydrous, normalized silica content from 57 to 63 wt % are generally regarded as andesites (Gill, 1981). Although many andesitic and dacitic flows have similar mineral assemblages and major element oxide concentrations, trace element abundances distinguish them. Sr increases are much larger than Rb with increasing silica content in mafic and intermediate compositions (Fig. 34). A large decrease in Sr and a small increase in Rb occurs after the SiO_2 compositional gap. Sr and Ba behave similarly although Ba values are an order of magnitude larger in the ~68-71% SiO_2 range of aphyric rhyolites (Fig. 35). Trends in Sr, Rb and Ba are most likely due to increased biotite±hornblende contents in the higher silica, rhyodacitic flows. The decrease in Sr after the compositional gap reflects decreased plagioclase concentrations, probably owing to the fractionation of plagiolcase from high silica melts and a lack of crystals in general in high silica tuffs.

Rhyodacites are felsic, biotite±hornblende-rich, siliceous flows with anhydrous, normalized silica contents of 68-71 wt % (Table A.1; Figs. 33, 34, 35). In addition to elevated TiO_2 contents, dacites are chemically distinguishable from rhyodacites by lower

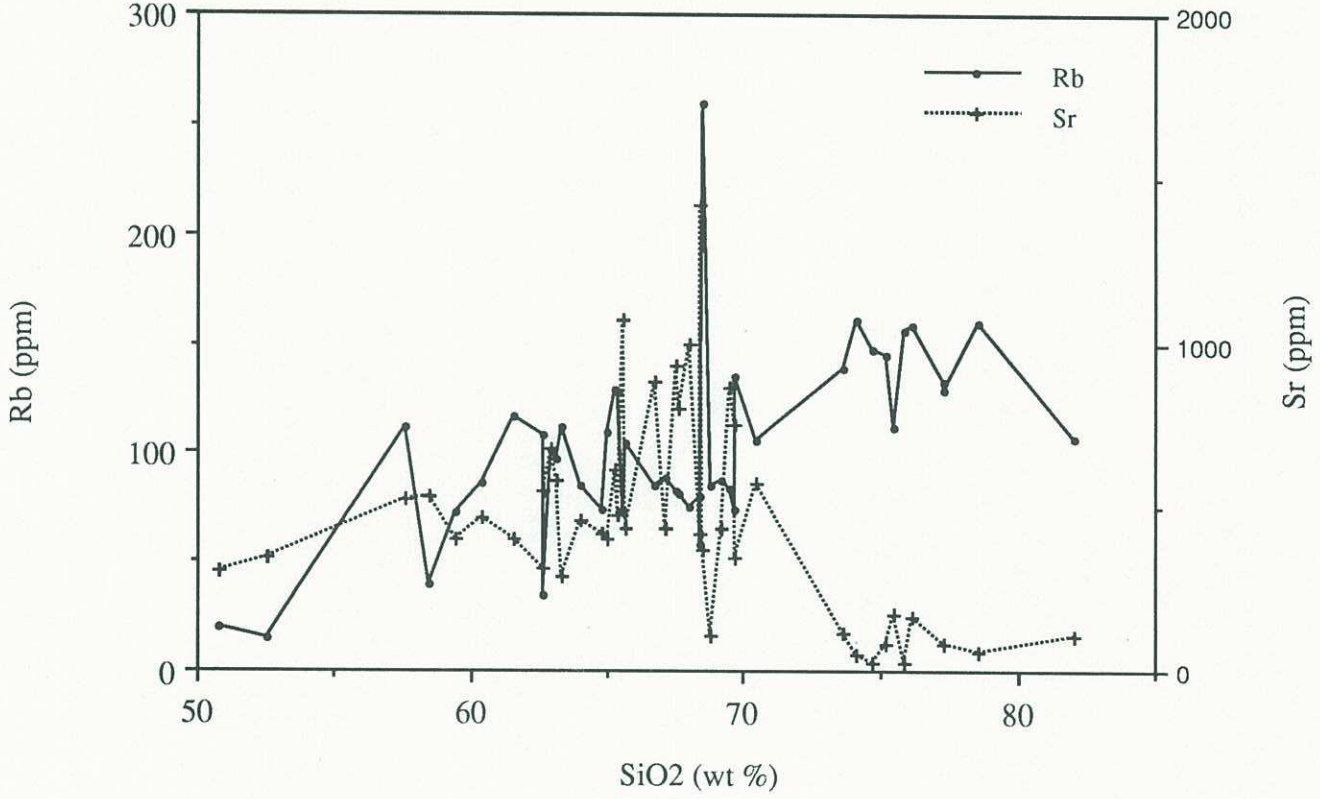

Figure 34. Sr, Rb vs. SiO_2 for all rocks from the Eagle Crags Volcanic Field.

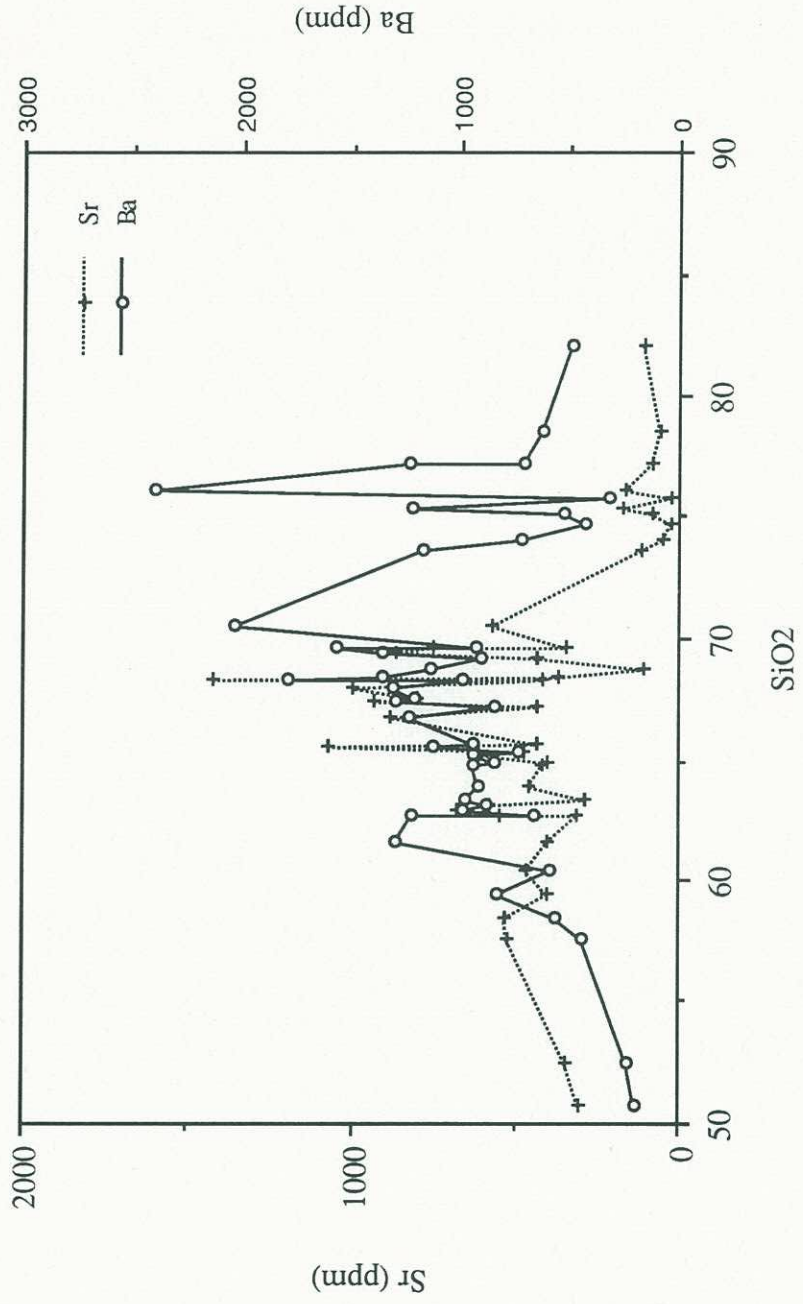

Figure 35. Ba, Sr vs. SiO_2 for all rocks from the Eagle Crags Volcanic Field.

silica, Sr, Ba and Y and higher Cr contents. The occurrence of hydrous silicate minerals and K-feldspar is reflected in higher Ba concentrations in rhyodacites than andesites and dacites. Although reported Cr values are not very precise, a relative Cr decrease also helps chemically distinguish rhyodacites from dacites and may reflect the absence of clinopyroxene in rhyodacites.

All rhyolites examined in the ECVF have anhydrous, normalized silica contents exceeding 74 wt %. These high-silica rhyolites (HSR's) occur as porphyritic flows, aphyric flows, tuffs, feeder dikes and in fissure vents. The porphyritic flows and feeder dikes from the Blue Chalcedony area are geochemically similar (Tables A.1 and A.2). They are both quartz-sanidine phyric rhyolites. With the exception of an aphyric rhyolitic clast sampled from a tuff from the Myrick Spring area (sample 1060), aphyric rhyolites have higher Ba concentrations than the rhyolitic flows. All of the aphyric rhyolitic outcrops are altered or near altered zones. Elevated Ba concentrations may reflect metasomatism related to alteration. Preliminary K-feldspar staining of fluid inclusion quick plates revealed that K was concentrated in the very fine-grained to glassy matrix of aphyric rhyolites. Ba and K may have both been added to these flows during metasomatism (procedure described in Appendix A).

Most of the rocks in the ECVF are peraluminous and generally metaluminous as evidenced by A/CNK ratios and normative corundum abundances (Table A.2). With the exception of K_2O and Na_2O, Harker variation diagrams illustrate negatively sloping linear trends and also illustrate the compositional gap (Fig. 36). Deviations in this trend include the scattered, positive slope of K_2O, an inflection point separating a relatively flat Al_2O_3 trend and a negatively sloping trend, and the inflection separating a steeply-dipping MgO-SiO_2 trend to a more gently-dipping trend. The scattered Na_2O vs. SiO_2 trend mimics the

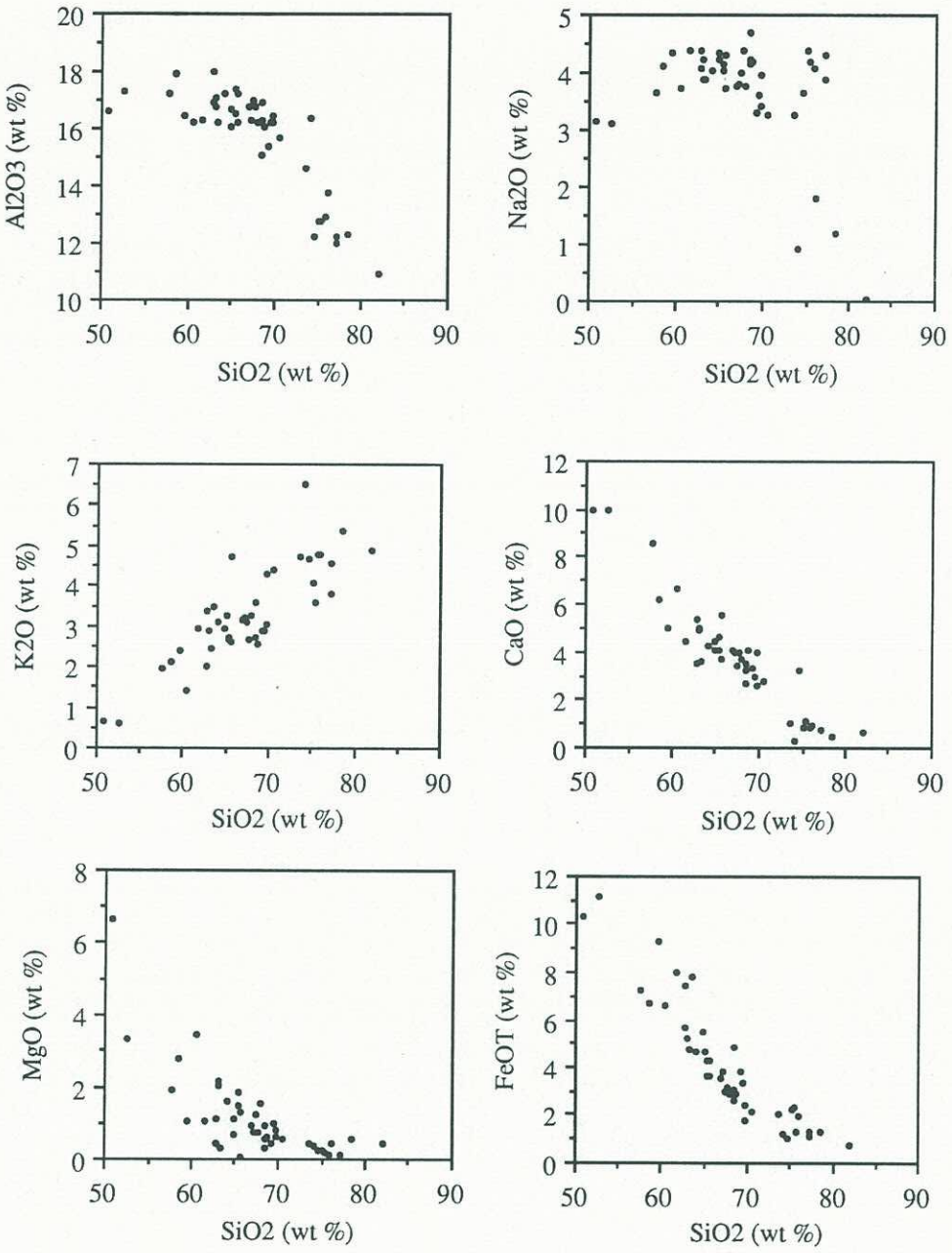

Figure 36. Harker plots for major element oxides.

Al_2O_3 trend and roughly approximates the Sr vs. SiO_2 trend (Fig. 34). The inflections observed in the MgO diagram may be related to decreased olivine concentrations. The inflections in the Na_2O and Al_2O_3 trends are similar and may relfect the removal of Na-plagioclase from high silica melts. Conversely, although rhyolitic flows are within the ECVF, they may be genetically unrelated to the other volcanic units of the ECVF.

2.4 Discussion

The ECVF is composed of flows, tuffs and pyroclastic units compositionally ranging from tholeiitic basalt to high-silica rhyolite. The complex, interfingered nature of tuffs and flows throughout the ECVF, their compositions and morphology and their distribution are analogus to a modern day, arc-related stratovolcano environment (Gill, 1981; Glazner, 1986; Cas and Wright, 1988).

A synthesis and interpretation of the stratigraphy, enigmatic mineralogical textures and geochemical characteristics from the Myrick Spring, Goldstone, Eagle Crags and Blue Chalcedony areas is presented below.

2.4.1 Stratigraphy

The Myrick Spring area is dominated by a pyroclastic eruptive center composed of greater than 100 m of multiple lithic-rich and lithic-poor tuffs. These tuffs rest unconformable on a basal andesite flow and are overlain by a thick sequence of porphyritic andesitic-dacitic flows. This entire package of volcanic rocks rest disconformably on granitic basement rocks. A poorly exposed, apparent fault contact separating the crystalline basement from volcanic rocks could be a local feature or may be genetically related to a profound, regional detachment fault where mylonitized granitoids are overlain by Tertiary

volcanic units (Glazner et al., 1989).

The sheet-like andesitic-dacitic flows and tuffs that constitute the bulk of volcanic rocks in the Myrick Spring area are compositionally and morphologically equivalent to those exposed in the fault scarp at Eagle Crags. Major differences between these two areas are that rocks from Eagle Crags are thicker and dip to the south while those from Myrick Spring dip to the north.

With the exception of a thin, enigmatic mafic flow interlayered within thick sequences of rhyolitic tuff, observed at both Myrick Spring and Eagle Crags areas, the overall stratigraphy of these areas is marked by unwelded, pyroclastic deposits overlain by less siliceous, porphyritic flows.

The apparent unconformable relationship between basal tuffs from the measured section at Myrick Spring and an underlying, steeply-dipping andesite could be the result of restrictions of pyroclastic flows to a paleovalley bordered by a steeply-dipping, vesicular andesite. The alluvial valley on the western side of this andesite (sample 1276; Plate 1) may have been the sight of volcanic flows that have long since eroded. Most likely, however, flows are only present east of this andesite because they were focused in a paleovalley, the western margin of which is marked by the vesicular andesite. Deeply incised valleys often control the flow of pyroclastic material after eruption in modern stratovolcanos (Cas and Wright, 1988).

The Myrick Spring area is bordered to the east and probably disconformably underlain by granitic rocks. A thin brecciated zone between tuffs and flows and the Granite Mountains suggests a fault contact, although the attitude and age of this fault are unknown. Another disconformity deduced from descriptions of several mines and prospects in Chapter 1 suggests that this region may have experienced thrusting, which could have

placed volcanic rocks of the Myrick Spring area over the Granite Mountains.

The conduit-shaped outcrop to the north of Myrick Spring (Plate 1; Fig. 20d) is interpreted to be a volcanic neck or plug composed of dacitic flows. A northeast-trending, high angle structure crosscuts this outcrop. The northeast-trending silica dike that terminates at this neck may have been a feeder for the flows. The feeder vent subsequently sealed by silica- and carbonate-bearing fluids.

The Goldstone area is marked by an apparently faulted, coalesced flow dome complex and one or more homogeneous, endogenous domes. Field relations indicate that these domes are the youngest silicic volcanic rocks. Their deposition was not preceded by pyroclastic eruptions. The flow dome complex is comprised largely of multiple rhyodacitic flows, each with macroscopic and mineralogical differences that allow them to be distinguished from one another. The combination of ±biotite±hornblende in a vesicular, glassy rock matrix suggests that these flows were viscous. Their limited areal extent throughout the study area (Fig. 37; Plate 1) supports the contention that most rhyodacites identified were probably viscous, slowly emplaced flows.

The morphological and mineralogical similarities among rhyodacites from the Goldstone area suggests that they are probably the result of subaerial dome growth. Their central location within the volcanic field, their proximity to an apparent central vent, and the alluvium-filled valley that almost surrounds the area suggests they were probably the last products from the central vent of the stratovolcano, analogous to presently-forming silicic domes at Mount St. Helens or at the Santa Marie volcano in Guatemala (Swanson et al., 1987; Rose, 1987). The non-explosive growth of domes such as these is believed to be the product of a continuous but slow supply of magma to the surface (Swanson et al., 1987). Plinian eruptions have often been followed by the growth of endogenous domes within

volcanic calderas (Gill, 1981). Usually these domes are composed of dacitic or rhyolitic rocks although Rose (1972) described acid andesites included among endogenous domes from the Santa Maria volcano.

Aphyric rhyolite, poorly exposed in the central portions of the ECVF, is overlain or interlayered with a 2-3 m thick lens of perlite. Perlite is generally a vent or vent-proximal rock because of the high viscosity of rhyolite (Whitson, 1982; Bonnichsen and Kauffmann, 1987). The location and viscous nature of these rhyolitic flows and their spatial association to rhyodacitic domes indicates that that the Goldstone area was probably the sight of the central vent.

The Eagle Crags area is separated from the Goldstone area by a horseshoe-shaped, alluvium-filled valley and a prominent, arcuate-shaped scarp. The area is comprised of thinning-to-the-south, laterally extensive tuffs, flows and lahars. The thickness of these units and the coarseness of clasts in breccias at Eagle Crags indicate that their paleosource was north of the scarp. The lack of lahars to the north of the scarp suggests that the scarp is a collapse feature similar in configuration and size to caldera collapse features identified from other stratovolcanic environments. The "intracaldera" geology north of this scarp is dominated by the previously described vent facies aphyric rhyolites and viscous, central vent-related rhyodacitic domes and flow domes. Unlike ash-flow tuff calderas, calderas that form in stratovolcanos are small (several km in diameter), vent-related features (Pike and Clow, 1981; Lipman, 1984). This scarp is interpreted to be the structural rim of a caldera that probably formed during or after the waning stages of doming.

At least one rhyodacitic dome lay along the Eagle Crags fault scarp. Its thickness, homogeneous mineralogy and quaquaversal attitude indicates that it is an endogenous dome genetically related to the flow dome complex at the Goldstone area. The location of these

silicic domes may be analogous to the location of Holocene domes described at the South Sister volcano in Oregon which are speculated to have originated from a radial dike that tapped the main magma chamber beneath the volcano (Scott, 1987).

The probable events at the Eagle Crags area yielding tuff-lahar successions and the caldera collapse feature probably began with a voluminous pyroclastic eruption. Recent well-studied analogs such as Mount St. Helens suggest that this eruption may have been on the flank of the volcano (Cas and Wright, 1988). Highly energetic pyroclastic eruptions and a concomitant degradation of the composite andesite-dacite cone centered north of the Eagle Crags area resulted in the thick, sheet-like tuff and lahar deposits. The lack of epiclastic rocks in most of the ECVF also attests to the central vent-proximity of the Eagle Crags area. Each successive eruption would have denuded vent-proximal and vent-medial erosional accumulations.

The Blue Chalcedony area is underlain by a basal andesite that extends eastward to Myrick Spring; the dominant rocks at Blue Chalcedony are rhyolitic flows, plugs and dikes. It is unclear how or if these rhyolites relate to the stratovolcano except that silicic, dome-forming rocks are often found on the flanks of stratovolcanos (Fink, 1987; Cas and Wright, 1988).

The Blue Chalcedony area is also notable for its west-northwest-trending rhyolitic feeder dikes and a northwest-trending fissure vent. The size and amount of black, cognate clasts in flat lying tuffs in Pilot Knob Valley (Plates 1 and 3) decrease away from the fissure vent. Most of these clasts were probably erupted as viscous blebs of molten silica and were rapidly quenched in the atmosphere. Their size and density, in contrast with pumice, probably restricted their transportation during an eruption.

2.4.2 Textures

Plagioclase phenocrysts are ubiquitous in most of the flows in the ECVF; however, disequilibrium textures were observed in plagioclases from most of the mafic flows. Pyroxene overgrowths on plagioclase, reverse and oscillatory zoning, clear Ca-rich plagioclase overgrowths on fretted Na-rich, plagioclase cores, and plagiolcase overgrowths on these fretted, glass-charged zones indicate that magma conditions were changing abruptly during magma evolution.

Volumetrically minor quartz xenocrysts were also observed in mafic flows of the region. Some have fine-grained overgrowths of unidentified, high birefringent minerals. Resorbed and embayed quartz was also identified in andesite flows from the Almond Mountains (Smith, 1964).

Plagioclase textures and xenocrystic quartx crystals reflect changing equilibrium conditions during the evolution of the ECVF magmaa(s). The combination of interlayered mafic flows within silicic tuffs and disequilibrium textures and mineral assemblages may indicate multiple magmas and magma sources that created the ECVF or may be the result of a single, continuously evolving magma subjected to assimilation, injection and mixing of other magma(s) and fractional crystallization.

2.4.3 Geochemistry

Similar to other volcanic rocks from the Mojave Desert, rocks from the Eagle Crags region are slightly alkaline in comparison to younger volcanic rocks from the northwestern United States (Fig. 33). The relationship between dacites and HSR's in the ECVF may be analogous to dacites and HSR's from the Turkey Creek caldera, Arizona. Anhydrous, normalized dacite and HSR compositions from Turkey Creek plotted on a TAS diagram are

separated by a compositional gap of 8 wt. % SiO_2 (DuBray and Pallister, 1991). This compositional gap may represent a sharp thermal and compositional interface separating two magmas in a zoned magma chamber. The compositional gap of 3.5% separating rhyolites from dacites in the ECVF could indicate that the HSR's were from a separate magma. Alternatively, if they are comagmatic then, as for the compositional gap separating HSR's from less silicic rocks at Turkey Creek, the compositional gap separating HSR's from less silicic rocks in the ECVF may attest to the stratified nature of the source magma chamber in the ECVF.

When normalized to chondrite compositions after Thompson et al. (1984), basalts and basaltic andesites exhibit an enrichment in Ba and Sr and a depletion in Rb and Nb. This suggests that the magma that formed these mafic rocks may have been contaminated by a lower crustal magma (Ragland, 1989).

The relative changes in Sr and Rb abundances after the compositional gap may either be due to may be due to settling of Ca-plagioclase from the silica-rich portion of a large, zoned magma chamber or may reflect the fact that HSR's were from a different magma, unrelated to the andesitic-dacitic magma (Figs. 5, 6). The relative increase in Rb probably represents the increased concentration of K-feldspar and/or biotite in the rhyolitic flows. Because the amount of K-feldspar in these tuffs is generally less than 1%, the bulk distribution coefficient for Rb in rhyolite, D_{Rb}, is less than 1.0 and the increase in Rb may also be partially due to the concentration of Rb in what is now the glassy matrix of these tuffs.

Chemical trends such as the steep drop in FeO^T, possibly TiO_2 vs SiO_2 and the sharp downward slope in MgO at low SiO_2 concentrations (Fig. 8), could reflect respectively, early titanomagnetite crystallization and subsequent olivine fractionation in a

basaltic source. K_2O is essentially incompatible in mafic and intermediate compositions and the scatter of K_2O vs silica could reflect crustal contamination. It has been suggested that rhyolites in the Mojave Desert are a product of crustal anatexis (Glazner, 1990). Perhaps siliceous flows and tuffs in the Eagle Crags volcanic field are a product of the contamination of a felsic melt, presumably of granitic composition, by basaltic magma.

Rhyolites are highly evolved with high differentiation index (DI), high SiO_2, and relatively low TiO_2 contents. Differences in CaO, MgO and trace element abundances among rhyolite analyses (Table 1) suggests that it may be possible to distinguish among rhyolitic tuffs and flows based on chemical composition. The two intermediate composition tuffs can easily be distinguished from rhyolites by their SiO_2 contents.

Harker diagrams display a strong linear relationship in CaO, FeO^T, TiO_2 and the silicic portions of MgO and P_2O_5 trends in intermediate through silicic compositions consistent with magma mixing processes (Vogel et al., 1983; Miller and Miller, 1991). Trace and major element variations with increased SiO_2 suggests that a mafic magma may have interacted with other rocks and/or mixed with a felsic magma to generate many of the stratovolcano products observed in this region.

CHAPTER 3

$^{40}Ar/^{39}Ar$ GEOCHRONOLOGY

3.1 Introduction

Selected samples were prepared and dated using the $^{40}Ar/^{39}Ar$ age spectrum method at the U.S. Geological Survey's argon laboratory, Branch of Isotope Geology, Denver. $^{40}Ar/^{39}Ar$ geochronology was performed to define the age of volcanism in the ECVF and to help unravel the complex volcanic stratigraphy. An estimated age on a granodioritic stock from the Blue Chalcedony area was also determined in order to compare it with other dated granitoids in the region.

Sampling locations were chosen in an effort to determine the oldest and youngest rocks in the ECVF. Samples were selected from unaltered portions of flows and tuffs containing potassium-bearing phenocrysts. Highly altered areas were also sampled for dating but they did not contain enough potassium-rich minerals such as illite, alunite and adularia for $^{40}Ar/^{39}Ar$ age determinations.

Several samples initially selected for $^{40}Ar/^{39}Ar$ geochronology were not used because of their limited amount of potassium-bearing minerals or because post-formational alteration precluded their usefulness. Results from five samples, including one rhyolite from a feeder dike, one rhyolitic flow, two rhyodacitic domal rocks and one granodiorite are discussed in this chapter.

A summary of $^{40}Ar/^{39}Ar$ geochronology and methods is included in Appendix B. Detailed $^{40}Ar/^{39}Ar$ calculations, equipment specifications and standards, and methods

employed in the use of the TRIGA nuclear reactor in Denver are described elsewhere (Dalrymple and Lanphere, 1969; Dalrymple et al., 1981; Roddick, 1983; Faure, 1986; Samson and Alexander, 1988; Snee et al., 1988).

3.2 $^{40}Ar/^{39}Ar$ Age Spectrum

Incremental heating of a potassium-bearing mineral separate in a furnace yields a discrete gas volume which is shunted through scrubbers to remove impurities. Relatively pure argon gas is then expanded into the mass spectrometer. For each increment of gas in the spectrometer, an "age" can be determined from $^{40}Ar^*/^{39}Ar_K$ (radiogenic 40 argon/potassium derived 39 argon) values after corrections are made for interfering isotopes of argon. A summary of the age spectrum dates and data for the five analyzed samples is included in Tables 2 and 3. Argon release spectra from the five mineral separates are illustrated figures 37-41.

K/Ca graphs, or 39/37 ($^{40}Ar/^{39}Ar$), illustrate the ratios of measured argon input from the respective decay of K and Ca. They are illustrated with their respective argon release spectra because they have identical abscissas and because the relative K and Ca inputs can help in interpreting the release spectrum.

A plateau age is the age of contiguous heating steps whose individual ages overlap within the experimental error and whose cumulative $^{39}Ar_K$ comprises greater than 50% of the total $^{39}Ar_K$ released from the sample (Snee et al., 1988). Heating steps in a plateau are statistically indistinguishable at the 95% confidence level (using the critical value test of Dalrymple and Lanphere, 1969). Initial, low temperature heating steps and final heating steps which were small (<5% $^{39}Ar_K$) or showed a large variance (>±1%) were excluded from plateaus. Error estimates for the apparent ages of individual temperature steps were

Table 2. $^{40}Ar/^{39}Ar$ age spectrum dates.

Sample ID[1]	Mineral/rock type	Area/plate number for sample location	Apparent age and error (Ma at 1σ)	Character of age spectrum
1213	biotite/rhyodacite	Goldstone/ Plate 3	12.40±.06	Plateau
1209	hornblende/rhyodacite	Goldstone/ Plate 1	14.54±.04	Maximum age from spectrum w/ excess argon.
1247	sanidine/rhyolitic dike	Blue Chalcedony/ Plate 1	18.37±.06	Plateau
1118	sanidine/rhyolitic flow	Blue Chalcedony/ Plate 4	18.75±.06	Plateau
1267	biotite/granodiorite	Blue Chalcedony/ Plate 1	80.78±.14	Preferred date; total gas age

Table 3. Summary of $^{40}Ar/^{39}Ar$ age spectrum data.

Sample: 1213/44/DD37 Mineral and weight: biotite, 52.6 mg J-Value: .007726±0.1

Temperature	Radiogenic ^{40}Ar	K-derived ^{39}Ar	F value	Radiogenic yield	% ^{39}Ar total	Apparent age & error (Ma at 1σ)
600	.01456	.02368	.615	4.8	.6	8.55±.51
750	.01882	.02422	.777	14.8	.7	10.80±1.60
800	.04034	.05178	.779	12.1	1.4	10.83±.22
850	.09898	.13314	.743	29.3	3.6	10.33±.22
900	.13712	.17034	.805	50.3	4.6	11.18±.21
950	.21223	.24489	.867	64.1	6.6	12.04±.11
1000	.15211	.18093	.841	59.6	4.9	11.68±.06
1050	.29658	.34110	.870	62.9	9.2	12.08±.02
1100	.40513	.45482	.891	71.2	12.3	12.37±.09
1200	1.61919	1.81319	.893	80.7	49.1	12.40±.02
1350	.24415	.25338	.964	78.1	6.9	13.38±.25
Total Gas			.877			12.19±.09
Plateau age	(1100°-1200°)				61.4	12.40±.06

Sample: 1209/45/DD37 Mineral and weight: biotite, 52.6 mg J-Value:.007726±0.1%

Temperature	Radiogenic ^{40}Ar	K-derived ^{39}Ar	F value	Radiogenic yield	% ^{39}Ar total	Apparent age & error (Ma at 1σ)
900	.01346	.00500	2.692	4.1	.4	37.54±9.34
1000	.00774	.00275	2.816	12.4	.2	39.25±33.79
1050	.02128	.00376	5.665	39.7	.3	78.10±7.02
1100	.03010	.01995	1.509	45.6	1.7	21.13±.03
1150	.25884	.23461	1.103	59.6	19.5	15.48±.02
1175	.49984	.48252	1.036	60.2	40.0	14.54±.04
1200	.26569	.24828	1.070	64.4	20.6	15.01±.25
1250	.15368	.13632	1.127	70.3	11.3	15.81±.11
1350	.07512	.07284	1.031	56.6	6.0	14.47±.85
Total Gas			1.099			15.42±.19
Preferred date	(excess argon)				40.0	14.54±.04

Table 3. (continued)

Sample: 1118/41/DD37 Mineral and weight: sanidine, 68.4 mg J-Value: .00778±0.1%

Temperature	Radiogenic ^{40}Ar	K-derived ^{39}Ar	F value	Radiogenic yield	% ^{39}Ar total	Apparent age & error (Ma at 1σ)
700	.08268	.03442	2.402	8.6	1.0	33.40±2.73
800	.33132	.23405	1.416	37.5	7.0	19.76±.07
850	.25235	.18351	1.375	60.0	5.5	19.20±.49
900	.27852	.20624	1.350	69.8	6.2	18.85±.11
950	.34907	.25966	1.344	76.7	7.8	18.77±.06
1050	.76713	.57237	1.340	81.5	17.2	18.71±.07
1150	1.46039	1.08762	1.343	86.5	32.6	18.75±.05
1250	.85039	.61062	1.393	77.4	18.3	19.44±.04
1350	.11593	.08128	1.426	36.2	2.4	19.91±.06
1450	.08580	.06761	1.269	38.0	2.0	17.72±.48
Total Gas						19.13±.11
Plateau age	(900°-1150°)				63.8	18.75±.07

Sample: 1267/12/DD38 Mineral and weight: biotite, 69.4 mg J-Value: .006374±0.1%

Temperature	Radiogenic ^{40}Ar	K-derived ^{39}Ar	F value	Radiogenic yield	% ^{39}Ar total	Apparent age & error (Ma at 1σ)
600	.64336	.16688	3.855	49.2	2.3	43.79±.26
700	8.51107	1.18146	7.204	88.8	16.4	80.99±.12
750	7.14995	.98229	7.279	96.7	13.7	81.81±.12
800	3.83645	.52546	7.301	95.4	7.3	82.06±.13
850	2.55817	.35082	7.292	93.6	4.8	81.96±.13
900	2.69242	.36579	7.361	88.3	5.1	82.71±.13
950	5.95374	.80607	7.386	93.5	11.2	82.99±.13
1000	11.48262	1.58109	7.262	97.0	22.0	81.63±.12
1050	8.23465	1.14217	7.210	97.2	15.9	81.05±.12
1150	.58458	.08134	7.187	83.3	1.1	80.81±.12
1300	.02720	.00843	3.226	17.1	.1	36.72±6.19
Total Gas			7.185			80.78±.14

Table 3. (continued)

Sample: 1247/11/DD38 Mineral and weight: biotite, 298.9 mg J-Value: .006258±0.1%

Temperature	Radiogenic ^{40}Ar	K-derived ^{39}Ar	F value	Radiogenic yield	% ^{39}Ar total	Apparent age & error (Ma at 1σ)
700	.07990	.04758	1.679	12.2	1.0	18.85±1.43
800	.32935	.20723	1.589	83.1	4.5	17.85±.15
900	.56678	.35209	1.610	88.3	7.6	18.08±.08
950	.60734	.37475	1.621	93.3	8.1	18.20±.15
1050	1.11766	.68517	1.631	90.5	14.8	18.32±.05
1100	.93063	.56704	1.641	91.7	12.2	18.43±.05
1150	2.00686	.22799	1.634	90.1	26.5	18.36±.06
1250	1.20561	.73856	1.632	88.8	15.9	18.34±.03
1350	.50910	.30645	1.661	84.3	6.6	18.66±.07
1450	.19948	.12772	1.562	74.3	2.8	17.55±.19
Total Gas			1.630			18.30±.08
Plateau age	(1100°-1350°)				69.5	18.35±.05

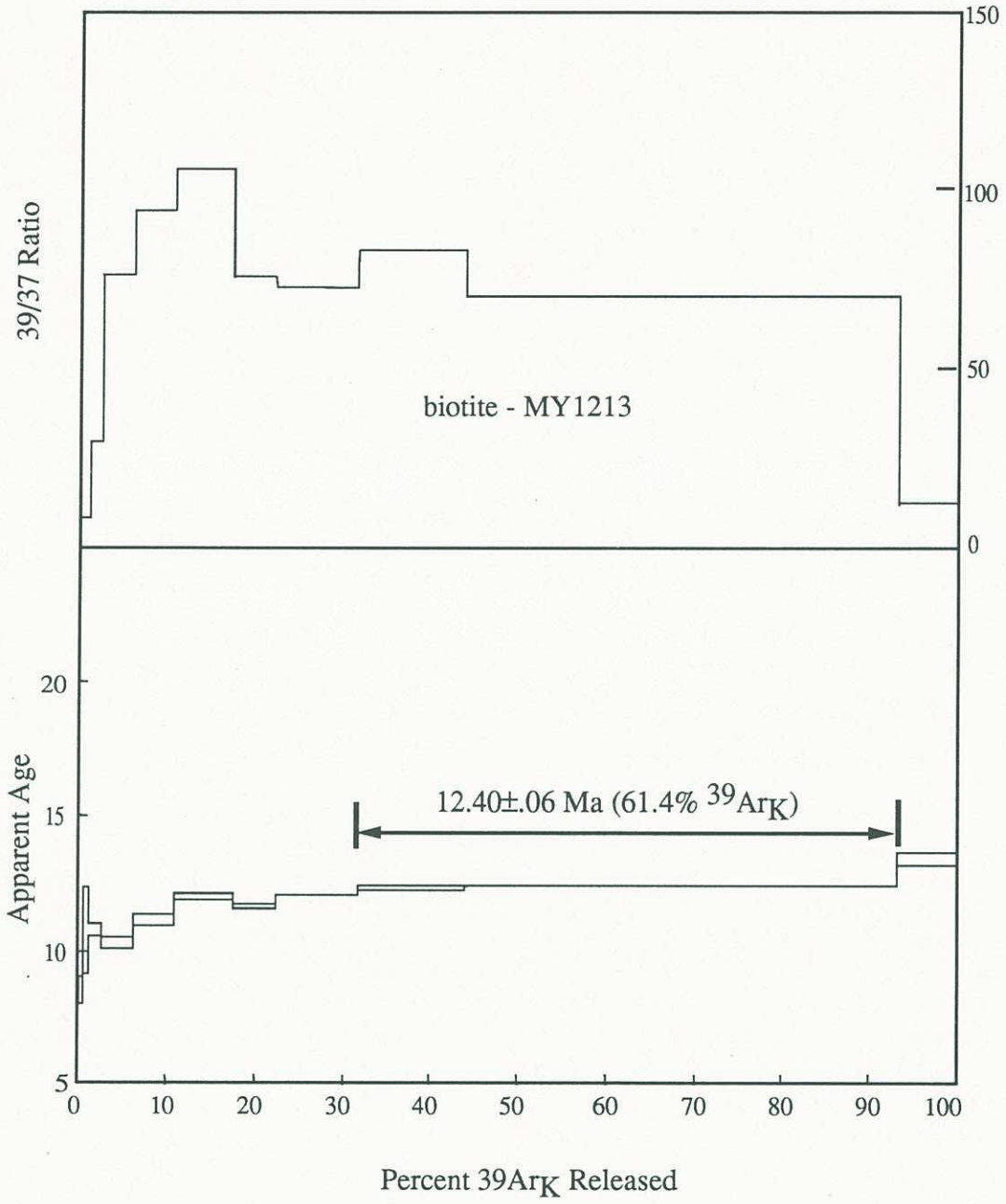

Figure 37. Argon release spectrum and $^{39}Ar/^{37}Ar$ spectrum for biotite illustrating a 12.40±.06 Ma rhyodacitic flow from the flow dome complex.

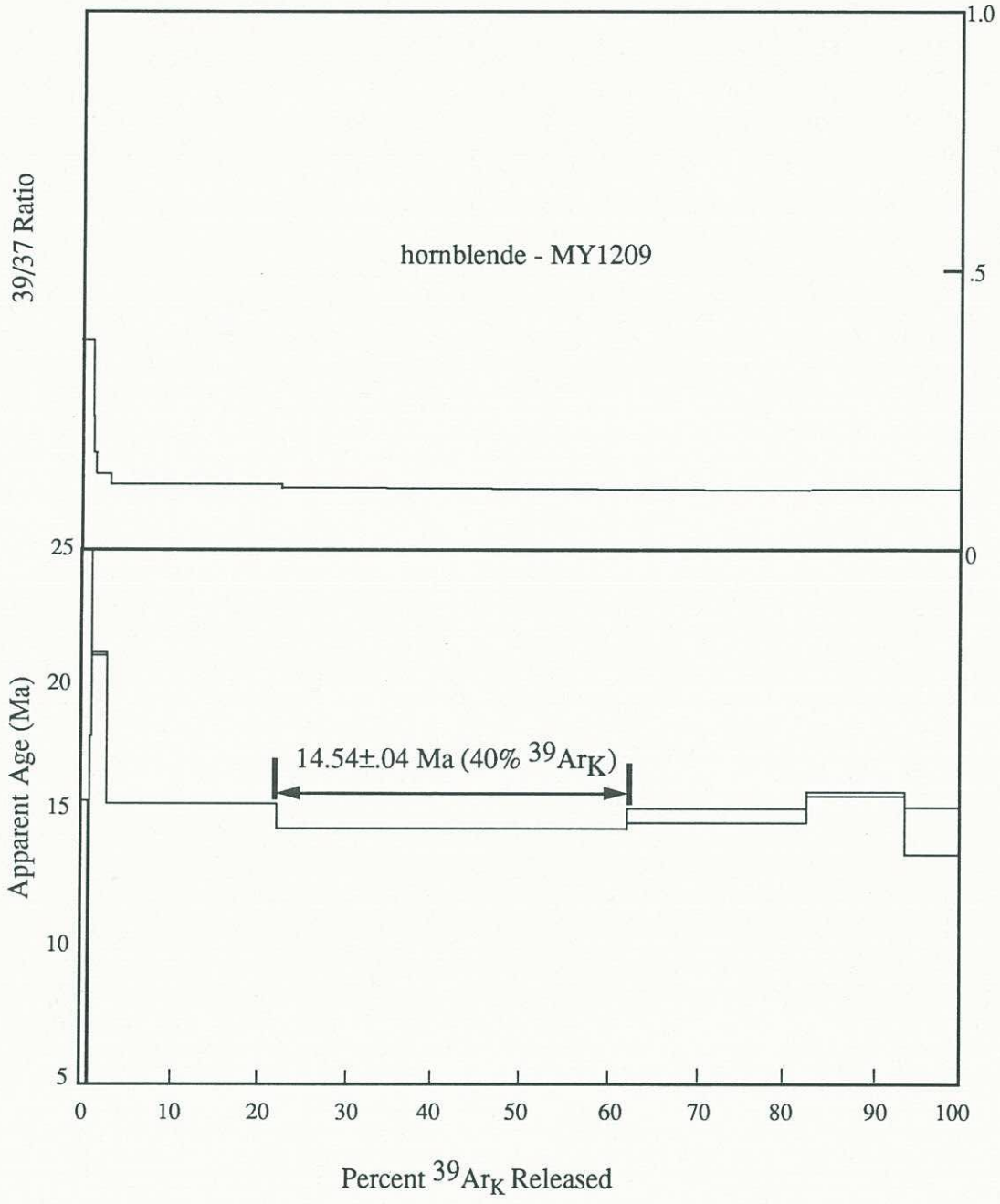

Figure 38. Argon release spectrum and $^{39}Ar/^{37}Ar$ spectrum for hornblende illustrating a 14.54±.04 Ma rhyodacitic flow from the flow dome complex.

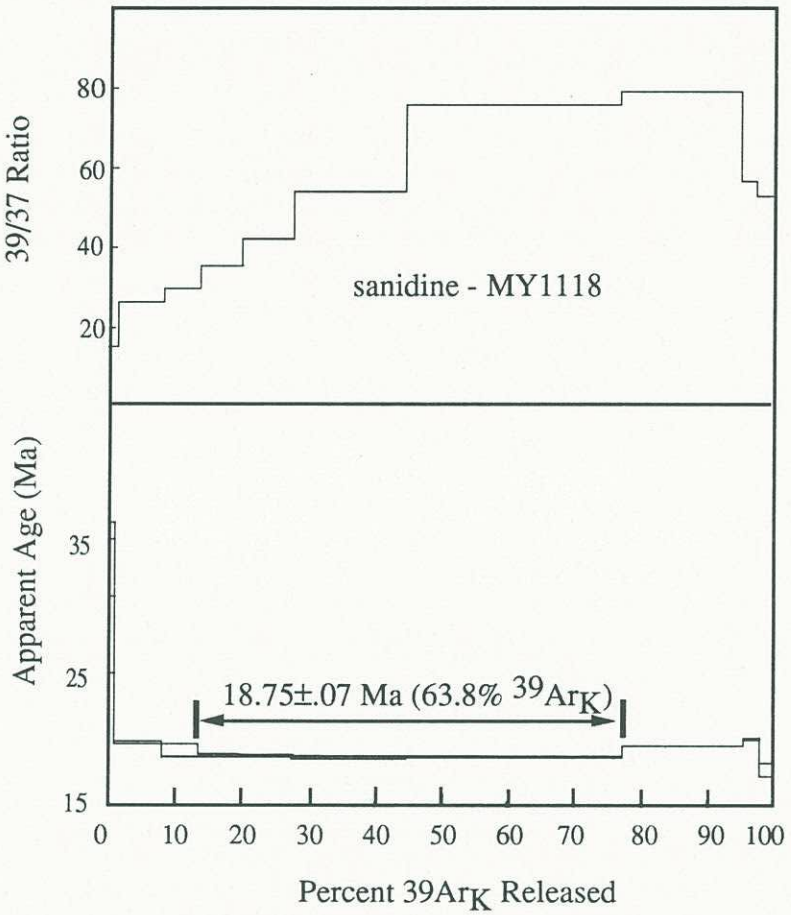

Figure 39. Argon release spectrum and $^{39}Ar/^{37}Ar$ spectrum for sanidine with a plateau age of 18.75±.07 Ma.

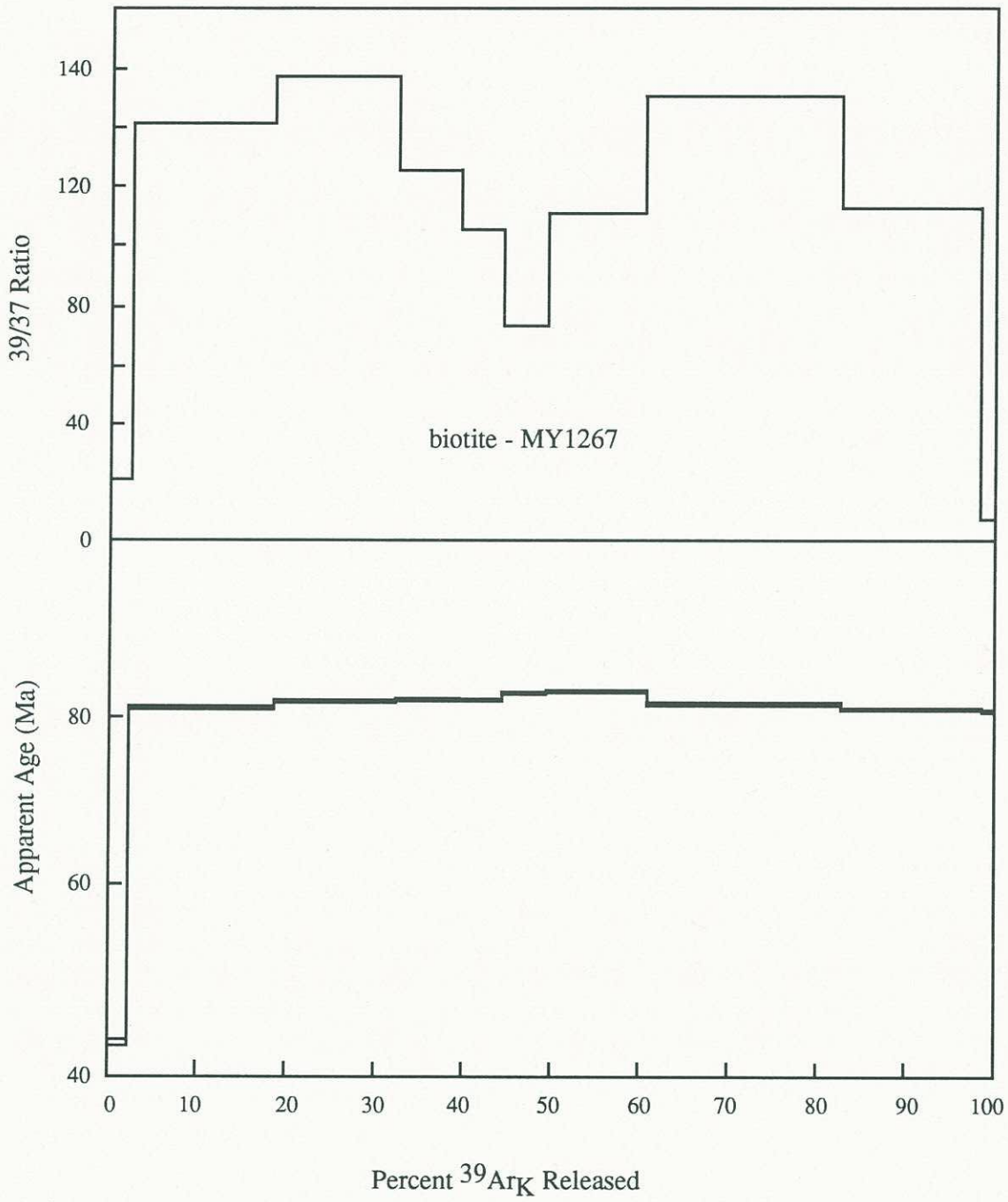

Figure 40. Argon release spectrum and $^{39}Ar/^{37}Ar$ spectrum for biotite illustrating a granodiorite that passed through the biotite closure temperature between 80-83 m.y.

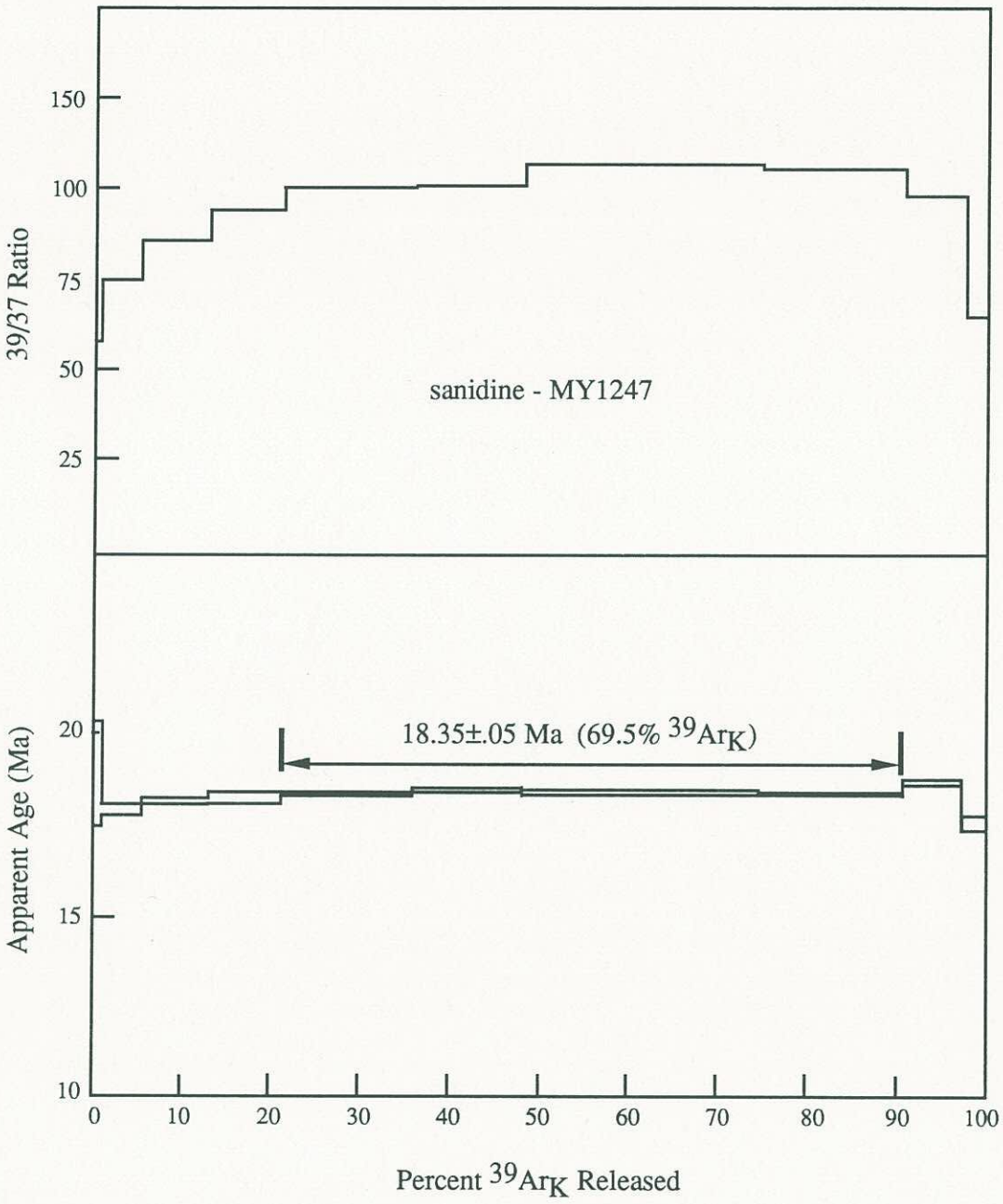

Figure 41. Argon release spectrum and $^{39}Ar/^{37}Ar$ plot for sanidine illustrating an 18.35±.05 Ma rhyolite flow.

based on the equations of Dalrymple et al. (1981) and modified to allow the option of choosing the larger of separately derived F-value ($^{40}Ar^*/^{39}Ar_K$) errors (Table 3), a calculated error from differential equations or an experimental error determined from the reproducibility of identical samples (Shubat and Snee, 1992). The total gas age of sample 1267 is a weighted average based on ragiogenic argon and apparent ages for all of the herating steps (Table 3).

3.3 Age Determinations and Discussion

Volcanic rocks in the ECVF range in age from greater than 18.75±.06 Ma to 12.40±.06 Ma. If the basal, intermediate composition rocks in this region, such as those intruded by rhyolitic dikes at the Blue Chalcedony area, are correlative with dated flows from the central Mojave Desert, then this volcanic field may be as old as 22-20 Ma (Burke et al., 1982; Glazner, 1986).

The oldest dated volcanic rocks in the ECVF are rhyolitic feeder dikes and flows. Two plateau ages determined for rhyolites from the Blue Chalcedony area are 18.37±.06 and 18.75±.06 Ma with a rhyolitic feeder dike being the youngest and a rhyolitic flow being the oldest (Figs. 39, 41). The argon release spectra and the K/Ca plots for the sanidine separates display slight age increases in the higher heating steps (Figs. 39, 41). This stepping-up feature, which often affects plateau age determinations, is commonly observed in sanidines although the reasons remain unclear (L. Snee, 1993, personal communication). The quartz-sanidine±biotite phyric nature of both the feeder dike and rhyolitic flow, their locations and their similar ages suggest that they are genetically related.

Rhyolitic feeder dikes intrude tuffs and flows, although it is unclear how much older these tuffs and flows might be. Age determinations indicate that rhyolitic flows are

mid-Miocene and that rhyolitic volcanism in this region persisted for at least 400,000 years. The ages of these rhyolites indicate that they could be correlative with units in the approximately 18.5 Ma Opal Mountain volcanic rocks to the south (Burke et al., 1982). The ECVF and Opal Mountain rhyolites are also the same age as the Peach Springs Formation, a regionally extensive ash flow sheet that extends from Arizona into the central Mojave desert (Glazner et al., 1986). This apparent relationship may be relevant to the evolution of rhyolitic magmatism in the Mojave Desert although at this point it is unclear.

Rhyolitic flows at Blue Chalcedony were preceded by a pyroclastic eruption(s). With the exception of thick tuff exposures in the fault scarp at Eagle Crags, most tuffs in the region are difficult to differentiate; consequently, it is not yet clear how many pyroclastic eruptions may have preceded or followed rhyolitic volcanism at Blue Chalcedony.

The youngest volcanic rocks in the ECVF are the dome-forming rhyodacitic flows in the Goldstone area (Fig. 37, 38). Field evidence indicates that formation of these domes was the last volcanism in the region. The argon release spectrum for hornblende from a steeply-dipping rhyodacitic flow (sample 1209, Fig. 38) does not conform to the plateau age criteria of Snee et al.(1988). The concave-up shape of the spectrum, often observed in hornblendes from intrusive rocks, is due to excess argon. The 14.54±.04 Ma age is therefore considered a maximum age for this sample. The 2 m.y. difference between this maximum age and the 12.40 Ma age determined for another rhyodacite (Fig. 37) could be a relic of excess argon or may indicate that the growth of domes persisted for up to 2 m.y.

A lens-shaped granodiorite in the Blue Chalcedony area is part of the Sierran-age, granitic basement in the northern Mojave Desert (Smith, 1964). The 80-83 Ma span illustrated by the age spectrum represents the approximate age of closure for biotite in this

rock (Fig. 40). It has been speculated that the granitic basement of the Mojave Desert may be 85-90 m.y. old but that biotites in the slow-cooling mass did not close to argon diffusion at approximately 280±40°C for another 5-10 m.y. (Miller and Sutter, 1982). Very irregular, step-like plateaus in spectra generated from similar granitoid rocks in the Goldstone Lake region at Fort Irwin have been interpreted to suggest that these rocks experienced several episodes of uplift, which in turn disrupted the initial argon rations in biotites (Miller and Sutter, 1982). This spectrum is similar to those from granitoids in Fort Irwin with the exception that the granodiorite from the Blue Chalcedony area has apparently not been severely disturbed.

CHAPTER 4

TECTONICS, STRUCTURAL GEOLOGY AND GEOPHYSICS

4.1 Introduction

Structures of variable styles and scales including homoclines, possibly associated with listric faults, strike-slip and normal faults, and arcuate faults associated with calderas were identified during field reconnaissance. Thrust faults and/or detachment faults could be inferred from previous investigations (Austin et al., 1983; Walker et al., 1990). Larger-scale features such as regional lineaments and possibly a shallow crustal volcano-tectonic depression have been identified on aerial photographs and through the interpretation of geology and geophysical data.

The origin of many of the structures and magmatic features in the study area are more clearly understood when considered in a regional context. The tectonic and related magmatic setting of eastern California is presented in the second and third sections of this chapter to outline the conventional thought regarding the tectonic and magmatic history of the Mojave Desert. Structures and structural-controlled vents are then described in the following sections. The seventh section of this chapter presents preliminary results of an ongoing gravity survey in the NAWS South Ranges and Fort Irwin. Results are contrasted with an earlier, regional gravity survey conducted by the State government (Nilsen and Chapman, 1971). Gravity anomalies delineated in the ongoing survey offer additional evidence related to the structural and magmatic evolution of the ECVF. The final section of this chapter discusses all of these features and presents an hypothesis for the structural and

tectonic history of the northern Mojave Desert.

4.2 Tectonics and Regional Structures

Glazner et al. (1989), Walker et al. (1990) and others identified the Waterman Detachment Fault, a major fault system in the Waterman Hills south of the ECVF in the central Mojave Desert. They suggested that this detachment system probably extends to the northwest into the China Lake NAWS but were unable to prove this for the lack of evidence. Results of geochronology and kinematic indicators were interpreted as indicating northeast-directed extension that lasted from 23 to 18 Ma.

Based on field investigations to the southeast and west of Barstow, California, Bartley et al. (1989) concluded that the entire Mojave block of central California experienced Miocene north-south compression that was superimposed on early Miocene crustal extension at about 19 Ma. They described reverse faulting, thrust faulting and isoclinal folds with east-west fold axes which were the result of north-south compression that began soon after extension ceased. Glazner et al. (1990) suggested that northwest-directed right-slip faults are transpressional and that there is active growth on compressional-related folds in the northern Mojave Desert.

Strock and Molnar (1988) calculated that approximately 1360 km of right-lateral displacement has occurred along the Pacific-North American transform since its inception near 35 Ma, although partitioning of the strain is not yet understood. Golombek and Brown (1988) suggested that remnant magnetism reveals that the western Mojave Desert experienced a period of clockwise rotation and right-lateral shear from 20-16 Ma. Shearing and subsequent northwest-striking, right-slip faulting that began at 13 Ma was probably compensating for movement along the San Andreas fault. Northwest-trending structures

with an apparent dextral sense of displacement constitute the most numerous structures in the Mojave Desert.

Dokka and Travis (1990) speculated that the Eastern California Shear Zone (ECSZ) of the eastern Mojave Desert-Death Valley region may have accommodated 9-23% of the motion between the Pacific and North American plates between 10 and 6 Ma. This zone includes the Mojave block and extends from east of the Sierra Nevada to possibly the Walker Lane belt of western Nevada. Additional but as yet unidentified, right lateral faults may exist beneath the northwest-trending alluvium-filled valleys of the Mojave block.

The Garlock fault separates the southwestern Basin and Range from the Mojave Desert and extends from the San Andreas fault through Death Valley. Left-slip movement along this fault was initiated by at least 10 Ma (Loomis and Burbank, 1988). Davis and Burchfiel (1973) described the Garlock fault as a major intracontinental transform structure and suggested that its origin was directly related to the onset of extension in the Basin and Range province immediately to the north. They stated that terrain south of this fault was relatively unaffected by Basin and Range extensional tectonics.

4.3 Tectonics and Associated Magmatism

Portions of the Mojave Desert underwent extensive Middle to Late Tertiary volcanism. Tertiary volcanic rocks of intermediate composition of the northern Mojave Desert are analogous to those of similar volcanic suites in the Basin and Range and are believed to be the product of subduction-related orogenesis (Dibblee, 1967; McKee, 1971; Lipman et al., 1972). By the time subduction of the Farallon Plate dramatically slowed and locally ceased, at about 20 Ma, right-slip movement commenced along the San Andreas fault in western California (Atwater, 1970; 1989). This gradual transition from convergent

to transform margin tectonism in the southwestern United States resulted in a correlative transition in volcanism, with intermediate to silicic compositions giving way to "fundamentally basaltic" compositions (Christiansen and Lipman, 1972; Snyder et al., 1976).

While the style and space-time patterns of volcanism in the Basin and Range and the Mojave Desert have been the subject of hundreds of studies that empirically support this hypothesis correlating Tertiary transitions in volcanism with a transition in tectonic styles, recent work suggests that volcanic rocks in portions of the Mojave Desert do not easily conform to this hypothesis (Lipman et al., 1972; Snyder et al., 1976). Glazner and Ussler (1989) pointed out that many synextensional volcanic rocks of the southwestern United States are not basaltic but are intermediate to silicic in composition and that basaltic volcanism seems to be influenced more by relative density differences between the magma and the crust and less by simple attenuation of the upper crust due to extension. In fact Spencer and Reynolds (1986), Glazner (1990) and Miller and Miller (1991) described synextensional rocks of intermediate to silicic composition in the central and eastern Mojave Desert. A generalized synthesis of the tectonic and volcanological history of the Mojave Desert is presented in Table 4.

4.4. Faults

Two principal sets of normal faults were identified in the ECVF (Plates 1-4). East-west trending, apparent left-slip faults may also transect the region. The only exposures of these faults were found along the eastern edge of the Myrick Spring area. The occurrence of a swarm of west-northwest-trending feeder dikes is assumed to be controlled by west-northwest-trending fractures although it is unclear if these dikes are related to the left-slip

Table 4. Generalized chronology of Cenozoic tectonism and magmatism in the Mojave Desert

Event	Features	Age	References
Uplift	Lack of pre-Miocene sed. rocks; Ar geochronology	Pre-Miocene 46.3-41.5 Ma	Hewett (1954); Miller and Sutter (1982); Dokka (1986)
NE-directed, core complex-style extension	Waterman Hills detachment fault	23-18 Ma	Dokka (1986); Dokka (1989); Glazner et al. (1989); Dokka (1990); Walker et al. (1990)
Intermediate to silicic magmatism	Flows, dikes, plugs, sills, pyroclastic and epiclastic rocks	mid-Miocene	Hewett (1954); Smith (1964); Dibblee (1967)
Clockwise rotation; right-lateral shear	Alignment of remnant magnetic poles; alignment of faults across major structures	20-16 Ma	Golombek and Brown (1988)
N-S compression	Overturned, isoclinal folds and warp-like folds w/ E-W axes	<19 Ma	Bartley et al. (1989)
Counterclockwise rotation	Restoration of NW-striking, right-slip faults	<16 Ma to ~2.5Ma (age of Black Mtn. basalt)	Dibblee (1961; 1967); Garfunkel (1974)
Right-slip faulting	NW-trending strike-slip faults	<13 Ma	Dibblee (1961); Golombek and Brown (1988)
Initiation of Garlock faulting	Offset of Jurassic Independence dikes	11-10 Ma	Loomis and Burbank (1988)
Transpression/oblique compression and strike-slips faulting			Bartley et al. (1989); Glazner et al. (1991)
Late Neogene volcanism	Black Mountanin basalt	<4 m.y.	Burke et al. (1982); Glazner et al. (1991)

faults at Myrick Spring. Most normal faults examined appear to have experienced both dip-slip and strike-slip movement.

Two northnortheast-trending, high angle, down-to-the-west normal faults were identified in the Eagle Crags areas (Fig. 42; Plate 1). Other similar structures have been identified on aerial photographs of the Eagle Crags and Goldstone regions although none have been field checked. A northeast-trending normal fault also bisects the volcanic neck region in the northeast portion of the Myrick Spring area. The fault plane has an attitude of N40E/60SE.

A northwest-trending fault was identified at the top of a basal rhyolite at the Blue Chalcedony region. Although this N50W/60SW fault surface appears to have undergone limited normal offset, the faulted area has been hydrothermally altered. The juxtaposition of certain flows at the Goldstone and Myrick Spring regions and lineaments identified on aerial photographs suggest that other N40W-striking faults may also transect these areas.

Several east-trending faults with left-lateral offset were observed in the Myrick Spring area. Strike-slip faulting is apparent only in the adjacent Granite Mountains (Figs. 8a, d). A westnorthwest-trending alluvial valley truncates the southern margin of the Myrick Spring eruptive center and may be an extension of this left-lateral fault or may be related to northwest-trending structures. A 2-3 m thick, vertically-oriented and highly silicified, 10-20 m sliver of brecciated, lithic-rich tuff borders the southern side of this valley and strikes west-northwest.

A 35-40 km long, east-northeast-trending lineament bisects the study area. It is defined by a break in topographic contours especially evident along the southern margin of the Granite Mountains (Fig. 43). Although no obvious faults are apparent along this trend, several features are situated on or are terminated at this trend including the eastern

Figure 42 Captions

Figure 42a. Eagle Crags faults scarp. Offset of white tuff (Mrp) is due to a high angle, northeast-striking normal fault.

Figure 42b. A relatively flat-lying dark green andesite from an area west of Eagle Crags and south of Blue Chalcedony. In figure 42a, this unit is dipping 25-30° to the southwest.

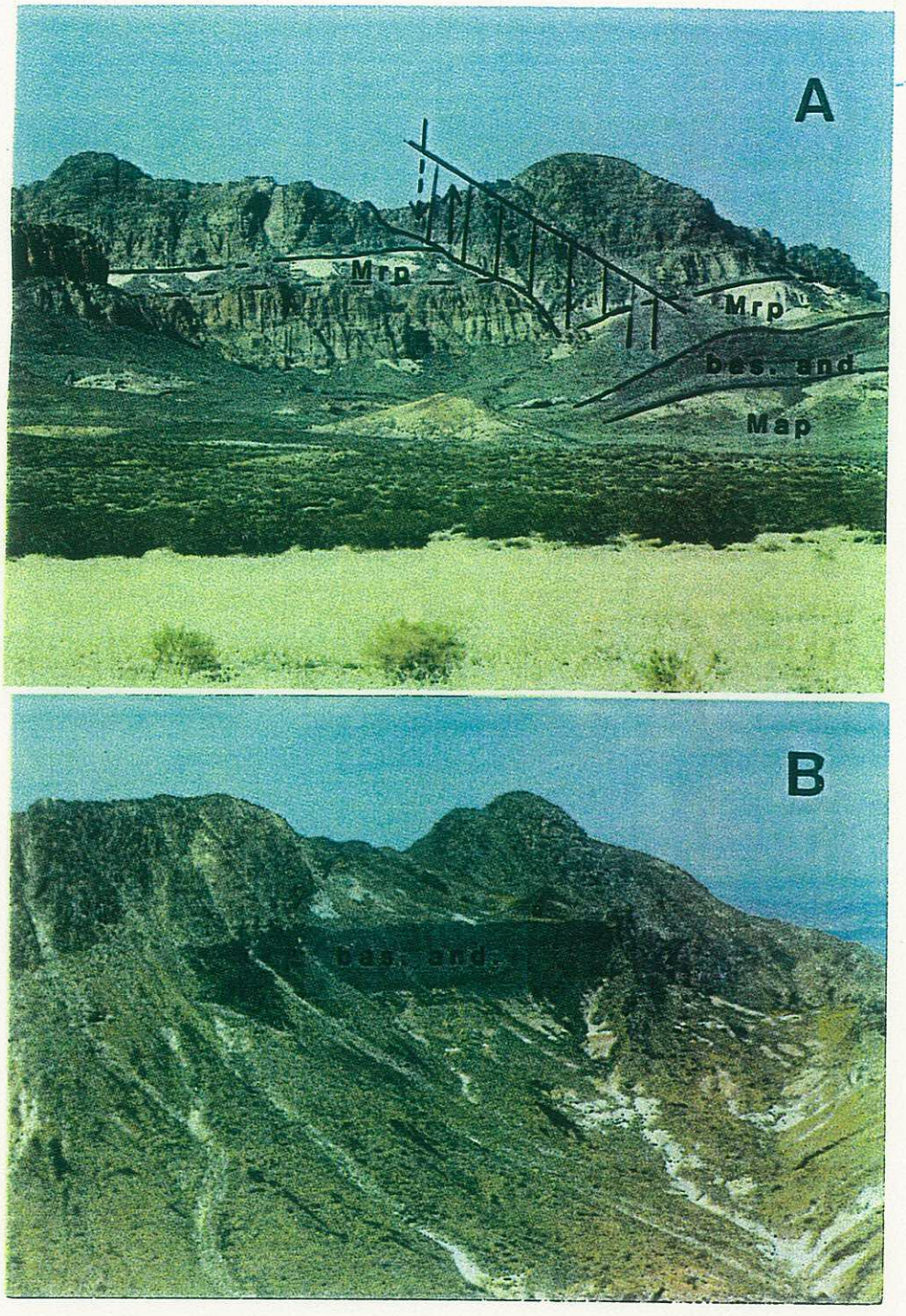
A
Mrp
Mrp
bes. and
Map
B
bes. and

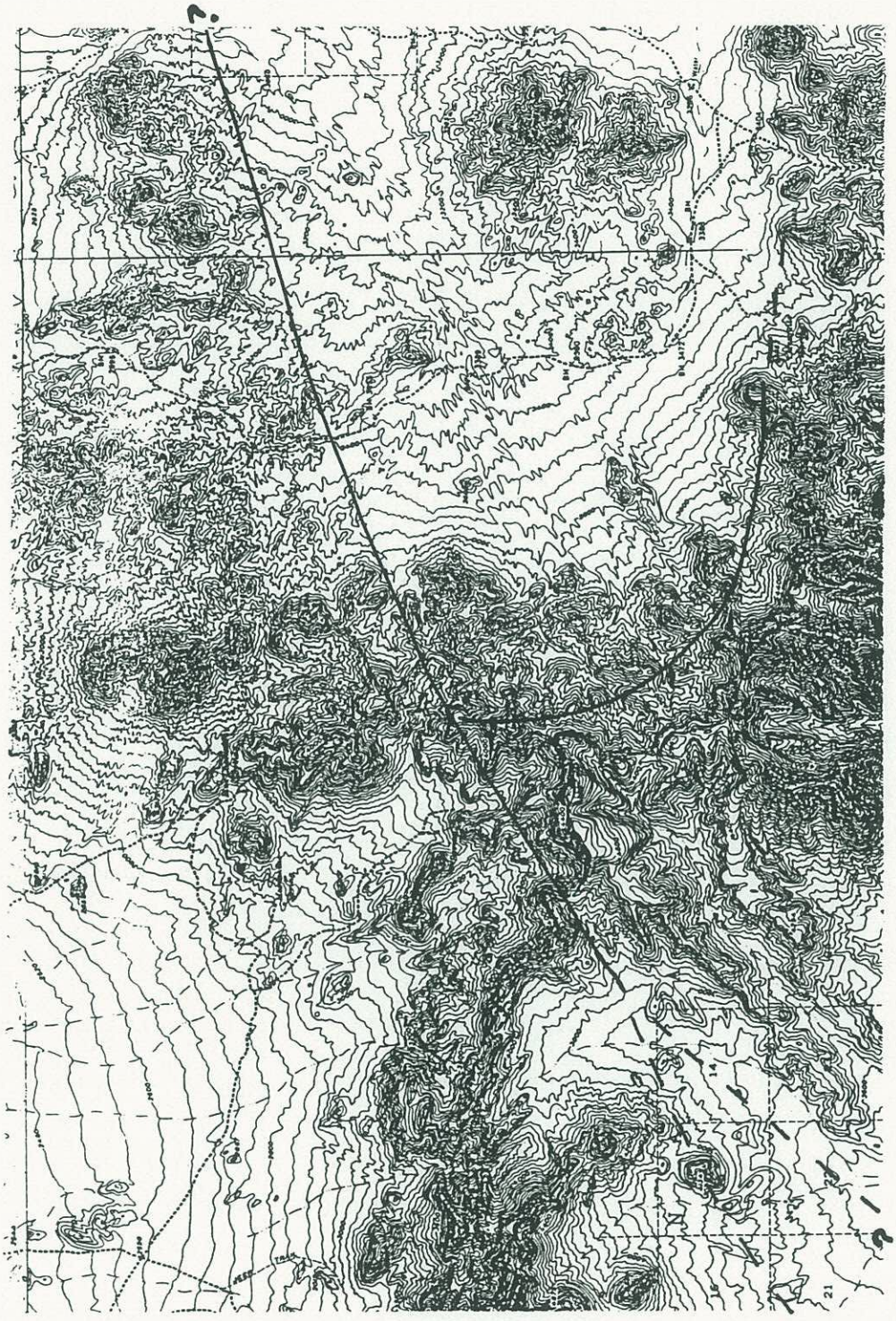

Figure 43. Topographic map of region with arcuate, concave up contours in bottom center of figure. Southwest-trending ridge line in bottom left of figure is the southwestern portion of the northeast-trending lineament that transects the region. Field of view is approximately 40x25 km. North is up.

termination of all feeder vents, alteration associated with a feeder vent and a break in the southeastern extent of many flows and pyroclastic rocks.

4.5 Arcuate Fault Scarp

An arcuate-shaped fault scarp defines the southern toographic rim of a central vent caldera in the ECVF and is most distinctly illustrated on regional topographic maps (Fig. 43). This fault scarp is about 2 km long with local relief exceeding 700 m. The scarp separates two structural domains. A compilation of measured attitudes of sheet-like flows from Eagle Crags illustrated in figure 44 indicates that most dip gently to the south-southwest. Flow-dome rhyodacites from the Goldstone area generally dip much more steeply to the west-southwest (Figs. 45, 46). Additionally, more sheet-like flows and tuffs exposed in the topographic rim are not observed northeast of the scarp. A 1-2 km wide, alluvial valley separates Eagle Crags from the Goldstone area.

Lithologic differences, field relations and geochronology indicate that sheet-like units exposed in the topographic rim are from an earlier period of volcanism than the steeply-dipping, flow-dome units of the Goldstone area. Rhyolitic feeder dikes that intrude similar sheet-like units to the west are approximately 18.5 Ma while an age determination from a steeply-dipping rhyodacitic flow from the Goldstone area is approximately 12.4 Ma. Structural measurements (Figs. 44, 45, 46) indicate that the Goldstone area apparently experienced block tilting while neither the Eagle Crags area to the south nor the Myrick Spring area, 10-15 km to the northeast, experienced none.

4.6 Fissure Vents

Many of the previously-described vents, fissure vents and feeder dikes and the

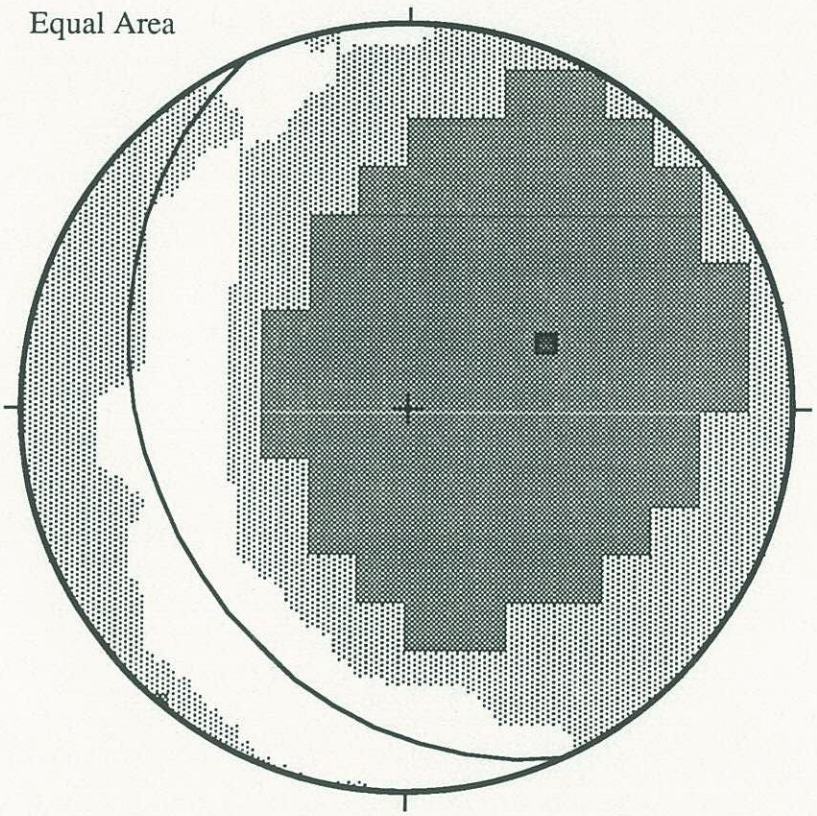

Figure 44. Equal area stereonet contour of poles to bedding from the Eagle Crags area. A N25W/33SW plane, described by the great circle, approximates the attitude of bedding at Eagle Crags.

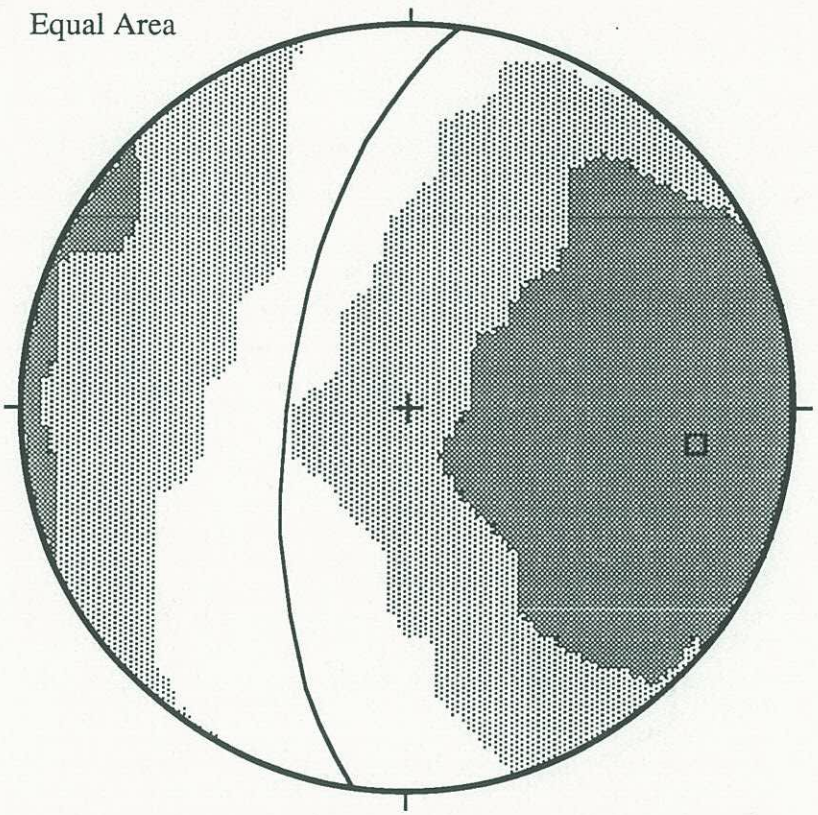

Figure 45. Equal area stereonet contour of poles to bedding from the Goldstone area. A N6E/66NW plane, described by the great circle, approximates the attitude of bedding at the Goldstone.

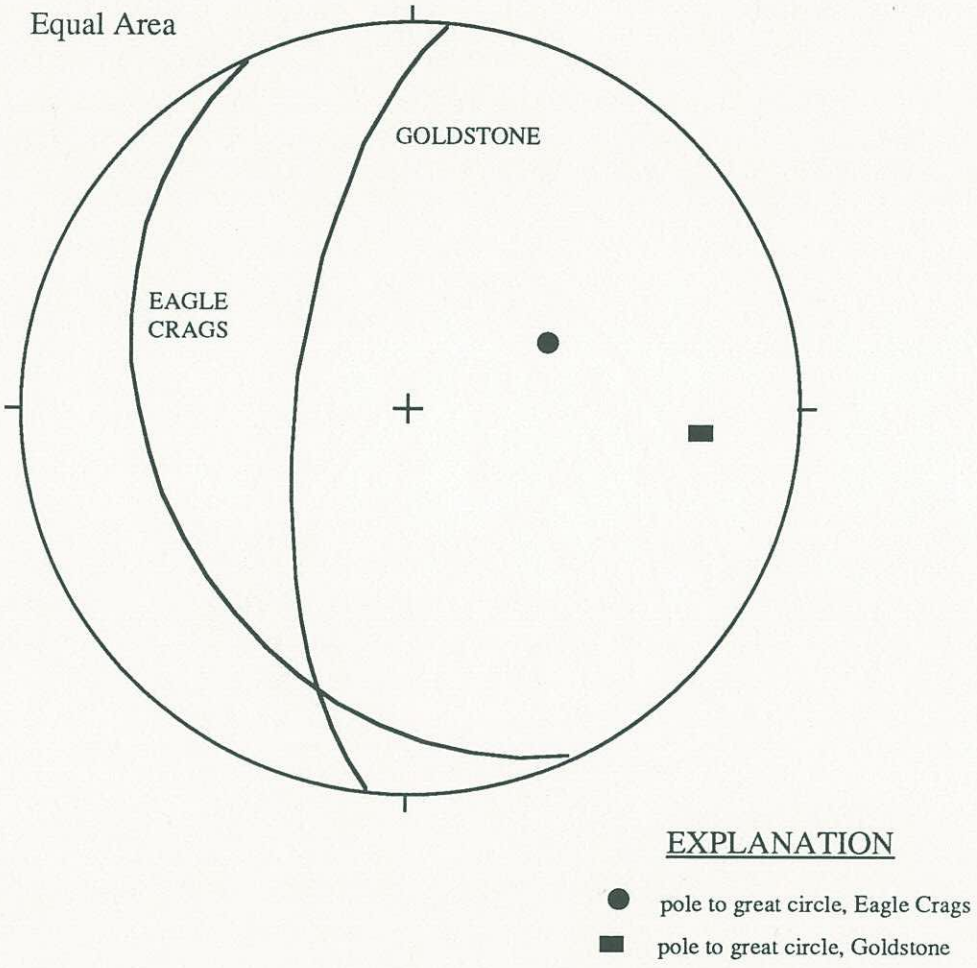

Figure 46. Great circles approximating bedding from the Goldstone and Eagle Crags areas are not coincident indicating that the Goldstone area experienced more severe southwest-directed block tilting the latter.

pyroclastic eruptive center at Myrick Spring appear to be situated along regionally extensive, northwest- and northeast-trending faults or their inferred extensions that cross the Mojave Desert.

At least two types of vents were the source of rhyolitic flows and tuffs in the Blue Chalcedony area. One vent has the form of a northwest-trending fissure and was the source of tuff that accumulated in the Pilot Knob Valley (Plate 1). The other source of rhyolitic tuff in the area is a central vent with a distinct tuff apron. It is located east of the feeder vents at the Blue Chalcedony area.

Most of the feeder dikes strike east-west to slightly northwest and are located in and around the Blue Chalcedony area (Plate 1 and 4). They are usually 1-3 m wide, vertically oriented and up to several hundred meters in length (Fig. 32). A feeder dike between the Blue Chalcedony and Myrick Spring areas is composed of sanidine+biotite+quartz rhyolite and trends N45W. Similar to dominantly west-trending feeder dikes at the southern edge of Blue Chalcedony, this dike is over 300 m long and less than 10 m thick. Unlike dikes at Blue Chalcedony, however, it is bordered by a 10-50 m wide zone of propylitically altered and silicified, brecciated dacite.

The eastern limit of these feeder dikes at Blue Chalcedony and the eastern limit of the N45W striking sanidine+biotite+quartz rhyolite feeder dike fall along a north-northeast-trending lineament that is defined by an obvious break in topographic contours (Fig.43). Along this lineament to the northeast is the pyroclastic eruptive center at Myrick Spring. Although vents and the eastern termination of feeder dikes appear to lie along or immediately north of this lineament, no major faults, shear zones or brecciated zones have been identified along this trend.

4.7 Gravity Data

A regional gravity survey conducted by the California Division of Mines and Geology reveals that a large negative Bouguer gravity anomaly exceeding -135 milligals is centered on the southeastern margin of the study area (Nilsen and Chapman, 1971). The anomaly is coincident with flows and pyroclastic rocks associated with the stratovolcanic complex. Most of the other anomalous gravity troughs in the region reflect wide, alluvial valleys.

Results of a gravity and magnetic survey conducted by the Geothermal Program Office, Department of Navy, yield details about the gravity anomaly in the southeastern portion of the ECVF (Fig. 47). Over 1000 stations at approximately 1000 ft spacings are contained in this data set. Locations of these stations were designed to traverse structures and lithologic discontinuities, such as the topographic rim at Eagle Crags, and to resolve the size of the gravity anomaly recognized by Nilsen and Chapman (1971).

Figure 47 is an oblique, three-dimensional illustration of the Bouguer gravity low outlined by the recent study. The gravity high depicted on the southeastern corner coincides with Tiefort Mountain, a granitic stock about 20 km east of the NAWS's western border. The large gravity low in the right center of the photograph is east of the NAWS-Fort Irwin boundary. This 25 mgal low is directly beneath the Goldstone and Eagle Crags areas. An east-west-trending density ridge extends from the gravity high at Tiefort Mountain to the western margin of the volcanic field. It appears to be truncated at the western base of the funnel-shaped gravity trough. An east-trending, left-lateral fault that extends to the NAWS-Fort Irwin border may be the surface reflection of this density ridge (Jenning et al., 1962). Apparent offset along this fault can be seen in the mapped Quaternary, nonmarine sediments and the Granite Mountains east of the study area in Fort

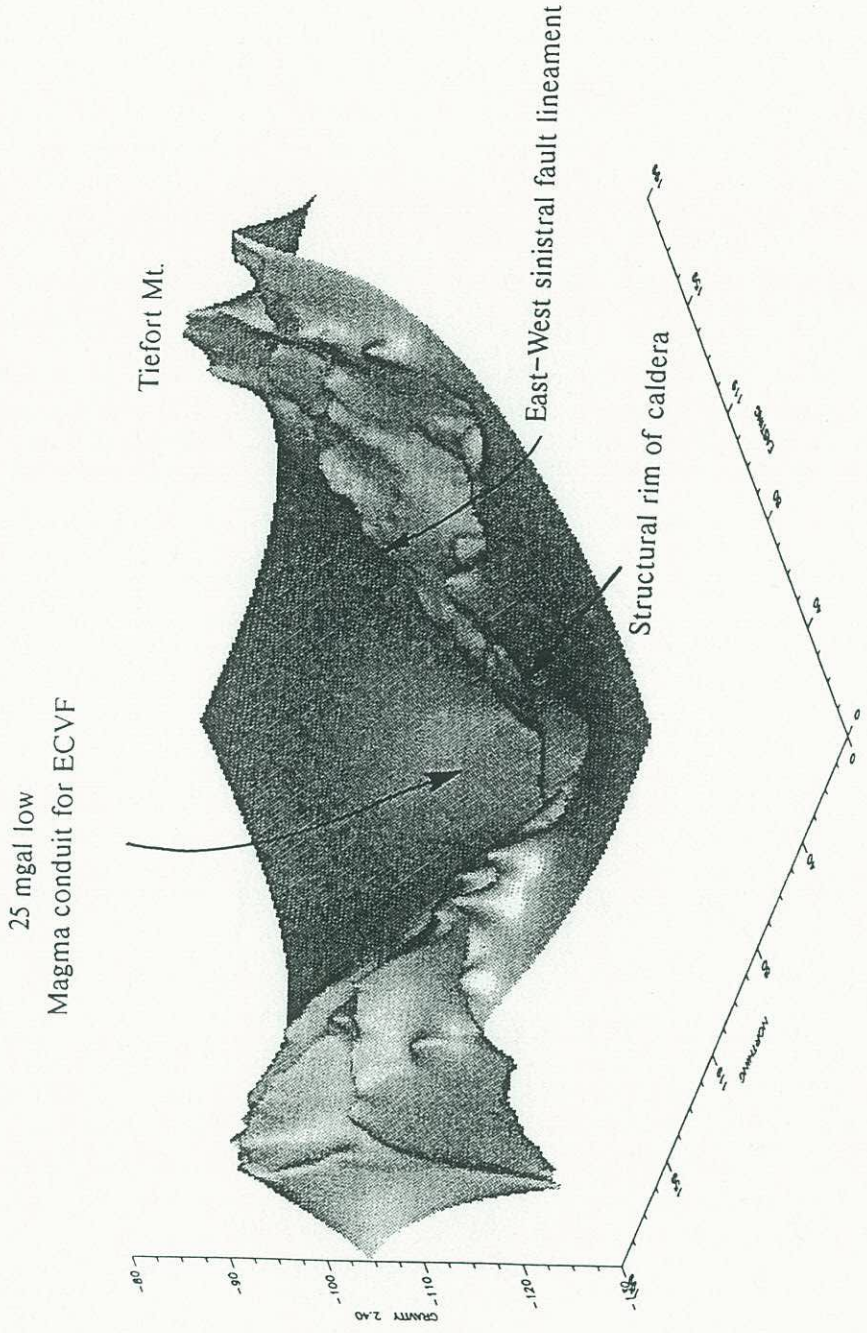

Figure 47. Oblique three-dimensional view of gravity anomaly depicting a very large gravity low coincident with the ECVF. Image represents approximately 40 miles along easting by 20 miles along northing axes.

Irwin (Jennings et al., 1962).

4.8 Discussion

The silica dike and other northeast-trending faults that crosscut altered andesitic-dacitic rocks in the southwestern Myrick Spring area apparently served as channelways for silica- and carbonate-rich hydrothermal fluids. The northwest-trending opalized breccia in the Myrick Spring area may be a hydrothermal breccia that was temporally related to these other structurally-controlled zones of alteration. Hydrothermal fluids may have been part of an epithermal system that was active during or after development of the northeast- and northwest-oriented structures.

The arcuate scarp at Eagle Crags probably developed during caldera collapse of a portion of the stratovolcano. Judging from its geometry and the rapid facies changes in pyroclastic rocks to the south, this relatively small caldera probably had a central eruptive vent similar to those in other stratovolcano calderas (Lipman, 1984). The uneven, down-dropped block(s) at the Goldstone area suggests a trap-door caldera (Rytuba and McKee, 1984; Lipman and Fridrich, 1990). Rhyodacitic domes are located on either side of this fault scarp. Development of the endogenous rhyodacitic domes was probably synchronous with caldera formation, as was suggested for the Mashu stratovolcano in Japan (Katsui et al., 1978).

The Bouguer gravity anomaly probably reflects relatively low density, crystalline rocks and contrasted with the denser granitoid basement of the northern Mojave Desert. Bouguer gravity lows are almost always associated with calderas, generally defining the roots of the volcanic material or possibly a magma reservoir in younger systems (Lipman, 1984; Hunt, 1992). The large continuous gravity trough (Fig. 47) is interpreted as a

subvolcanic intrusion marking the position of the former magma chamber that was the source of the andesitic through rhyolitic magmas.

The funnel shape of this gravity low is a function of the location of gravity stations and a function of the geometry of the intrusion. The northeast corner of the anomaly is not rigorously constrained by gravity stations. Granitic outcrops surround the volcanic field. Regional gravity data mimic this association with the gravity low surrounded by relatively denser, granitic material.

In addition to reflecting a trap-door style caldera, the scarp at Eagle Crags may have also served as a "breakaway zone" during caldera collapse and synchronous extension (Wernicke, 1981; Dokka, 1986). The east-northeast-trending lineament (Fig. 43) that transects the region could be a right-lateral fault, possibly related to and younger than the Waterman Detachment Fault. It would be right-slip because of the apparent dextral drag on feeder vents to the north of the fault and south of Blue Chalcedony, and dextral drag along the arcuate fault at Eagle Crags, south of the lineament. The alluvial valleys on the south side of this lineament and northeast of the breakaway fault, such as the valley between Eagle Crags and Goldstone areas, may be half-graben or pull-apart valleys (Fig. 48). The approximately 18.5 Ma rhyolitic feeder dikes are truncated by this northeast-trending lineament. The 12.4 Ma rhyodacites were probably erupted during and after caldera collapse and synchronous extension. The steeply-dipping monoclines may have been formed by sliding along a listric decollement (Fig. 49). The region north of this east-northeast-trending lineament forms a wedge bounded on the north by the Garlock fault.

If the northeast-trending lineament is a right-lateral fault that truncated 18.5 Ma rhyolitic feeder dikes south of Blue Chalcedony, then valleys directly southeast of this lineament may be extensional, or half-graben valleys. Formation of monoclines or half

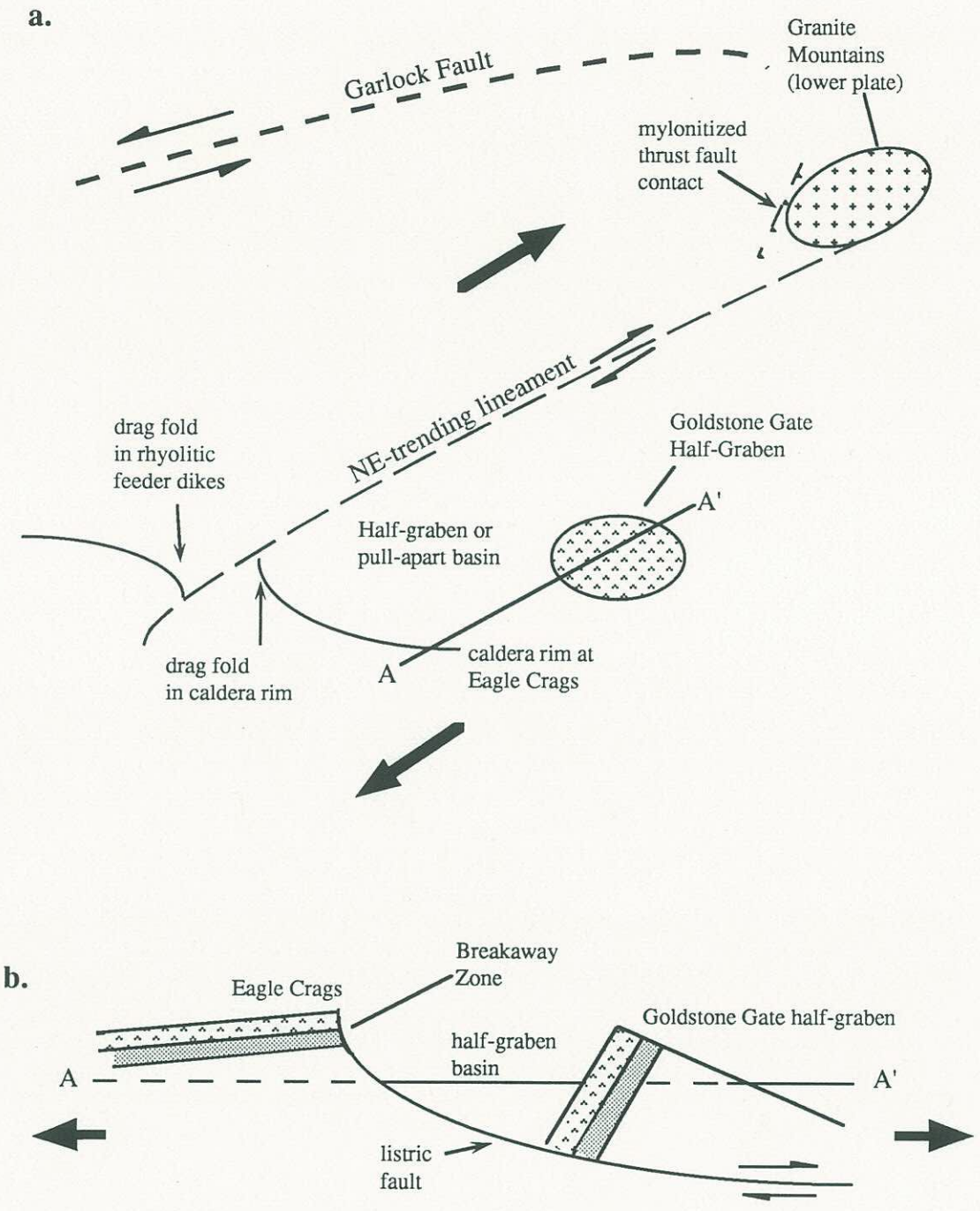

Figure 48. Hypothesized middle Miocene generation of pull-apart basin due to NE-directed extension; (a) plan view of entire field, (b) cross-section of "breakaway zone" and half-graben, pull-apart basin.

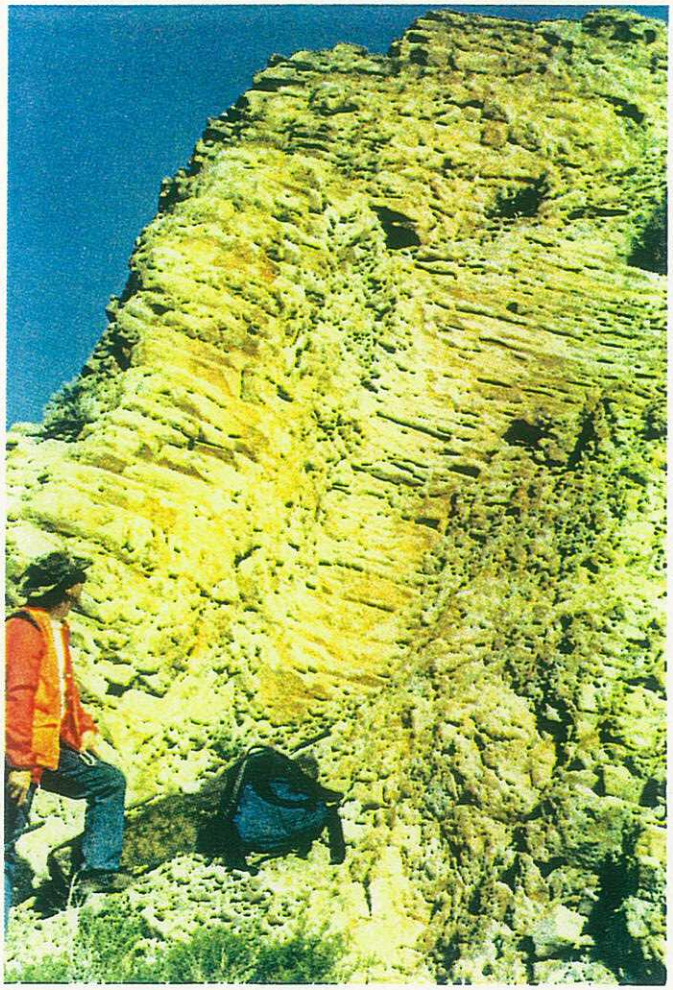

Figure 49. S70W-dipping rhyodacitic flow with columnar joints indicating original top of this 12.4 Ma flow.

grabens composed of 12.4 Ma flows suggests that movement along this fault and localized extension may have lasted for 6 m.y. or more. If the north side of this fault were moving northeast, then the brecciated and mylonitized zone at the contact between the Granite Mountains and Tertiary age volcanic rocks at Myrick Spring may be a thrust fault. Extension south of this lineament is could have been synchronous with the caldera development because most calderas generally develop in or adjacent to extended regions (Johnson, 1991).

A synthesis of regional tectonic relationships suggests that not only do the San Andreas and Garlock faults define the western and northern margins of the Mojave Desert, respectively, but they controlled much of the tectonic evolution of the Mojave Desert during Middle to Late Tertiary time. The relative style and timing of magmatism in the Mojave Desert does not directly accord with the hypothesis that andesitic-dacitic volcanism is the result of subduction while translational movement along the Pacific-North American transform, and accompanying extension in the Basin and Range and Mojave Desert physiographic provinces resulted in "fundamentally basaltic" magmatism (Christiansen and Lipman, 1972). If the Waterman Detachment Fault were a middle Miocene feature that affected the ECVF, then rhyolitic volcanism and presumably most volcanism that preceded it in the region was synextensional.

CHAPTER 5

ALTERATION

Silicic, argillic and propylitic alteration has been identified along fractures, veins and in brecciated volcanic flows within the ECVF. Geochemical analyses reveal that altered rocks contain anomalously high concentrations of As, Sb and Hg (Table 5). Au, Ag, Mn and Ba have also been identified from altered volcanic rocks in the ECVF (Austin et al., 1983).

The only altered regions examined in detail were in the Myrick Spring area . These regions include a silicified vein of matrix-supported breccia, the highly silicified fracture or "silica dike" and an altered portion of a hypabyssal, andesite-dacite flow (Plate 2). Other altered areas in the ECVF include the feeder-dike zone located between the Myrick Spring and Blue Chalcedony areas (Plate 1), argillic alteration associated with brecciated zones in the aphyric rhyolite (Mar) and a bleached and stockwork carbonate alteration (Fig. 23d) that crops out less than a km south-southeast of the altered feeder-dike zone.

The matrix-supported breccia at Myrick Spring forms a vertically-oriented, N40W-striking opalized vein. The vein is greater than 50m long and up to 2 m thick where exposed by a 5 m long prospector's drift. The breccia is composed of subangular to subrounded clasts of bleached and silicified dacite in a glassy, brick red matrix (Fig. 20c). Vugs of botryoidal silica and nonbrecciated veins of opal associated with this brecciated vein are dispersed throughout the dacitic host rock (Fig. 50a).

No cinnabar or realgar were observed although historic records indicate that both

Table 5. Results of neutron activation analyses from selected flows and tuffs[1, 2]

Trace	1255	1253	1254	1256	1257	1258	1259	1223	1081	1271	1211	1023
Na	29000	2400	8000	3700	2100	2200	3100	10000	20000	32000	15000	1600
Ca (%)	3	6	23	1	1	2	2	3	3	2	1	1
Sc	8.8	8.1	2.9	7.4	5.9	5.5	7	6.2	9	4.2	2.9	2.2
Fe (%)	3.3	2.5	1.1	3.9	2.6	1.6	2.3	2.2	2.1	1.5	1.4	3.1
Co	18	11	8	15	10	8	10	13	12	8	5	5
As	5	23	3	33	35	17	19	8	3	2	9	59
Rb	60	100	30	110	80	170	130	50	190	30	140	30
Sr	500	500	1300	500	500	500	500	500	500	500	500	500
Sb	101	76	1.7	44	270	43	72	15	.6	.8	1.2	1.8
Cs	3	6	4	7	11	10	6	4	4	3	3	9
Ba	900	27000	400	800	800	800	1000	600	400	1300	1100	300
La	27	21	9	25	18	21	31	21	31	14	44	19
Ce	54	44	20	51	35	41	61	39	60	28	80	34
Nd	20	10	10	20	20	20	20	20	20	10	30	10
Sm	4.1	3.4	1.4	4.1	2.6	3.3	5	3.3	4.5	1.9	5.4	2
Eu	1.4	1	.6	1.3	1.4	.9	1	1.1	.8	.6	1.2	.6
Yb	1.5	1.5	1.3	1.8	1.3	1.5	2.1	1.3	2.7	.7	2.4	.9
Lu	.2	.19	.18	.24	.18	.2	.32	.2	.37	.09	.35	.13
Hf	6	5	1	5	3	3	7	4	5	2	6	6
W	4	18	4	4	19	4	11	4	4	4	4	4
Hg (ppb)	49	1000	55	710	1000	531	1000	605	17	235	1000	155
Hg		3.5			4.85		6.81				1.98	
Th	6.5	6.5	2.2	6.3	4.9	7.7	9	5.4	29	3.4	11	6.9
U	1.9	2.4	1.2	2.7	1.1	2.8	12.8	1.7	3.5	1	2.6	2.4

1 Table includes only elements present above the detection limit. The following elements were also analyzed but concentrations were at or below the detection limits which follows: Au (5 ppm), Cr (10 ppm), Ni (100 ppm), Zn (50 ppm), Se (5 ppm), Br (1 ppm), Mo (5 ppm), Ag (5 ppm), Tb (0.5 per mil) and Ir (20 ppm).

2 All analyses in parts per million unless otherwise stated.

Figure 50 Captions

Figure 50a. A sample of an opaline vein that transects host dacitic flow adjacent to the opalized, matrix-supported breccia ("myrickite") in the Myrick Spring area (Plate 2).

Figure 50b. Clear to gray quartz and open-space deposited opal in the silica dike from the northeast of the Myrick Spring area (Plate 2).

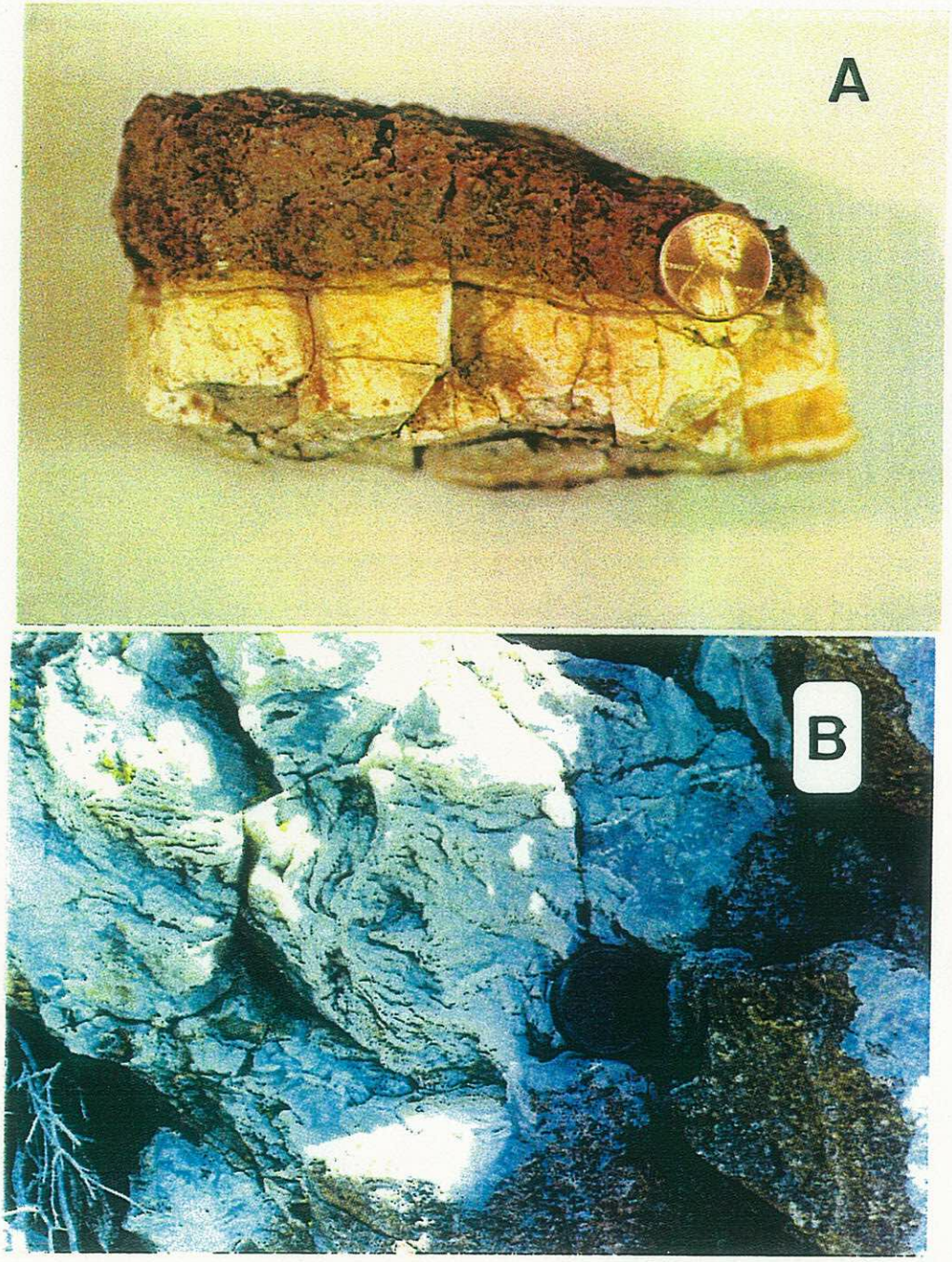
A
B

have been found in the Myrick Spring area (Austin et al., 1983). The matrix-supported breccia is termed "myrickite", a local rock collector's term for cinnabar-bearing opal. Table 5 includes an analysis of this breccia (sample 1223) and reveals anomalously high concentrations of Hg, but no Au or Ag. An examination of quick plates cut from opalized breccia, nonbrecciated opaline veins and unaltered host rock reveals that quartz and cristobalite do not contain fluid inclusions large enough for detailed geothermometry or geochemistry. These inclusions suggest that this breccia was the result of a low temperature, probably surficial hot-spring system (J. Reynolds, personal communication, 1991).

A sharp break in slope marking the northwestern margin of a stack of flat-lying andesitic-dacitic flows at Myrick Spring defines a northeast-trending lineament that transects the Myrick Spring area. A N35E-striking linear fracture roughly parallels this break along a narrow, 1.5 km trend. This fracture is in contact with an altered andesitic basalt, to the east (Plate 2). The alteration assemblage in the mafic flows is primarily chlorite±epidote and calcite. The fracture ort silica dike is so-named because it is a linear zone 2-5 m wide composed of clear to gray quartz and veins of white opal (Fig. 50b). Carbonate alteration in the adjacent basaltic andesite is a contact-related feature that decreases noticeably away from the silica dike. Although this dike is only about 35 m in length at this locality, its N35-40E strike parallels the trend of regional structures, such as high angle, normal faults observed at Eagle Crags. The silica dike terminates underneath a volcanic conduit or neck and may have been a feeder for the flows. This feeder dike was subsequently sealed by silica- and carbonate-bearing fluids. Throughout the study area, carbonate alteration is commonly found in vent or vent-proximal rocks suggesting that this alteration may be a vent-related phenomenon.

A set of approximately N20E-striking and vertically dipping fractures crosscut the altered andesitic-dacitic flows in the southwest portion of the Myrick Spring area (Plate 2). Alteration includes cm-scale quartz veinlets and bleached, white to yellow argillic alteration. A conjugate set of N70W-trending fractures also crosscuts the andesitic-dacitic flows. Propylitic alteration is pervasive along these fractures.

Samples from this altered zone were analyzed for Au, Ag and other elements commonly associated with epithermal, precious metal systems (Table 5). Figure 51 graphically shows the $\log_{10}$ ratio of the elemental concentration of each sample from this altered region (samples 1253-1258; Plate 2) divided by the same elemental concentration from sample 1255, an unaltered analog. Elements enriched during hydrothermal alteration include As, Sb, Hg and possibly Cs and W. The only significantly depleted element is Na. This enrichment is consistent with historic records of elemental and mineral concentrations discovered in this region (Austin et al., 1983).

The silica dike and other northeast-trending faults that crosscut altered dacitic flows in the southwestern Myrick Spring area apparently served as channelways for SiO_2- and CO_2-rich hydrothermal fluids. The northwest-trending opalized breccia in the Myrick Spring area may be a hydrothermal breccia that was temporally related to these other structurally-controlled zones of alteration. If these fluids were genetically related, then they all may have been part of a hydrothermal system that was active during or after development of the northeast- and northwest-oriented structures. The alteration and depositional environment of the Myrick Spring area resembles the hypothesized top of a low-sulfidation, hot spring-type gold-depositing system characterized by anomalous concentrations of Hg, As,.Sb, Ba (±Au+Ag), hydrothermal breccias, and silica alteration or siliceous sinter (Giles and Nelson, 1982; Silberman and Berger, 1985; Sillitoe and Bonham, 1992). The fine-grained silica growth in these veins and their lack of visible fluid

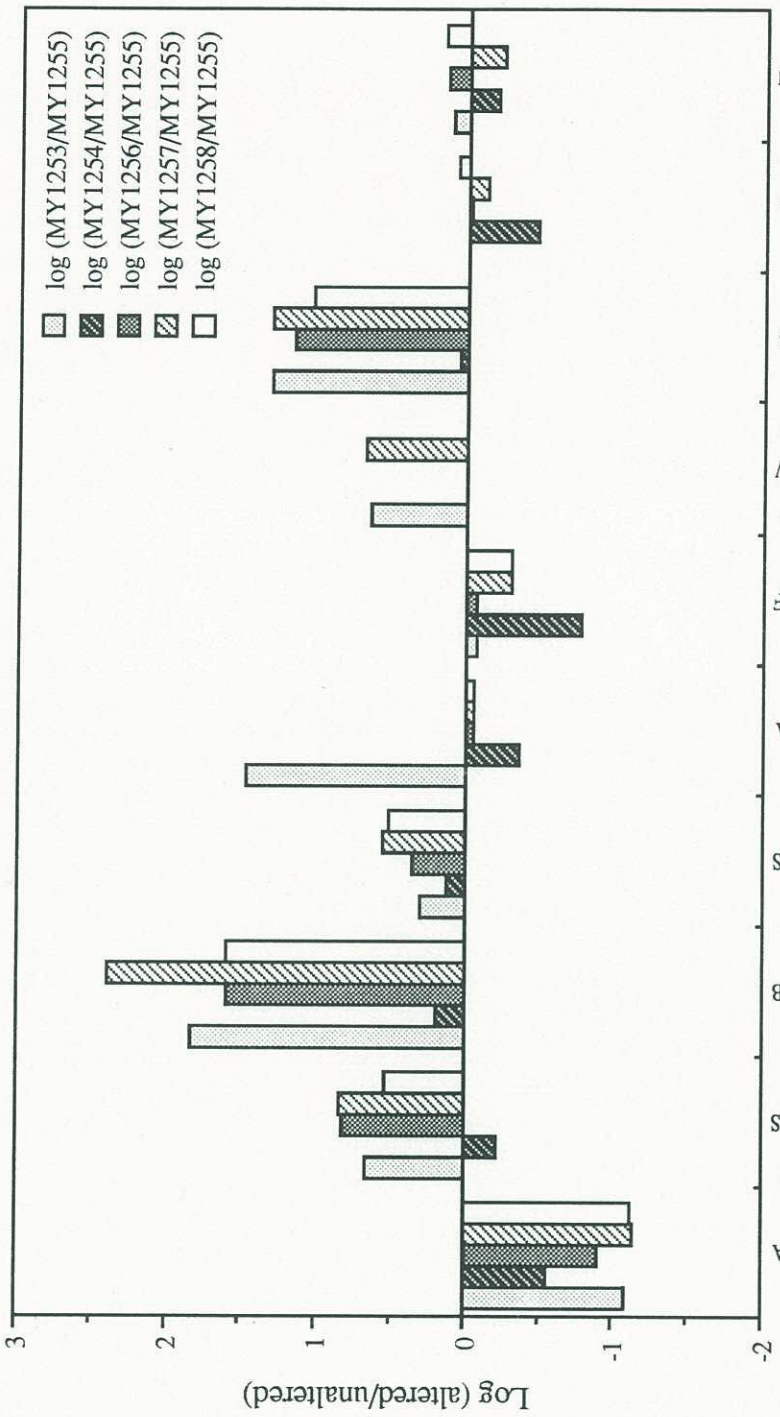

Figure 51. Bar chart illustrating elemental changes during hydrothermal alteration. The ordinate is log10 of the weight ratio (conc. in altered rock/conc. in unaltered rock).

inclusions suggests that they were deposited at relatively low (~100° C) temperatures probably in a shallow, hot-spring system (Roedder, 1984; Bodnar et al., 1985).

CHAPTER 6

PETROGENESIS

6.1 Introduction

It has been speculated that a mid-Miocene volcanic field in the central Mojave Desert with eruptive products similar to the ECVF was generated by a stratovolcano and is part of a northwest-trending, Miocene volcanic belt (Glazner, 1986). The location of the ECVF and other Mojave Desert volcanic fields inboard of the North American craton margin suggests that the ECVF stratovolcano, and presumably other stratovolcanos to the southeast, may be part of Miocene volcanic arc.

The ECVF is dominated by andesitic-dacitic tuffs and flows. Andesitic-dacitic rocks of the western United States are typically associated with subduction while "fundamentally basaltic" rocks, including bimodal, basaltic-rhyolitic volcanic fields, are associated with extensional tectonics (McKee, 1971; Christiansen and Lipman, 1972). The spatial relationship between the ECVF and other volcanic fields to the southeast with the former subduction zone on the western margin of the North American plate suggests that these fields probably were part of a volcanic arc related to subduction. The formation of the ECVF, however, was contemporaneous with the subduction-transform fault transition that occurred along the Pacific-North American plate margin (Atwater, 1970). Consequently, the apparent timing of volcanism in the ECVF defies simple tectonic categorization.

Field relations and petrographic characteristics from selected flows and tuffs from

the ECVF additionally indicate that the ECVF was probably generated from a heterogeneous source region. Many of the flows display disequilibrium characteristics suggestive of having originated from a hybrid magma. Similar features identified in other mid-Miocene volcanic rocks in the Mojave Desert have also been attributed to hybridization (Glazner, 1990).

Geochemical data from selected flows of the ECVF were used to evaluate several processes that may have generated hybrid magmas including crystal-liquid fractionation, mixing of dissimilar magmas, and combined mixing-fractionation. Units selected for evaluation were chosen from areas where, in the complexly interlayered and eroded ECVF, their relative stratigraphic positions were well constrained and adequate geochemical and petrographic information were available.

6.2 Characteristics of Selected Flows

Field relations and petrographic evidence indicating the formation of hybrid magmas in the ECVF include: 1) the contemporaneous eruption of bimodal magmas, 2) quartz xenocrysts in olivine-bearing andesites, 3) sieve-textured, glass-filled zones in sodic plagioclases mantled by clear rims of calcic plagioclase, 4) apparent basaltic inclusions in andesitic-dacitic flows, 5) partially assimilated granitic clots in andesitic-dacitic flows and 6) oscillatory-zoned plagioclase phenocrysts with normal and reverse zonation (Table 6).

Although disequilibrium textures and equivocal stratigraphic relationships, such as the interlayering of bimodal volcanic flows, were identified throughout the ECVF, the flows selected to evaluate petrogenetic models are from the Myrick Spring area (Plate 2). They were selected because stratigraphic control from the Myrick Spring area indicates that units are temporally and spatially related. The Myrick Spring area also has the only

Table 6. Summary of field and petrographic characteristics

Characteristics	Sample/location
Altered, basaltic andesitic lenses/flows interlayered within silicic tuff sequences.	1126/Plate 2; Fig. 11d
Acicular plagioclase+mafic mineral (hornblende?) in a basaltic(?), lens-like, rapidly-chilled inclusion within an andesitic flow.	1074/Plate 2; Fig. 52
Sieve-textured sodic-plagioclase phenocrysts mantled by calcic-plagioclase; wide range of An contents compositionally distinguish plagioclases.	1090,1015, 1078/Plate 2; Figs. 12a, 13c,d, 14a, 22a
Oscillatory zoned (normal and reverse) plagioclases phenocrysts with sieve-textured cores.	1232; Plate 1
Highly resorbed quartz xenocrysts in andesitic flows.	1215/Plate 3
Altered granitic clasts in tuff sequences.	Fig. 14c; Plate 2
Glomerophyric, partially resorbed granitic inclusions within andesitic-rhyodacitic flows.	1127/Plate 2; Fig. 12d

Figure 52 Captions

Figure 52. Acicular plagioclase forming spinifiex textures in a lens-like inclusion (sample 1074, Plate 2) of mafic (basaltic ?) rocks within an andesitic-dacitic host flow.

Figure 52. Typical plagioclase from a mafic flow (sample 1255, Plate 2) with a fretted marginal zone. Adjacent plagioclase has a clear plagioclase rimming the fretted zone.

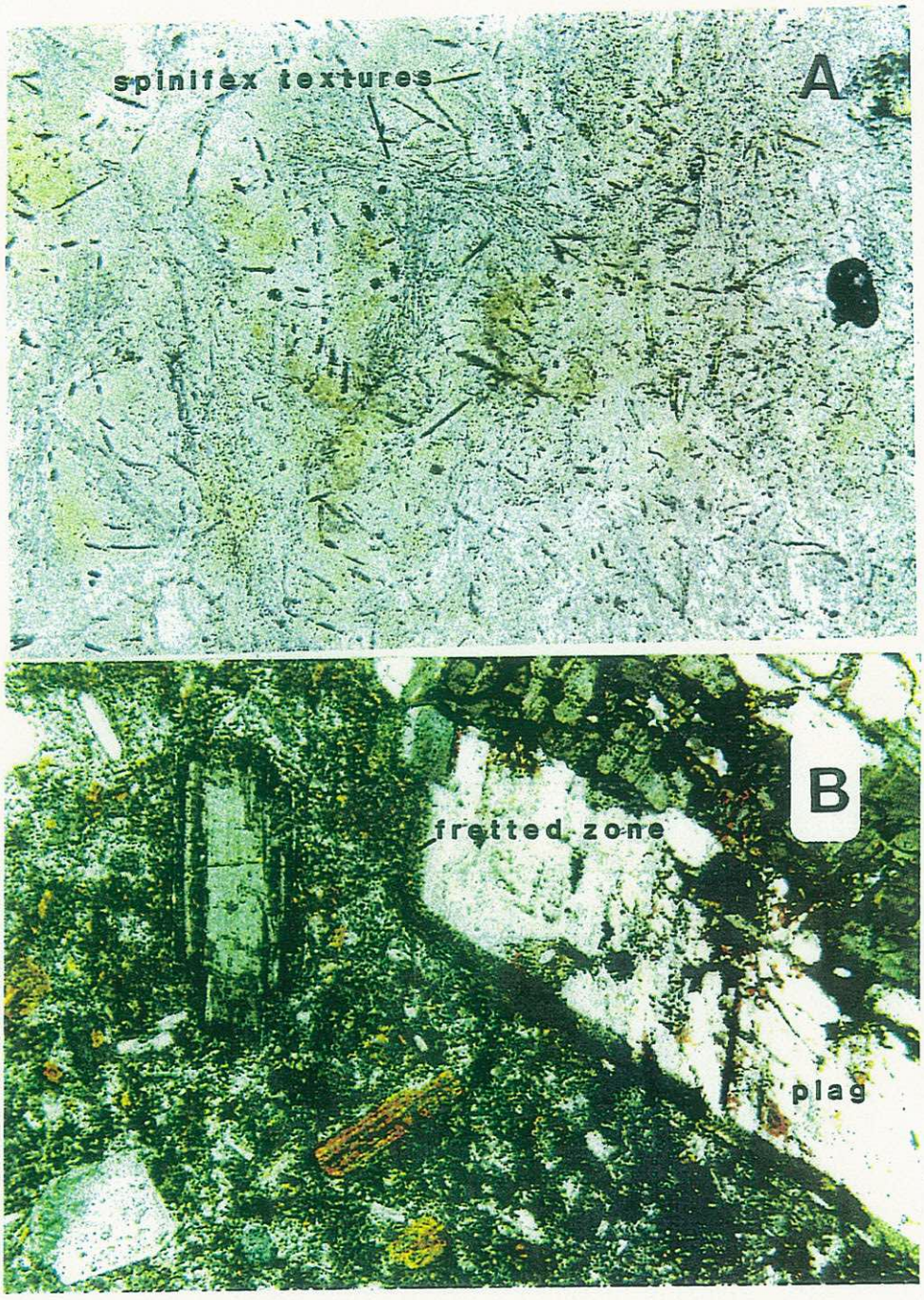
spinifex textures
A
fretted zone
B
plag

investigated outcrop of basalt. The basalt appears to be stratigraphically and, presumably, genetically related to the eruptive center that dominates the southern portion of the Myrick Spring area. Finally, the Myrick Spring area contains an excellent exposure of "bimodal" magmatism with a basaltic andesite flow interlayered among a thick sequence of tuff.

Anhydrous, normalized major and trace element data used in this evaluation are included in Table 7. Analyzed rocks from the Myrick Spring area not included in this data set are highly altered rocks and reworked tuffs. The "hybrid" rock used in this analysis is an andesite-basaltic andesite (sample 1126) that is interbedded within a thick sequence of tuffs. The end-member basaltic precursor used in this analysis is the hypabyssal basalt from the southern side of the area (sample 1133). The granite composition is from Ragland (1979). All rocks included in this discussion are described in Chapter 2. Additional rock analyses are included in Tables 2, A.1 and A.2. Samples are located on Plate 2.

6.3 Petrogenesis

Plagioclase-olivine-augite/orthopyroxene-magnetite (POAM) crystal-fractionation is considered the principal process in the development of andesitic flows (Gill, 1981). Crystal fractionation was evaluated as a process that could have generated intermediate composition, hybrid flows at the Myrick Spring area. Although the thick sequence of high-silica, rhyolitic tuffs toward the southeastern side of Myrick Spring (Plate 2) could have been tapped from a high-silica zone in a stratified magma chamber (Hildreth, 1981), it is not clear how crystal-fractionation within this chamber would yield a basaltic andesite flow interlayered among the sequence of rhyolitic tuffs. Crystal-fractionation also does not explain why disequilibrium textures were generated in the basaltic andesite and other intermediate flows in the region. Finally magnetite fractionation is required to generate a

Table 7. Water-free, normalized major and trace element analyses of flows from the Myrick Spring area.[1].

Rock type	basalt	ba	ba	and	and	and	and	dacite	dacite	dacite	aph rhy	aph rhy	granite[2]
Map ID	Mb	Mba	Mba	Ma[5]	Ma[3]	Ma[2]	Ma[3]	Md	Md	Md	Mar	Mar	Kg
Field ID	1133	1126	1018	1099	1034	1015	1079	1012	1010	1024A	1057	1093	
wt %													
SiO_2	50.9	57.6	60.4	59.5	63.2	65.3	65.0	64.8	68.4	69.2	75.4	77.3	71.9
Al_2O_3	16.6	17.2	16.2	16.5	17.1	17.4	16.7	16.1	15.1	15.4	12.8	12.2	14.4
CaO	10.0	8.59	6.63	5.03	4.98	4.58	4.03	4.41	3.20	3.29	1.09	0.70	1.86
MgO	6.67	1.91	3.45	1.06	2.15	1.47	1.09	0.68	0.53	0.45	0.21	0.10	0.72
Na_2O	3.17	3.67	3.72	4.35	4.24	4.15	4.24	4.33	4.15	3.29	4.20	4.32	3.71
K_2O	0.63	1.94	1.39	2.40	2.45	2.65	3.28	2.94	2.71	2.88	3.60	3.82	4.11
FeO^T	10.2	7.22	6.64	9.27	4.72	3.60	4.61	5.47	4.84	3.82	2.36	1.34	2.75
MnO	0.15	0.13	0.14	0.11	0.09	0.06	0.08	0.06	0.03	0.05	0.04	0.06	0.05
TiO_2	1.42	1.53	1.25	1.24	0.90	0.72	0.78	0.91	0.80	0.71	0.21	0.11	0.31
P_2O_5	0.16	0.24	0.22	0.57	0.22	0.17	0.20	0.23	0.20	0.21	0.12	0.04	0.12
ppm													
Cr	134	132	135	<10	<10	<10	46	<10	13	<10	<10	<10	....[3]
Rb	19	112	86	72	97	128	109	74	80	87	111	132	....
Sr	303	520	463	400	580	610	400	416	419	429	170	84	....
Y	35	18	24	36	13	10	33	27	38	35	39	64	....
Zr	115	174	182	328	203	219	242	228	261	234	264	241	....
Nb	<10	18	22	24	38	18	33	26	13	<10	19	11	....
Ba	196	437	586	834	884	943	849	943	996	906	1220	1235	....

[1] Abbreviations: and = andesite; ba = basaltic andesite; aph rhy = aphyric rhyolite; sums may not equal 100% because of rounding

[2] Composition from Ragland (1979)

[3] No value reported.

reasonable fit using major element data to calculate a hybrid basaltic andesite composition derived from crystal-fractionation of a basaltic precursor (sample 1126). Magnetite and/or titanomagnetite only constitute a minor portion of all unaltered flows from the ECVF.

End-member mixing of dissimilar magmas was also evaluated as a process that may have generated hybrid magmas in the ECVF. Hybridization would explain observed disequilibrium textures as well as the contemporaneous eruption of intermediate and high-silica magmas. Mixing of dissimilar magmas was believed to have generated volcanic sequences similar to those in the ECVF at the Gardiner River basalt-rhyolite complex, Wyoming, the Medicine Lake volcano, California, and in Tertiary volcanic rocks of the Lake Mead field, Nevada and Arizona (Wilcox, 1979; Gerlach and Grove, 1982; Smith et al., 1990).

Using major element data, the mixing of end-member granitic and basaltic (sample 1133; Plate 2) melts yields an intermediate composition similar to the hybrid, basaltic andesite (sample 1126). Linear, least squares mass-balance equations were solved for the major element data using XLFRAC (Stormer and Nicholls, 1978). The sums of the squares of the residuals (compositional difference between the observed and the calculated composition for each major oxide), which represents how well the data constrain the model, typically exceeded 2.0. Although mixing of granitic and basaltic melts forms a basaltic andesite composition, the residuals indicate that the evaluated end-member components in this model do not form the observed hybrid flow.

Magma mixing was also evaluated using trace element data. If mixing took place, trace element ratio-ratio plots will describe an hyperbolic curve (Langmuir and others, 1978). The asymptotic ends of the hyperbolic curve should approximate the elemental ratios of the mixed end-members. Companion diagrams with ratios of the denominators

plotted against one of the original ratios will describe a straight line. According to Langmuir and others (1978), each sample should additionally retain its relative position with respect to adjacent samples on these plots regardless of which element ratios are used. The trace elements Sr, Ba, Y and Nb from unaltered flows in the Myrick Spring area were used to evaluate magma mixing (Table 6).

Mixing calculations performed with trace element data demonstrate that mixing probably occurred. Plotted samples approximately describe an hyperbolic mixing curve on a Y/Nb-Sr/Ba plot (Fig. 53). Companion diagrams also roughly describe a straight line. Data scatter may indicate that other processes such as fractional crystallization were involved in the generation of these flows. Although it was assumed that mixing of basaltic and granitic melts generated the hybrid assemblage, basalt (sample 1133) does not correlate well with other data on the Y/Nb-Sr/Ba or the Y/Nb-Ba/Nb plots. Based on the asymptotes, the mafic end-member should have Y/Nb ratio of approximately 1.0 while the silicic end-member should have a Sr/Ba ratio of approximately 0.25. The hypothesized basaltic end-member does not conform with the Y/Nb ratio. This could be explained in several different ways including excess Y in the analyzed basalt, basalt sample 1133 not being part of the mixing process or mixing not being the sole process involved in the evolution of this suite of rocks.

Observed disequilibrium features in flows from the Myrick Spring area and other flows from the ECVF could also be the result of other mixing and/or assimilation processes. Sieve-textured, sodic plagioclase anhedra and oscillatory-zoned plagioclase euhedra have calcium-rich plagioclase overgrowths. These features could be the product of the interaction of basaltic and rhyolitic melts. Injection of a basaltic melt into a rhyolitic melt would result in mixing of broken basalt globules and rhyolitic magma at the basalt-

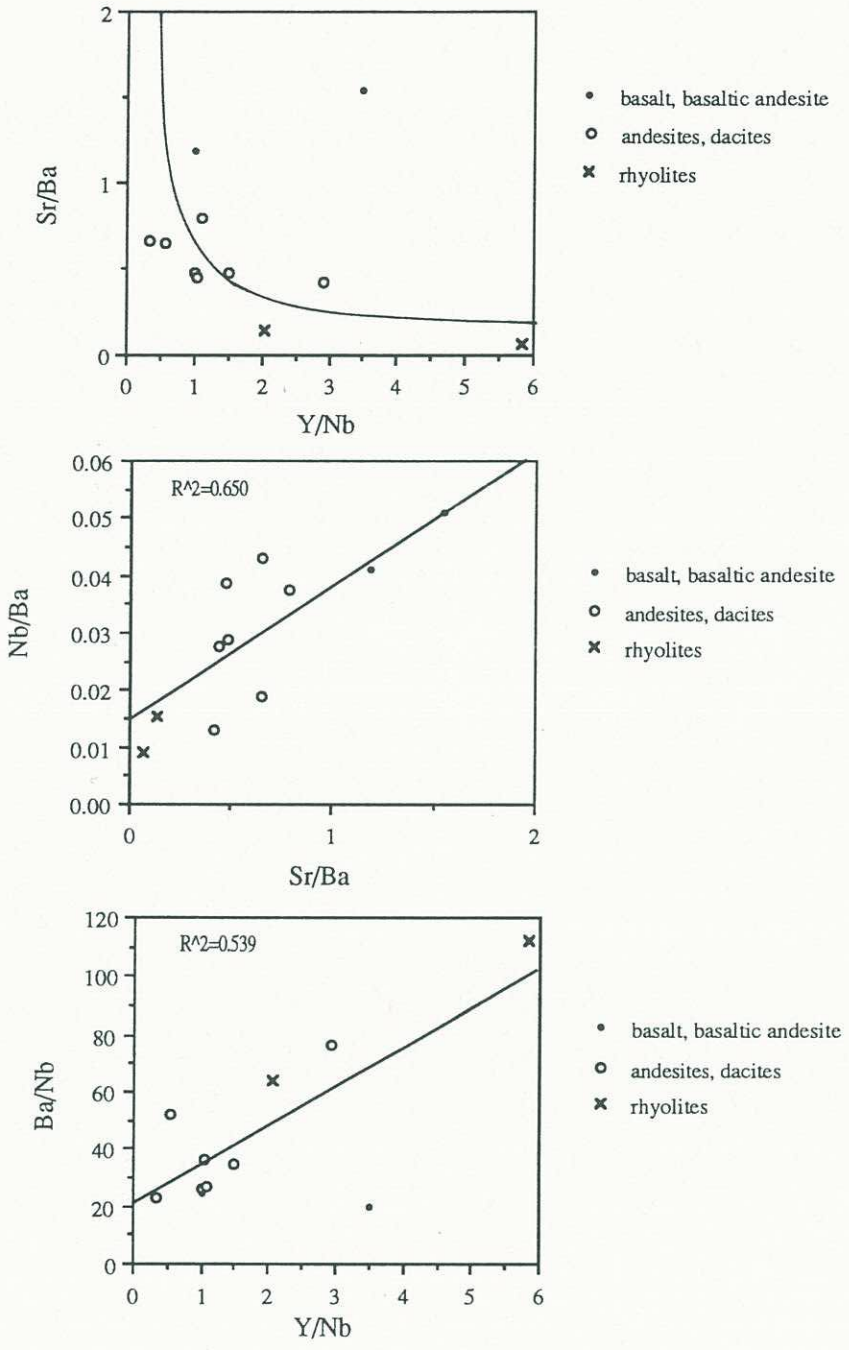

Figure 53. Y, Nb, Sr and Ba mixing curves. Data from selected samples from Myrick Spring area.

rhyolite interface (Eichelberger, 1975). Depending on the relative volume, temperature and composition of the interacting basaltic and rhyolitic magmas, rhyolite-derived sodium-feldspar phenocrysts would be partially melted. Renewed crystallization may result in overgrowths on these resorbed phenocrysts by a basalt-derived, calcic plagioclase. Cross-cutting relations and age determinations reveal, however, that such a mix could not have occurred in the ECVF because all rhyolitic flows are younger than hybrid andesitic flows.

The last petrogenetic model evaluated combines mixing and fractional crystallization (MFC). MFC processes have been attributed to the formation of mid-Miocene hybrid flows in the central Mojave Desert (Glazner, 1990). Previously described field relations and geochemical evidence indicates that both processes may have operated in the evolution of ECVF magmas.

Modal olivine concentrations in ECVF rocks range from approximately 3% in basalt (sample 1133) to much less than 1% in andesitic flows. Normative olivine is only found in basalt sample 1133 (Table A.2). An inflection point at about 58 wt. % SiO_2 on the MgO-SiO_2 plot could be due to olivine fractionating out of the basaltic melt (Fig. 54). The fractionation of clinopyroxene±orthopyroxene from intermediate composition magmas may be the reason for decreased modal cpx±opx (Table A.2); however, the fractionation of these minerals is not clearly reflected in the Harker variation diagrams. With the exception of Al_2O_3, Harker variation diagrams for the other major elements define linear trends suggestive of mixing (Fig. 54). Best-fit lines for CaO, FeO^T and K_2O have an R^2 greater than 0.8, indicate a linear trend. All of these trends pass through or near rhyolite, granite and basalt compositions. It has been speculated that the inflection point at 65 wt % SiO_2 on the Al_2O_3 plot may be due to the vector-addition effect of olivine subtraction coupled with silicic crustal material addition (Glazner, 1990). Additionally, crystal fractionation above

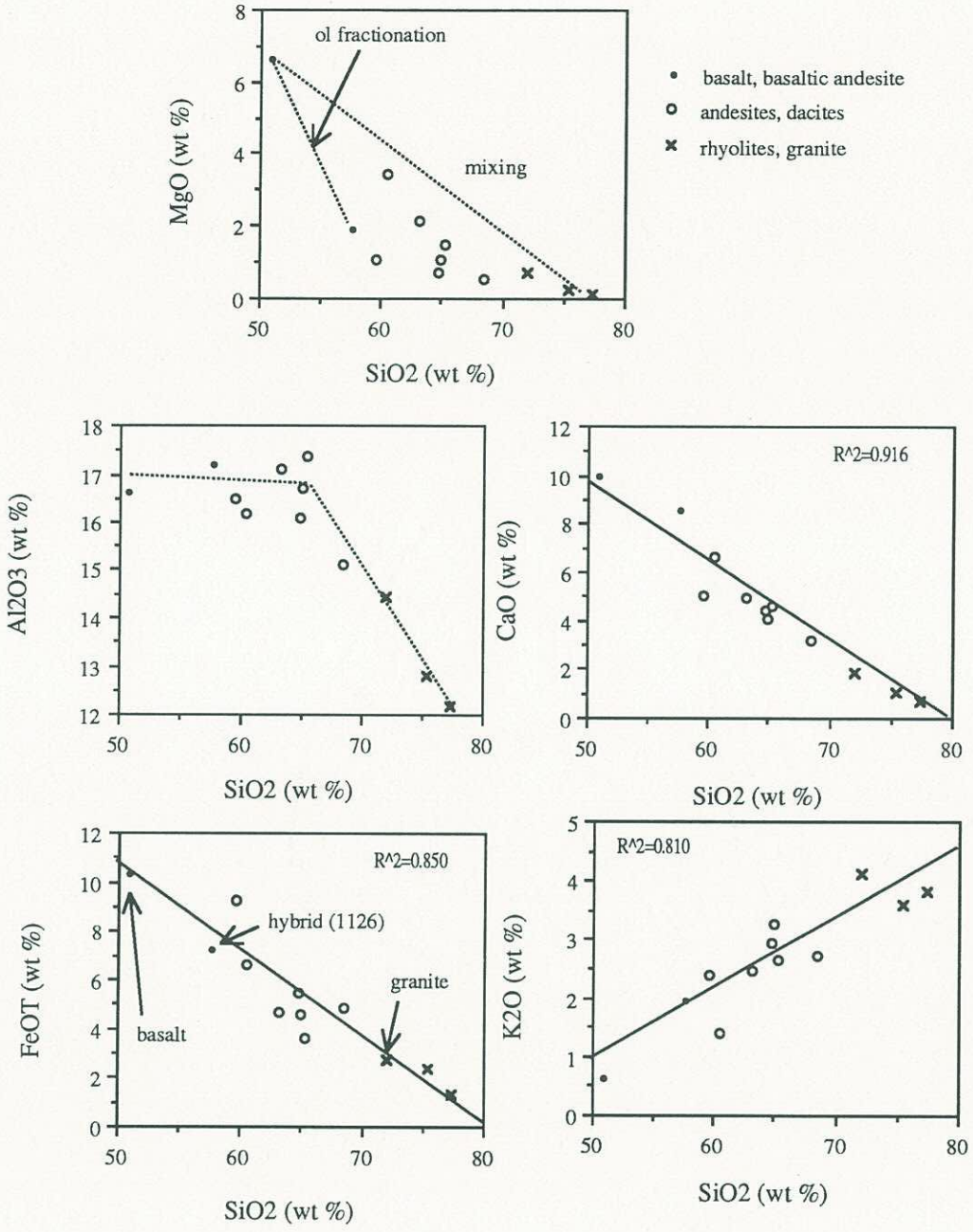

Figure 54. Harker variation diagrams for selected samples from Myrick Spring area.

this inflection probably did not occur because dense ferromagnesian minerals are absent and increased viscosities in the higher silica melts inhibit fractionation (Glazner, 1990).

Mixing-fractional crystallization calculations applied to the previously used end-member basalt and granite compositions yields a calculated composition similar to the daughter or hybrid product (Table 8). The major chemical differences are in FeO^T, K_2O, Al_2O_3 and TiO_2. These differences could be due to compositions used in the model that are not representative of the actual end-members, poorly estimated granite and olivine compositions and/or a poorly-constrained model.

6.4 Discussion

Field relations and disequilibrium textures in tuffs and flows from the ECVF suggest a complex evolution of magmas during the mid-Miocene. Processes that generated many of the examined flows probably included fractional crystallization and magma mixing. Additionally, previously described glomerophyric "clots" of granitic material found in intermediate composition flows and crystalline clasts in basal portions of tuff from the Myrick Spring area indicate that basement granitoids were incorporated in the pyroclastic eruptions and may have been assimilated in many of the hybrid magmas.

Major element and trace element trends suggest that intermediate composition flows may be the product of magma mixing. Additionally fractionation of some minerals may have also taken place during the evolution of magmas. Field interpretations and compositional data suggest that a tholeiitic basaltic melt(s), similar to that spatially associated with the pyroclastic eruptive center at Myrick Spring, may have interacted with a silicic melt to generate the hybrid basaltic andesite-andesitic flows. A good candidate for mixing and/or assimilation with a basaltic melt are the partial melts of the granitic basement

Table 8. Mixing-fractional crystallization model[1] (MFC)

Oxide	Basalt	Granite	Olivine	Observed	Calculated	Residual
SiO_2	50.91	71.94	38.34	57.63	57.72	-0.05
TiO_2	1.42	0.31	----	1.53	1.25	0.28
Al_2O_3	16.64	14.43	----	17.21	17.54	-0.33
FeOT	10.22	2.75	24.40	7.14	6.79	0.35
MgO	6.67	0.72	37.26	1.91	2.13	-0.22
MnO	0.15	0.05	----	0.13	0.14	-0.01
CaO	10.02	1.86	----	8.59	8.68	-0.09
Na_2O	3.17	3.71	----	3.67	3.61	0.06
K_2O	0.63	4.11	----	1.94	1.65	0.29
P_2O_5	0.16	0.12	----	0.24	0.16	0.08
coefficient	0.815	0.276	-0.094			

[1] Olivine composition based on average, Mojave Desert olivine (Glazner, 1990); granite composition from Ragland (1989)

Daughter observed (basaltic andesite, 1126) = 0.815 Parent basalt (1133) + 0.276 Parent granite - 0.094 Mojave olivine.

Sum of square of residuals = 0.463

of the northern Mojave Desert. Generation of basaltic andesites, andesites and perhaps all of the andesitic-dacitic flows and tuffs in the region may have been due to basalt-granitoid crust interaction.

Interlayering of intermediate flows and rhyolitic tuff, such as in the Myrick Spring area, suggests that these bimodal magmas were coeval. Mafic flows spatially associated with this vent facies, rhyolitic tuff at Myrick Spring could also be evidence of an eruptive triggering mechanism. Wiebe (1993) suggests that enough evidence exists to conclude that many large accumulations of silicic volcanic rocks erupted from long-lived silicic magma chambers that were repeatedly injected by basaltic magma. Pallister et al. (1992) indicate that products of many calc-alkaline volcanos, such as Pinatubo volcano in the Philipines, show evidence for mixing of basaltic and acidic melts. The authors further state that the injection of a basaltic magma may have actually triggered recent eruptions at Pinatubo.

Hybrid volcanic rocks and bimodal volcanism, described in other volcanic fields in the western United States, have been attributed to multiple processes including fractional crystallization and magma mixing (Christiansen and Lipman, 1972; Eichelberger, 1978; Glazner, 1986; Glazner and O'Neil, 1989; Smith et al., 1990; Stimac and Pearce, 1992; White, 1992). The combination of bimodal, basaltic andesite-andesitic flows interlayered within thick rhyolitic tuff sequences and disequilibrium textures observed in intermediate flows throughout the ECVF suggests that magma mixing and/or assimilation of crustal material was an important process in the generation of flows in the ECVF. The combination of field, petrographic and geochemical information suggests that these processes were operating during the evolution of the ECVF magmas. By analogy, active volcanism in the Cascades Range or dacitic volcanism of the southwestern Pacific Ocean region may be close approximations to the ECVF in terms of eruptive products and style.

CHAPTER 7
CONCLUSION

The central portion of the South Ranges of the China Lake NAWS is underlain by a Middle Miocene volcanic field herein called the Eagle Crags Volcanic Field. It is primarily comprised of dikes, flows, pyroclastic rocks, fissure vents and hypabyssal intrusions ranging compositionally from tholeiitic basalt to high-silica rhyolite. The remainder of the region is underlain by Cretaceous granitoids, Paleozoic metamorphic rocks and Quaternary alluvium.

The central portion of the ECVF is dominated by rhyodacitic flow domes within a caldera. Direct evidence of the caldera includes an arcuate fault scarp with over 700 m of local relief. Tables 9 and 10 list features typically found in a caldera environment and those found in the ECVF. Many calc-alkaline and alkaline caldera complexes have similar features to this greater than 400 km^2 region (Table 11). Gently south-southwest-dipping sheet-like flows and pyroclastic rocks up to 100 m thick are exposed in the fault scarp and become thinner to the south. A steeply-dipping half-graben to the northeast is separated from the scarp by a wide, horseshoe-shaped alluvial valley. The paleoflow direction of flows and pyroclastic rocks in the region, the occurrence of flows domes within the syncollapse valley, and the vent-proximal facies of the rocks exposed in the fault scarp suggest that the middle of this region was probably the site of the central, stratovolcano vent.

Volcanic stratigraphy in the Myrick Spring area is correlative with that from the

Table 9. Criteria for Identifying Caldera Complexes[1]

•Large volumes of intermediate to silicic pyroclastic rocks and flows or large volume ash flow eruptions ± cogenetic intermediate to silicic intrusions.
•Structural boundaries of the caldera such as ring faults or arcuate fault scarps that partially describe a circular ring fault system. Faults are high angle normal unless they have been denuded or partially scalloped by erosion or destroyed by subsequent tectonism.
•Low volume pyroclastic eruptions may result in incomplete hinged caldera subsidences or structural sags.
•Subequal amounts of outflow and intracaldera tuff/lava volumes. Outflow and intraflow volcanic material may be differentiated by types or amounts of lithic clasts in pyroclastic materials or alteration.
•Large intrusions related to post-collapse resurgence or volcanism reflecting renewed magmatic pressures. This may be manifest through central doming of the caldera floor or broad magmatic uplift of volcanic fields and/or an anomalously low regional gravity reading or negative Bouguer gravity anomalies reflecting shallow intrusion (this may not be directly underneath margin or caldera but is commonly associated with caldera complexes).
•Late synvolcanic or post-caldera collapse hydrothermal alteration and/or mineralization may be spatially associated with calderas. Although they may not necessarily be associated with caldera-related structures such as ring fractures, the caldera plumbing probably provided synvolcanic or later hydrothermal fluid pathways. Typically such caldera-related deposits in the western United States have experienced varying levels of supergene oxidation which may mask structural controlled alteration.
•Arcuate drainage(s) describing ring structure or internal drainage pattern due to ring-related, topographic scarp.

[1] Modified after Williams and McBirney, 1979; Lipman, 1984; Sillitoe and Bonham, 1984; Heald et al., 1986; Cas and Wright, 1988; Johnson, 1991. Data/observations biased toward large (rhyolitic) ignimbrite calderas such as in the San Juan volcanic field, Colorado, or Basin and Range calderas.

Table 10. Stratovolcano Caldera-Related Features of the Eagle Crags Volcanic Field.

•Distinct, arcuate-shaped fault scarp with up to 700 m of offset.
•A regional Bouguer gravity low centered on the western-southwestern margin of field area and spatially associated with young, silicic domes.
•Thick, unwelded rhyolite ash flows and lapilli-flows overlain by subsequent, cogenetic lavas; the largest exposed rock exceed 100 m thickness.
•At least 10 km^3 of cogenetic flows, tuffs and volcaniclastic breccias including lahars and debris flows (over 100 sq. km. of pyroclastic rocks, volcaniclastic breccias, and flows; calculated with a conservatively estimated minimum thickness of 100 m).
•Multiple fissure vents and rhyolitic feeder dikes that appear to radiate from the center of the volcanic field; vertical rhyolitic feeders crosscut a granitic rock and mark the southern margin (structural rim) of an hypothetical western caldera (e.g. near vertical dikes crosscut flows in the caldera wall of Ceboruco volcano, Mexico according to Cas and Wright, 1988).
•Syn- or post-volcanic (possibly syncollapse?) hydrothermal alteration controlled by same fracture system (northwest and northeast) that controlled location of some vents; includes Hg+As+Sb+W±Au±Ag±Pb.

TABLE 11. Characteristics and names of a few alkaline to calc-alkaline caldera-associated volcanoes and volcanic districts of the world[1]

Class	Basal diameter	Height (m)	Average volume (km^3)	Examples
1. Calc-alkaline w/ sector collapse scar	11-30	1020-2700	1.2-4.5	Mt. St. Helens, Lassen Peak
2. Calc-alkaline w/ caldera	7.5-68.5	500-3350	1.75-11	Aniakchat
3.Calc-alkaline w/ caldera, more silica and more pyroclastics than #2.	8-59	200-1700	2.2-18	Crater Lake, Krakatau
4. Alkaline w/ caldera.	6.5-87	350-4700	0.75-9	Tambora
5. Alkaline w/ caldera, more silica and more pyroclastics than #4.	7.5-64.5	100-1250	1.8-18.5	Vesuvius, Pantelleria

[1] After Pike and Clow (1981).

Eagle Crags area. Disconformably overlying a granitoid basement are basaltic andesitic-andesitic flows. Angular unconformities separating these flows from overlying, flat-lying to gently north-dipping tuffs may indicate that the early, intermediate composition flows were either structurally deformed and/or that they formed paleovalleys for subsequent pyroclastic deposits.

Three thick sequences of tuff separated by flows and volcaniclastic breccias indicate that the region experienced at least three extended periods of pyroclastic eruptions immediately followed by lahars and/or lava. An apparent, pyroclastic eruptive center is located in the Myrick Spring area. Individual pyroclastic eruptions within this greater than 100 m thick exposure are marked by lag breccias that grade upward into thick, unwelded tuff. Several such successions within this thick pyroclastic sequence indicates that there were multiple pyroclastic eruptions before an outpouring of lava. A 2-3 m thick, fine-grained, pyroclastic surge deposit, only identified within this thick succession of pyroclastic material, also suggests that this is an eruptive center.

West-northwest-trending rhyolitic feeder dikes and associated flat-lying rhyolitic flows are restricted to the Blue Chalcedony area. Feeder vents intrude intermediate composition tuffs and flows and a Cretaceous granodioritic stock. Hypabyssal intrusions of rhyolite in the area are interpreted to be central, rhyolitic flow vents. Rhyolitic tuffs preceded rhyolitic flows and drape over a basal andesitic flow (Ma^5) similar to a basal andesite described at the Myrick Spring area. Geochronology indicates that rhyolitic magmatism commenced at approximately 18.75 Ma.

The abrupt termination of rhyolitic feeder dikes and all associated rhyolitic flows along a northeast-trending lineament suggests that rhyolitic volcanism may be related to a poorly understood period of regional tectonism. This northeast-trending lineament,

subparallel to the east-northeast-trending Garlock fault, is apparent from topography and on NHAP images (Fig. 44; Plate 1). The eastern side of these dikes may have been offset to an undetermined location by strike-slip faulting or possibly, west-northwest-trending fractures and synchronous rhyolitic magmatism may have been generated during a period of north-northeast-directed extension.

Volcanic sequences of the Barstow Basin may be correlative with flows from the ECVF. Both are dominated by andesitic-dacitic rocks although no units in the Barstow Basin are described as vent facies (Burke et al., 1982). Age determinations from flows in the Barstow Basin indicate that volcanism in the ECVF may have begun as early as 21-20 Ma. Largely andesitic and dacitic volcanism of the ECVF was initially deposited on a desert pavement composed of Paleozoic metamorphic rocks and granitoids. Multiple pyroclastic eruptions followed by debris flows, lahars and lava flows ultimately formed a stratovolcano with a central vent and numerous, flanking domes. Material was fed to the surface through a series of west-northwest-trending feeder dikes.

The original magma may have been a product of melted, subducted oceanic crust and continental, lithospheric crust that was generated toward the waning stages of subduction of the Farralon Plate and the East Pacific Rise (Atwater, 1070; Fig. 55). This mafic material resided and interacted with sialic material in the middle crust (T_1, T_2). Field relations, disequilibrium textures and analyses of major and trace element concentrations in hypothesized parental and hybrid (daughter) flows from the Myrick Spring area indicate that periods of magma mixing, and possibly concommitant assimilation and fractional crystallization, took place during the evolution of the ECVF magmas. Periodic extensional tectonism in the Mojave Desert, possibly related to oblique shear translated from the San Andreas fault system which became active after cessation of subduction, created a thinning

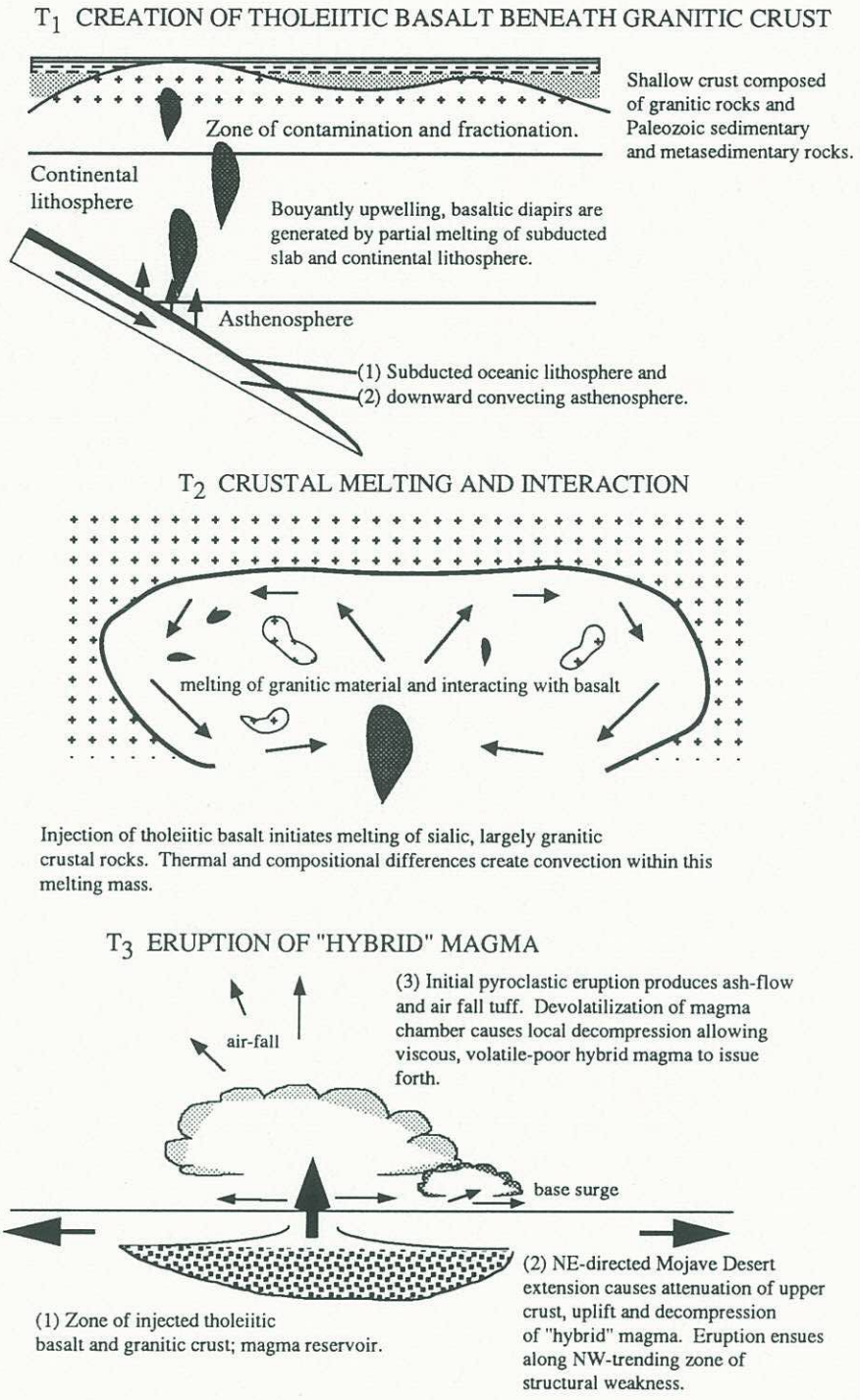

Figure 55. Illustrations depicting how "hybrid" intermediate and silicic rocks and high-silica rhyolites may have formed through time in the northern Mojave Desert.

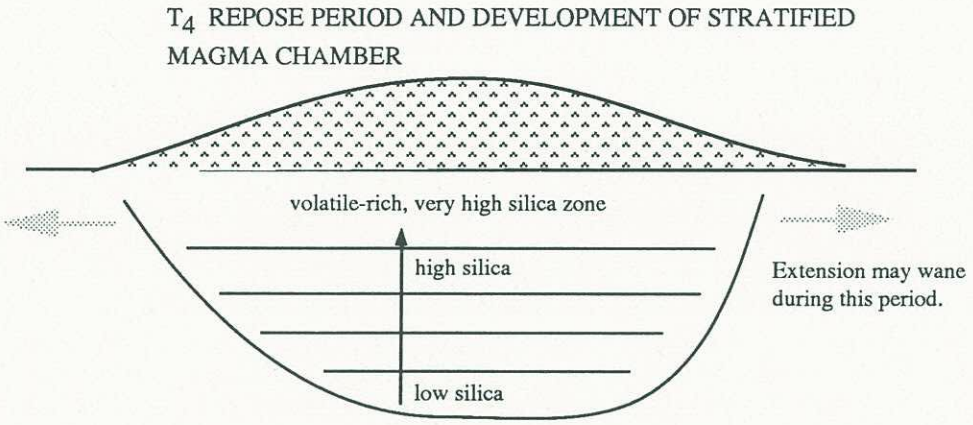

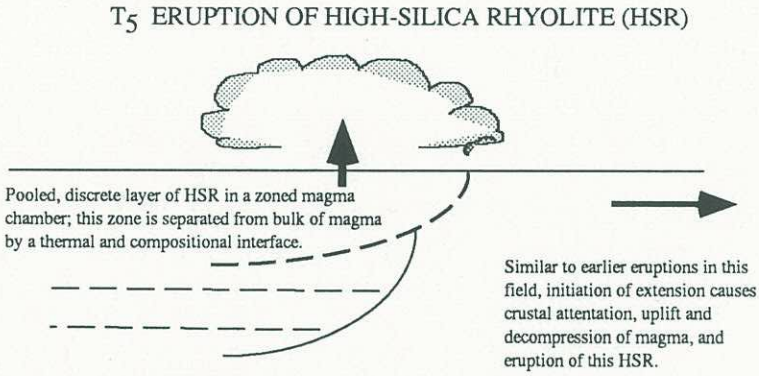

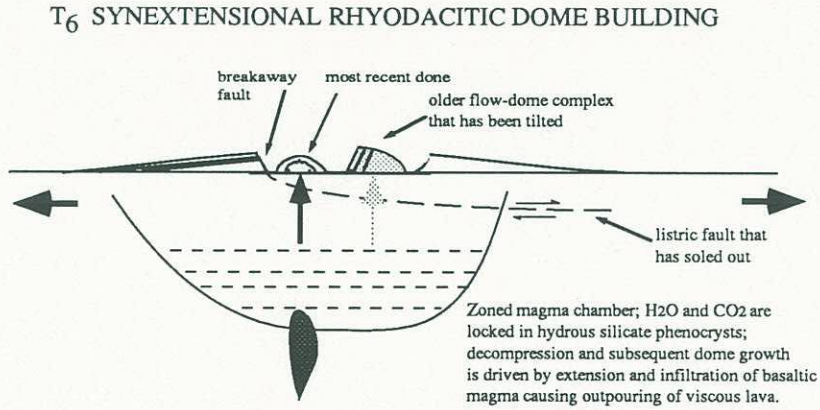

Figure 55. (continued)

of the upper crust and allowed melts to buoyantly rise to the surface (T_3).

During a hiatus in the construction of the andesitic-dacitic stratovolcano, a discrete high-silica zone formed at the top of this evolving magma (T_4). Eruption of rhyolite along the flanks of this dome occurred at about 18.5 Ma (T_5). In fact, throughout eastern California and western Arizona, many rhyolitic flows and tuffs such as the regionally extensive Peach Springs Formation were deposited at about 18.5 Ma (Glazner et al., 1986).

After one of the last major eruptions, a portion of the stratocone collapsed, followed by the slow growth of rhyodacitic domes. Synchronous with dome growth was a period of northeast-directed extension (T_6). Extension not only facilitated decompression and the subsequent eruption of a highly viscous magma but may have also facilitated caldera collapse. The high-angle normal fault that was the structural rim of the caldera evolved into a low-angle fault along which extension, and development of half-grabens took place. Because age determinations reveal that one of the steeply-dipping rhyodacites is about 12.4 m.y. old, then this extensional period lasted through the Late Miocene. Truncation of the 18.35 Ma rhyolitic feeder dikes by a northeast-trending lineament may indicate that this same extensional period could have begun in the Mid-Miocene. Although movement along the Garlock fault was believed have begun at about 10 Ma, the subparallel nature of this lineament to the Garlock fault and the apparent northeast-directed movement on the north side of this feature suggests that the lineament may be a right-lateral fault, possibly related to early movement along the Garlock fault.

A northeast-trending fracture transects the Myrick Spring area. Along this N45E trend are thin breccia zones within dacitic flows, a highly siliceous and calcareous zone of alteration ("silica dike") and an abrupt, northeast-trending break in topography. Two

north-northeast-trending, high-angle faults at the Eagle Crags area, north-northeast-trending, silicified and argillized fractures south of the Myrick Spring area and northeast-trending lineaments identified on NHAP images suggests these faults were post-volcanism and controlled the flow of post-volcanism, hydrothermal fluids.

One of the more highly altered areas in the volcanic field contains anomalously high concentrations of Hg, As and Sb. Propylitized and argillized zones are controlled by northeast and northwest fractures. Anomalously high concentrations of Hg are also found within a northwest-trending, breccia about 5 km to the north. Most likely, the flow of post-volcanism, hydrothermal solutions was channeled by northeast- and northwest-trending fractures. These fractures were a relic of volcanism and extensional tectonsim in the region.

The relationship between these hydrothermally altered areas , Au-Ag-Pb-Mn mineralization such as at the Chuckawalla mine and ephemeral hot-springs in the region is not clear. Although the genetic link between hot-springs, epithermal mineralization and geothermal resources has been demonstrated elsewhere (White, 1974; White, 1981; Fournier, 1983; Henley and Ellis, 1983; Hayba et al., 1985; Hedenquist and Henley, 1985; Henley, 1985; Nelson and Giles, 1985), no temporal relationship between alteration and hot-springs in the region has yet to be demonstrated. Hydrothermal alteration, local concentrations of Hg, Sb, As and Au, ephemeral hot-springs, a large regional Bouguer gravity low centered in the volcanic field and steam generation at Red Mountain all contribute to speculation that at least one hot-spring system was active in the region and the same system or a later system may still be active.

REFERENCES CITED

Atwater, T., 1970, Implications of plate tectonics for the Cenozoic tectonic evolution of North America: Geological Society of America Bulletin, no. 81, p. 3513-3536.

Austin, C.F., Danti, K., Neffew, J. and Whelan, J.A., 1979, Mineral resource evaluation of the Mojave B ranges: Naval Weapons Center Technical Memorandum, no. 5336, 179 p.

Austin, C.F., Durbin, W.F., AtienzaMoore, T., Featherstone, G., Bjornstad, S.C. and Roquemore, J.C., 1983b, Mineral deposits and mineral potential of the Randsburg Wash Test Range: Naval Weapons Center Technical Publication, no. 6465, 88 p.

Bartley, J.M., Glazner, A.F. and Schermer, E.R., 1989, North-south contraction of the Mojave block and strike-slip tectonics in southern California: Tectonics, v. 9.

Bassett, A.M. and Kupfer, D.H., 1964, A geologic reconnaissance in the southern Mojave Desert, California: Special Report, California Division of Mines, v. 83, 43 p.

Bloom, L., 1993, Man-made parameters in elemental analysis: Society for Mining, Metallurgy, and Exploration, Inc., Preprint Number 93-79, for presentation at the SME Annual Meeting, Reno, Nevada, February 15-18, 5 p.

Bodnar, R.J., Reynolds, T.J., and Keuhn, C.A., 1985, Fluid inclusion systematics in epithermal systems, in B.R. Berger and P.M. Bethke, eds., Geology and Geochemistry of Epithermal Systems: Reviews in Economic Geology, v. 2, p. 73-97.

Bonnichsen, B. and Kauffmann, D.F., 1987, Physical features of rhyolite flow flows in the Snake River plain volcanic province, southwestern Idaho, in J.H. Fink, ed., The Emplacement of Silicic Domes and Lava Flows: Geological Society of America Special Paper, no. 212, p. 119-145.

Bowen, N.L., 1928, The Evolution of the Igneous Rocks: Dover Publications, Inc., New York, 332 p.

Burbank, D.W., and Whistler, D.P., 1987, Temporally constrained tectonic relations derived from magnetostratigraphic data: Implications for the initiation of the Garlock fault, California: Geology, v. 15, p. 1172-1175.

Burchfiel, B.C., and Davis, G.A., 1980, Mojave Desert and surrounding environs, in Ernst, W.G., ed., The Geotectonic Development of California: Prentice Hall, New Jersey, p. 217-252.

Burke, D.B., Hillhouse, J.W., McKee, E.H., Miller, S.T., and Morton, J.L., 1982, Cenozoic rocks in the Barstow basin of southern California - stratigraphic relations, radiometric ages, and paleomagnetism: U.S. Geological Survey Bulletin, no. 1529-E, 16 p.

Carr, M.D., Harris, A.G., Poole, F.G., and Fleck, R.J., 1993, Stratigraphy and structure of Paleozoic outer continental-margin rocks in Pilot Knob valley, north-central Mojave Desert, California: U.S. Geological Survey Bulletin, no. 2015, 33 p.

Cas, R.A.F., and Wright, J.V., 1988, Volcanic Successions, Modern and Ancient: Unwin Hyman, Boston, 528 p.

Christiansen, R.L. and Lipman, P.W., 1972, Cenozoic volcanism and plate-tectonic evolution of the western United States. II. Late Cenozoic: Philosphical Transactions of the Royal Society of London, v. 271, p. 249-284.

Dalrymple, G.B. Alexander, E.C., Jr., Lanphere, M.A., and Kraker, G.P., 1981, Irradiation of samples for 40Ar/39Ar dating using the Geological Survey TRIGA reactor: United States Geological Survey Professional Paper, no. 1176.

Dalrymple, G.B. and Lanphere, M.A., 1969, Potassium-Argon Dating, Principles, Techniques and Applications to Geochronology: W.H. Freeman and Company, San Francisco, 258 p.

Davis, G.A. and Burchfiel, B.C., 1973, Garlock Fault: An intracontinental transform structure, southern California: Geological Society of America Bulletin, v. 84, p. 1407-1422.

Deer, W.A., Howie, R.A., and Zussman, J., 1966, An Introduction to Rock Forming Minerals: Longman Scientific and Technical, London, 528 p.

Dibblee, T.W.,Jr., 1961, Evidence of strike-slip faulting along northwest-trending faults in the Mojave Desert: U.S. Geological Survey Professional Paper, no. 424-B, p. B197-B199.

Dibblee, T.W.,Jr., 1967, Areal Geology of the Western Mojave Desert, California: United States Geological Survey Professional Paper, no. 522, 153 p.

Dibblee, T.W.,Jr., 1968, Geology of the Freemont and Opal Mountain quadrangles, California: California Division of Mines and Geology Bulletin, no. 188, 64 p.

Dokka, R.K., 1986, Patterns and modes of early Miocene crustal extension, central Mojave Desert, California, in Mayer, L., ed., Extensional Tectonics of the Southwestern United States: A Perspective on Processes and Kinematics: Geological Society of America Special Paper, no. 208, p. 75-95.

Dokka, R.K., 1990, Undocumented faults revealed in multisensor image analysis, Mojave

Desert, California, USA: Proceedings, Institution of Mining and Metallurgy, p. 27-33.

Dokka, R.K., and Travis, C.J., 1990, Role of the Eastern California Shear Zone in accomodating Pacific-North American plate motion: Geophysical Research Letters, v. 17, no. 9, p. 1323-1326.

Du Bray, E.A. and Pallister, J.S., 1991, An ash-flow caldera in cross section: ongoing field and geochemical studies of the mid-Tertiary Turkey Creek caldera, Chiricahua Mountains, SE Arizona: Journal of Geophysical Research, v. 96, no. B8, p. 13,435-13,547.

Eichelberger, J.C., 1978, Andesitic volcanism and crustal evolution: Nature, v. 275, p. 21-27.

Faure, G., 1987, Principles of Isotope Geology: John Wiley and Sons, New York, 589 p.

Fink, J.H., ed., 1987, The emplacement of silicic domes and lava flows: Geological Society of America Special Paper, no. 212, 153 p.

Fiske, R.S., Hopson, C.A., and Waters, A.C., 1963, Geology of Mount Ranier National Park, Washington: U.S. Geological Survey Professional Paper, no. 444, 93 p.

Fisher, R.V. and Schmincke, H.-U., 1984, Pyroclastic Rocks: Springer-Verlag, Berlin, West Germany, 472 p.

Fournier, R.O., 1983, Active hydrothermal systems as analogues of fossil systems. The role of heat in the development of energy and mineral sources in the northern Basin and Range province: Geothermal Resource Council Special Report, no. 13, 263 p.

Gaps, R.S., 1985, Mineral investigations of the Golden Valley Wilderness study area (BLM No. CDCA-170), San Bernardino County, California: United States Department of Interior, Bureau of Mines, MLA 1-85, 26 p.

Garfunkel, Z., 1974, Model for the Late Cenozoic tectonic history of the Mojave Desert, California, and for its relation to adjacent regions: Geological Society of America Bulletin, v. 85, p. 1931-1944.

Gerlach, D.C. and Grove, T.L., 1982, Petrology of Medicine Lake Highland volcanics: characterization of end-members of magma mixing: Contributions to Mineralogy and Petrology, v. 80, p. 147-159.

Gill, J.B., 1981, Orogenic Andesites and Plate Tectonics: Springer-Verlag, New York, 390 p.

Glazner, A.F., 1986, Stratigraphy, structure and potassic alteration of Miocene volcanic rocks in the Sleeping Beauty area, central Mojave Desert, California, in , Cenozoic Stratigraphy , Structure and Mineralization in the Mojave Desert; Guidebook and

Volume: Prepared for the 82nd Annual Meeting of the Cordilleran Section of the Geological Society of America, Los Angeles, California, March 25-28, p. 51-63.

Glazner, A.F., 1990, Recycling of continental crust in Miocene volcanic rocks from the Mojave block, southern California, in, J.L. Anderson, ed., The Nature and Origin of Cordilleran Magmatism: Memoirs of the Geological Society of America, no. 174, p. 147-168.

Glazner, A.F. and Bartley, J.M., 1991, Timing and tectonic setting of Tertiary low angle normal faulting and associated magmatism in the southwestern United States: Tectonics, v. 3, p. 385-396.

Glazner, A.F., Bartley, J.M., Caskey, S.J., Monastero, F.C., Nitchman, S.P., and Smith, G.I., 1990, New evidence for Miocene-to-Recent north-south contraction of the Mojave Block, California: American Geophysical Union Abstracts with Programs, December.

Glazner, A.F. and Bartley, J.M., and Walker, J.D., 1989, Magnitude and significance of the Miocene crustal extension in the central Mojave Desert, California: Geology, v. 17, p. 50-54.

Glazner, A.F., Farmer, G.L., Hughes, W.T., Wooden, J.L. and Pickthorn, W., 1991, Contamination of basaltic magma by mafic crust at Amboy and Pisgah Craters, Mojave Desert, California: Journal of Geophysical Research, v. 96, no. B8, p. 13,673-13,691.

Glazner, A.F., Nielson, J.E., Howard, K.A.and Miller, D.E., 1986, Correlation pf the Peach Springs Tuff, a large volume Miocene ignimbrite sheet in California and Arizona: Geology, v. 14, p. 840-843.

Glazner, A.F. and O'Neil, J.R., 1991, Crustal structure of the Mojave Desert, California: Inferences from Sr and O isotope studies of Miocene volcanic rocks: Journal of Geophysical Research, v. 94, no. B6, p. 7861-7870.

Glazner, A.F. and Ussler, W., III, 1989, Crustal extension, crustal density, and the evolution of Cenozoic magmatism in the Basin and Range of the western United States: Journal of Geophysics, v. 94, p. 7952-7960.

Golombek, M.P. and Brown, L.L., 1988, Clockwise rotation of the western MojaveDesert: Geology, v. 16, p. 126-130.

Hall, A., 1987, Igneous Petrology: John Wiley and Sons, New York, 573 p.

Hayba, D.O., Bethke, P.M., Heald, P., and Foley, N.K., 1985, Geologic, mineralogic, and geochemical characteristics of volcanic-hosted epithermal precious-metal deposits, in B.R. Berger and P.M. Bethke, eds., Geology and Geochemistry of Epithermal Systems: Reviews in Economic Geology, v. 2, p. 129-167.

Heald, P., Foley, N.K., and, Hayba, D.O., 1986, Comparative anatomy of volcanic-hosted epithermal deposits: acid-sulfate and adularia-sericite types: Economic Geology, v. 82, p. 1-26

Hedenquist, J.W. and Henley, R.W., 1985, Hydrothermal eruptions in the Waiotapu geothermal system, New Zealand. Origin, breccia deposit and effect on precious-metal mineralization: Economic Geology, v. 80, p. 1640-1668.

Henley, R.W., 1985, The geothermal framework of epithermal deposits, in B.R. Berger and P.M. Bethke, eds., Geology and Geochemistry of Epithermal Systems: Reviews in Economic Geology, v. 2, p. 1-24.

Henley, R.W. and Ellis, A.J., 1983, Geothermal systems, ancient and modern; a geochemical review: Earth Sciences Review, v. 19, p. 1-50.

Hess, F.L., 1910, Gold mining in the Randsburg quadrangle, California: U.S. Geological Survey Bulletin 430-A, p. 23-47.

Hewett, D.F., 1954, General geology of the Mojave Desert region, California, pt. 1, in Jahns, R.H., ed., Geology of Southern California: California Division of Mines, Bulletin 170, p. 5-20.

Hill, M.L., and Dibblee, T.W., Jr., 1953, San Andreas, Garlock and Big Pine faults, California-a study of the character, history and tectonic significance of their displacements: Geological Society of America Bulletin, v. 64, no. 4, p. 443-458.

Hunt, T.M., 1992, Gravity anomalies, caldera structure, and subsurface geology in the Rotorua area, New Zealand: Geothermics, v. 21, no. 1/2, p. 65-74.

Hulin, C.D., 1925, Geology and ore deposits of the Randsburg quadrangle, California: California Mining Bureau Bulletin 95, 152 p.

Hutchison, C.S., 1974, Laboratory Handbook of Petrographic Techniques: John Wiley and Sons, New York, p. 18.

Jennings, C.W., Burnett, J.L. and Troxel, B.W., 1962, Geologic map of California, Trona Sheet: Scale 1:250,000, California Division of Mines and Geology.

Johnson, C.M., 1991, Large-scale crust formation and lithosphere modification beneath Middle to Late Cenozoic calderas and volcanic fields, western North America: Journal of Geophysical Research, v. 96, no. B8, p. 13,485-13,507.

Katsui, Y. Ando, S., and Inabo, K., 1975, Formation and magmatic evolution of Mashu Volcano, East Hokkaido, Japan, Journal of Faculty of Science, Hokkaido University Serices, IV, v. 16, p. 533-552.

Le Bas, M.J., Le Maitre, R.W., and Woolley, A.R., 1992, The construction of the total alkali-silica chemical classification of volcanic rocks: Mineralogy and Petrology, v.

46, p. 1-22.

Lipman, P.W., 1984, The roots of ash flow calderas in western North America: windows into the tops of granitic batholiths: Journal of Geophysical Research, v. 89, p. 8801-8841.

Lipman, P.W., and Fridrich, C.J., 1990, Cretaceous Caldera Systems: Tucson and Sierreta Mountains, in, G.E. Gehrels and J.E. Spencer, eds., Geological Excursions through the Sonorran Desert Region, Arizona and Sonorra: Arizona Geological Survey Special Paper, no. 7., p. 51-65.

Lipman, P.W., Prostka, H.J. and Christiansen, R.L., 1972, Cenozoic volcanism and plate-tectonic evolution of the western United States. I. Early and middle Cenozoic: Philosphical Transactions of the Royal Society of London, v. 271, p. 217-248.

Loomis, D.P. and Burbank, D.W., 1988, The stratigraphic evolution of the El Paso basin, southern California: implications for the Miocene development of the Garlock fault and uplift of the Sierra Nevada: Geological Society of America Bulletin, v. 100, p. 12-28.

Marsh, B.D., and Charmichael, I.S.E., 1973, Benioff zone magmatism: Journal of Geophysical Research, v. 79, p. 1196-1206.

McKee, E.H., 1971, Tertiary igneous chronology of the Great Basin of western United States - implications for tectonic models: Geological Society of America Bulletin, no. 82, p. 3497-3502.

Miller, J.S. and Miller, C.F., 1991, Tertiary extension-related volcanism, Old Woman Mountains Area, Eastern Mojave Desert, California: Journal of Geophysical Research: v. 96, no. B8, p. 13,629-13,643.

Miller, E.L., and Sutter, J.F., 1982, Structural geology and $^{40}Ar/^{39}Ar$ geochronology of the Goldstone-Lane Mountain area, Mojave Desert, California: Geological Society of America Bulletin, v. 93, p. 1191-1207.

Musselman, T.E., 1987, A modified crustal source for the Colorado mineral belt: implications for REE buffering in CO_2-rich fluids: unpublished Masters degree thesis, T-3333, Colorado School of Mines, p. 122-127.

Nelson, C.E. and Giles, D.L., 1985, Hydrothermal eruption mechanism and hot spring gold deposits: Economic Geology, v. 80, p. 1633-1639.

Nilsen, T.H. and Chapman, R.H., 1971, Bouguer gravity map of California, Trona Sheet: California Division of Mines and Geology, Sacramento, 1:250,000.

Nixon, G.T., 1988, Petrology of the younger andesites and dacites of the Iztacciuatl Volcano, Mexico, I, Disequilibrium phenocryst assemblages as indicators of

magma processes: Journal of Petrology, v. 29, p. 213-264.

Norris, R.M., and Webb, R.W., 1990, Geology of California: John Wiley and Sons, New York, 541 p.

Pallister, J.S., Hoblitt, R.P., and Reyes, A.G., 1992, A basalt trigger for the 1991 eruptions of Pinatubo volcano? Nature, v. 356, p. 426-428.

Pike, R.J., and Clow, G.D., 1981, Revised classification of terrestrial volcanoes and catalogue of topographic dimensions, with new results on edifice volume: U.S. Geological Survey Open File Report, no. 81-1038, 90 p.

Ragland, P.C., 1989, Basic Analytical Petrology: Oxford University Press, New York, 369 p.

Roddick, J.C., 1983, High precision intercalibration of ^{40}Ar - ^{39}Ar standards: Geochimica et Cosmochimica Acta, v. 47, p. 887-893.

Roedder, E., 1984, Fluid Inclusions: Mineralogical Society of America, Reviews in Mineralogy, v. 17, 644 p.

Rose, W.I., Jr., 1972, Notes on the 1902 eruption of Santa Maria volcano, Guatamala: Bulletin of Volcanology, v. 36, p. 29-45.

Rose, W.I., Jr., 1987, Volcanic activity at Saniaguito volcano, 1976-1984, in J.H. Fink, ed., The Emplacement of Silicic Domes and Lava Flows: Geological Society of America Special Paper, no. 212, p. 17-27.

Rytuba, J.J., and McKee, E.H., 1984, Peralkaline ash flow tuffs and calderas of the McDermitt volcanic field, southwest Oregon and north-central Nevada: Journal of Geophysical Research, v. 89, p. 8616-8628.

Samson, S.D., and Alexander, Jr., E.C., 1987, Calibration of the interlaboratory 40Ar-39Ar dating standard, MMhb-1: Chemical Geology, Isotope Geoscience Section, v. 66, p. 27-34.

Scott, W.E., 1987, Holocene rhyodacite eruptions on the flanks of South Sister volcano, Oregon, in, J.H. Fink, ed., The Emplacement of Silicic Domes and Lava Flows: Geological Society of America Special Paper, no. 212, p. 35-53.

Sheridan, M.F., 1979, Emplacement of Pyroclastic Flows: A review: Geological Society of America Special Paper, no. 180, p. 125-136.

Self, S., Wilson, L., and Nairn, J.A., 1979, Vulcanian eruption mechanisms: Nature, v. 277, p. 440-443.

Shubat, M.A. and Snee, L.W., 1992, High-precision $^{40}Ar/^{39}Ar$ geochronology, volcanic

stratigraphy, and mineral deposits of Keg Mountain, west-central Utah, in C.H. Thorman, ed., Application of Structural Geology to Mineral and Energy Resources of the Central and Western United States: U.S. Geological Survey Bulletin, 2012, p. G1-G16.

Silberman, M.L. and Berger, B.R., 1985, Relationships of trace-element patterns to geology in hot-spring type precious metal deposits, in B.R. Berger and P.M. Bethke, eds., Geology and Geochemistry of Epithermal Systems: Reviews in Economic Geology, v. 2, p. 203-232.

Sillitoe, R.H. and Bonham, H.F., 1984, Volcanic landforms and ore deposits: Economic Geology, v. 79, p. 1286-1298.

Silver, L.T., 1986, Evidence for Paleogene low-angle detachment of the southern Sierra Nevada: Geological Society of America Abstracts with Programs, no. 99286, p. 750.

Smith, E.I., Feuerbach, D.L., Naumann, T.R., and Mills, J.G., 1990, Mid-Miocene volcanic and plutonic rocks in the Lake Mead area of Nevada and Arizona; production of intermediate igneous rocks in an extensional environment, in, J.L. Anderson, ed., The Nature and Origin of Cordilleran Magmatism, Boulder, Colorado: Geological Society of America, Memoir 174, p. 169-194.

Smith, G.I., 1964, Geology and volcanic petrology of the Lava Mountains, San Bernardino County, California: U.S. Geological Survey Professional Paper, no. 457, 97 p.

Smith, J.V., and Brown, W.L., 1988, Feldspar Minerals, v. 1: Springer-Verlag, Berlin, 828 p.

Snee, L.W., Sutter, J.G., and Kelly, W.C., 1988, Thermochronology of economic mineral deposits; dating the stages of mineralization of Panasqueira, Portugal by high-precision 40/39 Ar age spectrum techniques on muscovite: Economic Geology, v. 83, p. 335-354.

Snyder, W.S., Dickinson, W.R. and Silberman, M.L., 1976, Tectonic implications of space-time patterns of Cenozoic magmatism in the western United States: Earth and Planetary Science Letters, v. 32, p. 91-106.

Spencer, J.E., and Reynolds, S.J., 1986, Some aspects of the Middle Tertiary tectonics of Arizona and southeastern California: Arizona Geological Society Digest, v. XVI, p. 102-107.

Stimac, J.A., and Pearce, T.H., 1992, Textural evidence of mafic-felsic magma interaction in dacite lavas, Clear Lake, Claifornia: American Mineralogist, v. 77, p. 795-809.

Stock, J., and Molnar, P., 1988, Uncertainties and implications of the Late Cretaceous and Tertiary position of North America relative to the Farallon, Kula, and Pacific plates:

Tectonics, v. 7, p. 1339-1348.

Stormer, J.C., and Nicholls, J., 1976, XLFRAC: A program for the interactive testing of magmatic differentiation models: Computers and Geosciences, v. 1, p. 143-159.

Swanson, D.A., Dzurisin, D., Holcomb, R.T., Iwatsubo, E.Y., Chadwick, Jr., W.W., Casadevall, T.J., Ewert, J.W., and Heliker, C.C., 1987, Growth of the lava dome at Mt. St. Helens, Washington, (USA), 1981-1983, in J.H. Fink, ed., The Emplacement of Silicic Domes and Lava Flows: Geological Society of America Special Paper, no. 212, p. 1-16.

Thompson, D.G., 1929, The Mojave Desert region, California, a geographic, geologic and hydrographic reconnaissance: U.S. Geological Survey Water-Supply Paper 578, 759 p.

Thompson, R.N., Morrison, M.A., Hendry, G.L., and Parry, S.J., 1984, An assessment of the relative roles of a crust and mantle in magma genesis: an elemental approach: Philosphical Transactions of the Royal Society of London, no. A310, p. 549-590.

Vogel, , T.A., Noble, D.C., and Younker, L.W., 1983, Chemical evolution of a high-level magma system; the Black Mountain volcanic center southern Nevada: Livermore, California, Lawrence Livermore National Laboratory, 49 p.

Walker, J.D., Bartley, J.M. and Glazner, A.F., 1990, Large-magnitude Miocene extension in the central Mojave Desert: Implications for Paleozoic to Tertiary paleogeography and tectonics: Journal of Geophysical Research, v. 95, no. B1, p. 557-569.

Wernicke, B., 1981, Low-angle normal faults in the Basin and Range province: Nature, v. 291, p. 645-648.

Wernicke, B., Hodges, K and Walker, D., 1986, Geologic evolution of the Tucki Mountain and vicinity, central Panamint Range, in Field Trip Number 2, Parts A and B: Prepared for the 82nd Annual Meeting of the Cordilleran Section of the Geological Society of America, Los Angeles, California, March 25-28, 1986, p. 67-71.

White, C.M., 1992, Evolution of calc-alkaline magmas at the Quaternary Battle Ax volcano, western Cascade Range, Oregon: Journal of Volcanology and Geothermal Research, v. 52, p. 107-122.

White, D.E., 1974, Diverse origins of hydrothermal ore fluids: Economic Geology, v. 69, p. 954-973.

White, D.E., 1981, Active geothermal systems and hydrothermal ore deposits: Economic Geology, 75th Anniversary Volume, p. 392-423.

Whitson, D., 1982, Geology of the perlite deposit at No Agua peaks, New Mexico: New Mexico Bureau of Mines and Mineral Resources Circular no. 182, p. 89-95.

Wiebe, R.A., 1993, Basaltic injections into floored silicic magma chambers: Eos, v. 7, no. 1, p. 1-3.

Wilcox, R.E., 1979, The liquid line of descent and variation diagrams, in H.S. Yoder, ed., The Evolution of the Igneous Rocks: 50th Anniversary Perspectives: Princeton University Press, Princeton, New Jersey, p. 205-232.

Williams, H., 1932, Geology of the Lassen Volcanic National Park, California: University of California Publications in Geological Sciences Bulletin, no. 21, p. 51-146.

Williams, H. and McBirney, A.R., 1979, Volcanology: Freeman, Cooper and Co., San Francisco, 397 p.

Wohletz, K.H. and Sheridan, M.F., 1979, A model of pyroclastic surge, in Chapin, C.E. and Elston, W.E., eds., Ash-Flow Tuffs: Geological Society of America Special Paper, no. 180, p. 177-194.

Wright, J.V., Smith, A.L., and Self, S., 1980, A working terminology of pyroclastic deposits: Journal of Volcanology and Geothermal Research, v. 8, p. 315-336.

Wyllie, P.J., 1984, Constraints imposed by experimental petrology on possible and impossible magma sources and products: Philosphical Transactions of the Royal Society of London, A 310, p. 439-456.

Wyllie, P.J., Huang, W., Stern, C.R., and Maaloe, S., 1976, Granitic magmas: possible and impossible sources, water contents, and crystallization sequences: Canadian Journal of Earth Sciences, v. 13, p. 1007-1019.

APPENDIX A

SAMPLE PREPARATION

A.1 Introduction

Analytical work was performed to determine the mineralogy and chemical compositions of samples from the volcanic field. Of the over 300 samples collected over a two year period, almost 200 thin sections were made and seventy-two samples were sent to the X-Ray Assay Laboratories (XRAL), Don Mills, Ontario, for chemical analysis.

A.2 X-Ray Fluorescence Spectrometry

X-ray fluorescence spectrometry was performed on 61 samples to determine 11 major element oxide and 6 minor element concentrations. Preparation of samples by XRAL included crushing and grinding samples to minus 200 mesh in an agate crushing and grinding medium. Agate mills provide ±0.3% SiO_2 contamination and virtually no other elemental contamination. Details regarding analytical procedures are in Bloom (1993). A bead fused with lithium tetraborate was created for each sample and then analyzed in an X-ray spectrometer. The detection limit for major elements is 0.01 % and that of minor elements is 10 ppm.

Anhydrous, normalized major and trace element data and CIPW norms are included in Tables A.1 and A.2. Analytical precisions and other details about sample preparation are included on the pages following these tables.

Table A.1. Water-free, normalized major and trace element analyses from whole rock x-ray flourescence[1].

Rock type[2]	basalt	bas and	bas and	bas and	bas and	and	and	and	and	and	and	and	and	and
Map ID	Mb	Mba	Mba	Mba	Mba	Ma	Ma	Ma	Ma	Ma	Ma	Ma	Ma	Ma
Field ID	1133	1039	1040	1126	1315	1015	1018	1034	1244	1245	1246	1099	1215	1264
wt %														
SiO_2	50.8	45.4	52.5	57.6	58.5	65.3	60.4	63.2	61.6	62.7	63.4	59.5	63.0	60.8
Al_2O_3	16.6	15.6	17.3	17.2	17.9	17.4	16.2	17.1	16.3	16.9	16.2	16.5	16.8	18.1
CaO	10.0	19.0	9.97	8.59	6.20	4.58	6.63	4.98	4.40	3.52	3.57	5.03	4.88	6.05
MgO	6.66	4.89	3.35	1.91	2.76	1.47	3.45	2.15	1.03	0.42	0.32	1.06	2.04	1.12
Na_2O	3.16	2.58	3.11	3.67	4.13	4.15	3.72	4.24	4.37	4.39	3.88	4.35	3.90	3.69
K_2O	0.63	0.33	0.59	1.94	2.11	2.65	1.39	2.45	2.93	3.39	3.49	2.40	2.86	1.90
Fe_2O_3	1.13	1.13	1.23	0.79	0.73	0.40	0.73	0.52	0.88	0.82	0.86	1.02	0.57	0.69
FeO	9.18	9.17	9.96	6.43	5.92	3.20	5.91	4.20	7.16	6.65	6.95	8.25	4.63	5.61
MnO	0.15	0.40	0.15	0.13	0.10	0.06	0.14	0.09	0.17	0.03	0.04	0.11	0.10	0.06
TiO_2	1.42	1.31	1.59	1.53	1.36	0.72	1.25	0.90	0.79	0.83	0.93	1.24	0.98	1.64
P_2O_5	0.16	0.40	0.22	0.24	0.27	0.17	0.22	0.22	0.35	0.35	0.39	0.57	0.25	0.28
LOI	0.93	9.39	2.54	3.39	1.35	3.00	1.93	1.16	1.30	1.90	2.25	2.35	2.90	3.75
SUM[3]	100	98.7	99.6	98.9	99.5	98.6	99.0	99.5	99.8	100.2	100.0	100.1	100.0	99.7
ppm														
Cr	134	136	84	132	137	<10	35	<10	<10	196	14	<10	26	95
Rb	19	<10	15	112	39	128	86	97	116	108	112	72	100	74
Sr	303	318	346	520	533	610	463	580	403	308	287	400	675	452
Y	35	27	29	18	32	10	24	13	43	19	19	36	26	67
Zr	115	83	118	174	192	219	182	203	446	469	330	328	234	259
Nb	<10	38	35	18	20	18	22	38	41	105	44	24	18	46
Ba	196	106	235	437	564	943	586	884	1300	1230	980	834	994	697

[1] Data normalized to anhydrous values (less LOI) with Fe-weighting factor of 0.9 (1 cation mole % Fe_2O_3 for every 9 cation mole % FeO).

[1] Abbreviations: and = andesite; bas and = basaltic andesite; aph rhy = aphyric rhyolite; rhydac = rhyodacite; rhy fd = feeder dike (rhyolitic).

[2] Normalized data may not appear to equal Sum due to rounding of Sum to one significant figure.

Table A.1. Water-free, normalized major and trace element analyses from whole rock x-ray flourescence.

Rock type	and	and	and	and	tuff	tuff	dacite	dacite	dacite	dacite	dacite	rhydac	rhydac	rhydac
Map ID	Ma	Ma	Ma	Md	Map	pumice	Md	Md	Md	Md	Md	Mrd	Mrd	Mrd
Field ID	1327	1313	1079	1255	1340	1224	1012	1024A	1030	1010	1130	1205	1272	1260
wt %														
SiO_2	65.4	62.7	65.0	64.0	63.0	65.1	64.8	69.2	65.7	68.4	67.2	65.6	70.5	67.6
Al_2O_3	16.5	18.0	16.7	17.2	17.3	17.0	16.1	15.4	17.2	15.1	16.3	16.2	15.7	16.8
CaO	4.08	5.40	4.03	4.26	5.48	4.01	4.41	3.29	3.73	3.20	3.99	5.50	2.77	4.00
MgO	1.85	0.67	1.09	1.62	1.99	1.43	0.68	0.45	0.05	0.53	0.74	1.32	0.53	0.71
Na_2O	4.06	4.07	4.24	4.05	3.57	3.78	4.33	3.29	3.73	4.15	3.79	4.30	3.28	4.37
K_2O	2.74	1.97	3.28	3.12	2.28	2.82	2.94	2.88	4.73	2.71	3.19	2.62	4.37	2.67
Fe_2O_3	0.47	0.26	0.51	0.51	0.55	0.54	0.60	0.42	0.47	0.53	0.42	0.40	0.24	0.35
FeO	3.81	4.61	4.10	4.10	4.45	4.34	4.87	3.40	3.77	4.31	3.42	3.26	1.92	2.81
MnO	0.09	0.09	0.08	0.06	0.09	0.09	0.06	0.05	0.05	0.03	0.05	0.07	0.04	0.06
TiO_2	0.75	1.07	0.78	0.87	1.04	0.76	0.91	0.71	0.74	0.80	0.67	0.55	0.47	0.54
P_2O_5	0.18	0.09	0.20	0.19	0.27	0.19	0.23	0.21	0.28	0.20	0.18	0.20	0.17	0.14
LOI	2.90	2.65	1.60	2.80	5.60	6.55	2.23	1.70	1.47	2.47	2.10	1.45	3.20	1.45
SUM	99.4	99.2	99.9	99.8	99.1	100.2	99.8	99.1	99.5	99.3	99.7	99.6	99.7	99.7
ppm														
Cr	137	137	46	26	137	137	<10	<10	<10	13	24	68	17	54
Rb	127	34	109	84	76	132	74	87	104	80	88	72	105	81
Sr	474	550	400	457	547	495	416	429	429	419	435	1073	575	799
Y	42	26	33	<10	<10	23	27	35	34	38	<10	11	<10	23
Zr	219	150	242	229	217	284	228	234	225	261	237	143	137	150
Nb	<10	14	33	14	15	25	26	<10	<10	13	24	30	18	37
Ba	738	664	849	917	536	894	943	906	940	996	846	1124	2036	1216

Table A.1. Water-free, normalized major and trace element analyses from whole rock x-ray flourescence.

Rock type	rhydac	rhydac	rhydac	rhydac	rhydac	rhydac	rhydac	rhydac	rhydac	rhydac	rhydac	aph rhy	aph rhy	aph rhy
Map ID	Mrd	Mrd	Mrd	Mrd	Mrd	Mrd	Mrd	Mrd	Mrb	Mrd	Mrd	Mar	Mar	Mar
Field ID	1269	1213	1249	1232	1276	1212	1248	1206	1214	1209	1251	1057	1060	1323
wt %														
SiO_2	66.8	69.5	68.0	68.8	69.7	68.5	68.4	69.7	67.7	68.2	67.5	75.4	75.8	73.6
Al_2O_3	16.8	16.2	16.2	16.1	16.2	16.3	16.9	16.5	16.9	16.3	17.0	12.8	12.9	14.6
CaO	4.07	2.98	3.73	4.02	2.62	2.70	3.55	3.96	3.46	3.83	3.39	1.09	0.84	1.05
MgO	0.91	0.96	1.54	0.63	0.62	0.29	0.95	0.82	1.23	1.54	1.21	0.21	0.13	0.42
Na_2O	3.77	3.63	3.76	4.20	3.43	4.70	4.25	3.96	3.90	4.15	3.99	4.20	4.09	3.27
K_2O	3.15	2.87	3.25	2.57	4.30	3.58	2.73	3.06	2.92	2.70	3.12	3.60	4.79	4.74
Fe_2O_3	0.39	0.37	0.31	0.32	0.27	0.37	0.29	0.19	0.33	0.29	0.33	0.26	0.14	0.23
FeO	3.18	2.97	2.53	2.56	2.19	2.67	2.32	1.54	2.69	2.37	2.67	2.10	1.12	1.84
MnO	0.06	0.06	0.05	0.04	0.04	0.04	0.06	0.03	0.03	0.06	0.05	0.04	0.03	0.03
TiO_2	0.67	0.38	0.50	0.54	0.52	0.64	0.44	0.55	0.61	0.41	0.59	0.21	0.07	0.16
P_2O_5	0.27	0.11	0.17	0.16	0.13	0.20	0.15	0.18	0.18	0.16	0.18	0.12	0.03	0.04
LOI	3.00	2.15	2.20	1.15	3.10	1.50	3.00	2.50	4.10	3.60	3.05	1.39	0.54	3.25
SUM	99.9	99.0	99.7	99.7	100.1	99.7	99.9	99.8	99.7	100.2	99.9	98.6	98.3	98.4
ppm														
Cr	62	137	23	45	25	19	68	14	13	68	68	<10	<10	137
Rb	84	83	75	85	135	259	57	74	94	65	82	111	156	138
Sr	880	862	993	104	342	365	1418	752	962	1131	932	170	28	114
Y	15	<10	15	12	18	<10	26	<10	<10	<10	19	39	49	44
Zr	156	123	162	132	205	214	141	175	160	125	148	264	19	246
Nb	39	12	25	23	24	30	33	15	14	<10	18	19	37	17
Ba	1242	1357	1307	1139	929	1359	1790	1565	1143	1453	1304	1220	322	1177

Table A.1. Water-free, normalized major and trace element analyses from whole rock x-ray flourescence.

Rock type	aph rhy	aph rhy	rhyolite	rhyolite	rhy fd	tuff	tuff	tuff	tuff	tuff	tuff	tuff	tuff
Map ID	Mar	Mar	Br	Br	Brf	Mrp	Mrp	Mrp	Mrp	Mrp	Mrp	Mrp	Mrp
Field ID	1208	1093	1118	1031	1332	1333	1029	1339	1016	1123	1263	1314	1065
wt %													
SiO_2	76.1	77.3	77.3	74.7	78.6	74.1	70.8	78.8	79.0	75.8	76.2	77.8	75.2
Al_2O_3	13.8	12.2	12.0	12.2	12.3	16.4	12.6	12.7	11.2	13.9	13.0	12.3	13.4
CaO	0.95	0.70	0.73	3.23	0.46	0.30	1.50	1.88	0.33	1.72	0.86	1.39	1.93
MgO	0.41	0.10	0.15	0.27	0.56	0.37	2.22	2.40	0.48	0.62	0.24	0.57	0.35
Na_2O	1.82	4.32	3.89	3.65	1.21	0.93	9.02	1.20	3.38	2.57	3.04	2.10	3.08
K_2O	4.80	3.82	4.56	4.68	5.39	6.49	1.85	1.33	4.36	4.38	4.80	3.88	5.03
Fe_2O_3	0.30	0.15	0.13	0.11	0.14	0.13	0.19	0.16	0.12	0.09	0.19	0.20	0.09
FeO	1.65	1.19	1.01	0.90	1.15	1.07	1.65	1.32	0.99	0.72	1.49	1.58	0.73
MnO	0.03	0.06	0.03	0.04	0.02	0.02	0.35	0.08	0.02	0.03	0.03	0.02	0.06
TiO_2	0.19	0.11	0.14	0.12	0.20	0.17	0.15	0.13	0.11	0.09	0.17	0.16	0.07
P_2O_5	0.05	0.04	0.08	0.06	0.05	0.07	0.04	0.03	0.03	0.03	0.05	0.02	0.03
LOI	3.40	0.70	0.93	3.23	2.85	2.95	10.0	12.3	3.93	8.47	4.80	6.80	3.93
SUM	99.0	99.7	99.5	99.7	98.3	98.8	95.1	99.9	98.8	99.2	100.4	98.2	99.5
ppm													
Cr	<10	<10	<10	<10	137	137	<10	137	<10	<10	18	137	<10
Rb	158	132	128	147	159	161	98	81	134	243	201	127	247
Sr	160	84	79	27	54	51	251	303	188	407	90	165	112
Y	23	64	52	58	<10	13	82	88	184	21	73	72	58
Zr	262	241	171	178	146	166	465	539	478	95	363	426	92
Nb	39	11	13	29	14	17	41	31	48	37	42	62	53
Ba	2400	1235	712	424	622	721	324	142	786	608	268	315	465

Table A.1. Water-free, normalized major and trace element analyses from whole rock x-ray flourescence.

Rock type	tuff	vent	vent	vent	vent	vent
Map ID	Mrp	Brp	Brp	Brp	Brp	Brp
Field ID	1319	1233	1234	1235	1236	1237
wt %						
SiO_2	82.0	76.6	74.5	75.2	79.7	81.2
Al_2O_3	10.9	12.6	13.4	12.8	10.9	10.2
CaO	0.65	0.66	1.21	0.83	0.88	0.83
MgO	0.44	0.24	0.48	0.23	0.37	0.35
Na_2O	0.02	2.96	3.51	4.38	2.29	1.70
K_2O	4.86	5.16	4.44	4.09	4.15	4.11
Fe_2O_3	0.09	0.18	0.24	0.25	0.16	0.15
FeO	0.70	1.43	1.93	2.02	1.30	1.22
MnO	0.02	0.03	0.03	0.02	0.03	0.03
TiO_2	0.20	0.15	0.21	0.21	0.13	0.11
P_2O_5	0.08	0.03	0.03	0.05	0.03	0.04
LOI	3.40	4.00	4.25	1.15	6.45	5.55
SUM	99.8	99.7	99.9	100.1	99.8	99.8
ppm						
Cr	137	115	18	54	28	18
Rb	107	179	137	145	197	159
Sr	110	26	64	85	27	21
Y	<10	72	58	45	61	69
Zr	86	469	424	435	365	395
Nb	30	83	57	55	40	30
Ba	487	241	508	526	481	212

XRAL **X-Ray Assay Laboratories**
A Division of SGS Supervision Services Inc.

X-Ray Assay Laboratories
Summary of Precision Statistics Based on In-House Duplicates
Method: X-Ray Fluorescence on a Glass Disk
XRAL Method Code: 100-1

	Lower Limit of Detect'n	No. of Dupl. Pairs	Relative Standard Deviation by Class					Average
			1	2	3	4	5	
SiO_2	0.01%	10638	112.62	20.78	8.05	2.70	0.56	0.90
Al_2O_3	0.01%	10451	38.04	7.70	3.39	0.85	0.47	0.80
CaO	0.01%	10082	37.30	10.29	2.07	0.75	0.66	1.40
MgO	0.01%	10331	49.80	16.90	2.85	0.78	0.68	1.60
Na_2O	0.01%	9866	40.24	23.56	6.79	1.30	0.60	4.80
K_2O	0.01%	9671	34.71	2.01	2.71	1.10	0.59	1.70
Fe_2O_3	0.01%	10412	51.41	24.10	8.65	1.39	0.76	2.70
MnO	0.01%	9418	24.97	1.04	0.74	0.89	0.40	0.90
Cr_2O_3	0.01%	3166	2.30	2.69	1.35	0.30	2.31	2.50
P_2O_5	0.01%	9009	90.44	1.48	0.05	0.77	0.86	0.80
TiO_2	0.01%	11316	40.26	0.20	6.04	1.18	0.82	1.50
LOI	0.01%	9978	51.31	8.79	17.16	4.12	0.69	5.30
Ba	10ppm	8980	42.14	19.23	4.79	1.65	1.38	6.30
Nb	10ppm	5614	52.04	22.32	6.16	0.92	ND	21.70
Rb	10ppm	7386	52.15	15.16	4.23	2.79	ND	13.00
Sr	10ppm	8108	31.46	14.27	3.38	0.80	0.89	6.70
Y	10ppm	5123	39.06	22.47	4.61	0.37	ND	21.10
Zr	10ppm	8469	30.84	12.96	4.23	1.49	1.43	7.10

Notes: Between 8 to 15% of samples are analyzed in duplicate. The average relative standard deviation is calculated for each pair of data points. The data are divided into 5 classes based on lower limits of detection (LLD):

Class 1 - At least one of the data points is below the LLD. For the purposes of this calculation, data below the LLD is assigned a value of half the detection limit.
Class 2 - Mean of the 2 data points falls between 1 and 10 times the LLD.
Class 3 - Mean of the 2 data points falls between 10 and 100 times the LLD.
Class 4 - Mean of the 2 data points falls between 100 and 1000 times the LLD.
Class 5 - Mean of the 2 data points falls between 1000 and 10000 times the LLD.

Number of Duplicate Pairs - Total number of duplicate pairs;most data falls into Classes 2 and 3. RSD for other Classes may be overestimated.

MULTIELEMENT RESEARCH PACKAGE - INAA

	NBS-1632A	SDC-1	RGM-1	STM-1	BHVO-1
AG PPM	<2 (-)	<2 (-)	<2 (-)	<2 (-)	<2 (-)
AS PPM	9 (9.1)	<1 (-)	3 (-)	4 (-)	1 (-)
AU PPB	- (<5)	- (-)	- (-)	- (-)	- (-)
BA PPM	130 (130)	680 (650)	880 (800)	630 (560)	200 (135)
BR PPM	43 (43)	9.2 (-)	10 (-)	7.9 (-)	8.8 (-)
CA %	0.2 (.24)	1.2 (.99)	0.8 (0.82)	0.6 (.78)	9.9 (8.09)
CO PPM	6.9 (6.6)	16 (17)	2.0 (2.3?)	0.8 (1?)	45 (45)
CR PPM	35 (34.6)	66 (66?)	6.7 (4?)	4.1 (4?)	310 (300)
CS PPM	2.6 (2.5)	3.7 (3.9?)	9.6 (-)	1.3 (1.5?)	0.3 (.15?)
FE %	1.14 (1.11)	4.84 (4.81)	1.35 (1.31)	3.52 (3.65)	9.43 (8.56)
HF PPM	1.3 (1.6)	7.8 (8.1)	5.9 (6.0?)	26 (27?)	4.5 (4.3)
MO PPM	<2 (<4)	<2 (-)	<2 (2.3)	5 (5.2)	<2 (-)
NA PPM	960 (840)	15500 (15570)	32200 (30560)	63000 (66400)	16800 (17000)
NI PPM	<50 (19)	<50 (36)	<50 (6?)	<50 (3?)	80 (120)
RB PPM	20 (29)	120 (120?)	140 (155?)	100 (120?)	10 (10)
SB PPM	0.7 (0.7)	0.59 (0.54?)	1.36 (1.3?)	1.7 (1.7?)	0.2 (0.17?)
SC PPM	6.16 (6.3)	15.1 (15?)	4.65 (4.7)	0.50 (0.7?)	33.9 (31)
SE PPM	2.5 (2.7)	<0.5 (-)	<0.5 (-)	<0.9 (-)	<0.6 (-)
SR PPM	<100 (90)	200 (180)	100 (100)	700 (700)	400 (420)
TA PPM	<0.5 (0.40)	1.2 (1.3?)	0.9 (1.0?)	18 (18?)	<1.2 (1.1?)
TH PPM	4.4 (4.5)	11 (12?)	15 (15?)	29 (31?)	1.2 (1.0)
U PPM	1.2 (1.29)	2.8 (3.0?)	5.2 (5.8?)	10.2 (9.1?)	0.4 (0.4?)
W PPM	1 (0.8)	1 (0.8)	1 (1.6?)	4 (3.8)	<1 (-)
ZN PPM	27 (28)	100 (105)	35 (36)	170 (240)	120 (105)
LA PPM	14.9 (15)	42.0 (42)	24.1 (23?)	150 (150)	14.9 (17?)
CE PPM	30 (30)	95 (92)	49 (48?)	257 (260)	42 (39)
ND PPM	10 (12)	39 (38)	17 (19?)	74 (78)	26 (24)
SM PPM	2.28 (2.2)	7.42 (8.3?)	4.16 (4.3?)	11.4 (13)	5.90 (6.1)
EU PPM	0.45 (0.54)	1.78 (1.7?)	0.67 (0.7?)	3.67 (3.7)	2.30 (2.0)
TB PPM	0.4 (0.3)	1.0 (1.2?)	0.7 (-)	1.7 (1.6)	1.0 (1.0)
YB PPM	1.24 (1.10)	4.88 (4.2)	2.70 (2.5)	4.37 (4.3)	2.33 (-)
LU PPM	0.20 (0.19)	0.77 (-)	0.50 (-)	0.74 (-)	0.34 (-)

Note: ( ) are useable values as per Sydney Abbey, 1983 (G.S.C. paper 83-15) or Gladney, etal., 1984. (-) indicates no values available. This represents part of a group of reference materials used for calibration purposes. These standards represent a single analysis of each.

INSTRUMENT STABILITY

(10 REPLICATE ANAYSES NBS 1632a)

Element	Mean (ppm)	S.D. (ppm)
Ba	123	8
Sr	42.2	1.0
Ca	0.26	0.15
Co	6.2	0.2
Cr	34.3	0.5
Cs	2.3	0.1
Fe	1.11 %	0.01 %
Hf	1.35	0.05
Mo	1.5	0.9
Ni	<50	0
Rb	23	5
Sc	6.05	0.04
Se	2.7	0.4
Sr	100	-
Ta	<0.5	0
Th	4.39	0.08
Zn	32	2
La	15.5	0.4
Ce	29.4	0.7
Nd	11.5	0.8
Sm	2.23	0.03
Eu	0.53	0.04
Tb	0.31	0.03
Yb	1.10	0.08
Lu	0.186	0.007

XRAL **X-Ray Assay Laboratories**
A Division of SGS Supervision Services Inc.

X-Ray Fluorescence Spectrometry - 27 Elements - Pressed Pellet

Description:

At least 5 g of sample is required for the analysis of one or all of the above elements. A pellet is loaded into the holder of the automatic sample changer of a Philips PW1400 wavelength dispersive x-ray spectrometer. The 40 mm diameter sample pellets are loaded six to a tray with a total of 10 trays.

Elements are run in an inert nitrogen atmosphere employing a rhodium tube which also serves as an internal standard for some elements. For different combinations of requested elements various standard reference materials are inserted with these samples to verify calibration. Calibration is programmed into the instrument and inter-element corrections are applied to necessary analyte elements. Commonly requested element combinations are programmed to be determined individually or in groups.

Limitations:

This procedure is not suitable for mineralized materials. The presence of percentage levels of any element except the usual major rock constituents will have a adverse effect on the calibration.

The maximum concentration reported by these procedures is generally 5000 ppm. Analysis for elements with concentrations higher than 5000 ppm should be analysed by one of our assay procedures. The assay procedure involves a potassium pyrosulfate fusion of the sample followed by the preparation of a pressed disk. The pyrosulfate fusion produces a very homogeneous sample material with a uniform grain size. The fusion also saturates any matrix impact from the sample with the overwhelming matrix of the pyrosulfate flux itself thus allowing for synthetic standard calibrations. Internal standards are also used for assay grade analysis. This procedure is essential to produce the accuracy and precision requirements needed for assay grade analysis.

Elements:

Sb	3 ppm	Pb	2 ppm	Tl	5 ppm
As	3 ppm	Mo	2 ppm	Th	2 ppm
Ba	20 ppm	Nb	2 ppm	Sn	5 ppm
Bi	3 ppm	Ni	2 ppm	Ti	5 ppm
Cl	50 ppm	Rb	2 ppm	W	5 ppm
Co	2 ppm	Se	3 ppm	U	2 ppm
Cu	2 ppm	Sr	2 ppm	Y	2 ppm
Ga	3 ppm	S	50 ppm	Zr	3 ppm
Fe	3 ppm	TA	5 ppm	Zn	2 ppm

Prepared by	Approved by	Date

XRAL X-Ray Assay Laboratories
A Division of SGS Supervision Services Inc.

Mercury Determination by Cold Vapour Atomic Absorption Spectrometry

Description:

A 0.5 gram sample is digested with sulfuric - nitric acid and potassium permanganate and potassium persulfate for thorough oxidation. If during digestion the sample reduces all the permanganate (colour change), excess permanganate is added to prevent reduction of Hg to the elemental state. After digestion, reducing agents sodium borohydride and hydroxylamine sulfate are added producing a mercury vapour in a Leeman Lab PS200 automated mercury analyzer. The instrument is calibrated and SRM's are carried through the procedure.

Elements:

Hg 5 ppb

Prepared by	Approved by	Date

LONG LIVED RADIOISOTOPES

Up to 60 samples are irradiated simultaneously in a neutron flux of about $4e^{12}$ $n/cm^2/sec$. One or more international standard reference materials (NIST, CANMET, USGS, etc.) and a neutron flux monitoring foil are also irradiated with each batch of samples. Each batch of samples is wrapped in polyethylene and placed inside a water tight irradiation facility which is continuously rotated throughout the irradiation period.

The sample, standards, and flux monitoring foil are allowed to decay for approximately 7 days. At that time, the samples are counted for up to 2000 seconds on one of our high purity germanium (HPGE) detectors. Each detector has an efficiency >10% (relative to NAI) and an energy resolution of 1.9kev (at 1332.5kev) or better. Approximately 30% of the samples in each irradiation batch are recounted after 1 to 3 days as part of our quality control/quality assurance program. The flux monitoring foil is counted on one of our HPGE detectors. The information from the foil is used to compensate for any variation of the neutron flux during the irradiation.

The gamma-ray energy spectrum collected on our multi-channel analyzer is transferred to our multi-user computer system for analysis. Using a customized version of "TEABAGS" (trace element analysis by automated gamma ray spectroscopy), developed at the Missouri reactor by researchers from Washington University, peak identification, spectral interference corrections, and fission product corrections are determined. "TEABAGS" also allows us to identify and quantify more than one peak for most of the elements analyzed. The element concentration is calculated from a weighted average of the multiple peak data. The weighting factor is a function of the counting statistics associated with each peak identified by the program.

Table A.3. CIPW normative mineral determinations

Norm	1133	1039	1040	1126	1315	1015	1018	1034	1244	1245	1246	1099	1215	1264
q	0.0	.....[1]	3.23	7.71	6.99	17.56	12.56	13.80	10.54	12.39	15.68	9.19	14.19	15.18
c	0.0		0.0	0.0	0.0	0.0	0.0	0.0	0.0	0.47	0.49	0.0	0.0	0.0
or	3.74		3.51	11.48	12.48	15.67	8.23	14.48	17.30	20.04	20.59	14.15	16.88	11.22
ab	26.69		26.29	31.01	34.97	35.08	31.47	35.87	36.99	37.11	32.80	36.78	33.01	31.23
an	29.38		31.52	24.78	24.18	20.94	23.42	20.29	16.15	15.16	15.14	18.49	19.79	27.33
ac	0.0		0.0	0.0	0.0	0.0	0.0	0.0	0.0	0.0	0.0	0.0	0.0	0.0
ks	0.0		0.0	0.0	0.0	0.0	0.0	0.0	0.0	0.0	0.0	0.0	0.0	0.0
di/w	8.06		6.89	6.77	2.03	0.28	3.36	1.26	1.43	0.0	0.0	1.15	1.17	0.35
di:en	4.26		2.52	2.42	0.92	0.13	1.66	0.59	0.28	0.0	0.0	0.22	0.51	0.10
di:fs	3.56		4.51	4.51	1.10	0.15	1.63	0.66	1.25	0.0	0.0	1.02	0.66	0.26
hy:e	6.16		5.82	2.34	5.95	3.54	6.93	4.77	2.29	1.05	0.80	2.43	4.57	2.69
hy:fs	5.15		10.42	4.35	7.11	4.32	6.82	5.32	10.17	10.22	10.60	11.43	5.94	6.87
ol:fo	4.32		0.0	0.0	0.0	0.0	0.0	0.0	0.0	0.0	0.0	0.0	0.0	0.0
ol:fa	3.98		0.0	0.0	0.0	0.0	0.0	0.0	0.0	0.0	0.0	0.0	0.0	0.0
mt	1.64		1.78	1.15	1.06	0.57	1.06	0.75	1.28	1.19	1.24	1.47	0.83	1.00
il	2.70		3.01	2.91	2.59	1.37	2.37	1.71	1.50	1.57	1.76	2.35	1.86	3.11
ap	0.38		0.51	0.56	0.62	0.39	0.51	0.50	0.81	0.81	0.91	1.32	0.58	0.66
SUM	100		100	100	100	100	100	100	100	100	100	100	100	100
An#[2]	52	70	55	52		37	43	36	30	29	32	32	37	47
LOI	0.93	9.39	2.54	3.39	1.35	3.00	1.93	1.16	1.30	1.90	2.25	2.35	2.90	3.75
Mg#	56.39	48.78	37.45	34.63	45.37	45.11	51.0	47.70	20.48	10.13	7.58	18.71	43.95	26.30
DI[3]	34.17	.....[1]	33.03	50.20	54.44	68.31	52.26	64.15	64.83	65.23	69.07	60.12	64.08	57.63
A/CNK[4]	0.69		0.72	0.72	0.88	0.96	0.82	0.91	0.89	0.98	0.97	0.87	0.91	

1 Insufficient (non-normalized) silica content for normative mineral determations in CIPW program

2 An content determined from IGPET.bas "CIPW" program.

3 Differentiation Index - sum of the wt. % of normative quartz, orthoclase, albite, nepheline, leucite and kalsilite.

4 Molar Al_2O_3/Σmolar ($CaO+Na_2O+K_2O$).

Table A.3. CIPW normative mineral determinations

Norm	1327	1313	1079	1340	1224	1255	1012	1024	1030	1010	1130	1205	1272	1260
q	17.90	16.51	15.80	16.96	19.25	14.97	16.36	25.52	16.61	24.01	21.70	17.11	27.24	21.06
c	0.0	0.0	0.0	0.0	0.85	0.0	0.0	0.18	0.14	0.0	0.0	0.0	0.91	0.0
or	16.17	11.63	19.39	13.47	16.67	18.43	17.39	17.02	17.40	16.04	18.83	15.46	25.84	15.75
ab	34.33	34.46	35.90	30.20	31.95	34.28	36.61	33.90	40.02	35.12	32.10	36.41	27.77	36.99
an	18.84	25.07	16.73	24.47	18.64	19.53	15.84	14.99	16.72	14.51	18.16	17.02	12.67	18.21
ne	0.0	0.0	0.0	0.0	0.0	0.0	0.0	0.0	0.0	0.0	0.0	0.0	0.0	0.0
le	0.0	0.0	0.0	0.0	0.0	0.0	0.0	0.0	0.0	0.0	0.0	0.0	0.0	0.0
ac	0.0	0.0	0.0	0.0	0.0	0.0	0.0	0.0	0.0	0.0	0.0	0.0	0.0	0.0
ks	0.0	0.0	0.0	0.0	0.0	0.0	0.0	0.0	0.0	0.0	0.0	0.0	0.0	0.0
di/w	0.10	0.15	0.80	0.40	0.0	0.16	1.90	0.0	0.0	0.04	0.16	3.73	0.0	0.28
di:en	0.04	0.03	0.26	0.18	0.0	0.06	0.39	0.0	0.0	0.01	0.05	1.51	0.0	0.09
di:fs	0.05	0.13	0.57	0.22	0.0	0.09	1.64	0.0	0.0	0.04	0.12	2.25	0.0	0.20
hy:e	4.57	1.63	2.47	4.77	3.55	3.96	1.30	1.13	0.97	1.31	1.80	1.77	1.32	1.67
hy:fs	5.48	6.60	5.39	5.94	6.42	5.70	5.43	4.82	5.42	6.18	4.80	2.63	2.62	3.89
ol:fo	0.0	0.0	0.0	0.0	0.0	0.0	0.0	0.0	0.0	0.0	0.0	0.0	0.0	0.0
ol:fa	0.0	0.0	0.0	0.0	0.0	0.0	0.0	0.0	0.0	0.0	0.0	0.0	0.0	0.0
mt	0.68	0.90	0.73	0.80	0.78	0.73	0.87	0.61	0.68	0.77	0.61	0.58	0.34	0.50
hm	0.0	0.0	0.0	0.0	0.0	0.0	0.0	0.0	0.0	0.0	0.0	0.0	0.0	0.0
il	1.43	2.45	1.49	1.97	1.44	1.65	1.73	1.35	1.40	1.52	1.27	1.05	0.90	1.02
ap	0.41	0.43	0.47	0.62	0.45	0.43	0.53	0.48	0.64	0.46	0.40	0.47	0.39	0.33
SUM	100	100	100	100	100	100	100	100	100	100	100	100	100	100
An#[2]			32		37	29	30	31	29	29	36	32	31	33
LOI	2.90	2.65	1.60	5.60	6.55	2.80	2.23	1.70	1.47	2.47	2.10	11.45	3.20	1.45
Mg#	46.43	19.17	32.24	44.35	36.98	41.25	19.95	19.22	15.56	17.98	27.83	41.88	32.99	30.94
DI[3]	68.40	62.20	71.09	60.63	67.87	67.68	70.30	76.43	74.03	75.17	72.63	68.98	80.85	73.80
A/CNK	0.97	0.97	0.93			0.97	0.88	1.06	0.95	0.97	0.96	0.81	1.03	0.97

Table A.3. CIPW normative mineral determinations

Norm	1269	1213	1249	1232	1276	1212	1248	1206	1214	1209	1251	1057	1060	1323
q	21.43	27.82	22.24	24.02	25.72	20.27	23.03	25.97	23.47	22.07	22.12	33.36	31.24	32.29
c	0.41	1.94	0.08	0.0	1.50	0.33	0.81	0.73	1.45	0.0	1.31	0.34	0.0	2.31
or	18.60	16.96	19.21	15.16	25.40	21.13	16.14	18.07	17.23	15.95	18.41	21.26	28.28	27.99
ab	31.88	30.68	31.78	35.57	29.03	39.76	35.99	33.46	33.02	35.13	33.73	35.51	34.60	27.70
an	18.42	14.06	17.40	17.44	12.09	12.04	16.66	16.18	16.01	17.86	15.64	4.57	2.74	4.95
ne	0.0	0.0	0.0	0.0	0.0	0.0	0.0	0.0	0.0	0.0	0.0	0.0	0.0	0.0
le	0.0	0.0	0.0	0.0	0.0	0.0	0.0	0.0	0.0	0.0	0.0	0.0	0.0	0.0
ac	0.0	0.0	0.0	0.0	0.0	0.0	0.0	0.0	0.0	0.0	0.0	0.0	0.0	0.0
ks	0.0	0.0	0.0	0.0	0.0	0.0	0.0	0.0	0.0	0.0	0.0	0.0	0.0	0.0
di/w	0.0	0.0	0.0	0.75	0.0	0.0	0.0	0.0	0.0	0.05	0.0	0.0	0.51	0.0
di:en	0.0	0.0	0.0	0.24	0.0	0.0	0.0	0.0	0.0	0.03	0.0	0.0	0.08	0.0
di:fs	0.0	0.0	0.0	0.54	0.0	0.0	0.0	0.0	0.0	0.02	0.0	0.0	0.47	0.0
hy:e	2.27	2.40	3.84	1.34	1.54	0.71	2.37	2.05	3.06	3.80	3.02	0.51	0.25	1.05
hy:fs	4.52	4.64	3.67	3.09	3.02	3.59	3.42	1.82	3.71	3.53	3.76	3.38	1.41	2.98
ol:fo	0.0	0.0	0.0	0.0	0.0	0.0	0.0	0.0	0.0	0.0	0.0	0.0	0.0	0.0
ol:fa	0.0	0.0	0.0	0.0	0.0	0.0	0.0	0.0	0.0	0.0	0.0	0.0	0.0	0.0
mt	0.57	0.53	0.45	0.46	0.39	0.47	0.42	0.27	0.48	0.42	0.48	0.38	0.20	0.33
hm	0.0	0.0	0.0	0.0	0.0	0.0	0.0	0.0	0.0	0.0	0.0	0.0	0.0	0.0
il	1.27	0.72	0.95	1.02	0.99	1.22	0.83	1.04	1.16	0.77	1.12	0.38	0.14	0.31
ap	0.62	0.26	0.38	0.38	0.31	0.47	0.34	0.41	0.41	0.36	0.41	0.29	0.07	0.10
SUM	100	100	100	100	100	100	100	100	100	100	100	100	100	100
An#[2]	37	31	35	11	29	23	32	33	33	34	32	7	33	
LOI	3.00	2.15	2.20	1.15	3.10	1.50	3.00	2.50	4.10	3.60	3.05	1.39	0.54	3.25
Mg#	33.82	36.64	52.06	30.50	33.51	16.19	42.23	48.90	44.90	53.60	44.67	14.92	17.49	28.96
DI[3]	71.77	75.46	73.20	74.75	81.15	81.16	75.16	77.50	73.72	73.15	74.26	90.13	94.12	87.98
A/CNK	0.99	0.99	0.98	0.94	1.08	0.99	1.03	0.97			1.05	1.00	0.96	1.18

Table A.3. CIPW normative mineral determinations

Norm	1208	1093	1333	1118	1031	1332	1029	1339	1016	1123	1263	1314	1065
q	43.45	35.31	42.11	35.24	30.43	48.47	15.83	58.20	40.62	39.11	36.93	45.80	33.17
c	4.04	0.0	7.47	0.0	0.0	3.74	7.98	5.95	0.42	1.92	1.36	2.14	0.0
or	28.30	22.58	38.33	26.92	27.70	31.85	10.94	7.84	25.68	25.87	28.38	22.92	29.75
ab	15.43	36.54	7.87	32.87	30.84	10.21	54.60	10.16	28.63	21.70	25.73	17.80	26.09
an	4.39	2.52	1.03	1.85	33.14	1.95	7.20	9.08	1.42	8.34	3.92	6.76	7.92
ne	0.0	0.0	0.0	0.0	0.0	0.0	0.0	0.0	0.0	0.0	0.0	0.0	0.0
le	0.0	0.0	0.0	0.0	0.0	0.0	0.0	0.0	0.0	0.0	0.0	0.0	0.0
ac	0.0	0.0	0.0	0.0	0.0	0.0	0.57	0.0	0.0	0.0	0.0	0.0	0.0
ks	0.0	0.0	0.0	0.0	0.0	0.0	4.91	0.0	0.0	0.0	0.0	0.0	0.0
di/w	0.0	0.29	0.0	0.52	5.22	0.0	0.0	0.0	0.0	0.0	0.0	0.0	0.6
di:en	0.0	0.04	0.0	0.11	0.68	0.0	0.0	0.0	0.0	0.0	0.0	0.0	0.25
di:fs	0.0	0.28	0.0	0.45	1.44	0.0	0.0	0.0	0.0	0.0	0.0	0.0	0.36
hy:e	1.02	0.22	0.91	0.27	0.0	1.38	5.52	5.98	1.21	1.54	0.60	1.42	0.62
hy:fs	2.60	1.71	1.61	1.13	0.0	1.70	2.59	2.24	1.56	1.16	2.36	2.52	0.91
ol:fo	0.0	0.0	0.0	0.0	0.0	0.0	0.0	0.0	0.0	0.0	0.0	0.0	0.0
ol:fa	0.0	0.0	0.0	0.0	0.0	0.0	0.0	0.0	0.0	0.0	0.0	0.0	0.0
mt	0.29	0.21	0.19	0.18	0.16	0.21	0.29	0.24	0.18	0.13	0.27	0.28	0.13
hm	0.0	0.0	0.0	0.0	0.0	0.0	0.0	0.0	0.0	0.0	0.0	0.0	0.0
il	0.36	0.22	0.32	0.27	0.23	0.38	0.29	0.24	0.21	0.16	0.33	0.30	0.12
ap	0.12	0.09	0.17	0.19	0.15	0.12	0.08	0.08	0.07	0.08	0.12	0.05	0.07
SUM	100	100	100	100	100	100	100	100	100	100	100	100	100
An#[2]	22	5		28	9		0		5	44	47		23
LOI	3.40	0.7	2.95	0.93	3.23	2.85	10.0	12.3	3.93	8.47	4.80	6.80	3.93
Mg#	30.68	13.18	37.94	21.16	35.06	46.36	71.13	76.37	46.82	60.64	22.34	39.14	45.79
DI[3]	87.18	94.43	88.31	95.03	88.97	90.53	81.37	76.20	94.93	86.68	91.04	86.52	89.01
A/CNK	1.39	0.97	1.80	0.95	0.72	1.42							

Table A.3. CIPW normative mineral determinations

	1319	1233	1234	1235	1236	1237
Norm						
q	61.08	36.95	32.46	30.76	47.25	52.54
c	4.62	1.01	0.69	0.0	1.17	1.57
or	28.72	30.46	26.25	24.18	24.54	24.29
ab	0.18	25.00	29.70	37.03	19.34	14.38
an	2.70	3.07	5.82	3.10	4.15	3.83
ne	0.0	0.0	0.0	0.0	0.0	0.0
le	0.0	0.0	0.0	0.0	0.0	0.0
ac	0.0	0.0	0.0	0.0	0.0	0.0
ks	0.0	0.0	0.0	0.0	0.0	0.0
di/w	0.0	0.0	0.0	0.29	0.0	0.0
di:en	0.0	0.0	0.0	0.05	0.0	0.0
di:fs	0.0	0.0	0.0	0.27	0.0	0.0
hy:e	1.09	0.60	1.20	0.53	0.91	0.87
hy:fs	0.92	2.29	3.05	2.92	2.09	1.99
ol:fo	0.0	0.0	0.0	0.0	0.0	0.0
ol:fa	0.0	0.0	0.0	0.0	0.0	0.0
mt	0.12	0.26	0.34	0.36	0.23	0.22
hm	0.0	0.0	0.0	0.0	0.0	0.0
il	0.38	0.29	0.40	0.40	0.25	0.21
ap	0.19	0.07	0.07	0.12	0.07	0.10
SUM	100	100	100	100	100	100
An#[2]		16			18	21
LOI	3.40	4.00	4.25	1.15	6.45	5.55
Mg#	52.69	23.05	30.85	17.07	33.43	33.84
DI[3]	89.98	92.41	88.41	91.97	92.13	91.21
A/CNK	1.68			0.97		

A.3 Neutron Activation and Atomic Absorption

Twelve samples were analyzed for 32 elements including Au, Ag, As, Sb and base metals at XRAL. These samples were also analyzed for mercury by cold vapor atomic absorption spectrometry. Analyses were performed on altered vein and brecciated rocks. These samples were also crushed and ground in an agate medium at XRAL. Results of these analyses are included in Table 3.

A.4 Petrography

Almost 200 thin sections were prepared for examination either in-house or at San Diego Petrographics, San Diego, CA. Twelve of these sections were stained for potassium-rich mineral identification. This was performed to facilitate the identification of adularia or another potassium-rich alteration mineral that might be a product of the hydrothermal system at Myrick Spring.

The staining method employed is after Hutchison (1974) and entails etch the uncovered, mounted thin section surface in hydrofluoric acid. The section is then immersed in saturated sodium cobaltinitrite and rinsed. The potassium-rich minerals are colored yellow upon immersion in sodium cobaltinitrite. Subsequent petrography demonstrated that potassium is only present in the glassy matrix of most of the samples; however, no K-rich phenocrysts were identified in any of the samples.

After a method employed by Reynolds (J. Reynolds, 1991, personal communication), seventy-two "quick plates" were made for fluid inclusion analysis. A quick plate is a 75-100 mm thick section with no cover slip. The sections were cut to this thickness in order to observe three dimensions of the section. Quick plates allow for both initial petrography and fluid inclusion work to be performed on the same section. The

extremely fine-grained fluid inclusions precluded the application of fluid inclusion investigations.

APPENDIX B

GEOCHRONOLOGY

B.1 Sample Preparation

Twenty-one, 1-3 kg samples were selected for age determinations. Throughout the sample preparation process, many of these samples were discarded because of their insufficient content of potassium-bearing minerals and/or alteration.

Field sampling entailed selecting approximately 2 kg of the least altered portion of a flow or tuff. Generally flows selected for sampling were porphyritic, with what appeared to be unaltered biotite±hornblende±sanidine phenocrysts. Subsequent petrography of these samples usually determined whether the amount and alteration of K-bearing minerals were sufficient to proceed with the mineral separation. In several instances, sanidine was identified in a thin section of a tuff but could not be adequately separated for irradiation.

Selected samples were air-dried and then crushed and pulverized at the U.S. Geological Survey's rock preparation laboratory at the Denver Federal Center. Proper handling and cleaning techniques were employed during the jaw-crushing and pulverizing to ensure that none of the samples were contaminated. The -60 to +140 mesh sieved split of each sample was then removed from the crushed samples for further separation.

Each selected split was washed and dried and then funnelled through a Frantz magnetic separator to remove magnetically susceptible minerals. For biotite separations, paper shaking and hand picking under a binocular microscope were the last separation techniques employed to yield a greater than 99% pure biotite split.

Sanidine- and hornblende-bearing splits were poured into a funnel filled with

bromoform for gravity separation. The specific gravity of bromoform was decreased by diluting it with acetone. After the desired physical separation between mineral fractions was achieved, the heavy fraction (which sunk to the bottom of the funnel) would be drained into a beaker. Repeating this procedure at different specific gravities usually ensured a fairly pure hornblende split. Further separation of hornblende was achieved by hand picking to yield a pure (>99%) split.

Separation of sanidine usually required an additional step. The sanidine-rich split was centrifuged in a sodium paratungstate solution which was also diluted with acetone to achieve the desired specific gravity. Since the glass content of many of the flows is very high, two of the sanidine separates were placed in a an ultrasonic bath for 24 hours. Sanidine is much more refractory than glass which becomes totally disaggregated during ultrasonic treatment.

Pure mineral separates were washed, redried, weighed and packaged in foil. Samples were then placed in a glass container that was loaded into the reactor. The coordinates of each sample and standard within the glass container, and the coordinates of the glass container within the reactor were recorded so that an accurate J-value could be calculated. All samples were irradiated for 30 hours in the T.R.I.G.A. reactor (parameters of which are described in Dalrymple, 1981). After approximately two weeks of cooling, the irradiated samples were loaded into a glass sidearm above the furnace in the U.S. Geological Survey's mass spectrometer laboratory.

B.2 40Ar/39Ar Methodology

Use of the $^{40}Ar/^{39}Ar$ technique requires a mineral separate to be irradiated in a nuclear reactor with a mineral of known age (standard). $^{39}Ar_K$ is generated from ^{39}K in

the sample by fast neutrons that cause the reaction $^{39}K(n,p)^{39}Ar$. In addition to $^{39}Ar_K$ produced from the positron decay of ^{39}K, $^{40}Ar^*$ is produced from ^{40}K, ^{39}Ar is also produced from ^{42}Ca and ^{36}Ar is produced from ^{40}Ca. Corrections for these isotopes are reactor-specific and are made by measuring argon production ratios generated by the irradiation of pure potassium and calcium salts. All samples analyzed in this study were irradiated on the U.S. Geological Survey's TRIGA reactor in Denver, CO. Argon production ratios are listed in Snee et al. (1983). A correction for atmospheric ^{40}Ar is made by using ^{36}Ar and an $^{40}Ar/^{39}Ar$ ratio of 296.6 (L. Snee, personal communication, 1992). A correction was also made for the production of unstable, reactor-produced ^{37}Ar.

The irradiated sample is then loaded into a furnace. Heating the sample at a fixed temperature yields a gas volume which is then cleaned of impurities and expanded into a gas-source mass spectrometer. $^{40}Ar/^{39}Ar$ ratios are determined after Ar isotope corrections for atmospheric contamination and neutron reactions with K and Ca are made in the spectrometer. This process is repeated for each gas volume driven off of the sample at incrementally higher temperatures (steps) until all of the argon has been driven off. Generally by the last and highest temperature increment, all gases have been driven off; this temperature increment essentially destroys the remaining sample and partially cleans out the furnace for the next sample. This entire process is repeated for each unknown sample and for the standard.

The age, t, of an unknown sample is derived from the following equation:

$$t = 1/\lambda \ln (^{40}Ar^*/^{39}Ar_K J + 1) \qquad \text{(i)}$$

where λ is the decay constant of ^{40}K, $^{40}Ar^*$ is the radiogenic daughter Ar produced from

the decay of ^{40}K and ^{40}Ca, ^{39}Ar is the potassium-derived argon, and J is the flux parameter, calculated according to the relationship:

$$J = (e^{\lambda tm} - 1)/(^{40}Ar^{*}/^{39}Ar)_m \qquad \text{(ii)}$$

Simplistically put, the flux parameter is a quantitative measurement of the amount of radiation (neutron flux) a particular sample experiences in the nuclear reactor. Tm is the age of the flux monitor (standard) and $^{40}Ar^{*}/^{39}Ar_K$ is the measured ratio of the standard. The standard is hornblende MMhb-1 (Minnesota hornblende) with a K-Ar age of 520.4±1.7 Ma (Samson and Alexander, 1987).

The age of the unknown sample is determined by comparing its $^{40}Ar^{*}/^{39}Ar_K$ ratios with those from the standard. The abundances of potassium and argon need to be measured independently with the K-Ar age-dating method. Utilizing independent measuring techniques on separate aliquants of potassium and argon could potentially introduce error into the determined dates because different quantities of potassium and argon could exist in each aliquant. Only Ar isotopes need to be measured in a gas source mass spectrometer with the $^{40}Ar/^{39}Ar$ age dating method thereby mitigating against any sample inhomogeneities.

The incremental or step heating of selected samples employed in this $^{40}Ar/^{39}Ar$ technique has the added benefit (over K-Ar methods) of yielding a series of ages from one sample. This spectrum of ages can be interpreted to reveal tectonic or alteration episodes experienced by the sample. Both altered and unaltered samples yield a plateau of dates that potentially offer a more precise age than does K-Ar dating.

B.3 40Ar/39Ar Calculations

The $^{40}Ar^*/^{39}Ar_K$ (Table 3) is calculated from the relationship:

$$F = {}^{40}Ar^*/^{39}Ar_K = \{(40Ar/39Ar) - 296.6[(36Ar/39Ar) - (36Ar/37Ar)Ca(37Ar/39Ar)] - (40Ar/39Ar)K\}/1 - (39Ar/37Ar)Ca(37Ar/39Ar) \quad \text{(iii)}$$

The number of ^{39}Ar atoms formed in the sample by neutron irradiation is:

$$^{39}Ar = {}^{39}K\ \Delta T \int \varphi(\varepsilon)\sigma(\varepsilon)\, d\varepsilon \quad \text{(iv)}$$

where ^{39}K is the number of atoms of this isotope in the irradiated sample, ΔT is the length of time for the irradiation, $\varphi(\varepsilon)$ is the neutron flux density of energy ε and $\sigma(\varepsilon)$ is the capture cross section for ^{39}K for neutrons having energy, ε. The integration encompasses the entire energy spectrum created by the flux of fast neutrons.

The number of $^{40}Ar^*$ atoms present in the sample due to the decay of ^{40}K during the sample's lifetime is illustrated by equation xiii. The $^{40}Ar^*/^{39}Ar_K$ ratio after irradiation is:

$$^{40}Ar^*/^{39}Ar = \lambda_e/\lambda\ {}^{40}K/{}^{39}K\ 1/\Delta T\ (\int \varphi(\varepsilon)\sigma(\varepsilon)\, d\varepsilon)^{-1}\ (e^{\lambda t} - 1) \quad \text{(v)}$$

If 1/J is equal to $[\lambda_e/\lambda\ {}^{40}K/{}^{39}K\ 1/\Delta T\ (\int \varphi(\varepsilon)\sigma(\varepsilon)\, d\varepsilon)^{-1}]$, then substituting J into equation xviii yields:

$$^{40}Ar^*/^{39}Ar_K = (e^{\lambda t} - 1)/J \quad \text{(vi)}$$

Since the energy spectrum of the fast neutrons in the reactor and the capture cross section

of ^{39}K are not well known, J is a difficult value to determine; however, by irradiating a mineral of known age (flux monitor, m, or standard) with the samples of unknown age, then J can be calculated as:

$$J = (e^{\lambda t_m} - 1)/(^{40}Ar^*/^{39}Ar) \qquad \text{(vii)}$$

where t_m is the known age of the flux monitor and $^{40}Ar^*/^{39}Ar_K$ is the measured value of this ratio from the hornblende monitor. By determining the $^{40}Ar^*/^{39}Ar_K$ value of the monitors from mass spectrometry, the J values for the flux monitors can be determined. Since most irradiation packages contain many samples of unknown age, flux monitors are precisely located throughout the irradiation package that will be dropped into the reactor chamber. The determined J values are then plotted on a graph with the ordinate axis representing a measured distance from the center line of the reactor chamber. Since the location of each unknown in the reactor chamber is also precisely known, then J values for the unknown can be derived by interpolating between the known J values for the flux monitors that are positioned directly above and below each unknown sample.

The $^{40}Ar^*/^{39}Ar_K$ ratios of the unknown samples are then measured and the dates are derived by the following equation:

$$t = 1/\lambda \ln (^{40}Ar^*/^{39}Ar\ J + 1) \qquad \text{(viii)}$$

The flux monitor used for this study contains 1.555% K and 1.624×10^{-9} mole/g of $^{40}Ar^*$ (Snee et al., 1988).